of the CERAMIC SOCIETY of Japan, International Edition 第97集 第1128号 平成元年8月25日発行（毎月1回25日発行）ISSN 0912-9200

Journal of the CERAMIC SOCIETY of Japan, International Edition

Vol.97 Aug. 1989

Papers from Nippon Seramikkusu Kyokai Gakujutsu Ronbunshi, Vol.97 No.8 1989

NI SERAMIKKUSU KYOKAI GAKUJUTSU RONBUNSHI Vol.97 1989

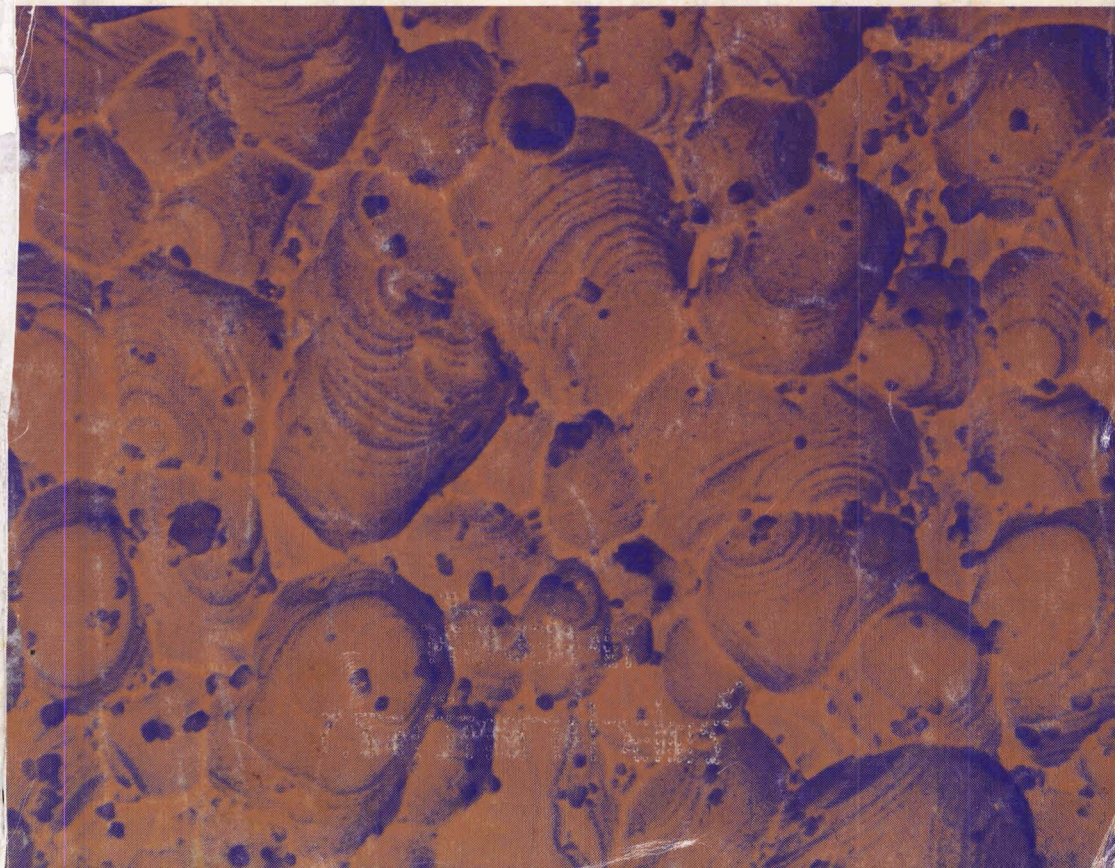

Journal of the CERAMIC SOCIETY of Japan, International Edition

Vol.97 No.8
Aug. 1989

Published Monthly by
FUJI TECHNOLOGY PRESS LTD.
7F Daini Bunsei Bldg.
11-7, Toranomon 1-chome
Minato-ku, Tokyo 105, Japan
Tel:(03)-508-0051
Fax:(03)592-0648

One year subscription
Air Mail ¥200,000

CONTENTS

Papers, Letters and Notes

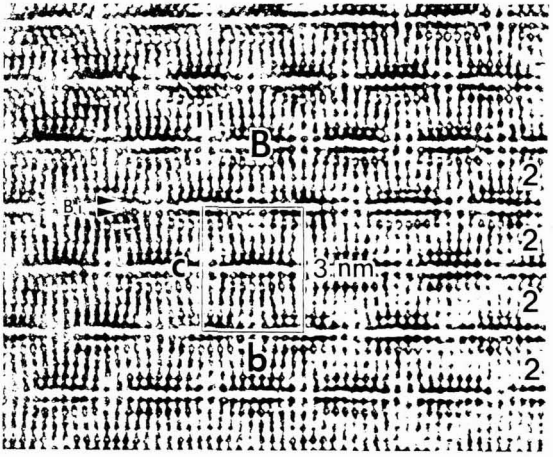

High resolution electron microscope photograph of the modulation doped structure of $Bi_2Sr_2CaCu_2O_y$ (T_c=80K) in the [100] direction. Figures at right side indicate number of copper layers, symbol B indicates bismuth rich region.

Structure of MgO Films Prepared by Ion Beam Sputtering

Tsuguo Ishihara and Muneyuki Motoyama

Industrial Research Institute of Hyogo Prefecture
3-1-12, Yukihira-cho, Suma-ku, Kobe 654, Japan

Preferred orientation and microstructure of MgO films prepared by ion beam sputtering were investigated. The crystallographic orientation of MgO films was a function of the substrate angle(δ), O_2 gas partial pressure (P_{O_2}) and the substrate temperature(T_S). As δ changed from 90° to 0°, the transmission electron diffraction(TED) pattern of the films deposited in P_{O_2} of 1×10^{-4} Torr at T_S=R.T. changed from a random orientation to the (111) preferred orientation in which the crystallographic (111) plane was parallel to the substrate surface. An increase in P_{O_2} from 0.1×10^{-4} to 10×10^{-4} Torr caused the (111) preferred orientation. At T_S>100°C, the TED pattern of the films on NaCl(200) deposited with δ=90° showed epitaxial growth in contrast with a random orientation at T_S<100°C. Annealing below 500°C did not change the orientation and size of the crystallite. Annealing above 1000°C for 30 min, however, caused crystallite growth from 5nm to 20nm without any change in orientation. This size is still smaller than that of the crystallites deposited on a heated substrate. The origin of the crystallographic preferred orientation of the MgO thin film deposited by ion beam sputtering was explained in terms of the growth competition. The (111) preferred orientation becomes predominant in the growth competition over others with decreasing the arrival ratio of Mg/O.

[Received August 20, 1988; Accepted May 16, 1989]

Key-words: MgO film, Preferred orientation, Microstructure, Ion beam sputtering

1. Introduction

MgO film has recently been investigated[1-9] with special attention to the excellent high temperature chemical stability, electrical insulating property, optical property and thermal conductance. Many electron and X-ray diffraction investigations have shown that the crystal orientation of vapor deposited MgO films depends on deposition process.

Chemical vapor deposition (CVD) processes[1] have been developed using organometallic compounds for depositing MgO. The crystallite of MgO films deposited at 310°C or above by CVD was found to possess a (200) preferred orientation in which the crystallographic (200) plane is parallel to the substrate surface.

The crystal orientation of MgO films by thermal evaporation onto amorphous and single crystal substrates varied with film thickness. According to the studies by Aboelfotoh et al. on amorphous substrates, the MgO films initially nucleate in a random orientation. As the film thickness increases, a (111) preferred orientation develops on the surface.[2,3,5] On single crystal substrates, the orientation of crystallite in thin films (below 3nm) depends on the crystal face and temperature of the substrates. In the range of thickness from 3 to 50nm, the crystallite tends to orient randomly, and in thick films (above 50nm) the surface structure has a (111) preferred orientation independent of the substrate orientation and temperature.[4,6]

MgO film formed by rf-sputtering of MgO target was found to have a strong tendency to form a columnar structure of the (200) orientation normal to the substrate. However, by decreasing the sputtering pressure less oriented coatings of denser structure can be obtained at a moderate temperature.[7,8]

Reactive ion beam sputter deposition (RIBSD) method[9] using a magnesium target was found to produce smooth MgO film dielectrics with low electrical loss, good mechanical stability, and excellent reproducibility.[9] This technique has received attention with respect to the low temperature production of ceramic thin films for recent ten years. However, microstructure and preferred orientation of the MgO film deposited by RIBSD have not been investigated yet, although these are the important aspects of the thin film.

In this study, we report on the influence of preparation conditions of MgO films on the crystallographic orientation and on the microstructure of the film in comparison with the previously reported results.

2. Experimental

MgO films were prepared by a Koon Denki ion beam sputtering apparatus. The apparatus and preparation condition were described in Fig.1 and Table 1. The magnesium target was a metallic disk of 4N grade with 100mm diameter and 5mm thickness. Argon ion beam generated in a Kaufman-type ion gun was accelerated to 4 - 5kV energy with 10 - 12mA current and sputtered the target at an incident angle of 30°. The target was located at a distance of 200mm from the acceleration grids of the 40mm-diameter ion source. An aluminum plate with a 40mm-diameter hole was placed between the ion gun and the target to reduce the ion beam spread. The ion beam spot on the target was elliptic with its major axis of about 60mm and its minor axis of about 50mm. The sputtering chamber was once evacuated to a pressure of 2×10^{-6} Torr, and then argon gas was introduced to a pressure of 1×10^{-4} Torr. During the deposition, oxygen gas was also introduced to the partial pressure (P_{O_2}) between 0.1×10^{-4} and 10×10^{-4} Torr. The resulting deposition rates were 0.05 to 0.3nm/min. Film thickness was determined from crystal

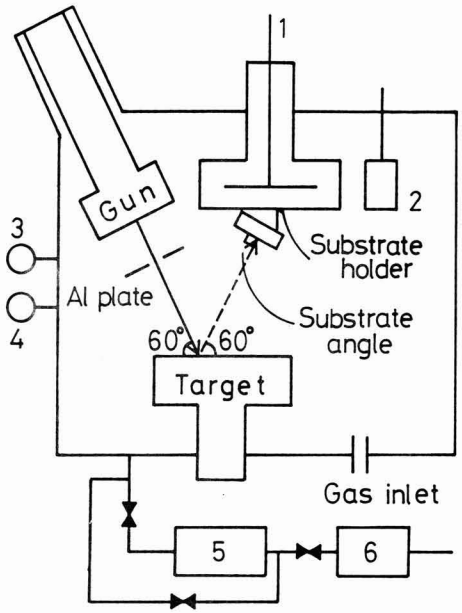

Fig. 1. Schematic diagram of the ion beam sputtering apparatus and relationship between δ and incident ion beam. 1:substrate heater; 2: thickness monitor; 3: Pirani gauge; 4: Penning's gauge; 5: molecular turbo pump; 6: rotary pump.

Table 1. Deposition conditions.

Target	Mg(99.99%) 100ϕ X 5T
Ar^+ ion beam	
pressure	1.0×10^{-4} Torr
accelerated voltage	4-6 kV
current	10-12 mA
spot size on the target	elliptic with its major axis of about 60mm and its minor axis of about 50mm
Reaction gas	
pressure	0.1×10^{-4}, 1.0×10^{-4}, 10×10^{-4} Torr
Substrate	
material	collodion membrane, NaCl(200)
temperature	R.T., 100, 200, 300°C

quartz thickness monitor readings. The thickness was 20 to 30nm. The substrates used were collodion membrane on a Pt mesh and cleaved single crystal NaCl(200). The substrates were placed at an angle of 30° from the target normal and on the incident plane of the ion beam. The incident angles of sputtered particles measured from the substrate surface (or the substrate angle δ) were chosen to be 0°, 60° and 90°. In Fig. 1, δ is illustrated to be 90°. The distance between the target and the substrate was adjusted to be 50-70mm. The substrate temperature(T_S) during film deposition was set at a room temperature (R.T.), 100°C, 200°C and 300°C. The microstructure and the crystallographic orientation of the MgO film were examined by an analytical electron microscope (JEOL 2000FX). Possible impurities in the MgO films originated from the ion source, the aluminum plate and the other parts of the apparatus such as the target holder were not detected by EDX detector. The reason why the impurities originated from the ion source were not detected is because of the use of a carbon electrode for a rf-electrode and an acceleration electrode.[10] The reason why the impurities originated from the hole edge of the aluminum plate were not detected is probably because of the low sputtering yield of an aluminum atom by an argon ion beam and the low current density of an argon ion near the aluminum hole edge.

3. Results

3-1. The Effect of Substrate Angle on the Diffraction Patterns

Figure 2 shows the transmission electron diffraction (TED) patterns of films deposited on collodion membrane at T_S=R.T., $P_{O_2}=1.0\times10^{-4}$ Torr and each δ. All the diffraction patterns were not spots but continuous rings, indicating that the films consist of fine crystals. It is clear from these diffraction patterns that the crystallite orientation changes with δ. At $\delta=0°$ the TED pattern (Fig. 2(a)) showed a strong (220) diffraction ring and weak (111) and (200) diffraction rings. At $\delta=60°$ the relative intensity of the (111) and (200) diffraction rings (Fig. 2(b)) became stronger than in Fig. 2(a). At $\delta=90°$ the relative intensity of the diffraction rings (Fig. 2(c)) approached those of the random orientation such as MgO fine powder as shown in Fig. 2(e). Figure 3 shows the relationship between TED patterns and preferred orientations in the case of the face-centered cubic lattice. From Fig. 3 the MgO film of the TED pattern (Fig. 2(a)) is known to possess a (111) preferred orientation. On a cleaved NaCl(200) substrate, the TED patterns showed the same tendency. Therefore, the crystallographic orientation at T_S=R.T. is not affected by substrates.

3-2. The Effect of O_2 Gas Partial Pressure on the Diffraction Patterns

Figure 4 shows TED patterns of films deposited on collodion membrane at $\delta=60°$, T_S=R. T. and each P_{O_2}. At $P_{O_2}=0.1\times10^{-4}$ Torr the TED pattern (Fig. 4(a)) showed diffraction rings assigned to a random orientation. On the other hand, in the TED pattern (Fig. 4(b)) of the film deposited at $P_{O_2}=1.0\times10^{-4}$ Torr, the relative intensity of the (200) diffraction ring decreased, while that of the (220) diffraction ring increased. Further, at $P_{O_2}=10\times10^{-4}$ Torr, only the (220) diffraction ring was observed. These results suggest that as P_{O_2} increases, the TED pattern changes from a random orientation to the (111) preferred orientation.

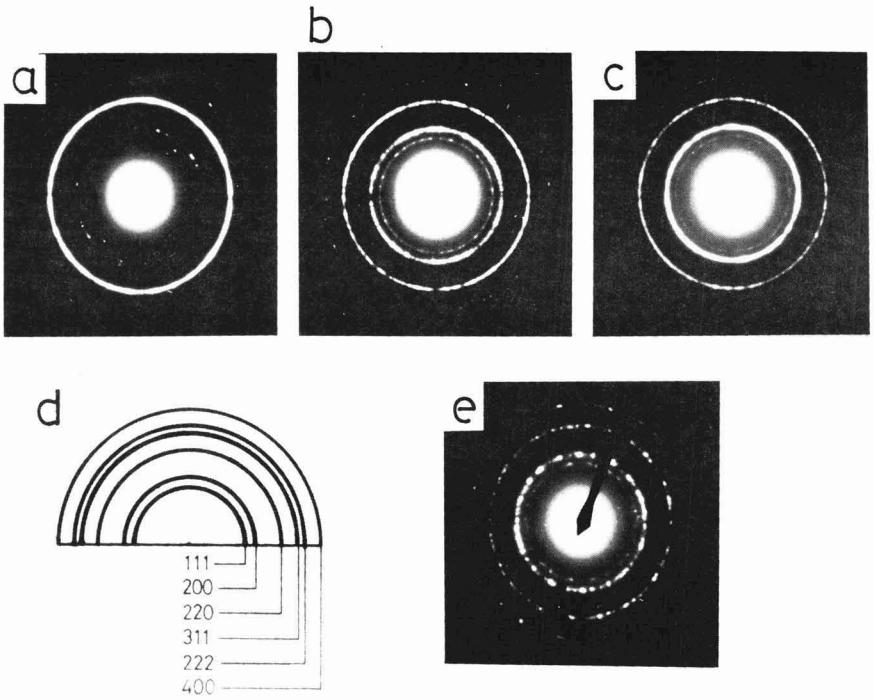

Fig. 2. TED patterns of MgO film deposited on collodion membrane at T_S=R.T., P_{O_2}=1.0×10^{-4} Torr and δ (a)0°, (b)60° and (c)90°. (d) schematic representation of the diffraction pattern, (e) TED pattern of MgO fine powder.

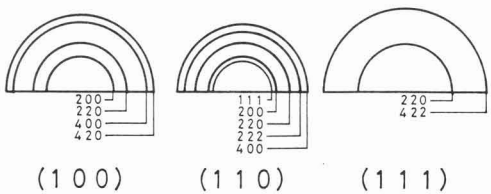

Fig. 3. The relationship between TED patterns and preferred orientations in the case of face-centered cubic lattice.

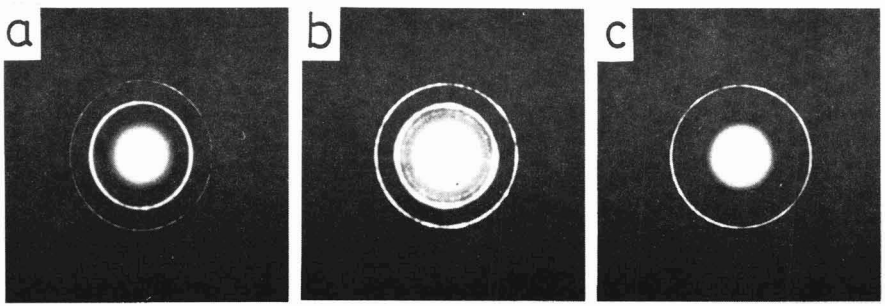

Fig. 4. TED patterns of MgO film deposited on collodion membrane at T_S=R.T., δ=60° and P_{O_2} (a) 0.1×10^{-4}, (b) 1.0×10^{-4} and (c) 10×10^{-4} Torr.

3-3. The Effect of Substrate Temperature on the Diffraction Patterns

Figure 5 shows the TED patterns of films deposited on a cleaved NaCl (200) surface at $\delta=60°$, $P_{O_2}=10\times10^{-4}$ Torr and each T_S. At T_S=R.T. the TED pattern showed only diffraction rings assigned to a random orientation of crystallite as mentioned before. The TED pattern changed with increase in T_S. At T_S=100°C the TED pattern showed both diffraction rings and spots. And then at T_S=200°C, the TED pattern showed the diminution of diffraction rings, and further at T_S=300°C it showed only diffraction spots. The TED pattern (Fig. 5(d)) shows epitaxial growth of MgO films on NaCl(200). From these results it is confirmed that the interaction between the substrate and MgO molecules becomes weak with T_S and then the film grows epitaxially.

3-4. The Effect of Annealing of Deposited Film on the Structure

The change of the preferred orientation and the crystallite size of the films subjected to the annealing was examined. Figure 6 shows the TED patterns and high resolution electron microscope (HREM) images obtained from the film (a) at $\delta=0°$, T_S=R.T. and $P_{O_2}=1.0\times10^{-4}$ Torr deposited on collodion membrane and the films annealed for 30min in air at (b) 500°C and (c) 1000°C. The as-deposited film appeared to be a continuous sheet, the average crystallite size being about 5nm. The continuous rings of the TED patterns in Fig. 2 are attributed to these fine crystallites showing the (111) preferred orientation. The 500°C annealing did not cause any change in TED pattern. The HREM image showed that crystallite size did not change. However, Fig. 6(c) shows the 1000°C annealing caused no change in crystallographic orientation but a change from a continuous ring to a discrete ring. This change of the ring shape arises from the growth of the crystallite up to 20nm in size which is observed in the HREM image in Fig. 6(c). The microstructure of the film annealed at 1000°C was different from the one deposited on cleaved NaCl(200) at $\delta=60°$, $P_{O_2}=1.0\times10^{-4}$ Torr and T_S=300°C (Fig. 6(d)).

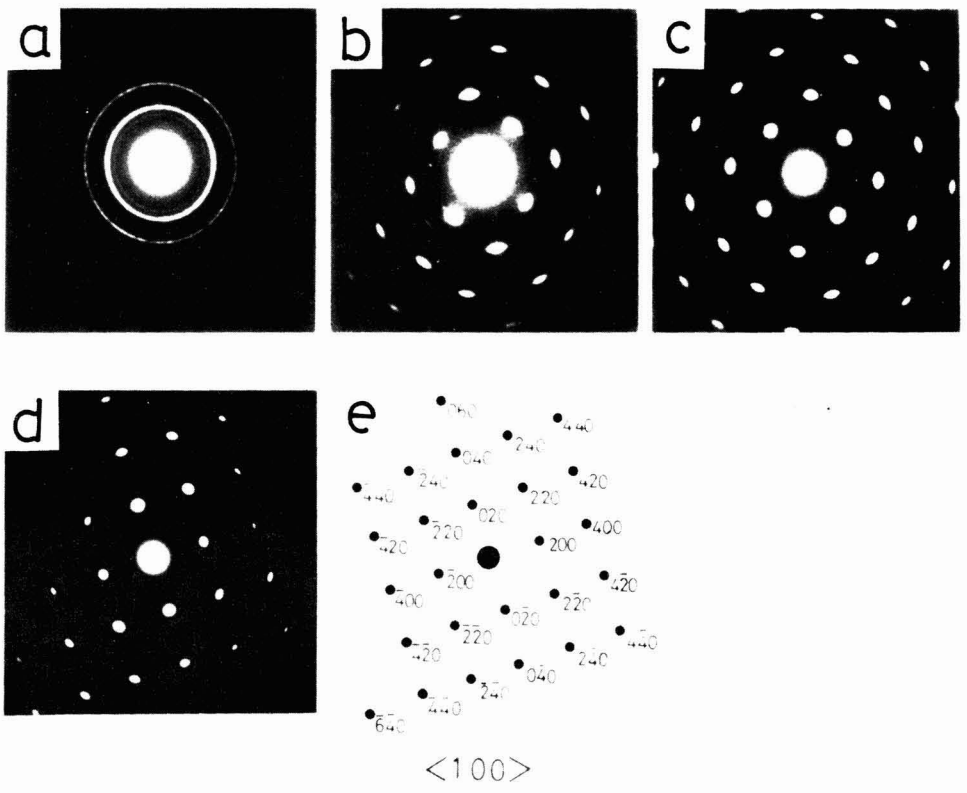

Fig. 5. TED patterns of MgO film deposited on NaCl(200) at $\delta=60°$, $P_{O_2}=1.0\times10^{-4}$ Torr and T_S (a) R.T., (b) 100°C, (c) 200°C and (d) 300°C. (e) interpretation of the diffraction pattern(d).

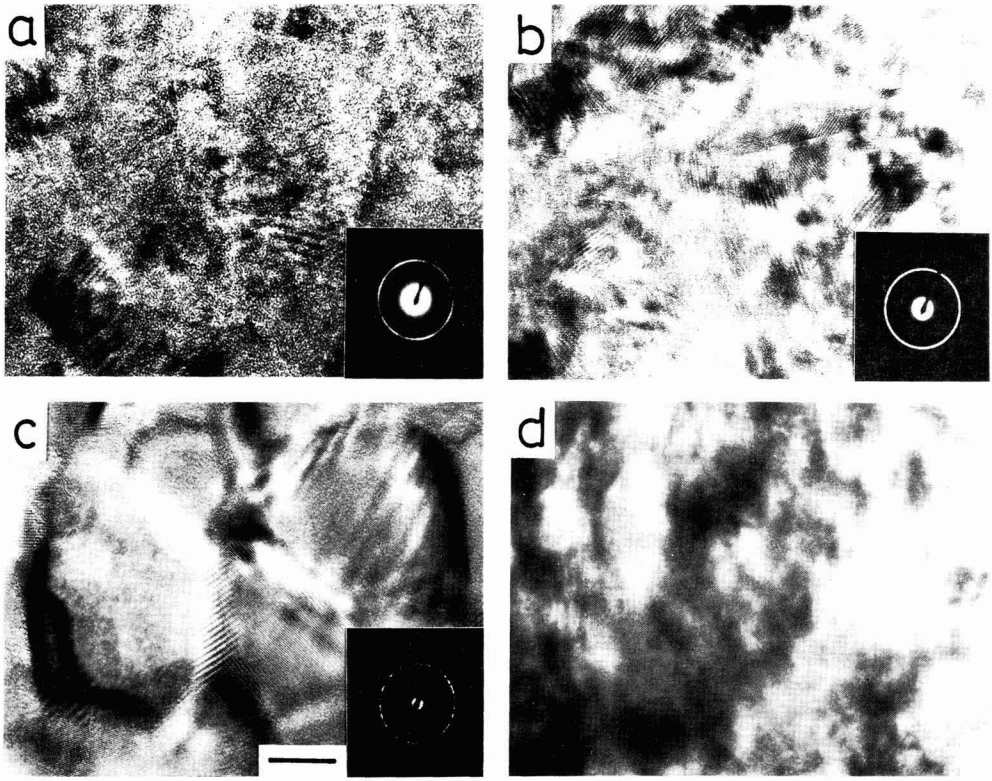

Fig. 6. HREM images and TED patterns of MgO film (a) deposited at T_S=R.T., P_{O_2}=1.0×10^{-4} Torr and δ=60°, (b) annealed at 500°C, (c) annealed at 1000°C for 30 min in air and (d) deposited on cleaved NaCl(200) at 300°C. All micrographs in this figure are presented to the same magnification.

4. Discussion

The (200) preferred orientation appeared in CVD or rf-sputtering MgO films has been explained by the Bravais's rule,[1,7] that is, the crystal orientation of a minimum energy configuration takes place. The (111) preferred orientation appeared in thermally evaporated films has been considered to be caused by the growth competition between differently oriented crystals.[5] The growth competition is due to the differences in the number of ions or molecules condensing on differently oriented crystals. For example, the condensation rate on <111> oriented crystals is higher than that on <200> oriented crystals when the ions or molecules arrive at the substrate at the rate of 130-150nm/min.[5]

The (111) preferred orientation observed in the present experiment can be also explained by the growth competition scheme, judging from the resemblance of the δ dependence of the crystal orientation to its P_{O_2} dependence. The (111) preferred orientation took place at a small δ and a high P_{O_2}; both of which are connected with the low value of the arrival ratio of Mg/O as shown in Fig. 7. The oxygen excess acts to the advantage of <111> oriented crystallites in the growth competition through the following mechanism; the creation ratio of crystalline nuclei with low surface free energy is larger than that of crystalline nuclei with high surface free energy as the magnesium particles energy lowers. The magnesium particles lose some of their excess energy by transferring it to the excess oxygen. <111> oriented crystallites develop in the growth competition as a (111) plane has minimum surface free energy. A similar result is found in the dynamic mixing method,[11] that is, the preferred orientation of TiN films is dependent on the arrival ratio, Ti/N on the substrate. In their paper, it is considered that the variation of orientation arises from the variation of the energy deposition rate from the ion beam per titanium atom. The energy deposition rate is determined by the arrival ratio. In this experiment, it is not clear whether the same energy deposition takes place in the low energy particles system. But, the change of preferred orientation with the arrival ratio resembles Sato's result.[11]

The small δ and high P_{O_2} are also connected with

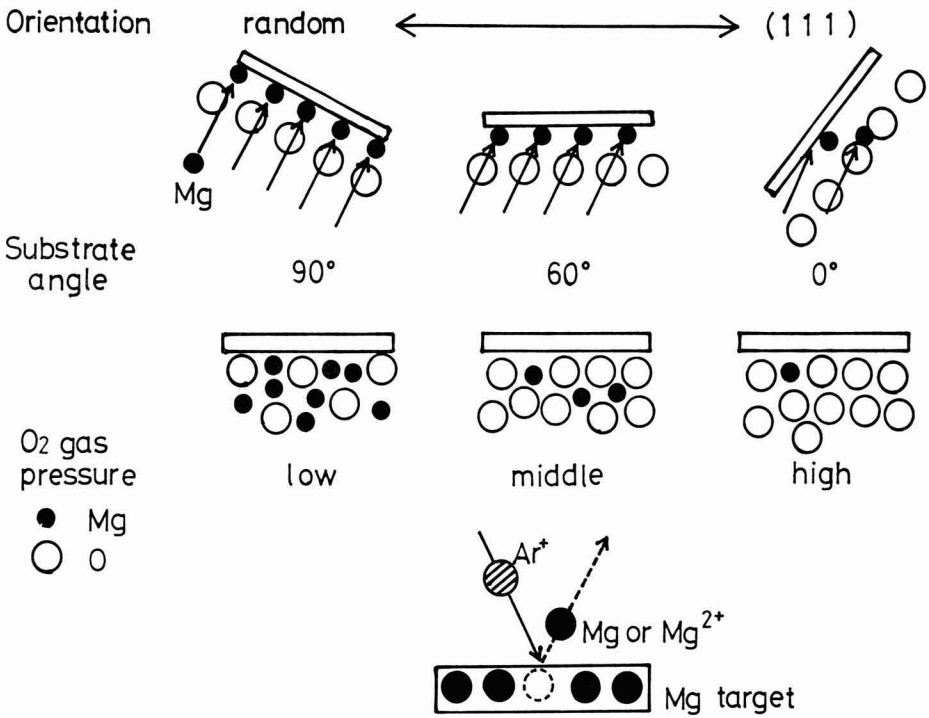

Fig. 7. Schematic diagram of relationship between crystallite orientation, δ and P_{O_2}.

the low deposition rate, the former through the geometrical sinδ scheme and the latter through the low sputtering rate of the oxidized target surface. The low deposition rate may act to the advantage of <111> oriented crystallites in the growth competition. But we don't think that the (111) preferred orientation arises only from the low deposition rate. If the (111) preferred orientation is caused by the low deposition rate, the size of crystallites should become large with decreasing the deposition rate. As shown in Fig. 6(a), however, all the films of the present experiment consisted of small crystallites regardless of both δ and P_{O_2}.

We deny the possibility that high energy species involved in this RIBSD process (such as energetic neutralized argons) might affect the preferred orientation because no trace of the argon was detected in the film by the analytical electron microscope.

5. Conclusion

The orientation of MgO films prepared by ion beam sputtering was strongly influenced by the substrate angle(δ), O_2 gas partial pressure (P_{O_2}) and the substrate temperature (T_S). As δ changed from 0° to 90°, the TED pattern of the films changed from the (111) preferred orientation to a random orientation. As P_{O_2} increased from 0.1×10^{-4} to 10×10^{-4} Torr, the TED pattern changed from a random orientation to the (111) preferred orientation. At $T_S > 100$°C, the TED pattern of the films on NaCl(200) showed epitaxial growth in contrast with a random orientation at $T_S < 100$°C. Annealing below 500°C did not change the orientation and size of the crystallite. Annealing above 1000°C, however, caused crystallite growth from 5nm to 20nm in size without any change in orientation. This size is still smaller than that of the crystallites deposited on a heated substrate. The Mg/O ratio on the substrate at T_S=R.T. was considered to be the most important factor to affect the crystallographic orientation of the MgO thin film.

Acknowledgments:

The authors would like to thank Mr. K. Shibatomi of JEOL Ltd. for HREM observations.

References:

1) K. Kamata, Y. Shibata and Y. Kishi, J. Mater. Sci. Lett., 3, 423-426 (1984).
2) M.O. Aboelfotoh, J. Vac. Sci. Technol., 10(5), 621-625 (1973).
3) M.O. Aboelfotoh, Appl. Phys. Lett., 24(8), 347-349 (1974).

4) M.O. Aboelfotoh, J. Vac. Sci. Technol., 12(1), 67-70 (1975).
5) M.O. Abeolfotoh, K.C. Park and W.A. Pliskin, J. Appl. Phys., 48(7), 2910-2917 (1977).
6) M.O. Aboelfotoh, J. Appl. Phys., 49(5), 2770-2776 (1978).
7) K. Kamata, H. Hosono and T. Yamashita, Yogyo-Kyokai-Shi., 94, 910-912 (1986).
8) P. Vuoristo, T. Mantyla and P. Kettunen, J. Vac. Sci. Technol., A4(6), 2932-2936 (1986).
9) A.F. Hebard, A.T. Fiory, S. Nakahara and R.H. Erick, Appl. Phys. Lett., 48(8), 520-522 (1986).
10) M. Motoyama, K. Ishima, M. Kashihara and S. Koshiba, Appl. Surface Sci., 33/34, 567-577 (1988).
11) M. Sato, K. Fujii, M. Kiuchi and F. Fujimoto, Nuclear Instrument and Method in Physics Research., in press.

This article appeared in English in Nippon Seramikkusu Kyokai Gakujutsu Ronbunshi (Japanese version), Vol. 97, No.8, 1989.

A BET Surface Area Measurement Technique for Evaluation of Crack Extension in Alumina Pellets Subjected to Thermal Shock

Masaomi Oguma and Takeo Motomiya

Nippon Nuclear Fuel Development Co., Ltd.
2163, Narita-cho, Oarai-machi, Higashi-ibaraki-gun, Ibaraki 311-13, Japan

Crack initiation and propagation behavior in alumina pellets subjected to thermal shock with various temperature differences (ΔT) were investigated. Change in specimen surface area, i.e., in crack surface area, resulting from the thermal shock was measured non-destructively by a BET surface area measurement technique. The extent of crack propagation at a certain ΔT was compared on the specimens subjected to only a single thermal shock and specimens repeated thermal shock with a gradual increase in the temperature difference up to the ΔT. The single thermal-shocked specimens sustained severer damage than the repeatedly thermal-shocked specimens. Good coincidence was obtained between calculated and measured crack surface areas, demonstrating the validity of the BET technique as a non-destructive method for evaluating the thermal shock damage.

[Received December 21, 1988; Accepted May 16, 1989]

Key-words: Thermal shock, Crack propagation, Crack surface area, BET, Alumina, Non-destructive measurement

1. Introduction

Ceramic materials are known, because of inherent brittleness, to be susceptible to catastrophic failure under thermal shock conditions.[1,2] Therefore it is necessary to understand accurately not only initiation of thermal shock crack, but also propagation of the crack caused by subsequent thermal shock in order to employ ceramic materials as structural or component material under conditions in which environmental temperature varies frequently.[3,4] The relation between thermal shock temperature difference (ΔT) and damage of ceramic materials is usually evaluated in terms of the change in fracture strength of specimens before and after thermal shock testing.[4-10] The fracture strength measurement method provides adequate information on the crack initiation,[4-11] but no information on how extensive the cracks propagate inside the specimen as ΔT increases, because it is a destructive method. Non-destructive methods, such as an acoustic emission method[12] or an ultrasonic method,[13] are also able to detect crack initiation. However, since these methods have a generally poor resolution to detect the extent of inside cracks, sufficient information which can allow precise evaluation of the crack extension as a function of ΔT has not been provided so far by them.

In this paper, the crack surface areas of alumina pellets subjected to thermal shock at various ΔT are evaluated non-destructively by applying the BET (Brunauer - Emmett - Teller) method[14] in which surface of a body is determined in terms of change in gas pressure due to absorption onto the body surface. These crack surface areas with ΔT are compared with the areas derived from a theoretical consideration based on a thermal shock theory proposed by Hasselman.[15] Differences in thermal shock damage behavior are also discussed for specimens which are thermal-shocked at the same ΔT but with different ways of thermal shocking.

2. Theoretical Consideration

Assuming that a ceramic material contains mechanical flaws in the form of Griffith cracks which are of uniform size, with a length of l, and distributed uniformly throughout the material with a density of N, then crack propagation, caused by thermal shocking, is taken to occur by simultaneous extension of all the cracks without interaction between neighboring cracks. The absence of external forces is also assumed. Under thermal shock conditions, the total energy per unit volume, W, is the sum of the elastic energy, Wp, being stored in the material plus the fracture energy of the cracks, Wg. Using the theoretical solution of Walsh's study on the compressibility of rock,[16] and plane strain condition in the material,[17] Wp is given by

$$Wp = \frac{3(1-2\nu)S^2}{2E}\left(1+\frac{16(1-\nu^2)}{9(1-2\nu)}N l^3\right)^{-1} \quad \cdots\cdots (1)$$

where ν is Poisson's ratio; E, Young's modulus; S, the thermal stress, and S is expressed as

$$S = \frac{E\alpha}{(1-2\nu)}\phi\,\Delta T \quad \cdots\cdots (2)$$

where α is the thermal expansion coefficient; and ϕ, the nondimensional thermal stress which indicates the severeness of the thermal shock.[1] The ϕ is given by $\phi=(1+4/B)^{-1}$, where B is the Biot's modulus, $B=h\,r/K$; r, the specimen radius; h, the surface heat transfer coefficient; and K, the thermal conductivity.

Rearranging Eqs. (1) and (2), and using the expression for the fracture energy, $Wg=2\pi N\gamma l^2$, where γ is the fracture surface energy, the total energy per unit volume, W, can be calculated as

$$W = \frac{3(\alpha\Delta T)^2 E\phi^2}{2(1-2\nu)}\left(1+\frac{16(1-\nu^2)}{9(1-2\nu)}N l^3\right)^{-1} + 2\pi N\gamma l^2 \quad \cdots\cdots (3)$$

When the initial cracks (length=l_o) are exceedingly short, the elastic energy reduction due to new crack formation exceeds the fracture surface energy increase.[4,15] The final crack length, l_f, is given from Eq. (3) by equating the energies of the system at the initial and final stages, $W(l_o) = W(l_f)$.

$$\frac{3(\alpha\Delta T)^2 E\ \phi^2}{2(1-\nu)} = 2\pi N\ \gamma l_f^2 \quad \cdots\cdots (4)$$

The surface area of a disk shaped crack, a, is given as $a=2\ \pi l_f^{\ 2}$ so that the total crack surface area A_1 existing in volume V can be calculated by

$$A_1 = \frac{3\alpha^2\ E\ \phi^2\ V}{2\gamma(1-\nu)}\ \Delta T^2 \quad \cdots\cdots (5)$$

Equation (5) indicates that when a virgin ceramic material with initially short cracks is thermal-shocked and develops crack extension, the crack surface area increases proportionally to the square of ΔT.

Considering the case in which the newly developed cracks with a length of l_f extend further, exceeding the length of l_f on a successive thermal shock with a higher ΔT. Then, the crack length has already become long enough to grow in a static manner. Therefore the crack length can be derived by substituting Eq. (3) in the crack extension condition, $dW/dl=0$, followed by rearrangement,

$$\frac{2(\alpha\Delta T)^2\ E\phi^2(1-\nu^2)}{(1-\nu)}\left(1+\frac{16(1-\nu^2)}{9(1-\nu)}N\ l^3\right)^{-2} l-\pi\gamma=0 \quad \cdots\cdots (6)$$

Since the unity term is negligible compared to the term $16\ (1-\nu^2)\ Nl^3\ /\ 9(1-2\nu)$, the total crack surface area A_2 contained in the material with volume of V can be expressed by

$$A_2 = \left(\frac{81\pi^{1.5}\ \alpha^2\ E\ \phi^2}{128\ (1-\nu^2)\gamma}\right)^{0.4} N^{0.2}\ V\ \Delta T^{0.8} \quad \cdots\cdots (7)$$

As indicated in Eqs. (5) and (7), in the thermal shock test using destructive methods in which the specimen is exchanged when changing ΔT, the crack surface area of the specimen (A_1) is proportional to the square of ΔT, while in the thermal shock test in which a specimen is successively thermal-shocked with a gradual increase of ΔT, the crack surface area (A_2) increases according to the four-fifths power of ΔT.

3. Experimental

3-1. Specimens

The specimens used in this study were pellets (8mm in diameter and 15mm in length) of sintered alumina (ADS-11, Toshiba Ceramics Co.) with density of 3.90g/cm^3. Table 1 shows the data for properties pertinent to thermal shock behavior of the specimens.

3-2. Thermal Shock Experiments

The thermal shock experiments were made by holding the specimen for about 20 minutes in a vertical furnace maintained at a predetermined temperature and subsequently dropping them into a water bath at room temperature.[4,18] In order to avoid the initiation of thermal fracture from the edges, both ends of the specimen were thermally insulated by wrapping with Teflon tape. The furnace temperature was raised at a slow rate of 5°C/min to prevent thermal stress fracture of the specimen during temperature increases. By varying the temperature of the furnace, the specimens were subjected to thermal shock over a range of temperature difference (ΔT) values.

Table 1. Property data for alumina specimens.

Property		Value
Density	(kg/m^3)	3.90×10^3
Fracture strength	(Pa)	3.4×10^8
Young's modulus	(Pa)	3.5×10^{11}
Thermal conductivity	(W/m・K)	2.9×10
Thermal expansion	(C^{-1})	7.1×10^{-6}
Poisson's ratio		2.7×10^{-1}
Fracture toughness	(M・N/m$^{3/2}$)	4.5

In order to compare the damage behavior of specimens thermal shocked at an equal ΔT, but in different ways, two different experiments were performed (experiments A and B). In experiment A, the specimens were thermal-shocked repeatedly, from low ΔT to a higher, predetermined ΔT using a small increment of ΔT. In experiment B, every time the thermal shock condition of ΔT was changed, the specimen was exchanged, which is the same way as adopted in fracture strength measurement which are generally used for evaluation of thermal shock damage of ceramic materials.

In both experiments, the ΔT varied from 0 - 450°C with increments of 100 - 200°C over the low ΔT region where crack initiation was not expected, and 10 - 20°C beyond the region.

3-3. Crack Surface Area Measurements

The surface areas of the specimens were measured by the BET technique[14] before and after the thermal shock testing to evaluate the thermal shock damage due to crack propagation. The specimen was placed in a quartz ampule after cleaning with acetone and drying. The ampule was then set in the BET equipment and heated to degas the specimen. This was followed by cooling down with liquid nitrogen and supplying the predetermined volume of absorbing gas into the ampule for a certain period of time to absorb the gas on the surface of the specimen. Pure krypton (Kr) was chosen as an absorbing gas by reason of its low vapor pressure. Changes in pressure of the Kr resulting from surface absorption were measured by using a high accuracy capacitance pressure sensor (diaphragm type, 310CA-10

MKS Instrument) which made it possible to measure surface area to a minimum of 20cm² with the reproducibility of approximately ±30%.

Prior to the practical measurement, in order to check whether the temperature change during the crack surface measurement produce any newly crack in the specimens, a preliminary test was performed. In the preliminary test, a virgin specimen and a specimen thermal-shocked at $\Delta T=300°C$ were subjected to a repeated surface area measurement of three to five times, and then examined whether the initial surface area changed as the measurement was repeated. The results confirmed that the heating and cooling cycle in the degassing and absorbing process had no influence on surface area of specimen.

4. Results and Discussion

Figure 1 shows changes in surface area of the specimens with ΔT obtained from experiments A and B. The data from both experiments show no change in the surface area of the specimen up to ΔT of about 200°C. Though scattering of the measured values increases when ΔT draw near $\Delta T=200°C$, the average of these values indicates that the surface area increases rapidly at ΔT of about 220°C. This rapid increase of the surface area implies crack initiation due to the thermal shock. Therefore this ΔT (=220°C) is the critical temperature difference,[4,17] ΔT_c, defined as the temperature difference required to initiate fracture. This measured $\Delta T_c=220°C$ coincides with ΔT_c calculated from the following relation given by Hasselman,[15]

$$\Delta T_c=\left(\frac{\pi\gamma(1-2\nu)^2}{2E\ \alpha^2(1-\nu^2)\phi^2}\right)^{0.5}\left(1+\frac{16(1-\nu^2)Nl^3}{9(1-2\nu)}\right)l^{-0.5} \quad \cdots\cdots (8)$$

In the calculation, the initial crack radius, l, was given as $l=20\mu m$ based on microstructural observation of the specimens and since the term $16(1-\nu^2)Nl^3 / 9(1-2\nu)$ was small enough compared to unity, this term was neglected. In the range of $\Delta T_c \leq \Delta T$, the surface areas increase with ΔT for both specimens in the experiments A and B. In spite of the similarity in the thermal shock behavior of both specimens, there is a clear difference in the extent of the damage between them. For experiment A, where a single specimen was forced to receive repeated thermal shocks with a gradual increase of ΔT, the crack surface area of the specimen increases gradually with ΔT. This is in comparison to experiment B, where the thermal shock was always applied to a new specimen every time ΔT was changed and the crack surface area increases rapidly against ΔT. At $\Delta T=400°C$, for instance, the damage to the experiment B specimen exceeds the corresponding value for experiment A specimen by a factor of approximately 1.5.

The calculated crack surface areas derived from Eqs. (5) and (7) are also shown with dotted and solid lines, respectively, in Fig. 1. In the calculations, the heat transfer coefficient h was assumed as 1×10^4W/m K (2400 cal/m² s°C), and the value of 2×10^{11} m^{-3} was used for the crack density N calculated from the relation $N = (S_B-R_f\cdot S_g)/2\pi l^2V$, where S_B is the measured BET surface area ($S_B=3.38\times10^{-3}$ m²); R_f, the roughness factor ($R_f=7$);

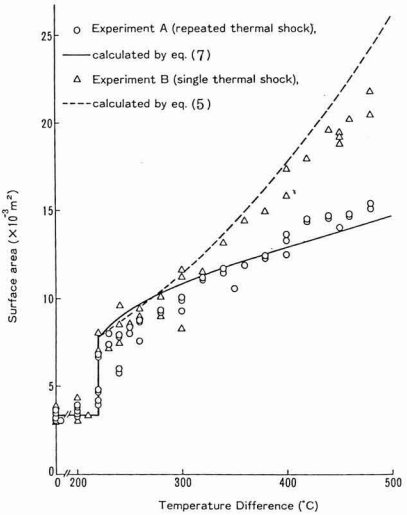

Fig. 1. Change in surface area of alumina specimens as a function of the thermal shock temperature difference, comparing measured and calculated values.

S_g, the geometrical surface are; l, the radius of the initial flaws ($l=20\mu m$); and V, the specimen volume ($V=7.51\times10^{-7}$ m³). This relation was based upon the assumptions that the measured BET surface area is attributed to the surface area of the initial flaws open to the specimen surface, and the surface area is related to surface roughness of the specimen, and also the initial flaws are all thin disks with equal radius, distributed uniformly in the specimen surface. Under plane strain condition, the fracture surface energy, γ, was calculated from the relation,[19] $\gamma=(1-\nu^2)K_{IC}^2/2E$, where K_{IC} is the critical stress intensity factor or fracture toughness given in Table 1. As described in the previous section, Eq. (5) expresses the damage of the specimen subjected to thermal shock for the first time at ΔT, while Eq. (7) gives the damage of the specimen repeatedly thermal-shocked with a small increment of ΔT. The comparison in the figure shows a good agreement between calculated and measured crack surface areas for experiment A and Eq. (7), and experiment B and Eq. (5). The results suggest that in the range of $\Delta T_c \leq \Delta T$, the specimens subjected to severe thermal shock for the first time sustain much more extensive damage than the specimens to which have experienced a single or repeated thermal shock with lower ΔT (but higher than ΔT_c) before being subjected to thermal shock with the same severity (ΔT).

Figure 2 compares crack configuration of the specimens, which were displayed by a dye penetration technique, after thermal-shocking at $\Delta T=450°C$ in experiments A and B. It is apparent from the figure that the crack density of the specimen from experiment B is higher than that of experiment A. From this observation it can be considered that the severer damage observed

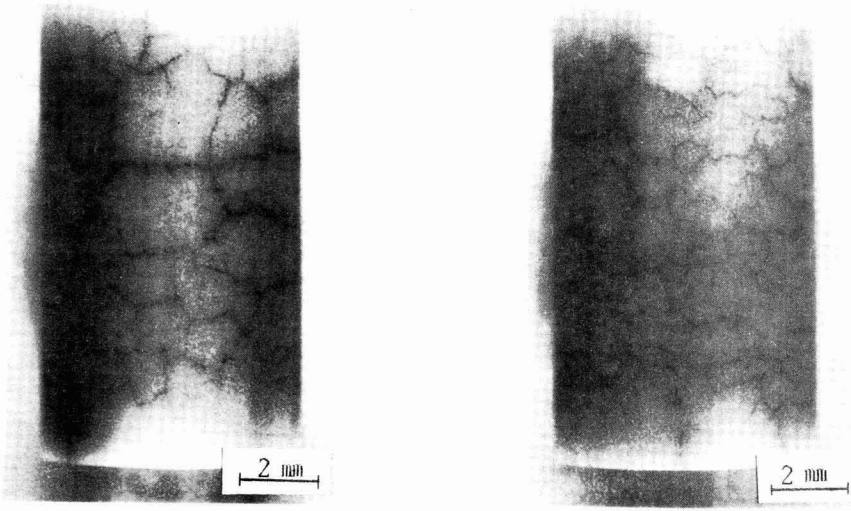

(a) (b)

Fig. 2. Comparison of crack configurations in specimens (a) subjected to thermal shock repeatedly with a gradual increase in ΔT up to $\Delta T = 450°C$ and (b) subjected to thermal shock for the first time with $\Delta T = 450°C$.

in the experiment B specimen over the range of $\Delta T_c \leq \Delta T$ is attributed to not only longer crack length resulting from the higher elastic energy developed by ΔT as expressed in Eq. (5), but also the higher crack density produced in this specimen as shown in Fig. 2. Considering that for the higher ΔT, the higher crack density is produced, the experimental values should shift up and away from the calculated values shown by the dotted line as ΔT increases, because the calculated values only taken into account the extension of crack length. However, the effect of the crack density is not apparent in the measured values as shown in Fig. 1. This may be due to limits of the BET method in which only cracks open to the surface can be objects for measurement, while at high ΔT a large number of cracks are coincidently generated over a wide area inside the specimen.

The results of this study suggest that the relation between thermal shock damage and ΔT ($\Delta T_c \leq \Delta T$) derived from the theory based on the assumption of constant crack density over the range of ΔT cannot be verified by destructive methods such as the fracture strength measurement method. This is because the thermal shock conditions in which crack growth occurs quasi-statically[17] under a constant crack density with increasing ΔT are almost completely absent in the destructive methods. For a virgin specimen thermal-shocked for the first time, the higher ΔT, the higher the crack density as observed in Fig. 2, as well as the greater is the kinetic crack propagation as indicated by Eq. (4). On the contrary, the BET method used here can solve these problems so that this technique is valid as a nondestructive method for thermal shock damage evaluation. However, it has a weak point in that it is difficult to measure cracks enclosed in the specimen. Therefore the method may not be valid under such thermal shock conditions that crack initiation and propagation occur only inside part of the specimen as under rapid heating conditions.

5. Conclusion

Crack initiation and propagation behavior of alumina specimens subjected to thermal shock were investigated. The cylindrical specimens were thermal shocked by a quenching method with various temperature difference (ΔT) values. In the experiments, some specimens were thermal shocked only once at a predetermined ΔT, while other specimens were subjected to repeated thermal shocks with a gradual increase of ΔT up to the ΔT for comparison. The crack initiation and its propagation with various ΔT were evaluated in terms of the change in surface area of the specimen, and thus crack surface area, by applying the BET surface area measurement technique. The results showed that even though at the same ΔT, a larger extension of the crack surface area was observed in the virgin specimen thermal-shocked once (single thermal shock) compared to the specimen which had already experienced repeated thermal shocks and had developed thermal shock cracks inside. It was considered that for the single thermal-shocked specimen, the higher ΔT, the higher the elastic energy and the higher the crack density developed, based on the obser-

vation of crack morphology after thermal shocks and theoretical considerations based on thermal shock theory. The results also suggested that the fracture strength measurement method which has been widely used for thermal shock damage evaluation was not well suited to estimate crack static propagation as ΔT was gradually increased. Good agreement was obtained between calculated and measured crack surface areas over the range of ΔT in both cases of the single and repeated thermal shocks.

References:

1) W.D. Kingery, J. Am. Ceram. Soc., 38, 3-15 (1955).
2) T.K. Gupta, J. Mater. Sci., 8, 1283-86 (1973).
3) M. Oguma, Nucl. Eng. Des., 76, 35-45 (1983).
4) M. Oguma, J. Nucl. Mater., 127, 67-76 (1985).
5) R.W. Davidge and G. Tappin, Trans. Brit. Ceram. Soc., 66, 405-22 (1967).
6) T.K. Gupta, Science of Ceramics, 7, 71-86 (1973).
7) T.K. Gupta, J. Am. Ceram. Soc., 55, 249-53 (1972).
8) J.A. Coppola, D.A. Krohn and D.P.H. Hasselman, J. Am. Ceram. Soc., 55, 481 (1972).
9) R.D. Smith, H.U. Anderson and R.E. Moore, Am. Ceram. Soc. Bull., 55, 979-82 (1976).
10) M. Oguma, C.J. Fairbanks and D.H.P. Hasselman, J. Am. Ceram. Soc., 69, C-87-C-88 (1986).
11) B.E. Bertsch, D.R. Larson and D.P.H. Hasselman, J. Am. Ceram. Soc., 57, 235-36 (1974).
12) A.G. Evans, M. Linzer, H. Johnson, D.P.H. Hasselman and M.E. Kipp, J. Mater, Sci., 10, 1608-15 (1975).
13) P.L. Swanson, "Fracture Mechanics of Ceramics," Vol. 8, Edited by R.C. Bradt, A.G. Evans, D.P.H. Hasselman and F.F. Lange, Plenum Publishing Corp.. (1986) pp.299-317.
14) S. Brunauer, P.H. Emmett and E. Teller, J. Am. Ceram. Soc., 60, 309-15 (1938).
15) D.P.H. Hasselman, J. Am. Ceram. Soc., 52, 600-04 (1969).
16) J.B. Walsh, J. Geophy. Res., 70, 381-89 (1965).
17) D.P.H. Hasselman, J. Am. Ceram. Soc., 53, 490-95 (1970).
18) M. Oguma, K. Chyung, K.Y. Donaldoson and D.P.H. Hasselman, J. Am. Ceram. Soc., 70, C-2-C-3 (1987).
19) T. Nishida and E. Yasuda, "Seramikkusu no Rikigakuteki Tokuse Hyouka," Nikkan Kogyo Shinbun-sha (1986) pp.64-66.

This article appeared in English in Nippon Seramikkusu Kyokai Gakujutsu Ronbunshi (Japanese version), Vol. 97, No.8, 1989.

Study on High Temperature Thermistor Made of $MoSi_2$-Granular Al_2O_3 Composite

Hirotaka Yamamoto and Satoshi Sendai

R&D Labs., TDK Corporation
2-15-7 Higashi-Ouwada, Ichikawa City, Chiba Pref. 272, Japan

A sintered composite, which was made of $MoSi_2$ and granulated Al_2O_3 by a new technique, realized high electric conductivity even in the range of much Al_2O_3 and was used as a material for heating element. It was already reported. This study shows the material was not appropriate for high temperature thermistor, however was attained by obtaining a superior material in high temperature stability as a result of improving its surface from forming aluminosilicate glass layer.

Moreover it was found to be a peculiar material to positive temperature characteristics of electric resistance and to stabilize B constant at a smaller number, compared with properties of the other present materials for high temperature thermistors.

Key-words: Ceramic, Composite, Grainboundary controlling, $MoSi_2$, Thermistor, Resistor, High temperature material

1. Introduction

In our previous reports[1,2] we showed that a sintered composite made of $MoSi_2$ and granulated Al_2O_3 realizes high electric conductivity even in the range of much Al_2O_3 and is suitable for heating elements. From this, we undertook the present study to obtain a material to be used for heat-resistant high temperature thermistors based on the above-mentioned sintered composite by utilizing the logarithmically linear temperature characteristic of electric resistance of $MoSi_2$. As a result, by improving the material's surface we have obtained a high temperature thermistor having unique features that the conventional high temperature thermistor does not offer.

Materials such as spinel like CoO-Al_2O_3 series, NiO-Al_2O_3 series, $Mg(Al,Cr,Fe)_2O_4$ series and Cr_2O_3-Al_2O_3 series, as well as ZrO_2 series materials have been proposed or practically used for high temperature thermistors used in about 1000°C.[4-9] All these materials have a negative temperature characteristic of electric resistance. However, a material having a positive temperature characteristic is in demand for some applications in high temperatures. The positive temperature characteristic of electric resistance is a feature of the material we developed. Another feature of this material is that it has a B constant smaller than those of the above-listed materials. These features were attained by utilizing the temperature characteristic of electric resistance in high temperatures of $MoSi_2$ using as elements of thermistors.

Thermistor materials are required to have a higher thermal response characteristics, small temperature change detecting ability, heat resistance in high temperatures and reliability, in addition to a temperature characteristic of electric resistance and B constant. The improved material obtained in this study has satisfied these requirements.

2. Experimental Method

Thermistors were made by using the sintered composite prepared by the method reported previously[1] to evaluate the heat resistance and reliability in high temperatures as well as electrical properties under severe conditions.

2-1. Preparation of Samples

(1) Preparation of sample A

From $MoSi_2$-granular Al_2O_3 material reported previously,[1] a sintered composite was prepared consisting of Al_2O_3 granules of 140 - 160μm and 8 vol% of $MoSi_2$. The material was sintered at 1650°C in vacuum for 1 hour.

The sintered composite was cut up into samples with a cross sectional area of 1 × 1mm and a length of 2mm, at each end of which Pt electrode was formed for termination. The electrical resistance of the sample was controlled by varying the sample size.

(2) Preparation of sample B

In the course of sample A preparation, samples that were heat-treated at 1500°C in air for 30 minutes before the electrodes forming were called sample B. After the end surfaces were ground, electrodes were formed on the surfaces, as in sample A, for termination. Figure 1 shows the procedure for preparing sample B. The microstructure of sample B is shown in Fig.2.

2-2. Measurement

(1) Measurement of electrical resistance

The electrical resistance was measured 5 seconds after the applying of 1V dc voltage between the electrodes of the sample in accordance with JIS draft.[10] The samples were placed at room temperature or a specified temperature in an electric furnace heated. The other ends of the 0.3mm-diameter Pt terminal wires directly welded to the terminals were led to the outside of furnace to make the measurements.

(2) Measurement of temperature characteristic of electrical resistance

The temperature characteristic of electrical resistance was determined by varying the temperature of sample from 800°C to 1100°C, in 50°C steps, maintaining

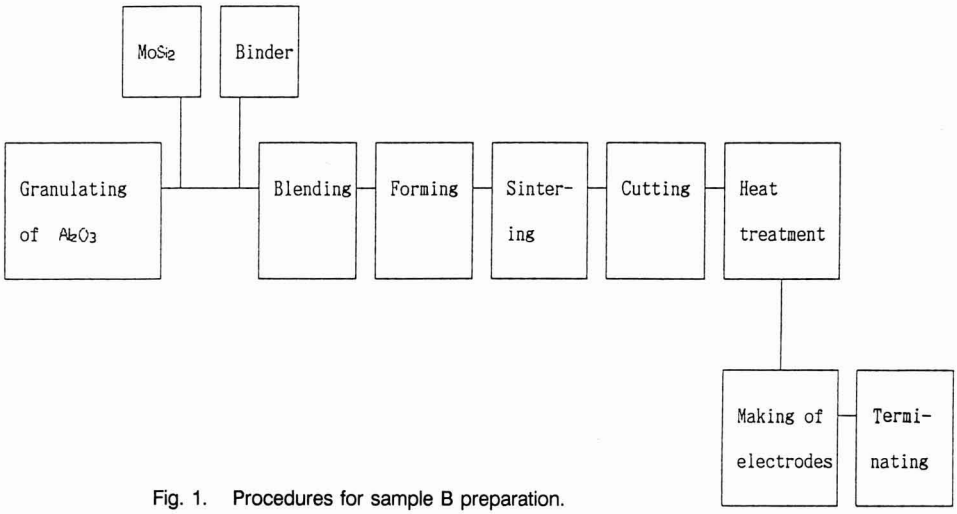

Fig. 1. Procedures for sample B preparation.

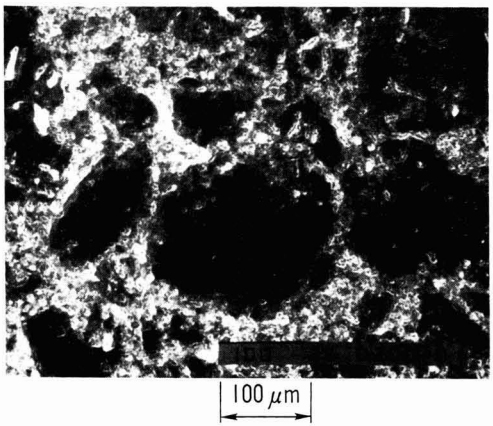

Fig. 2. Microstructure of the sample B sintered composite.

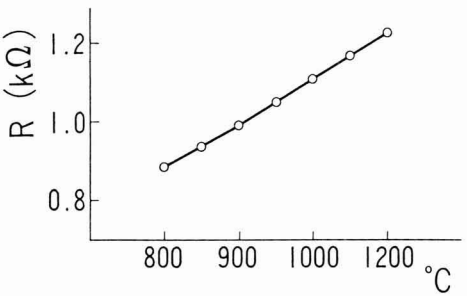

Fig. 3. Temperature characteristic of electric resistance of sample B.

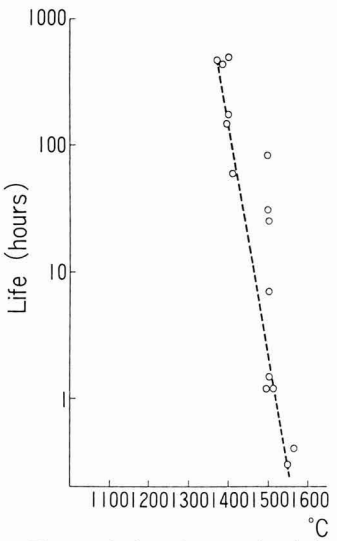

Fig. 4. The result of continuous electric load test of sample A in air high temperature.

each temperature for 10 minutes and then measuring the current. The results are shown in Fig.3. The B constant was calculated from the electrical resistance values at 800°C and 1100°C.

(3) Measurement of life at high temperatures

Several samples A were placed in various high-temperature air furnaces at different temperatures and 1V dc voltage was continuously applied to determine the time taken in break the samples within 1000 hours. The results are shown in Fig.4. Although similar measurements were made for sample B, none had broken the samples within 1000 hours of continuous voltage applying at 1400°C or lower.

(4) Measurement of change in properties in aging test in high-temperature hydrogen gas

Several samples each for sample A and B were heated to 1200°C in hydrogen gas. These samples were

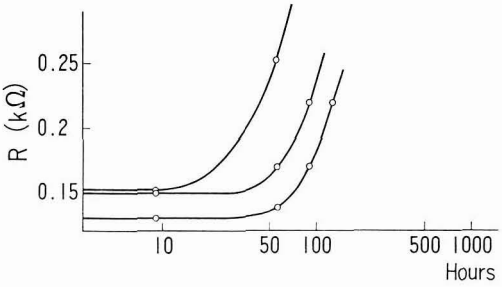

Fig. 5. The result of aging test for sample A in a hydrogen atmosphere at 1200°C.

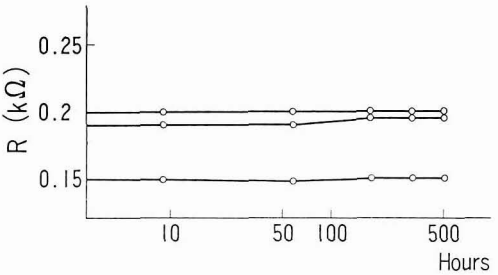

Fig. 6. The result of aging test for sample B in a hydrogen atmosphere at 1200°C.

taken out at various times and the change in electric resistance was measured for the sample at 20°C by the method described in (1). In sample A, deterioration started after 10 to 50 hours as shown in Fig.5, while in sample B, the change in electrical resistance was kept within ±1%, as shown in Fig.6, measured until 500 hours.

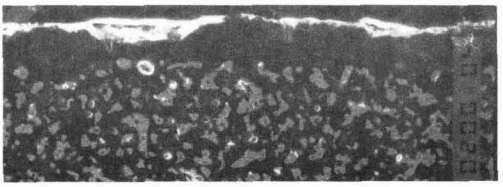

Fig. 7. Microstructure near surface of sample B.

3. Results and Discussion

First, the requirements for high temperature thermistor materials will be listed and then each of the requirements will be considered. The requirements are listed below by referring to the features and conditions reported by many studies[11-17] from the viewpoint of the application of materials used for normal temperature thermistor elements.

(1) The signal output for thermal response is high.
(2) Small temperature changes can be detected. Also, the operating temperature range is wide.
(3) Heat resistance is provided in high temperatures in air, particularly in a reducing atmosphere. The change of properties in aging in high temperatures is small.
(4) The elements are interchangeable.

Whether these requirements are satisfied by the material developed in this study will be discussed in 3.1 and the subsequent sections in this chapter on the basis of the experimental results described in the preceding chapter. The discussion about requirement (4) will be omitted because of the problem of producing elements consistently.

3-1. Discussion About Signal Output for Thermal Response and Others

(1) Signal output

The signal output is about 1mA when 1V dc voltage is applied to samples at 1000°C. This output is sufficient for thermistors.

(2) Temperature characteristic of electric resistance and detection of small temperature change

This material has a positive temperature characteristic of electrical resistance. This is the feature that conventional materials used for high temperature thermistors do not offer.

The B constant according to 2.2(2) is 2700K. This value is equal to or slightly lower than that of Mn-Co spinel series material generally used for normal temperature thermistors. The material developed in this study is advantageous because the smaller B constant extends the range of operating temperature. So far, B constants of materials used for high temperature thermistors were inherently large.

The detecting capability of small temperature change is 1% of electrical resistance change for a temperature change of 5°C during 800°C and 1000°C. This value is satisfactory.

3-2. Discussion About Heat Resistance at High Temperature

From the measurement of life in 2.2(3), the material developed in this study is judged to withstand temperatures higher than 1300°C for sample A and 1400°C for sample B in air. The data on heat resistance in a reducing atmosphere will be discussed later.

(1) Heat resistance at high temperature in air

The measurement results of sample A shown in Fig.4 indicate that the life varies at 1500°C, i.e., some samples were observed to withstand long-term operation. To clarify the reason for this, an analysis of samples was performed. The analysis revealed that the sample surface is covered with a dense aluminosilicate glass layer at 1500°C.

It was expected that sample B would prove to be a highly heat resistant element, if sample B is prepared by heat treating sample A at 1500°C as described in 2.1(2). Figure 7 shows the microstructure near the surface of

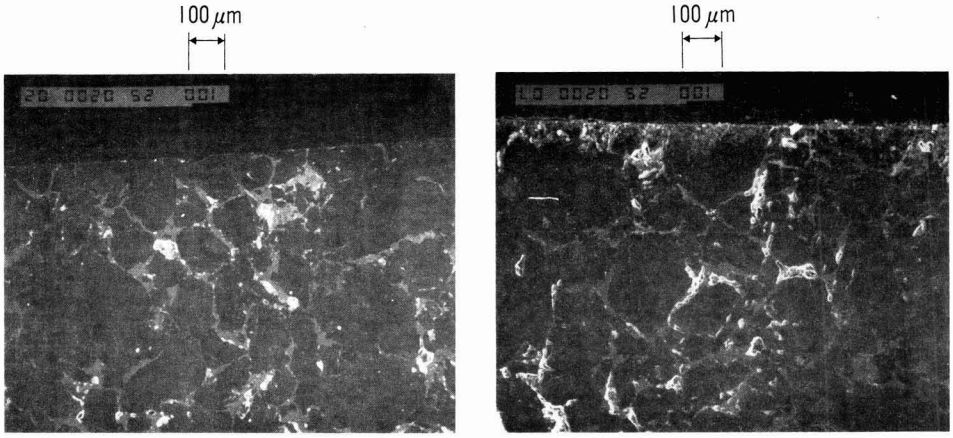

Fig. 8. Microstructure near surface in aging test for sample A in hydrogen atmosphere at 1200°C. (White-part is $MoSi_2$ network and pores.)

sample B, which indicates that the glass layer thickness is 20μm. The reason why sample B has longer life than sample A is probably due to this glass layer.

(2) Heat resistance at high temperatures in a reducing atmosphere

The measurement results described in 2.2(4) indicate that the electrical resistance of sample A suddenly increases after a certain length of time and finally the samples breaks if the sample is heated to 1200°C in hydrogen. On the other hand, the electric resistance of sample B remains almost unchanged for 500 hours as shown in Fig.6. These facts suggest that the improvement in the element surface provide sufficient heat resistance at 1200°C.

It has been reported that $MoSi_2$ decomposes gradually in air at high temperatures, but rapidly in a reducing atmosphere.[19,20] The composite developed in this study is stable in high temperatures not only in air but also in reducing atmosphere because it contains much Al_2O_3 which is stable at high temperatures. Our previous report[1] confirmed that decomposition caused a weight reduction of only 0.0001g/cm^2 per day in hydrogen gas as a particularly severe reducing atmosphere, even when 1000 hours elapsed after heating to 1200°C. The sample used in the previous report[1] corresponds to sample A in the present study.

For sample A, deterioration begins after 10 to 50 hours in hydrogen gas after heating to 1200°C. It is probably because decomposition of $MoSi_2$ not only occurs on the surface, but proceeds inward. Figure 8 shows the microstructure near the surface of sample A. For samples heated at 1200°C in hydrogen, changes are found not only on the surface layer but also in the inner part after 40 hours. That is, decomposition of $MoSi_2$ produces voids, which break a part of network of $MoSi_2$, resulting in increase in electrical resistance. The glass layer of sample B after the test showed same microstructure as Fig.7 which was essentially equal to that before being tested.

Hence, the material of sample B is considered to not deteriorate after a practical aging. High temperature thermistors may be sealed in a suitable protective tube to prevent them from being exposed to a reducing atmosphere.

4. Conclusions

We previously reported that for a sintered composite of $MoSi_2$-granular Al_2O_3, Al_2O_3 that was stable at high temperatures inhibited the decomposition of $MoSi_2$ to some extent even in the severest reducing atmosphere at high temperatures.[1] In previous study in which the material is used for high temperature thermistors, the effect of decomposition on electrical properties come suddenly after a certain length of time. Therefore, the material was heat treated so that a glass layer was formed on the surface. It was found that this layer significantly prevent to decomposition.

As a result, we have developed a material for use in high temperature thermistors with a wide operating range by utilizing the high temperature properties of conductivity of $MoSi_2$. This material features a positive temperature characteristic of electrical resistance and a smaller B constant, which conventional materials do not offer.

References:

1) H. Yamamoto and S. Sendai, Yogyo-Kyokai-Shi, 87 [2] 76 (1979).
2) S. Sendai, H. Yamamoto and H. Ninomiya. Official Patent

Gazette Sho 60-18081.
3) H. Yamamoto, S. Sendai and H. Ninomiya, Official Patent Gazette Sho 56-21242.
4) Government Industrial Research Institute, Osaka, "Research Report on Conductive Inorganic Materials," p.122 (1984).
5) Y. Matsuo, Industrial Materials, 31 [2] 116 (1984).
6) Y. Nakamura, Chemical Industry, 50, 241 (1984).
7) M. Komori, et al., Official Patent Gazette Sho 48-31857, etc.
8) Y. Matsuo, et al., Official Patent Gazette Sho 52-50393, etc.
9) M. Suzuki, et al., Official Patent Gazette Sho 54-41716, etc.
10) JIS, not published.
11) T. Naito, et al., General Description of Sensors (extra issue of Newton), Kyoikusha, B109 (1985).
12) T. Nitta, "Recent Sensors," The Institute of Electrical Engineers of Japan, p.117 (1985).
13) H. Futaki, "Sensor Electronics" Shoko-sha, p.76 (1987).
14) H. Futaki, "Practice of Thermo-sensitive Semiconductors," Sanpo, p.7 (1973).
15) S. Sumikama, "Introduction to Thermal Sensors," Keigaku-Shuppan, p.60 (1984).
16) K. Kimura, "Ceramic Temperature Sensors," Trikeps, p.60 (1979).
17) Japan Regular Sensor Research Association, "Operation and Best Application of Sensors," Gijyutsu-hyoronsha, p.159 (1981), etc.
18) TDK catalogue.
19) K. Tamura, Research Report of National Research Institute for Metals, 5[1] (1962).
20) R.G. Giler, Metals Eng. Quarterly [11] 48 (1973).

This article is a full translation of the article which appeared in Nippon Seramikkusu Kyokai Gakujutsu Ronbunshi (Japanese version), Vol.97, No.8, 1989.

Estimation on Glass Shaping Mold in Reducing Atmosphere

Masamitsu Sawada, Tsuneo Uetsuki*, Moriya Suzuki*, Junji Hayakawa* and Thoru Komiyama*

Shinko-Pfaudler Co., Ltd., Chemical Process Equipment Division,
Technical Department, Products Development Section
1-4-78, Wakinohama-cho, Chuo-ku, Kobe, 651, Japan
* Glass and Ceramic Material Department, Government Industrial Research Institute, Osaka
1-8-31, Midorigaoka, Ikeda-shi 563, Japan

Molds were estimated by using 4 kinds of molds and 4 kinds of pure metals for soda-lime-silica glasses (colorless and amber container glasses) below 900°C in a reducing atmosphere. The estimation was based on sessile drop measurement and observation of metal surfaces. The sessile drop measurement showed wettability by measuring the contact angle and interfacial diameter between glass and metal.

Copper and copper alloy showed poor wettability, and their surface roughness increased. Iron showed good wettability and roughening of its surface. In metals except copper, grain boundary development and surface film formation were observed after heating. The contact angle on nickel was determined as a function of roughness, and the following empirical formula was obtained.

$$\theta_r = 26.4r^2 + 18.6r + 77.1$$

θ_r : contact angle (degree)
r : surface roughness (μm)

These results suggested that the wettability and the surface roughness, owing to the reacted materials, crystal growth and kind of metals, are the essential factors for glass shaping molds.

[Received December 21, 1988; Accepted May 16, 1989]

Key-words: Mold, Wettability, Surface roughness, Sessile drop, Contact angle

1. Introduction

At present, martensite and austenite stainless steels, super heat-resisting alloys, and tool alloys for hot working are widely used in metal molds for glass shaping.[1,2] Also, special types of molds have been proposed such as a mold whose surface is improved by hard plating or ceramic spraying and single crystal molds for aspheric lens shaping.[3]

To evaluate molds, the temperature at which glass adheres to the metal has been studied;[4,5,6,7] however, there have been few reports on glass wettability and surface roughness of molds. In particular, the interaction between glass and metal mold in a reducing atmosphere has been little studied. It is generally said that metal surfaces are oxidized in an oxidizing atmosphere, and the resultant oxides diffuse into the glass, accelerating the wetting and contact processes;[8] while in a reducing atmosphere, the oxidation of metal is prevented, resulting in suppressed wetting.

This report discusses the wettability of glass on metal and the change in metal surface roughness with glass in a reducing atmosphere to evaluate glass shaping molds.

2. Experimental Method

2-1. Preparation of Samples

Table 1 lists the chemical composition and thermal properties of glass used in this experiment. Glass was prepared by the ordinary method and shaped into cylinders with a diameter and height of 5±0.5mm. Their end surfaces were ground with #1000 SiC abrasive grains and the samples were used for wettability measurements.

A total of eight kinds of metal samples were used, including copper, iron, nickel, chromium, and alloys containing these metals as major components that are actually used in molds. Table 2 lists the chemical compositions of these alloys. The samples are plates measuring 20×25mm with a thicknesses of about 0.8-5.0mm. Their surfaces in contact with the glass were mirror finished with #4000 SiC abrasive grains.

Table 1. Chemical composition and thermal properties of glass.

Chemical composition (mol%)		
	SiO_2	71.0
	Na_2O	14.0
	CaO	13.0
	Al_2O_3	2.0
Thermal expansion coeff. 25-350°C	($\times 10^{-7}$/°C)	82.7
Transformation point	(°C)	584
Softening point	(°C)	637
Flow point	(°C)	900

2-2. Experimental Apparatus

Figure 1 shows a schematic diagram of the experimental apparatus. The apparatus consists of reducing gas supply system, sample heating system, and gas exhaust system. A mixture gas of 5%H_2 + 95%N_2 was used as reducing gas. The gas was sent to the sample by removing oxygen with a copper strip heated to 500°C and a titanium sponge placed next to the sample. The sample was heated with a nichrome furnace that was program-controlled so that each sample had the same temperature history.

The experiment was carried out as follows: After glass and metal specimens were digressed and cleaned with acetone and then dried, the glass specimen was placed on the mirror finished surface of the metal specimen. The specimens were placed horizontally on a stand of sintered alumina in a silica glass tube. After the pressure in the silica glass tube was reduced (to 10^{-3}mmHg), reducing gas was passed at a flow rate of 2*l*/min through the silica gas tube. The specimens were heated rapidly to 400°C in about 15 minutes to prevent oxidation of the metal surface at low temperatures. Then, the specimens were heated to 900°C, corresponding to the flow point of the sample glass, at a rate of 200°C/hr and held at that temperature for 30 minutes.

Table 2.Chemical compositions of metals.

Metals	Classification	Ni	Cr	Cu	Fe	Others
HPM38*	Martensite SUS	0.6	13.0	-	bal.	C:0.1,Mo:0.5,Si,Mn,P
ZHB11*	Martensite SUS	3.0	16.0	-	bal.	Si:2.0,Mn:0.4,Mo:0.1
SKD*	Tool alloy	-	12.0	-	bal.	C:1.5,Si,Mn,Mo,P,S,V
CN*	Copper alloy	13.0	-	bal.	1.5	Zn:8.5,Al:7.5
Copper	-	-	-	99.9	-	
Iron	-	-	-	-	99.9	Enameling iron
Nickel	-	99.9	-	-	-	
Crom.#	-	-	99.9	-	-	

* : Molds
\# : Vacuum deposited cromium on HPM38

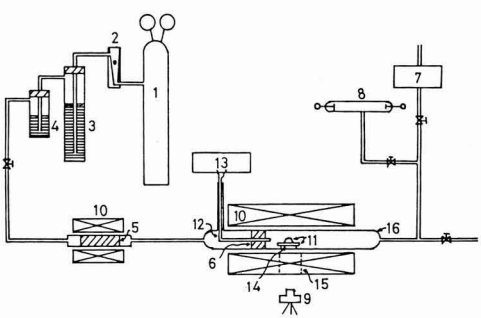

Fig. 1. Schematic diagram of apparatus for sessile drop measurement.
1: Reducing gas (5%H_2 + 95%N_2)
2: Flow meter
3: Silica gel
4: Phosphorus pentoxide
5: Active copper
6: Sponge titanium
7: Rotary pump
8: Geissler tube
9: Camera
10: Nichrome furnace
11: Glass and metal specimens
12: Thermocouple
13: Temperature recorder
14: Sample stand
15: View window
16: Silica glass tube

2-3. Evaluation of Wettability by Sessile Drop Measurement

Wettability was evaluated by measuring the contact angle and interfacial diameter at the glass-metal interface. During measurement, the samples at various temperatures and holding times were photographed through an observation window of the furnace. Figure 2 shows typical photographs. The contact angle and interfacial diameter of the interface were defined as shown in Fig. 3.

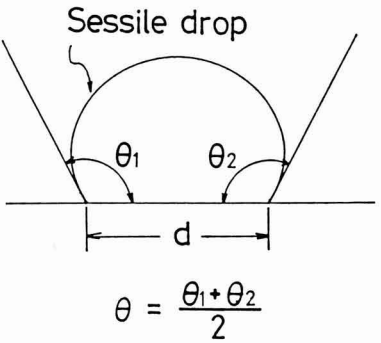

Fig. 3. Schematic representation of contact angle (left θ_1, right θ_2, average θ) and interfacial diameter (d).

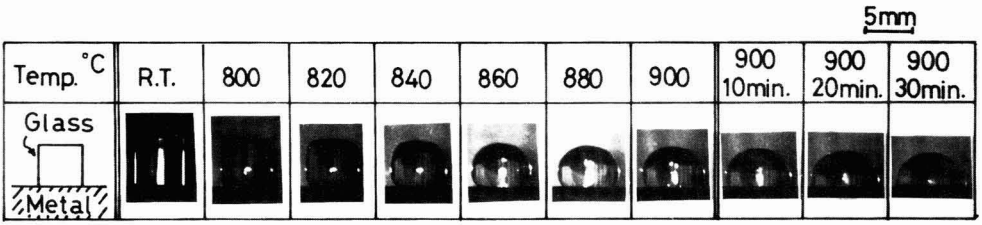

Fig. 2. Photograph of typical samples with temperature and holding time at 900°C.

2-4. Measurement and Observation of Metal Surface Roughness

To ascertain the change in the metal surface due to heating and penetration of glass, the surface from which glass had been removed was observed with a scanning electron microscope (SEM) and the roughness was measured. For the surface roughness the arithmetical mean roughness was measured at two places, a place where glass had contacted (contact area) and a place where glass had not contacted (non-contact area) with a contact-type roughness meter SURFCOM from Tokyo Seimitsu Co., Ltd.

3. Results

3-1. Contact Angle

Figure 4 shows the contact angle of glass on various metals. Figure 4(a) shows the contact angle of glass during heating to 900°C, while Fig. 4(b) shows the contact angle of glass held at 900°C for 30 minutes. The contact angle increases above 770°C for all metals. For HPM38 (martensite stainless steel), ZHB11 (martensite stainless steel containing increased Ni, Cr, and Si), SKD (tool alloy without Ni), nickel, chromium, and iron, the contact angle reaches a maximum of about 120° at 850°C, decreasing in the temperature range above 850°C, and being about 105° at 900°C. When the sample is held at 900°C, the contact angle decreases further to about 80° in 30 minutes. For copper and CN, after the maximum angle has been reached at 870°C, the shape is unchanged even if the sample is heated to 900°C or held at 900°C for 30 minutes; the contact angle is nearly constant, being about 135° for CN and about 145° for copper.

In addition to glass prepared by the ordinary method, carbon amber glass of the same composition was prepared by melting in a reducing atmosphere to measure the contact angle on various metals. The result is shown in Fig. 5.

The degrees of contact angle and the dependence on temperature, holding time, and type of metal are similar to those shown in fig. 4. It was found that the contact angle does not depend greatly on the oxidation-reduction of the glass

3-2. Interfacial Diameter of Glass-Metal Interface

Figure 6 shows the interfacial diameter of the glass-metal interface as a function of temperature and time. The ordinate represents the ratio (d/d_0) of interfacial diameter before (d_0) and after (d) heating. For HPM38, ZHB11, SKD, chromium, iron, and nickel, the interfacial diameter increases after reaching a minimum of about 820°C, and then increases further even when the sample is held at 900°C for 30 minutes. For copper and CN, on the other hand, the interfacial diameter decreases with an increase in temperature and remains nearly constant when the sample is held at 900°C for 30 minutes.

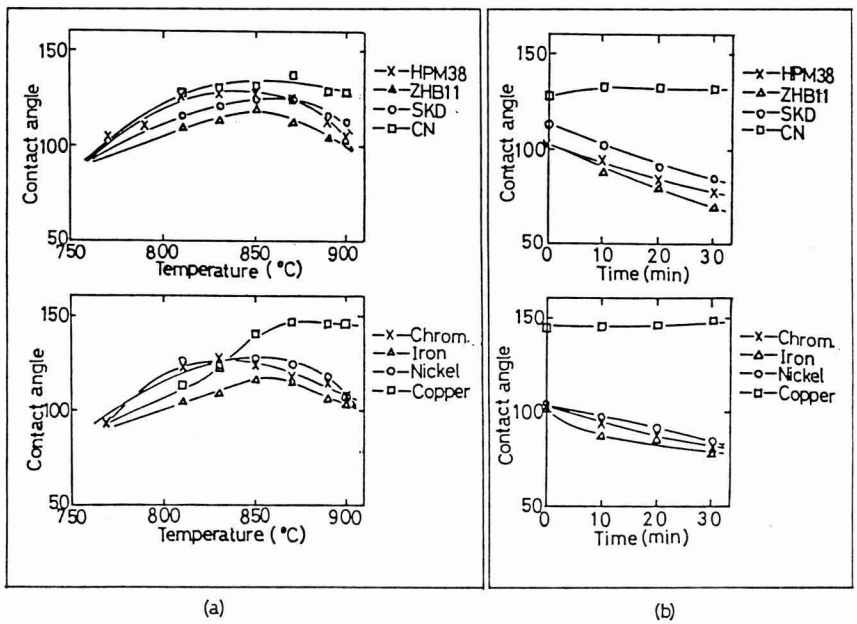

Fig. 4. Contact angle of glass on metal. (a) With temperature. (b) With holding time at 900°C.

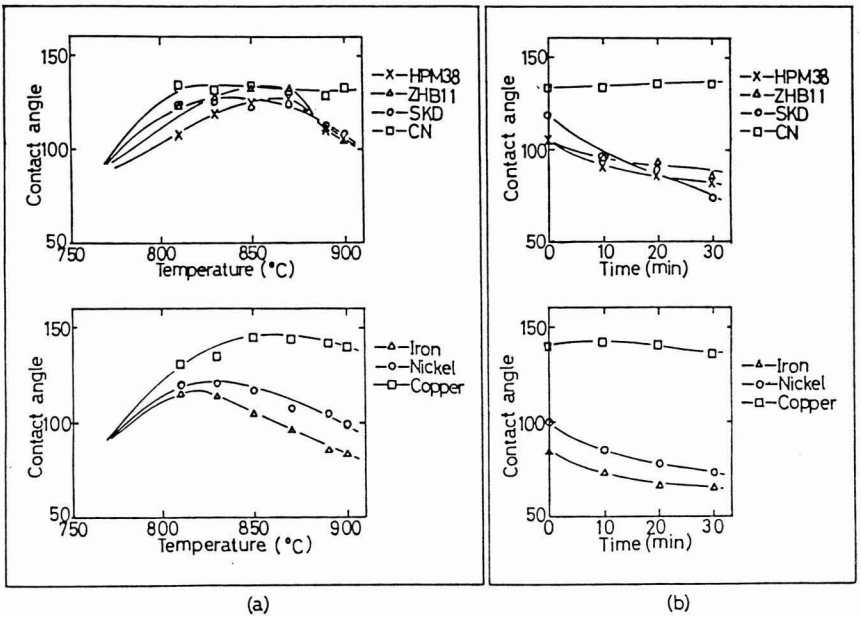

Fig. 5. Contact angle of carbon amber glass on metal.
(a) With temperature.
(b) With holding time at 900°C.

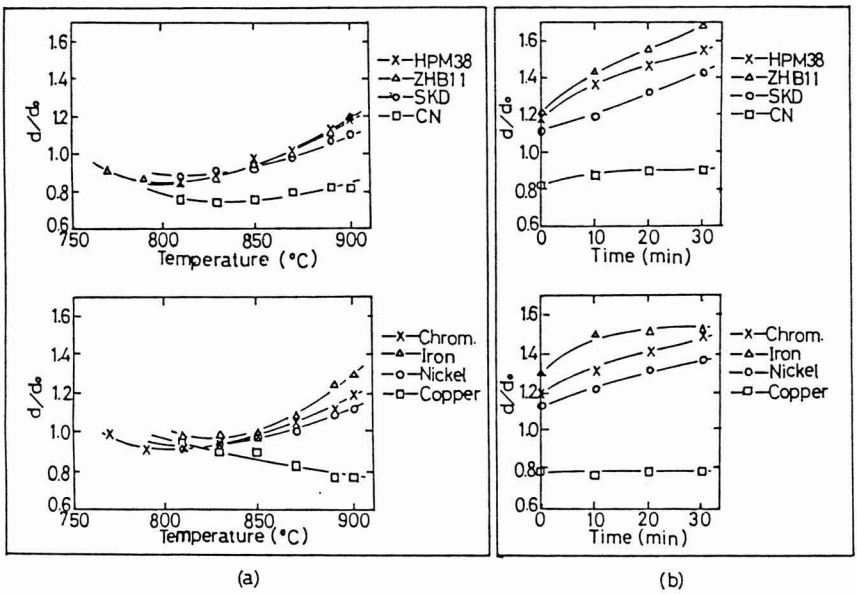

Fig. 6. Ratio (d/d_o) of interfacial diameter before (d_o) and after (d) heating.
(a) With temperature.
(b) With holding time at 900°C.

3-3. Surface Roughness of Metal

Figure 7 shows the results of measurement of metal surface roughness at contact and non-contact areas. The ordinate represents the ratio (r/r_o) of arithmetical mean roughness before (r_o) and after (r) heating. At the contact area, copper exhibited a far larger increase in roughness than other metals as seen from Fig. 7. This could easily be observed by visual method. CN and iron had the next in largest increase in surface roughness after copper. For HPM38, ZHB11, and SKD, the roughness after heating is two to three times greater than before heating. For nickel and chromium, the roughness scarcely changes. The change in roughness at the contact area is 0.10μm - 0.96μm for copper and 0.03μm - 0.06μm for HPM38.

At the non-contact area, the change in metal surface roughness caused by heating was similar to that at the contact area.

The roughness at the contact area is greater than that at the non-contact area for metals other than nickel and chromium, particularly for CN and iron.

3-4. SEM Observation of Metal Surface

SEM observation was performed on various metals to evaluate the change in the surface caused by heating. Typical SEM images are shown in Figs. 8 - 10.

For copper, abrasions found before heating (Fig.8(a)) are removed by heating. This tendency is observed on other metals. Grain boundaries are found at the non-contact and contact areas, and copper features larger crystal growth than those of other metals (Figs.8(b) and 8(c)).

On CN, insular patterns are observed in addition to abrasions before heating (Fig.9(a)). The non-contact area, except insular areas, is covered with film after

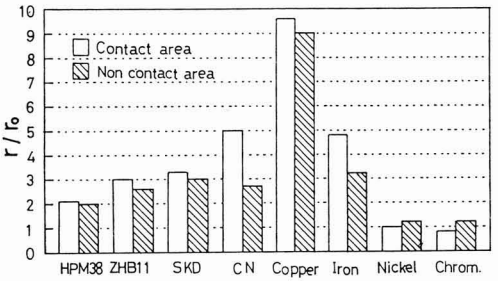

Fig. 7. Ratio (r/r_o) of surface roughness of metal before (r_o) and after (r) heating.

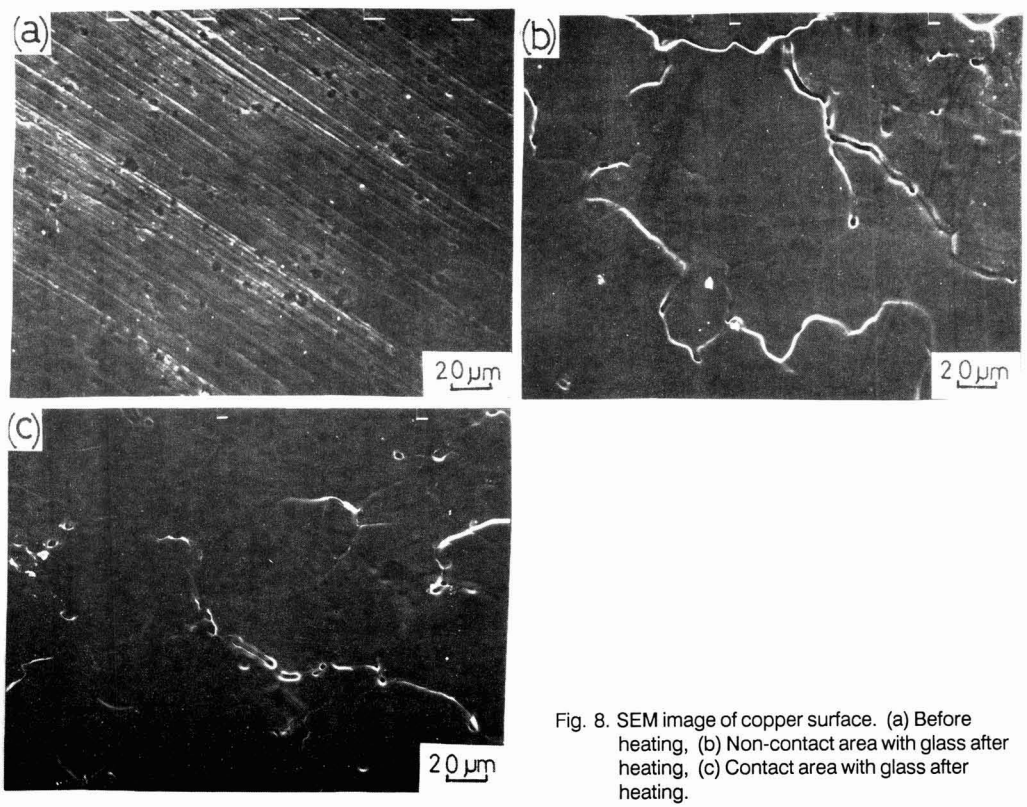

Fig. 8. SEM image of copper surface. (a) Before heating, (b) Non-contact area with glass after heating, (c) Contact area with glass after heating.

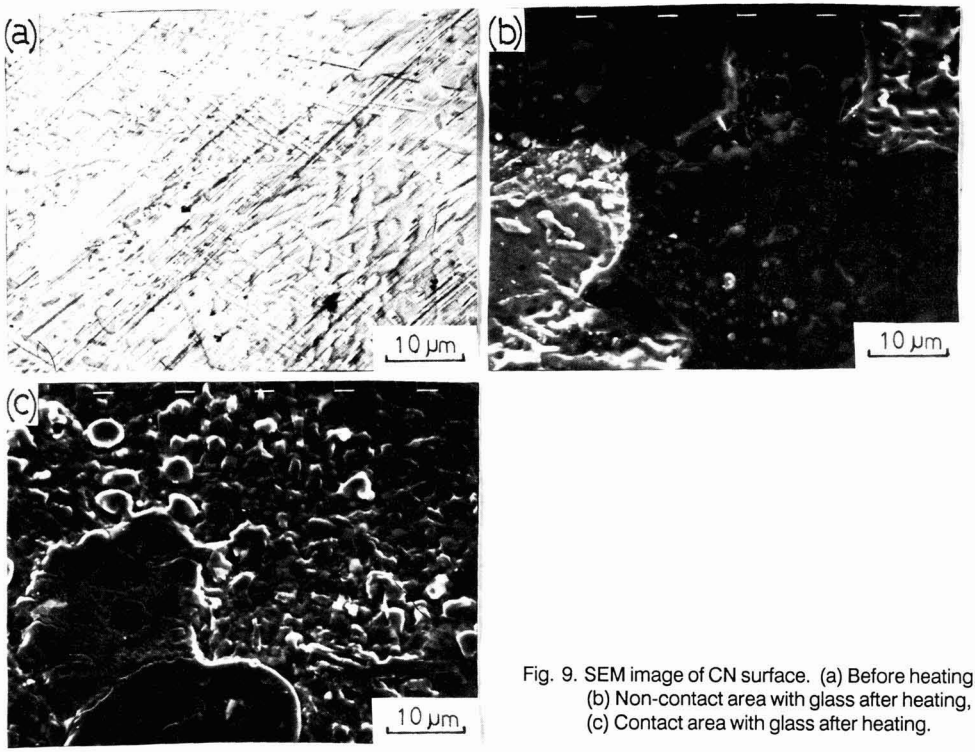

Fig. 9. SEM image of CN surface. (a) Before heating, (b) Non-contact area with glass after heating, (c) Contact area with glass after heating.

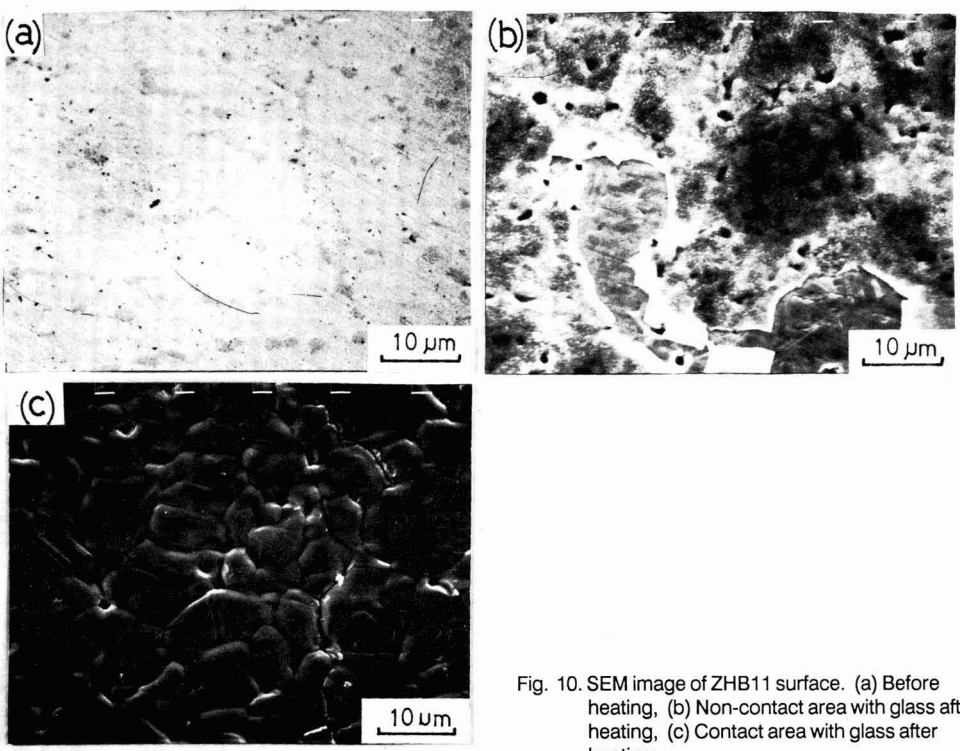

Fig. 10. SEM image of ZHB11 surface. (a) Before heating, (b) Non-contact area with glass after heating, (c) Contact area with glass after heating.

heating (Fig.9(b)). The contact area is attacked by glass, and the degree of attack is higher in areas other than insular areas (Fig.9(c)). The smaller change in roughness at the non-contact area than at the contact area is probably caused by the formation of a film.

For ZHB11, film is formed over the entire non-contact area, although a part of the area is separated; while grain boundaries and crystal grains are clearly observed at the contact area (Fig.10(c)).

Although the measurement of surface roughness revealed no significant difference in roughness change at the contact and non-contact areas, the change of microstructure caused by heating differed. This tendency was found on HPM38, SKD, iron, nickel, and chromium as well.

4. Discussion

Factors affecting the wettability of glass on metal include:

(a) Atmosphere
(b) Surface roughness of metal,
(c) Chemical composition of metal, and
(d) Impurities in metal.

Among these, atmosphere is not a factor governing the difference in wettability of metals, since all experiments were performed in a reducing atmosphere in this study. Among the eight metals, copper and CN have relatively lower wettability, and there is no significant difference in wettability between HPM38, ZHB11, SKD, iron, nickel, and chromium. These observations may result from metal surface roughness and chemical composition including impurities.

(1) To evaluate the effect of metal surface roughness on wettability, the contact angle and interfacial diameter were measured for nickel which had a nearly constant surface roughness before and after heating. The nickel specimens were roughened with emery papers to various roughnesses, and held at 900°C for 30 minutes before measurement. The result is shown in Fig. 11. As the surface roughness before heating increases from about 0.10μm to 0.90μm, the contact angle increases from about 80° to 115°, while the interfacial diameter decreases by about 50%. It means that the wettability of glass on metal decreases with an increase in roughness in a reducing atmosphere.

(2) Next, the correlation between contact angle, surface roughness, and chemical composition was considered on the basis of the above result. To deduce the correlation, an assumption was made that the value of contact angle θ_M measure can be expressed by the sum of the surface roughness-dependent factor θ_r and chemical composition-dependent factor θ_C.

$$\theta_M = \theta_r + \theta_C \quad \cdots\cdots (1)$$

The relationship between the contact angle and surface roughness shown in Fig. 11 can be expressed approximately by

$$\theta_r = 26.4r^2 + 18.6r + 77.1 \quad \cdots\cdots (2)$$

θ_r in Eq.(1) was estimated by assuming that Eq.(2) holds irrespective of chemical composition. The surface roughness r of each metal is the value measured at the contact area after the sample was held at 900°C for 30 minutes. The value is, for example, 0.90μm for copper, 0.54μm for iron, and 0.11μm for nickel.

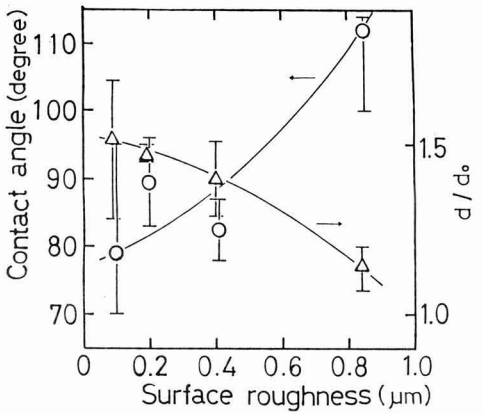

Fig. 11. Variation of contact angle and ratio of interfacial diameter with increasing surface roughness for nickel.

Table 3. Dependence of contact angle on surface roughness and chemical composition of metal.
θ_M: Measured value.
θ_r: Value depending on surface roughness.
θ_C: Value depending on chemical composition.

Contact angle (degree)	Samples							
	HPM38	ZHB11	SKD	CN	Copper	Iron	Nickel	Chrom.
θ_M	78	72	87	131	149	78	79	84
θ_r	78	79	79	81	115	95	79	78
θ_C	0	-7	8	50	34	-17	0	6

Table 3 lists the values of θ_M, θ_r, and θ_C. In Table 3, the relatively high value of θ_M on copper may be caused mainly by the increase in θ_r. CN, whose major component is copper, has nearly the same value of θ_r as compared with other metals, while it has the highest value of θ_C. In other words, θ_M of CN is heavily dependent on θ_C. This is probably because CN contains Zn having a relatively low boiling point (907°C). Zn evaporates during heating, and stays at the interface between glass and CN, which may increase the interfacial energy and reduce the wettability. Iron has a low θ_C and a high θ_r value. This suggests that θ_M is given by the increase in surface roughness caused by heating, although the wettability is high. Although it was explained in the discussion on Fig.7 that the surface roughness increased on metals other than nickel and

chromium, there was no significant difference in θ_r on metals other than copper, CN, and iron. This is probably because the value of r is low even if the surface roughness increases by a factor of 2 - 3 by heating since the surface roughness of HPM38, ZHB11, and SKD before heating is as small as 0.03μm.

(3) It is well known that the contact angle between the glass and metal depends on the chemical composition of metals.[10,11] Although the relationship between the contact angle and chemical composition has been discussed in the preceding section, SEM observation of surface condition reveals the following.

For copper, crystal growth was observed at about 600°C. This significantly increases the surface roughness, resulting in a relatively larger contact angle.

For HPM38, ZHB11, SKD, and iron, the formation of a film is found after heating. This may be an oxide film produced in the low-temperature region, where no reduction effect due to hydrogen occurs, by small amounts of oxygen or moisture present in the reducing gas, experimental apparatus, and inside of metal. Therefore, although the wettability of glass increases,[12,13] the reaction between glass and metal is accelerated mainly near chemically active grain boundaries, leading to the increase in surface roughness.

5. Conclusions

The wettability with soda lime-silica glass and the change in surface roughness for eight metals and alloys, HPM38, ZHB11, SKD, CN, copper, iron, nickel, and chromium were evaluated in the temperature range up to 900°C in a reducing atmosphere, with the following conclusions.

1) Alloys whose major component was copper had a lower wettability and the surface roughness increased by heating. HPM38, ZHB11, SKD, nickel, and chromium had higher wettability than copper-base metals, while their surface roughness was changed relatively less by heating. Iron had high wettability and a large increase in surface roughness.

2) Heating made for the crystal growth of the copper, sharpened the grain boundaries and formed film on CN, ion, iron-base metals, nickel, and chromium.

3) For nickel, the effect of surface roughness on contact angle was clarified.

4) The difference in wettability for metals and alloys was evaluated on the basis of the change in surface roughness caused by heating and the chemical composition of the metal alloy.

5) The wettability and surface roughness dependent on the reaction product, crystal growth, and kind of alloy are essential factors for evaluating glass shaping molds.

References:

1) T. Mochizuki, New Glass Technology, 4, 45 - 52 (1984).
2) S. Mishima, *ibid.*, 3, 25 - 30 (1983).
3) T. Shibazaki, Official Patent Gazette, Sho 61-270227.
4) T. Yoshio and M. Hara, "*Asahi Glass Research Report*", 15, 103 - 112 (1965).
5) R.C. Dartnell, H.V. Fairbanks and W.A. Koehler, *J. Am. Ceram. Soc.*, 34, 357 - 360 (1951).
6) W.C. Dowling, H.V. Fairbanks and W.A. Koehler, *ibid.*, 33, 269 - 273 (1950).
7) J.A. Kapnicky, H.V. Fairbanks and W.A. Koehler, *ibid.*, 32, 305 - 308 (1949).
8) R.B. Adams and J.A. Pask, *ibid.*, 44, 430 - 433 (1961).
9) Metal Handbook, 3rd revision, edited by Japan Institute of Metals, Maruzen, pp. 1660 - 61.
10) K. Sameshima and M. Nishiyama, Yogyo-kyokai-shi, 74, 301-312 (1966).
11) V.F. Zackay, D.W. Mitchell, S.P. Mitoff and J.A. Pask, *J. Am. Ceram. Soc.*, 36, 84 - 89 (1953).
12) Y. Ikeda, *Materials*, 17, 979 - 989 (1968).
13) B.W. King, H.P. Tripp and W.H. Duckworth, *J. Am. Ceram. Soc.* 42, 504 - 525 (1959).

This article is a full translation of the article which appeared in Nippon Seramikkusu Kyokai Gakujutsu Ronbunshi (Japanese version), Vol.97, No.8, 1989.

Mechanical Properties of SiC Whisker Reinforced Glass Ceramic Composites

Masahiro Ashizuka, Yoshinori Aimoto* and Masahiko Watanabe*

Kyushu Institute of Technology
1-1, Sensui-cho, Tobata-ku, Kitakyushu 804, Japan
*Graduate School, Kyushu Institute of Technology,
1-1, Sensui-cho, Tobata-ku, Kitakyushu 804, Japan

Flexural strength, Young's modulus, Vickers hardness and fracture toughness of SiC whisker reinforced glass ceramics (diopside, anorthite and cordierite) were measured. Maximum strengths of these composites were 550MPa for 30vol% whisker-diopside, 427MPa for 25vol% whisker-anorthite and 391MPa for 30vol% whisker-cordierite. Young's modulus and Vickers hardness of the composites increased with increasing whisker contents, exhibiting maximum at 25 - 30vol% whisker. While they decreased with more whisker contents. Apparent fracture toughness of SiC whisker-glass ceramic composites obtained by the indentation fracture technique was dependent on the indenter load. The maximum values of fracture toughness at indenter load of 10kg were 4.53MPa·m$^{1/2}$ for 40vol% whisker-diopside, 4.37MPa·m$^{1/2}$ for 30vol% whisker-cordierite and 4.13MPa·m$^{1/2}$ for 25vol% whisker-anorthite. It was assumed that the strengthening mechanism of SiC whisker-glass ceramic composites was load transfer. While, it was suggested that the toughening mechanisms of these composites were whisker pullout, crack deflection and load transfer to whisker for diopside glass ceramics, and crack deflection and load transfer for anorthite glass ceramics, and load transfer to cordierite glass ceramics.
[Received January 6, 1989; Accepted May 16, 1989]

Key-words: Glass ceramic composites, SiC whisker, Strength, Young's modulus, Fracture toughness, Load transfer, Crack deflection, Whisker pullout

1. Introduction

Ceramics have the advantages of being highly heat-resistant, high strength at elevated temperature, lightweight, and highly corrosion-resistant, and have attracted considerable attention as new mechanical and structural materials. However, they suffer one disadvantage; they have poorer fracture toughness than metals. To overcome this disadvantage, studies have been extensively carried out by the addition of long fibers[1-4] or whiskers to ceramics. The increase in strength and toughness of ceramics achieved by the addition of long fibers or whiskers depends upon the difference in physical properties, such as thermal expansion coefficient and Young's modulus, between the matrix and fiber or whisker.[12,13] The authors previously reported the physical properties of various silicate ceramics.[14] In the present study, we chose three kinds of glass ceramics with different thermal expansion coefficients as matrices: diopside ($CaO \cdot MgO \cdot 2SiO_2$), anorthite ($CaO \cdot Al_2O_3 \cdot 2SiO_2$), and cordierite ($2MgO \cdot 2Al_2O_3 \cdot 5SiO_2$). Among these three, diopside has the highest strength, Young's modulus, and hardness. Comparing the thermal expansion coefficients, anorthite has a thermal expansion coefficient close to that of SiC (4.5×10^{-6} 1/K)[15]; diopside has a higher thermal expansion coefficient, while cordierite has a lower one. In the present study, we investigated the mechanical properties of these glass ceramics reinforced with SiC whiskers.

2. Experimental Method

Commercially available $CaCO_3$, MgO, SiO_2 and Al_2O_3 Class 1 reagents were used as the powder materials for preparing three kinds of glass ceramics. These materials were blended into the prescribed composition. The blended material, put into a graphite crucible, was melted at 1500° - 1550°C, and then water-quenched. The resultant glass was finely ground to below 3μm. The glass powder and SiC whiskers (supplied by Tateho Chemical Industries Co., Ltd.), were put into an alumina ball mill and mixed for 10 hours with ethyl alcohol solvent to form the mixed powder of glass and whisker. The mixed powder was hot-pressed (200kg/cm^2) at 1250° - 1300°C for 1 hour with a graphite mold to form 18mm-dia, 18mm-long cylindrical sintered bodies. The density was determined by the Archimedean method. The Young's modulus was calculated by combining density with longitudinal and shear wave sound velocities measured with a sing-around sound velocity measuring apparatus. The Vickers hardness was measured under an indenter load of 200g on a Vickers hardness tester. The flexural strength was measured by three-point bending with spans of 15mm. The specimen for the bending test was cut from the cylindrical ceramic composite to a size 4mm wide and 2mm thick, and mirror-polished with 1μm diamond paste. The fracture toughness was determined by the indentation fracture technique (IF technique). Several equations have been proposed to determine the fracture toughness K_{IC} by the IF technique. In this study, the following equation proposed by Evans[17] was used.

$$\log [(K_{IC}/Ha^{0.5})(H/E)^{0.4}] = -1.59 - 0.34[\log(c/a)] - 2.02[\log(c/a)]^2 + 11.23[\log(c/a)]^3 - 24.97[\log(c/a)]^4 + 16.32[\log(c/a)]^5 \quad \ldots\ldots (1)$$

where, E is Young's modulus, H is hardness, a is the length of the crack formed by the Vickers hardness tester, and C is one half the diagonal length of indentation. The pressing face of the Vickers indentor for measuring hardness and fracture toughness was perpendicular to the direction of hot pressing.

3. Experimental Results and Discussion

3-1. Effect of SiC Whisker Content on Density

Figure 1 shows the density and relative density as a function of SiC whisker content for three kinds of glass ceramics. The relative density was calculated on the basis of additivity on the assumption that the density of SiC whisker was 3.18g/cm^3.[15] The relative density was under 1 for diopside and cordierite containing 30vol% or more SiC whisker and for anorthite containing 25vol% or more SiC whisker. This is probably because the addition of 25 to 30vol% or more SiC whisker causes whiskers to come into contact with each other depending on the type of matrix, resulting in difficulty in densifying.

3-2. Effect of SiC Whisker Content on Flexural Strength

Figure 2 shows the flexural strength as a function of SiC whisker content (vol%). The flexural strength increases with increasing SiC whisker content. The maximum strength is 550MPa for 30vol% whisker-diopside, 427MPa for 25vol% whisker-anorthite, and 391MPa for 30vol% whisker-cordierite. The SiC whisker contents in glass ceramics exhibiting the maximum strength correspond to those at which relative densities begin decreasing to under 1.

3-3. Effect of SiC Whisker Content on Young's Modulus

Figure 3 shows the Young's modulus as a function of SiC whisker content (vol%). Since the Young's modulus of SiC whisker is higher than that of the matrix, the Young's modulus of SiC whisker reinforced glass ceramics increases linearly with increasing SiC whisker content. However, the Young's modulus reaches a maximum at 30 - 40% whisker content for diopside, at 30% for cordierite, and at 25% for anorthite, and decreases when the whisker content further increases. For anorthite and cordierite, the tendency for Young's modulus to reach a maximum and then decrease corresponds to the tendency for relative density shown in Fig. 1. For diopside, the SiC whisker content exhibiting the highest Young's modulus is higher than the content when relative density begins decreasing to under 1. Since Young's modulus generally has additivity, it increases linearly with increasing content of SiC whisker having higher Young's modulus. The Young's modulus of composite decreases with decreasing density. When the density decreases slightly, the increase in Young's modulus caused by increasing SiC whisker content predominates over the decrease in Young's modulus caused by decreasing density. This may be the reason why the SiC whisker content exhibiting the highest Young's modulus

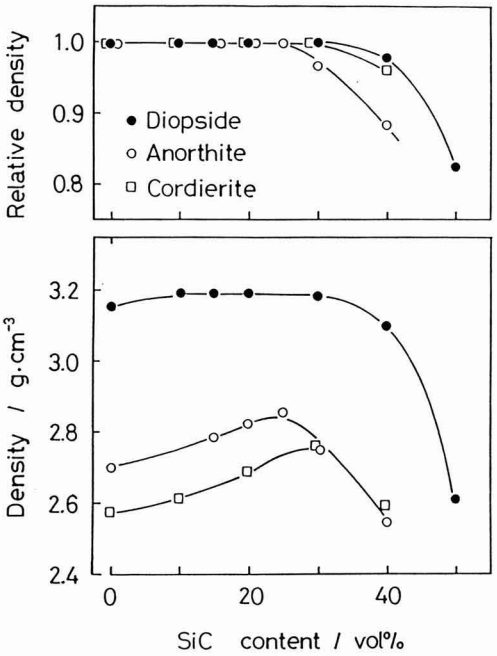

Fig. 1. Density and relative density as a function of SiC whisker content (vol%).

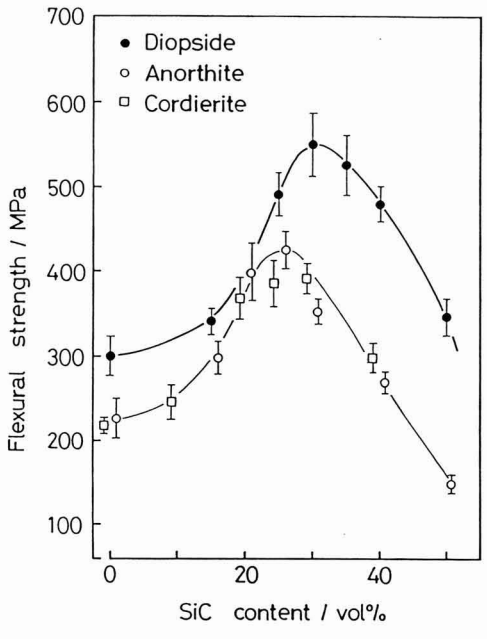

Fig. 2. Flexural strength as a function of SiC whisker content (vol%).

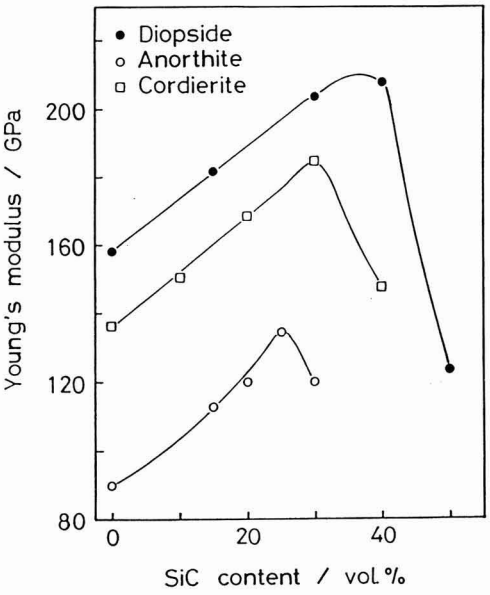

Fig. 3. Young's modulus as a function of SiC whisker content (vol%).

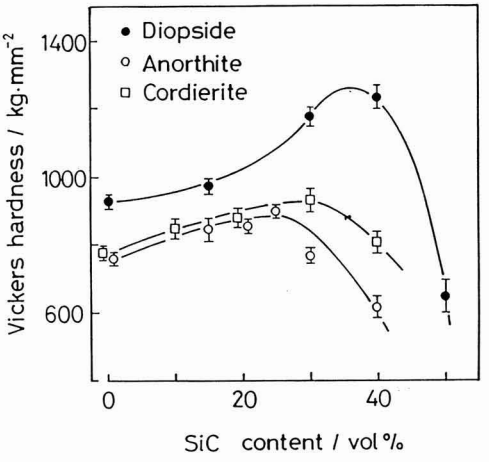

Fig. 4. Vickers hardness as a function of SiC whisker content (vol%).

is higher than the content when relative density begins decreasing to under 1. When the SiC whisker content increases further and the density decreases greatly, the Young's modulus of composite may decrease. The Young's moduli shown in Fig. 3 were calculated from the sound velocity in the hot pressing direction. The Young's moduli of some specimens were calculated on the basis of measurements of the sound velocity perpendicular to the hot pressing direction. No difference was found between them.

3-4. Effect of SiC Whisker Content on Hardness

Figure 4 shows the Vickers hardness as a function of SiC whisker content (vol%). The Vickers hardness was measured at the surface perpendicular to the hot pressing direction. Although the hardness of the SiC whisker is unknown, it is estimated to be as high as 2800kg/ mm^2 [19] by referring to the value of high purity SiC. The hardness of the composite increases monotonously with increasing SiC whisker content. As with the Young's modulus, however, the hardness reaches a maximum at 30 - 40% whisker content for diopside, at 30vol% for cordierite, and at 25vol% for anorthite, and decreases when the whisker content further increases. For cordierite and anorthite, the SiC whisker content exhibiting the highest hardness is equal to the content for relative density to begin decreasing to under 1. For diopside, as with Young's modulus, the SiC whisker content exhibiting the highest hardness is higher than the content when the relative density begins decreasing to under 1.

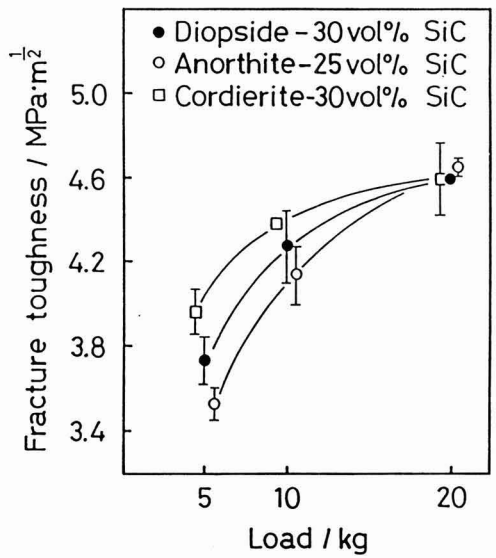

Fig. 5. Apparent fracture toughness as a function of Vickers indenter load (kg).

3-5. Effect of SiC Whisker Content on Fracture Toughness

Figure 5 shows the apparent fracture toughness K_{IC} determined by the IF technique as a function of Vickers indenter load (kg) for glass ceramics having the SiC whisker content exhibiting the highest strength. The

fracture toughness K_{IC} increases as the indenter load increases from 5kg to 10 to 20kg, not being constant. This means that it is unreasonable to use the IF technique for measuring the fracture toughness of the whisker reinforced glass ceramics. In this study, however, this technique was used because only the relative change in fracture toughness with SiC whisker content was evaluated.

Figure 6 shows the fracture toughness as a function of SiC whisker content (vol%) for the indenter load of 10kg. The fracture toughness K_{IC} increases monotonously with increasing SiC whisker content, reaches a maximum at 40vol% whisker content for diopside, at 25vol% for anorthite, and at 30% vol% for cordierite, and decreases when the whisker content further increases. For the indenter load of 5kg, the fracture toughness showed a tendency similar to that in Fig. 6. For anorthite and cordierite, the SiC whisker content exhibiting the highest fracture toughness was nearly equal to the content exhibiting the highest strength. For diopside, the SiC whisker content exhibiting the highest fracture toughness was higher than the content exhibiting the highest strength.

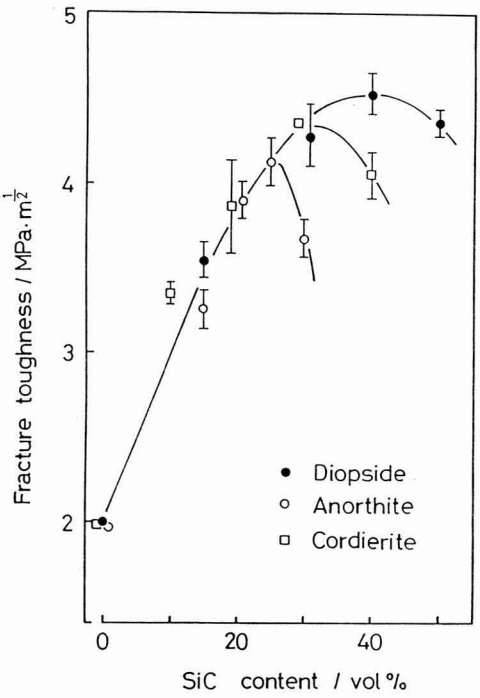

Fig. 6. Fracture toughness (Indenter load: 10kg) as a function of SiC whisker content (vol%).

3-6. Observation of Fractured Surface

Figures 7 through 9 show the scanning electron micrographs of fractured surfaces photographed after the measurement of strength. Figure 7 shows the micrographs of fractured surfaces for glass ceramics containing no SiC whiskers. Diopside shown in Fig. 7(a) consist of very fine grains, and has a rougher fractured surface than the other two glass ceramics. Figures 7(b) and 7(c) show the fractured surfaces of anorthite and cordierite, respectively, which are more smooth than that of diopsite. Figure 8 shows the scanning electron micrographs of fractured surfaces for 30vol% whisker-diopside, 25vol% whisker-anorthite, and 30vol% whisker-cordierite. Diopside has a rougher fractured surface than anorthite and cordierite. The observation of whiskers on the fractured surfaces revealed that more whisker having been pulled out were found in diopside than anorthite and cordierite. Reflecting this, holes made by whisker pullout were observed as shown in Figs. 9(a) and 9(b). Figure 9(b) is the enlarged view of the arrowed H area in Fig. 9(a). Although the pullout of many whiskers was observed for diopside, the proportion of whiskers broken at the same level as the matrix was higher on the fractured surface. In anorthite and cordierite, whisker pullout was partially found, although the number of pulled-out whiskers was small. In cordierite, most whiskers were broken at the same level as the matrix. Sakamoto and Ito[20] reported that for SiC whisker reinforced glass ceramics with a matrix of enstatite and cordierite having a thermal expansion coefficient nearly equal to that of SiC whisker, the maximum strength of 490MPa was achieved, but no whisker pullout was found.

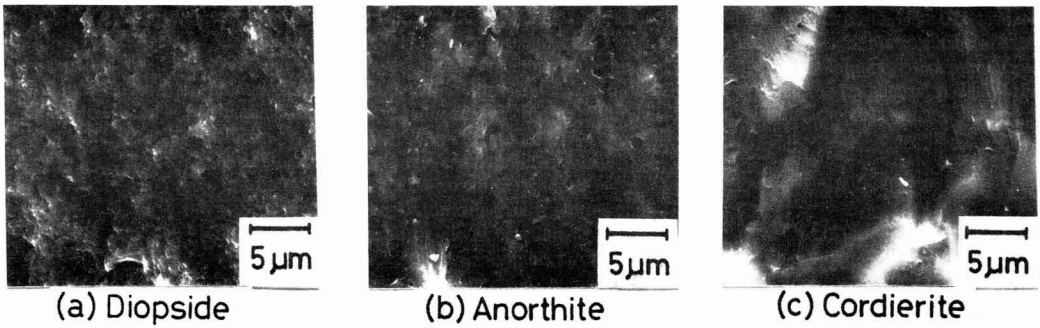

Fig. 7. Scanning electron micrographs of fracture surface for glass-ceramics.

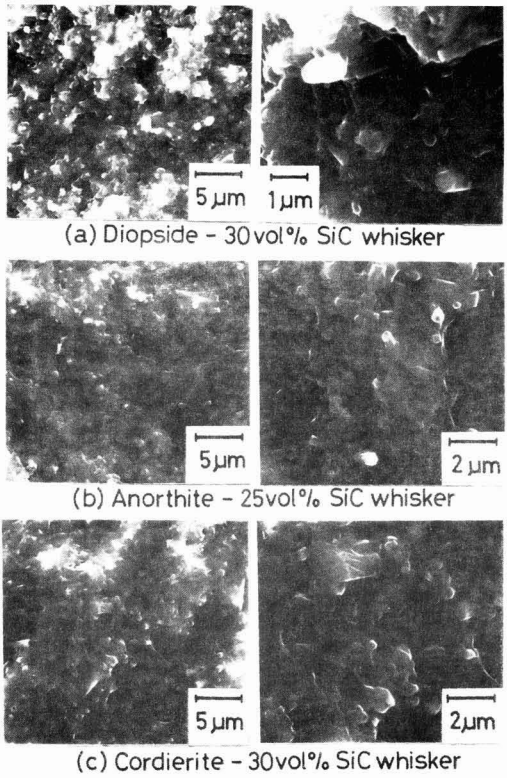

Fig. 8. Scanning electron micrographs of fracture surfaces for SiC whisker reinforced glass ceramics.

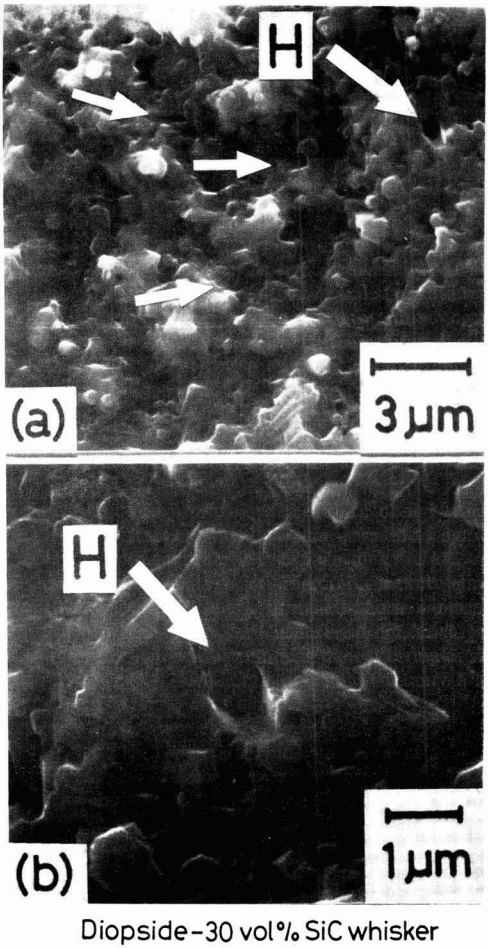

Fig. 9. Scanning electron micrographs of fracture surfaces for 30vol% SiC whisker reinforced diopside glass ceramics.
Arrows indicate whisker pullout and arrow H in Fig. 9(b) corresponds to that in Fig. (a).

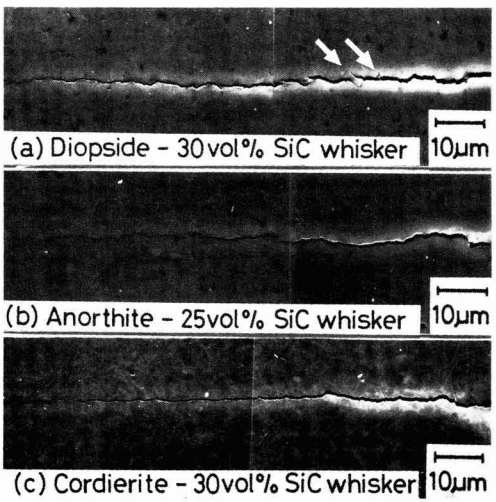

Fig. 10. Propagation of crack induced by Vickers indenter for SiC whisker reinforced glass ceramics.

3-7. Crack Configuration

Figures 10(a) through 10(c) show the propagation of cracks induced by a Vickers indenter on the mirror-polished specimen surfaces of SiC whisker reinforced glass ceramics. Diopside glass ceramics shown in Fig. 10(a) have a greater degree of crack deflection than the other two glass ceramics, and the crack deflection mechanism may affect the propagation of cracks in diopside glass-ceramics. Cordierite glass ceramics shown in Fig. 10(c) have a straighter crack than diopside and anorthite glass ceramics. Figure 11 shows the partially enlarged photograph of the crack in the vicinity of the arrows in Fig. 10(a). The arrow in Fig. 11 indicates whisker pullout caused during the propagation of crack.

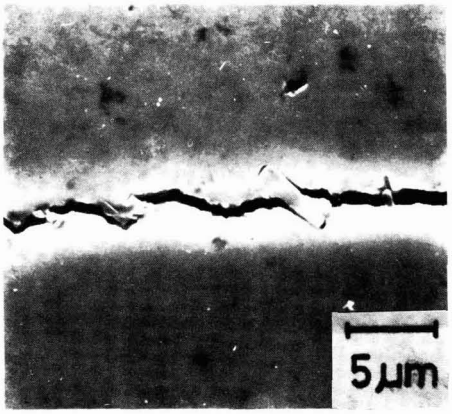

Fig. 11. Close up photograph of the crack in the vicinity of arrows in Fig. 10(a).

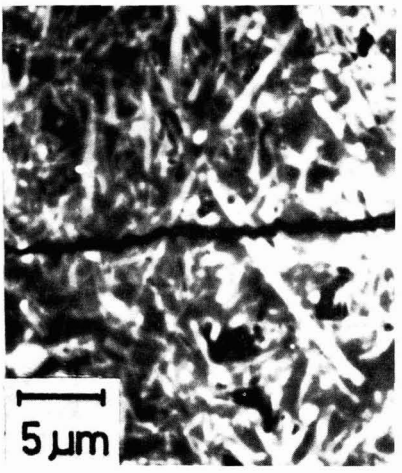

Fig. 12. Microstructure of cordierite-SiC whisker composites around crack in the compositional back scattered electron image.

Figure 12 shows the microstructure of the cordierite-SiC whisker composite. The crack goes through the SiC whiskers. This corresponds to the fact that most whiskers on the fractured surface in Fig. 8(c) are broken at the same level as the matrix. From the consideration of the toughening mechanism of the three kinds of SiC whisker reinforced glass ceramics based on the above results, it is believed that whisker pullout and crack deflection play a big role in diopside glass ceramics and crack deflection does in anorthite. As seen from Fig. 10(c), crack deflection may play a smaller role in toughening cordierite glass ceramics than the other two ceramics.

Rice[21] has reported that the Young's modulus ratio of fiber to matrix E_{fiber}/E_{matrix} needs to be 2 or higher because load transfer works effectively as a strengthening mechanism. The Young's modulus ratio of glass ceramics to SiC whisker is 3.0 for diopside glass ceramics, 5.4 for anorthite, and 3.5 for cordierite, which suggests that load transfer is effective as a strengthening mechanism. Generally, the load transfer mechanism works effectively when the elongation of the matrix is greater than that of the fiber. Therefore, when the matrix fracture before the fiber breaks as with ceramic matrices, the load transfer may contribute less to strengthening.[13] As with this study, however, when there is a bond between the whisker and matrix, some force is transferred to the whiskers through the unbroken matrix area even if the matrix is cracked.[22,23] As shown in Fig. 2, the breaking strength increased with increasing SiC whisker content even for cordierite in which crack deflection or whisker pullout is hardly found. This is probably because the load is transferred to whiskers by breaking in the vicinity of the fractured surface of the matrix. As seen from Fig. 8, the proportion of whiskers breaking at the same level as the matrix is higher than that of the pulled-out whiskers even for diopside in which crack deflection and whisker pullout contribute most. It is therefore supposed that the effect of load transfer is also great. Assuming that the size of crack within the material is constant, the fracture toughness increases with increasing strength. As similar relationship between the fracture toughness and SiC whisker content for the three glass ceramic composites as shown in Fig. 6 suggests that the same toughening mechanism works for the three composites. That is, load transfer plays a great role as a toughening mechanism in addition to the mechanism inferred from the observation of fractured surface and crack propagation. In summary, it is supposed that the three mechanisms of load transfer, whisker pullout, and crack deflection have important roles in toughening diopside glass ceramics, the two mechanisms of load transfer and crack deflection in toughening anorthite glass ceramics, and the mechanism of load transfer in toughening cordierite glass ceramics.

4. Conclusions

The flexural strength, Young's modulus, Vickers hardness, and fracture toughness of SiC whisker reinforced glass ceramic composites of diopside, anorthite, and cordierite were measured. Results obtained are as follows.

1) The flexural strength increased with increasing SiC whisker content, and reached a maximum at 30% whisker for diopside glass ceramics, at 25% whisker for anorthite, and at 25 - 30% whisker for cordierite.

2) The Young's modulus and Vickers hardness increased with SiC whisker content, and reached a maximum at 35 - 40% whisker for diopside, glass ceramics, at 25% whisker for anorthite, and at 30% whisker for cordierite.

3) The fracture toughness increased with increasing SiC

whisker content, and reached a maximum at 40% whisker for diopside glass ceramics, at 30% whisker for anorthite, and at 30% whisker for cordierite.

4) Pullout of many whiskers was found on the fractured surface of SiC whisker reinforced diopside glass ceramics. However, most whiskers were broken at the same level as the matrix.

5) Pullout of whisker, although rare, was found on the fractured surface of SiC whisker reinforced anorthite glass ceramics. However, most whiskers were broken at the same level as the matrix.

6) Whiskers on the fractured surface of SiC whisker reinforced cordierite glass ceramics were broken at the same level as the matrix.

7) Crack defection was the largest for diopside glass ceramics, and the smallest for cordierite glass ceramics.

8) It was suggested that the toughening mechanisms of SiC whisker reinforced glass ceramic composites were crack deflection, whisker pullout, and load transfer for diopside glass ceramics; crack deflection and load transfer for anorthite glass ceramics; and load transfer for cordierite glass ceramics.

References:

1) K.W. Prewo and J.J. Brennan, J. Mater. Sci., 17, 1201-06 (1982).
2) J.J. Brennan and K.W. Prewo, J. Mater. Sci., 17, 2371-78 (1982).
3) J. Guo, Z. Mao, C. Bao, R. Wang and D. Yan, J. Mater. Sci., 17, 2371-78 (1982).
4) M.A. Herron and S.H. Risbud, Am. Ceram. Soc. Bull., 65, 342-46 (1986).
5) T.A. Michalske and J.R. Hellmann, J. Amer. Ceram. Soc., 71, 725-31 (1988).
6) G.C. Wei and P.F. Becker, Am. Ceram. Soc. Bull., 64, 298-304 (1985).
7) N. Claussen, K.L. Weisskopb and M. Ruhle, J. Amer. Ceram. Soc., 69, 288-92 (1986).
8) K.P. Gadkaree and K. Chyung, Am. Ceram. Soc. Bull., 65, 370-76 (1986).
9) N. Tamari, I. Kondo, K. Sodeoka, K. Ueno and Y. Toihata, Yogyo-Kyokai-shi, 94, 1177-79 (1986).
10) P.F. Becker and T.N. Tiegs, J. Amer. Ceram. Soc., 70, 651-654 (1987).
11) R. Ruh, K.S. Mazdiyasni and M.G. Mendiratta, J. Amer. Ceram.Soc., 71, 503-12 (1988).
12) E. Fitzer, "Proc. Int. Symp. of Factors in Densification and Sintering of Oxide and S. Saito, Gakujutsu Bunken Fukyukai, (1978), p.618-73.
13) S. Inoue, T. Uchiyama and K. Niihara, Ceramics, 21, 621-69 (1986).
14) M. Ashizuka, Y. Aimoto and T. Okuno, J. of the Ceramic Society of Japan 97; 544-48 (1989). Inter. Ed. Vol. 97, 535-39 (1989).
15) Tateho Chemical Industries Catalogue
16) A.G. Evans and E.A. Charles, J. Am. Ceram. Soc., 59, 371-72 (1976).
17) A.G. Evans, "Fracture Mechanics Applied to Brittle Materials, ASTM STP 678," Ed. by S.W. Freiman, American Society for Testing and Materials (1979), p.112-35.
18) K. Niihara, R. Morena and D.P.H. Hasselman, J. Am. Ceram. Soc., 65, C-116 (1982).
19) S. Udagawa, H. Yanagida and G. Sudo, "Inorganic Silicon Compounds for Fine Chemicals," Kodansha (1982), p.65.
20) O. Sakamoto and S. Ito, Asahi Glass Research Repot, 37, 1-12 (1987).
21) R.W. Rice, Ceram. Eng. Sci. Proc., 2, 661-701 (1981).
22) R.W. Davidge, "Mechanical Behavior of Cemamics," Cambridge University Press (1979), p.111-117.
23) Compiled by M. Doyama and R. Yamamoto; A. Ohkura, H. Fukuda, Y. Kagawa and T. Nishi, "Composites: Material Technology 17," Tokyo University Shuppankai (1984), p.166-174.

This article is a full translation of the article which appeared in Nippon Seramikkusu Kyokai Gakujutsu Ronbunshi (Japanese version), Vol.97, No.8, 1989.

Characteristics of Thermal Shock Durability of Porous Al_2O_3 Ceramics

Toshiaki Arato, Kousuke Nakamura and Masahisa Sobue

Hitachi Research Laboratory, Hitachi, Ltd.
832-2 Horiguchi, Katsuta-shi 312, Japan

Bending strengths of porous Al_2O_3 ceramics with relative densities of 97, 74 and 60 to 65% were measured before and after the thermal shock by water quenching.
An instantaneous decrease in strength was observed when the ceramics with relative densities of 97 and 74% were thermally shocked through the temperature difference of larger than 200°C. On the other hand, the strength of the ceramics with relative densities of 60 to 65% did not show the instantaneous decrease, but gradually decreased with an increase in quenching temperature.
The width of the cracks caused by the thermal stress fracture was 2 to 3μm when the temperature difference in quenching was 585°C.
Thermal shock fracture resistance parameter(R') and thermal shock damage resistance parameter (R") were calculated for each ceramics, which resulted that the high density ceramics showed highest.
[Received February 2, 1989, Accepted May 16, 1989]

Key-words: Thermal stress, Porous Al_2O_3, Water quenching, Bending strength, Thermal shock fracture resistance parameter, Thermal shock damage resistance parameter

1. Introduction

The heater of the indirect heating system used in cathode ray tubes consists of a W coil and insulation film on the surface. The insulation film is required to have a high thermal shock resistance, because it is exposed to instantaneous heating and quenching with the ON/OFF switching of the circuit. This insulation film consists normally of a high-purity, porous Al_2O_3 sintered body. The bending strength of porous Al_2O_3 sintered body is discussed in the reports of Coble and Kingery,[1] but they do not mention the thermal shock characteristics. There are some reports on the thermal shock characteristics of porous Al_2O_3 sintered bodies. There are many reports on refractories such as Meredith et al.[2] and Larson et al.[3] The thermal shock characteristics of dense Al_2O_3 sintered bodies were discussed by Davidge et al.[4] and Hasselman[5] and Gupta,[6] but the dependence of thermal shock characteristics upon porosity has not been investigated. In the present work the authors produced a specimen of porous Al_2O_3 sintered body through the slurry casting/forming process (slip casting process) and filtering process, using some kinds of powder made of Al_2O_3. The change in strength was measured before and after thermal shock and the effect of differences in the Al_2O_3 materials powder on the thermal shock resistance characteristics of the porous Al_2O_3 sintered body and the effect of the porosity of the sintered body on the thermal shock resistance characteristics of the porous Al_2O_3 sintered body were examined.

2. Experimental Method

2-1. Production of Specimen

Four powder Al_2O_3 materials as shown in Table 1 were used. In the slip casting process 300g of Al_2O_3 powder, 0.3g deflocculating reagent (sodium metaphosphoric acid) and 80 to 100g distilled water were mixed to make an Al_2O_3 suspension. This suspension was poured into a gum mold set on the gypsum plate and a compact (5×10×200mm) obtained, absorbing the water content with the gypsum. On the other the filtration process can produce a specimen with a lower relative density than the slip casting process. The outline of the filtration apparatus to produce specimens is shown in Fig. 1. The process of specimen production by filtration is as follows: The above mentioned deflocculating reagent and special grade reagent $Al(NO_3)_3$ 2.7g to promote sintering were dissolved into the distilled water (80ml), and mixed with special grade reagent ethyl alcohol (80ml). Al_2O_3 powder (120g) was added to the mixed solution to produce an Al_2O_3 suspension. This solution was poured into a mold made of fluororesin as shown in Fig. 1 (40mm inner diameter, 25mm inner depth) to filter the solution contents. Both the Al_2O_3 remaining and the mold were dried, obtaining a compact (40mm dia., about 10mm thick). To sinter the compact, a hydrogen atmosphere furnace with a N_2-H_2 mixed atmosphere (P_{N2}=50kPa, P_{H2}=50kPa) was used. The rate of temperature rise was about 400°C/h, and specimen was held at 1650±15°C for half an hour, and cooled in the furnace. A specimen (4×3×36mm) was made from the sintered body obtained and the surface polished to obtain a specimen for thermal shock testing. The

Table 1. Specification of Al_2O_3 powder.

No.	1	2	3	4
purity	>99.9%	>99.9%	>99.9%	>99.95%
shape	crushed	spherical	spherical	spherical
mean particle size(μm)	3.5 ~ 4.1	0.5	3.8	5.6

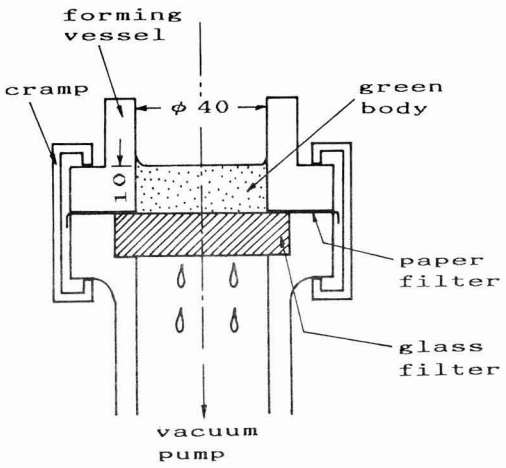

Fig. 1. Schematic diagram of filtration apparatus.

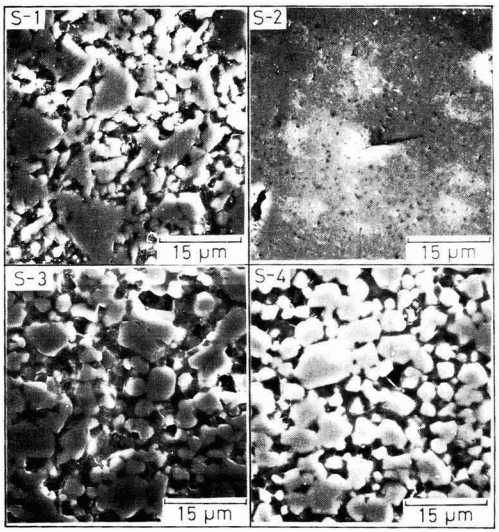

Fig. 2. Scanning electron micrographs of polished sections of S-series specimens.

Table 2. Relative density of specimen (unit: %).

method / Al_2O_3 No.	slip casting S-series		filtration F-series	
1	S-1	75.6±1.2	F-1	60.0±2.0
2	S-2	97.1±0.5	-	—
3	S-3	74.0±1.0	F-3	65.0±4.0
4	S-4	74.0±0.5	F-4	60.0±3.0

relative density of the specimen was measured by a displacement method. The specimens obtained under various conditions were impregnated with epoxy resin in preparation for polishing. The structure of the cut surface was observed with a scanning electron microscope (SEM), thermal etched in H_3PO_4 at 200°C for 10min. and the grain size (mean value) of the Al_2O_3 body measured.

2-2. Thermal Shock Test

The thermal shock specimen was thrown into water, at a given temperature below 20°C, after which the specimen was kept at the given temperature in an atmospheric furnace for 10 min. The specimen was then dried carefully and the 3-point bending strength was measured according to JISR-1601.

3. Results and Discussion

3-1. Structure and Density of Specimen

The relative densities of both the compact and specimen after sintering are shown in Table 2. The cutting face of the specimen obtained by the slip casting process (S-Series) under a SEM is shown in Fig. 2. The cutting face of the specimen obtained by the filtration process (F Series) under a SEM is shown in Fig. 3. The white space is Al_2O_3 grain, and the black space around the grain is impregnated with resin. The relative density of the specimens obtained from Al_2O_3 with a mean grain size of 0.5μm after sintering at 1600°C is 97%. The pores are distributed finely into the sintered compact. On the other hand, sintered compacts made from other powders Al_2O_3 have porous structures with continuous pores as shown in Fig. 2. In the S-Series, both the Na contained in the deflocculating reagent and Mg contained in $Mg(NO_3)_2$ promote sintering, contributing to the densification of grains. Accordingly, comparing the in F-series with the S-series, the porosity is high according to differences in the molding process, but little grain densification was observed.

3-2. Relationship Between Strength And Quenching Temperature Difference

The relationship between the quenching temperature difference and bending strength is shown in Fig. 4 for S-Series specimens (relative density 74-97%). The bending strength was measured using 5 samples for each quenching temperature difference. The bending strength is clearly divided into several ranges. For specimen S-3, the strength of the specimen without quenching and

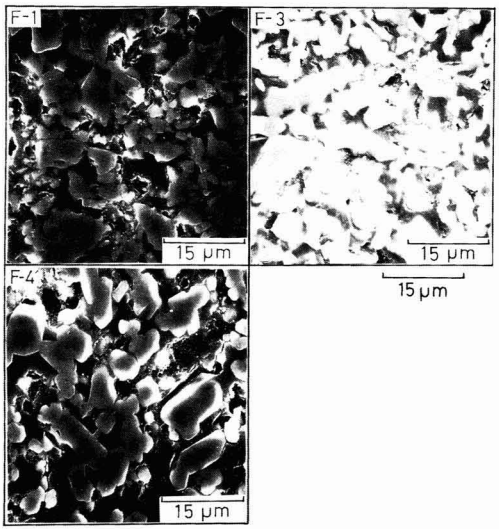

Fig. 3. Scanning electron micrographs of polished sections of F-series specimens.

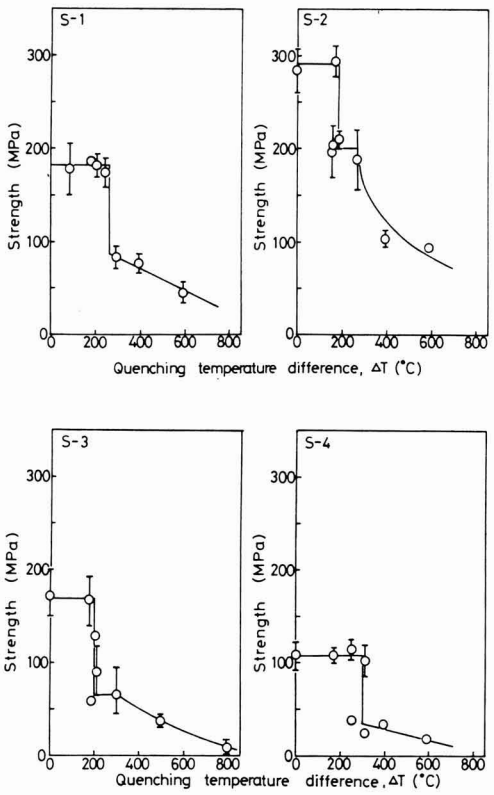

Fig. 4. Strength as a function of quenching temperature difference for S-series specimens.

Table 3. Al_2O_3 particle sizes of sintered bodies.

No.	particle diameter(μm)	No.	particle diameter(μm)
S−1	4.4	F−1	4.5
S−2	1.3	−	−
S−3	5.2	F−3	5.4
S−4	6.3	F−4	6.7

that quenched by thermal shock within 200°C are both within measurement error range, at about 170MPa. The strength of the specimen quenched in the narrow range of temperatures 190°-220°C changed rapidly, dropping to 60 to 90MPa. When the quenching temperature difference was larger than that the strength decreased as the temperature increased. The trend of change in strength agrees with the data reported by Davidge et al.[4] for dense Al_2O_3 sintered compacts, as well as Hasselman[5] and Gupta.[6] As shown in Fig. 4, the value of the quenching temperature difference (T_c) which causes the strength to drop rapidly does not depend upon Al_2O_3 grain size and relative density, and is stabilized in the range 200° to 300°C. Accordingly, we assumed that the occurrence of cracks due to the rapid quenching and the mechanism of damage are similar to those in Al_2O_3 sintered bodies with high density, if the relative density exceeds 74%. In Table 3 shows the mean value of grain sizes of Al_2O_3. Comparing the mean bending strength under T_c, the higher the relative density, the higher the strength of the specimen becomes, in addition, at the same density, the smaller the grain size of Al_2O_3 sintered compact, the larger the strength. This observation agrees with the trend obtained from a regular sintered compact. Comparing the dependance of Al_2O_3 particle shape in the cases of S-1 and S-3, the crushed particles has somewhat higher strength than the spherical one. This is presumably due to the fact that the crushed particle has a more irregular shape than spherical one and the contact area between particles in a porous sintered body is larger for crushed shapes than for spherical shapes. Comparing S-3 and S-4, both having almost the same relative density, a difference in strength below T_c was observed. As shown in the Fig. 2 structure micrographs, the cause of this difference consists of the degree of neck growth between particles, joining of particles and particle size, etc. In other words, in the case of S-4, the degree of neck growth is low, because the purity of Al_2O_3 is higher than in S-3. Accordingly, the densification of particles is relatively low. On the other hand, the relationship between the difference in quenching temperature and the change in strength of specimens produced by the filtration process is shown in Fig. 5. There is no T_c for the specimens produced by the filtration process, in contrast to those by the slip casting process, and the strength gradually decreased with the increase in quenching temperature difference. The trend of this result agrees with the results of Larson et al. on refractories containing 90% Al_2O_3. The reason why there is no T_c is because the crack is easily introduced even if the quenching temperature difference

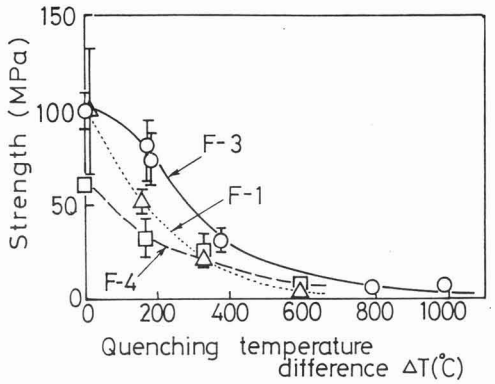

Fig. 5. Strength as a function of quenching temperature difference for F-series specimens.

is low; and the crack, once introduced, increases continuously with the quenching temperature difference. In other words, because the S-series specimen which is porous can absorb elastic energy, similarly to a dense sintered body, when a fracture generating stress is generated by thermal shock the crack grows rapidly, and the strength of sintered body decreases sharply beyond T_c. However, for F-series specimens, the crack expansion is better controlled control than in the S-series because the strain is changes with time.[12]

3-3. Observations on Fracture Sections and Cracks in Thermal Shock Specimens

The authors previously used a color contrast penetration method to measure the crack length.[1] It is impossible to use this method except for the S-2 specimen, because the color penetrated into the pores of specimens and the crack was indistinguishable. In the present work we used a color contrast penetration method for the S-2 specimen, but in other cases the fracture surface of the thermal shock specimen and the cracks on the surface of specimen were observed. The fracture surfaces of specimens of both the S-series and F-series after thermal shock are shown in Figs. 6 and 7. There is no great difference in fracture surfaces between the series. In other words, the fracture surface where $\Delta T=0$ to 200°C was relatively smooth, and no crack was detected, but a remarkable unevenness could be seen in the fracture surfaces of specimens when the quenching temperature difference exceeded T_c. The crack extends from the surface to the inside of the specimen when it is quenched. In this case, comparing specimens belonging to the same series, it can be assumed from the relative change in the unevenness of the fracture surface that both in the length and number of cracks in the specimen increased with an increase in the quenching temperature difference. Then some 3-5 locations at which a crack was detected were measured to obtain l_f. The results are shown in Fig. 8. Although the scattering of l_f values is considerable, the cracks grew with an increase in ΔT in accordance with the change in strength shown in Fig. 7.

An example of observation of a crack on the fracture face of a specimen is shown in Fig. 9. This crack was detected on the fracture surface of a S-1 specimen with $\Delta T=585$°C. The crack was generated in an area parallel to the longitudinal side of the specimen. The center of Fig. 9(a) is expanded as shown in Fig. 9(b). As can be seen, the crack is 2-3μm wide. Hasselman[5] observed cracks on the surface of dense specimens with Al_2O_3 composition ($\Delta T=800$°C) quenched quickly in water. According to Hasselman the crack was 2μm wide. The shape and size of the crack in our specimens is in good agreement with Hasselman's results. But the width of the cracks in specimens belonging to other series could not be measured so the relationship between the crack width and density of sintered body could not be investigated. However, no crack could be detected in the fracture section of specimens with a relative density of 60-65%. One of the reasons may be that it is difficult for a crack generated secondarily by thermal shock to grow, because the F-series specimen has a large volume between particles and another may be that the crack is generated non-linearly, because it is predominantly inter-particle bonding strength that is lost. Further investigation is necessary to identify the causes.

3-4. Comparison of Measured and Theoretical Values of Crack Length

The crack length on the surface of specimens stressed by thermal shock quenching were calculated based upon Hasselman's theoretical expression[5] and compared with the measured values of l_f as shown in Fig. 8.

According to Hasselman[5] the strength after the thermal shock quenching at T_c (σ_2) is given by Eq. (1) on the assumption that the depth from the specimen surface to the top of the crack is l_f.

$$\sigma_2 = [G_2 \cdot E/\{\pi \cdot l_f \cdot (1-\nu^2)\}]^{1/2} \quad \ldots\ldots (1)$$

The equation holds for cases where σ_2<strength (σ_1) before thermal shock, G_2 is the surface destruction energy corresponding to the thermal shock test environment, E is Young's modulus of the specimen without cracking, ν is Poisson ratio. Equation (2) can be derived from Eq. (1).

$$l_f = G_2 \cdot E/(\pi \cdot \sigma_2^2 \cdot (1-\nu^2)) \quad \ldots\ldots (2)$$

According to Coble et al.[1] it is clear that the values E and ν change with the relative density of specimen. The relative density of the specimen series was calculated and substituted into Eq.(1). In the present work G_2 and l_f were unknown. According to Hasselman,[5] σ_2 is calculated on the assumption that G_2 is 40-60Pa·m for a dense Al_2O_3 sintered body. Hasselman reported that the theoretical value calculated on the basis of G_2=40Pa·m agreed well with the experimental results.

Accordingly, it is reasonable to use this value for the comparatively dense Al_2O_3 sintered body among our specimens. In the case of a porous sintered body we can assume that the surface destruction energy of a porous specimen (G_2) is smaller than that for a dense sintered body, because the inter-particle bonding strength is smaller than for the dense sintered body. We can infer that the G_2 of S-1, S-3 and S-4 is smaller

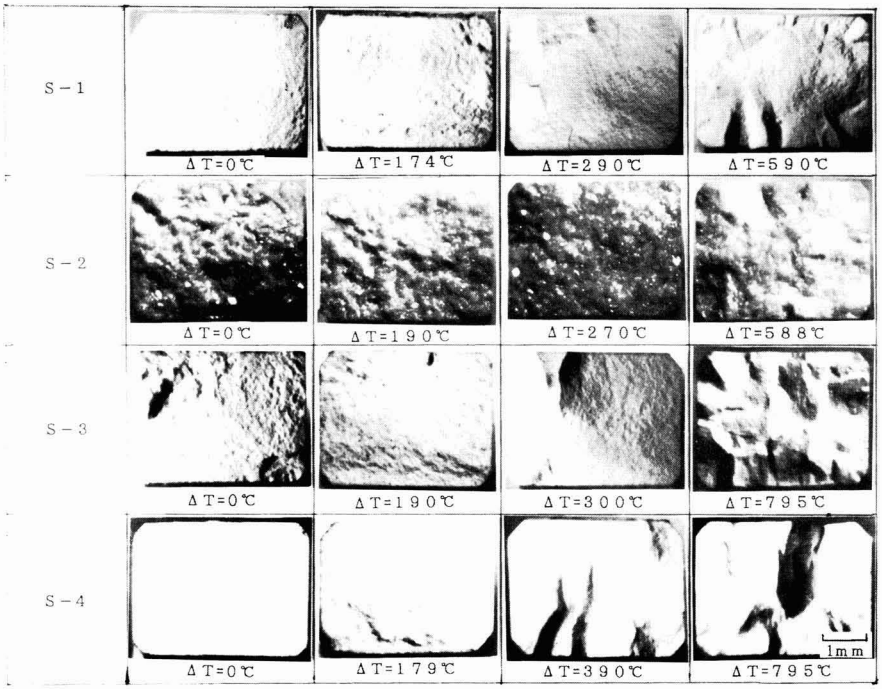

Fig. 6. Fracture surfaces of samples quenched to room temperature (S-series).

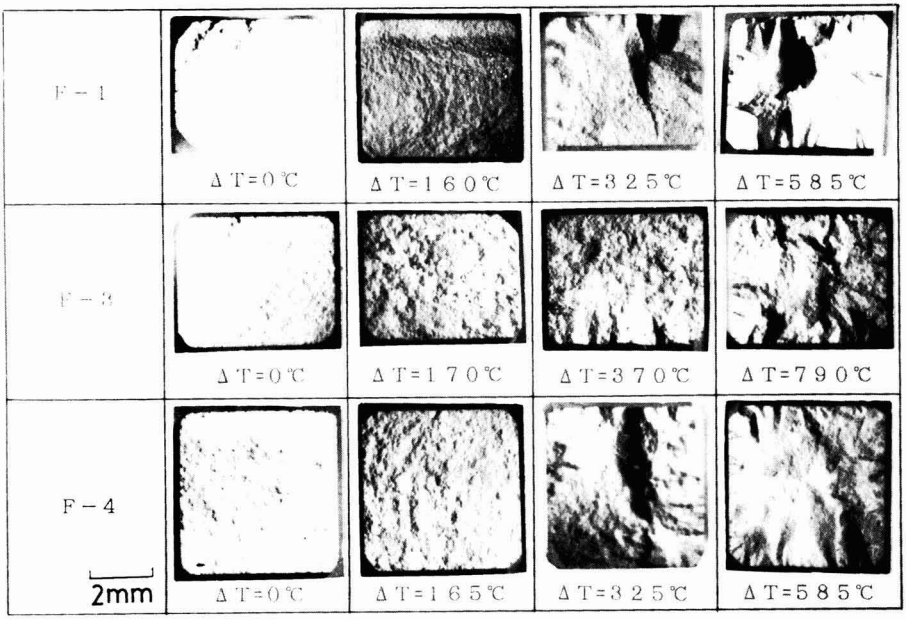

Fig. 7. Fracture surfaces of samples quenched to room temperature (F-series).

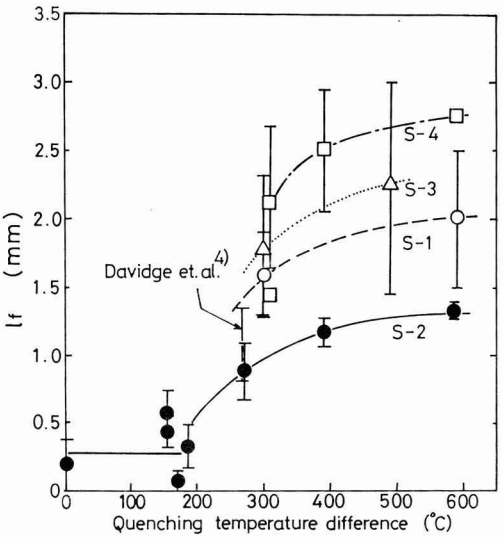

Fig. 8. Relationship between l_f and ΔT of S-series specimens.

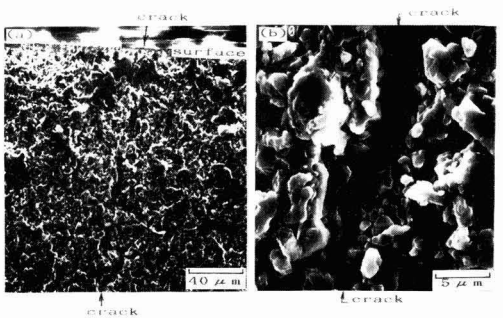

Fig. 9. Scanning electron micrographs of cracks in quenched specimen (specimen No. S-1, $\Delta T = 580°C$).
(a) fracture surface, (b) crack at higher magnification

Table 4. Calculated l_f values of quenched S-series specimens.

specimen No.	by Hasselman[3] G_2 (Pa·m)	by Coble et.al.[4] E (GPa)	ν	observed σ_z (MPa)	calucu-lated ℓ_f (mm)
S-1	<40	213	0.31	87	<0.40
S-2	40	370	0.27	200	0.13
S-3	<40	199	0.31	65	<0.67
S-4	<40	199	0.31	35	<0.67

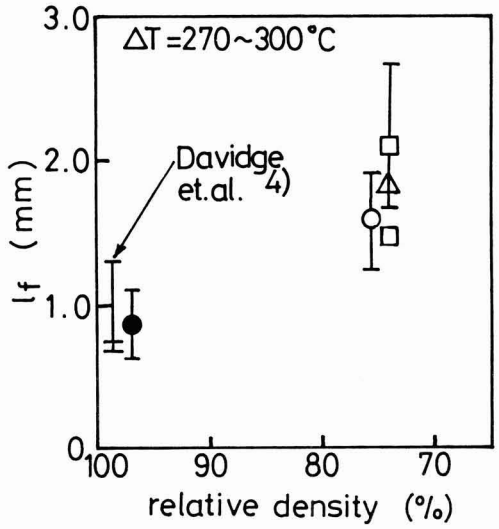

Fig. 10. Relationship between l_f and relative density of S-series specimens.

Table 5. Comparison of data of Davidge et al.[2] and present work.

researcher		dimension of specimen (mm)	σ_1† (MPa)	σ_2‡ (MPa)	T_c (°C)	ℓ_f (mm)
Davidge et.al		5×5×15	193 ~ 473	81 ~ 189	185 ~ 220	0.75 ~ 1.30
present work	S-1	4×3×30	182.5	87	260	<0.40
	S-2		289.5	200	190	0.13
	S-3		166.7	65	200	<0.67
	S-4		110.5	35	300	<0.67

†) three point bending strength at room temperature
‡) three point bending strength after quenching

than G_2 of S-2. But, because the dependence of G_2 upon porosity is not clear, we assumed $G_2 < 40$Pa·m in the case of specimens S-1, S-3 and S-4. The values of l_f calculated from Eq. (2) using the above assumption is shown in Table 4. Davidge et al.[4] measured the value of l_f when dense Al_2O_3 specimens with dimensions 5mm×5mm×15mm (σ_1 = 193-478MPa) were quenched from 270°C to room temperature (σ_2 = 81-189MPa) and reported it was 0.75-1.30mm (Table 5). Because the accuracy of the measured values is low in the range of ΔT below T_c, for specimens excluding S-2, the theoretical value is comparatively close to the value measured from the fracture surface. However, the l_f of the S-2 specimen is only a tenth of the value measured by Davidge et al. According to Hasselmann,[5] the decrease in strength at T_c of a dense Al_2O_3 sintered body with a relative density of more than 95% is about 220-390MPa. The decrease in strength at T_c of specimen S-2 is about

90MPa which is regarded as fairly small. This is because the thermal conductivity on the surface of the specimen is small at a quenching temperature near to T_c, so the crack introduced by thermal shock is short. Further investigation is required to find why the thermal conductivity of S-2 only is small. The relationship between l_f and the relative density of S-series specimens is shown in Fig. 10. The value of l_f has a wide scatter because it was estimated from the unevenness of the fracture section. A trend can be observed where the value l_f becomes smaller with an increase in the relative density of the sintered body.

3-5. Thermal Shock Fracture Resistance and Thermal Shock Damage Resistance Coefficients

We tried to calculate the fracture resistance coefficient and damage resistance coefficient for porous Al_2O_3 sintered body. The fracture resistance coefficient measures the degree of resistance of the sintered body to crack generation when a thermal shock stresses the sintered body. The damage resistance coefficient measures the growth of cracks when a thermal shock stresses the sintered body. Various expressions have been proposed for the fracture resistance coefficient according to the thermal shock type. We chose Eq. (3) or (4),[9] considering the condition of quenching in water.

$$R = S_1 \cdot (1-\nu)/(E \cdot \alpha) \quad \ldots\ldots (3)$$

$$R' = R \cdot \kappa \quad \ldots\ldots (4)$$

where, S_1=tensile strength of the specimen at room temperature (MPa) ($S_1 \simeq 0.57\sigma_1$),[9] σ_1=bending strength=measured value, ν=Poisson's ratio, κ=thermal conductivity at room temperature. These values change, depending upon the relative density of the specimen.[1,10] The value α is the coefficient of linear expansion and does not depend upon the relative density according to Coble et al.[1] Here, we adopted the value of 7×10^{-6} (K^{-1}). The selection of factor R or R′ was determined, depending upon the factor showing the degree of thermal shock, by the Biot modulus β (Eq. (5)).[7,11] When $\beta \geq 10$-20, Eq. (3) was used and when $\beta < 10$, Eq. (4) was used.

$$\beta = r_m \cdot h/\kappa \quad \ldots\ldots (5)$$

where $r_m = 1/2$ thickness of specimen, for S-series specimens $r_m = 1.5\times10^{-3}$(m), for F-series $r = 2.0\times10^{-3}$(m), h is the thermal conductivity of the quenching medium. As water was used the value 4.2×10^4 ($W/m^2 \cdot K$) was adopted.

The calculation results for β are shown in Table 6. The value β tends to increase with a decrease in relative density but in any case β is smaller than 10, so Eq. (4) was used to calculate the fracture resistance coefficient.

The value of the damage resistance coefficient R"[8] was calculated using Eq. (6)

$$R'' = E/(S_1^2 \cdot (1-\nu)) \quad \ldots\ldots (6)$$

The calculation results for R′ and R" are shown in Table 7. Examining the relationship between the fracture resistance coefficient R′ becomes larger with an increase in relative density, we can assume that the greater the relative density is, the higher the fracture resistance coefficient is regarding the initial crack generation caused by thermal shock. If the relative density is under 65%, the difference in resistance to crack generation due to thermal shock is decreased.

However, for R", because there is a strong effect of Young's modulus E, the specimens with low relative density had an apparently larger value, so far as the data are concerned, so it was not easy for the crack to develop, checked by the existing pores.

Table 6. Relationship between polosity of Al_2O_3 and Biot modulus (β).

porosity (%)	thermal conductivity*) k (W/(m·K))	Biot modulus(β) $r_m = 1.5\times10^{-3}$ (m)	Biot modulus(β) $r_m = 2.0\times10^{-3}$ (m)
0	32.4	1.94	2.58
10	28.3	2.22	2.96
20	24.5	2.56	3.42
30	20.0	3.14	4.19
40	18.3	3.43	4.57

Table 7. Calculated values of physical properties of specimens.

properties / specimen	tensile strength S_1 *1 (MPa)	tensile strength S_2 *2 (MPa)	Young's modulus E (GPa)	poisson's ratio ν (−)	thermal conductivity k (W/(m·K))	R′ (J/(m·s))	R" (1/Pa)
S-1	104	46	213	0.31	23.2	1.1×10^3	2.9×10^{-3}
S-2	165	92	370	0.27	31.0	1.4×10^3	1.9×10^{-3}
S-3	95	37	199	0.31	22.6	1.2×10^3	3.2×10^{-3}
S-4	63	23	199	0.31	22.6	0.7×10^3	7.3×10^{-3}
F-1	48	15	123	0.25	18.3	0.8×10^3	7.1×10^{-3}
F-3	57	27	151	0.27	19.7	0.8×10^3	6.4×10^{-3}
F-4	34	13	123	0.25	18.3	0.5×10^3	14.2×10^{-3}

*1) calculated value by bending strength at room temperature(20℃)

*2) calculated value by bending strength after water quenching(ΔT=300℃)

4. Conclusions

The following conclusions were obtained by measuring the strength of porous Al_2O_3 sintered bodies with relative densities of over 74% and 60 - 65%, before and after thermal shock quenching.

1) In the case of specimens with a relative density of over 74%. The strength decreased sharply at a quenching temperature difference of about 200°C.

2) In the case of specimens with a relative density of 60 - 65%. No sharp decrease in strength was observed at a quenching temperature difference of about 200°C. The strength gradually decreased with an increase in quenching temperature difference.

3) Observing the crack on the surface of specimens after the thermal shock, the crack was 2 - 3μm wide.

4) Calculating R′ (thermal shock fracture resistance coefficient) and R" (thermal shock damage resistance coefficient), the value R′ had the larger value with an increase in the relative density of specimens, but the value R" had an apparently larger value with a decrease in relative density, due to the effect of the decrease in elastic modulus.

(Lecture delivered to the 106th general meeting of the Japan Institute of Metals).

References:

1) R.L. Coble and W.D. Kingery, J. Am. Ceram. Soc., 39, 377-385 (1956).
2) H. Meredith, C.W. Newey and P.L. Pratt, Proc. Br. Ceram. Soc., 20, 299-316 (1972).
3) D.R. Larson, J.R. Coppola and D.P.H. Haselman, J. Am. Ceram. Soc., 57, 417-421 (1974).
4) R.W. Davidge and G. Tappin, Tans. Br. Ceram. Soc., 66, 405-422 (1967).
5) D.P.H. Hasselman, J. Am. Ceram. Soc., 53, 490-495 (1970).
6) T.K. Gupta, J. Am. Ceram. Soc., 55, 249-253 (1972).
7) W.D. Kingery, Introduction to Ceramics: John Wiley and Sons Inc., New York (1969) p.633.
8) D.P.H. Hasselman, J. Am. Ceram. Soc., 46, 535-540 (1963).
9) "Machinery Characteristics of Ceramics," Ed. Lecture Committee of the Ceramics Society of Japan, p.65 (1979).
10) J. Francl and W.D. Kingery, J. Am. Ceram. Soc., 37, 99-106 (1954).
11) W.R. Buessem, J. Am. Ceram. Soc., 38, 15-17 (1955).
12) R.W. Davidge, H. Suzuki and T. Iseki, Intensity and Fracture of Ceramics: Kyoritsu Shuppan, (1982) p.139.

This article is a full translation of the article which appeared in Nippon Seramikkusu Kyokai Gakujutsu Ronbunshi (Japanese version), Vol.97, No.8, 1989.

Thermal Shock Resistance of ZrO_2-Toughened MgO

Takashi Okamoto, Yasuro Ikuma, Mitsutaka Shimaoka, Tsukasa Shirotori and Wazo Komatsu,

Kanagawa Institute of Technology
1030 Shimo-ogino, Atsugi-shi, Kanagawa 243-02, Japan

The effect of a second phase (ZrO_2 particles) on the thermal shock resistance of MgO was investigated. MgO doped with 1mol% LiF and MgO dispersed with 10mol% ZrO_2 (t-ZrO_2 or c-ZrO_2) was fabricated by sintering. Sintered specimens were heated to various temperatures, quenched into water or lubricating oil, and then examined by the 4-point bending test to investigate the severity of the thermal shock. The critical temperature difference ΔT_c at which the fracture stress of specimens decreased considerably was higher in MgO dispersed with c-ZrO_2 (200K in water and 650K in lubricating oil) or t-ZrO (250K and 620K) than that in MgO doped with LiF(115K and 300K). These results have been attributed partially to the increase in fracture stress of MgO due to the existence of dispersed ZrO_2. The strength of MgO dispersed with t-ZrO_2 did not decrease instantaneously at the temperature difference in excess of ΔT_c. This behavior was not observed in other specimens. It was thought to be caused by the microcracks created by m-ZrO_2 which were also present in the specimen. The critical temperature difference ΔT_c of specimens quenched in lubricating oil was higher than ΔT_c quenched in water. It was qualitatively in accordance with the prediction of the calculation of the heat-transfer coefficient.

[Received February 10, 1989; Accepted May 16, 1989]

Key-words: Thermal shock, Sintered MgO, ZrO_2, Fracture stress, Toughened ceramics

1. Introduction

MgO is a typical basic oxide ceramic, but is inferior in its thermal shock resistance characteristic.[1,2] Because of the low mechanical strength and low thermal conductivity of MgO in comparison to other kinds of oxide ceramics, its thermal shock resistance characteristic seems to be difficult to improve to a great extent. However, the improvement of this characteristic, even to a small extent, should be effective for the expanded applications of MgO ceramics in the future.

In our previous reports,[3,4] the authors confirmed that fracture toughness and fracture stress of sintered MgO samples were improved by dispersing ZrO_2 in MgO. Since thermal shock fracture is caused by thermal stress, the improvement of fracture stress of sintered MgO dispersed with ZrO_2 suggests a possible improvement of the thermal shock resistance characteristic of sintered MgO dispersed with ZrO_2. In this study, therefore, we prepared sintered specimens of MgO mixed with ZrO_2, and investigated their thermal shock resistance behaviors.

2. Experimental Procedure

Two kinds of ceramic samples in the powder state were prepared. One was MgO of 99.0% purity (heavy grade, made by Wako Junyaku Co.) which was mixed with 3mol% of LiF of 98.0% purity (made by Wako Junyaku Co.). The other was the same MgO mixed with 10mol% of ZrO_2 (made by Kanto Kagaku Co.). These ceramic powder materials were respectively added with 2-propanol and made in a slurry state, ground by a wet ball mill for 20h with grinding media of columnar alumina, and then dried to obtain powder samples. About 0.8g of these powder samples were taken, pressed uniaxially under a pressure of 1.5t/cm^2, obtaining a beam specimen with rectangular cross section in size of about 3.5×4.1×30mm.

The beam specimen of MgO doped with LiF was sintered at 1300°C for 1h. The beam specimen of MgO dispersed with ZrO_2 was sintered at 1390° or 1450°C for 1h. In the case of MgO dispersed with ZrO_2, the crystalline structure of ZrO_2 was identified by X-ray diffraction analysis, the heights of respective diffraction peaks by $(11\bar{1})$ and (111) planes of monoclinic ZrO_2 (m-ZrO_2), and by (111) plane of tetragonal ZrO_2 (t-ZrO_2) or cubic ZrO_2 (c-ZrO_2) were measured from which the ratio of respective phases was calculated.[5] Distinction between t-ZrO_2 and c-ZrO_2 is difficult by X-ray diffraction analysis, therefore, we distinguished them based on a phase diagram.[6] According to X-ray diffraction analysis results, it was revealed that, when sintered at 1390°C, a specimen of MgO dispersed with ZrO_2 contained about 50% of ZrO_2 in t-ZrO_2 phase and the other 50% in m-ZrO_2 phase. Hereafter, we will call this specimen MgO dispersed with t-ZrO_2. It was also revealed that, when sintered at 1450°C, a specimen of MgO dispersed with ZrO_2 contained ZrO_2 almost all of which was in c-ZrO_2 phase. Hereafter, we will call this specimen MgO dispersed with c-ZrO_2.

After measuring the density by the Archimedean technique, the sintered specimen was fabricated with a grinder into a rod 2×3×24mm in size and was finally polished to a mirror-finish using alumina powder of 0.06μm in size. After polishing, adhered moisture was removed by heating at 400°C for 1h, followed by natural slow cooling.

In order to investigate the thermal shock resistance characteristic of these beam specimens, we measured the thermal shock fracture of the specimens by the following procedure. A specimen was hung by a platinum wire in a vertical electric furnace and heated from room temperature to a prescribed temperature, which was maintained for longer than 30min. Then it was quenched by immersing it together with a platinum wire

into a cooling medium in a vessel which was located underneath the electric furnace. Temperature difference ΔT in quenching was defined as the difference between the temperature of electric furnace and that of cooling medium. We used two kinds of cooling media, namely, water and lubricating oil. The average water temperature was 18°C and ΔT was set in the range of 0 to 300K. The average lubricating oil temperature was 28°C and ΔT was set in the range of 0 to 1000K. In order to investigate the damage of specimen caused by thermal shock, we measured the fracture stress by the 4-point bending test method (upper span = 8.0cm, lower span = 20.0cm) at a loading rate of about 1kg/min. In addition, we investigated the damage to the specimen caused by thermal shock by means of a fluorescent dye penetration flaw detection technique, and we observed the fractured surface of the specimen (after the fracture test) by means of SEM (JXA-840A).

3. Experimental Results

By means of X-ray diffraction analysis we identified the crystalline phases of both MgO dispersed with t-ZrO_2 and MgO dispersed with c-ZrO_2 before and after they were affected by thermal shock, finding little difference between the phases of respective materials. It is interpreted that the crystalline phases of ZrO_2 were not changed by the heating in our thermal shock tests.

Table 1 shows mean density, mean grain size, etc., of the specimens used in our present experiments. Relative density was higher than 96% in all specimens and did not differ significantly with each other. As for grain size, MgO doped with LiF was the largest, which differed significantly from other specimens.

Figure 1 shows the experimental results for fracture stress of various specimens which were quenched into water. Each data point represents a mean value of the measured results obtained with 3 to 8 specimens, and the vertical bar at each data point indicates the standard deviation. In the range of ΔT in which fracture stress is not decreased by thermal shock, it is seen that MgO doped with LiF shows a fracture stress σ_f at room temperature of about 110MPa, whereas, MgO dispersed with t-ZrO_2 shows σ_f of about 140MPa which is about 1.3 times as high as that of the former. In the same way, MgO dispersed with c-ZrO_2 shows a fracture stress at room temperature of about 310MPa, which is about 2.8 times as high as that of MgO doped with LiF. In summary, fracture stress σ_f increases when MgO is dispersed with ZrO_2, independent of the crystalline phase of ZrO_2. This figure indicates that, when the temperature difference ΔT in thermal shock is increased beyond the critical temperature difference ΔT_c, fracture stress abruptly decreases., In the case of MgO doped with LiF, ΔT_c is about 115K, while ΔT_c is about 250K and about 200K in the respective cases of MgO dispersed with t-ZrO_2 and MgO dispersed with c-ZrO_2, which are respectively 2.2 times and 1.7 times as high as that of MgO doped with LiF.

Figure 2 shows the experimental results for fracture stress when the specimens were quenched into lubricating oil. In the range of ΔT in which fracture stress is

Table 1. Densities and grain sizes of specimens

Specimen	density (g/cm^3)	standard deviation	relative density (%)	grain size (μm)
MgO doped with LiF	3.467	0.025	96.8	10.0
MgO dispersed with t-ZrO_2	3.777	0.028	96.2	1.5
MgO dispersed with c-ZrO_2	3.875	0.027	98.7	2.5

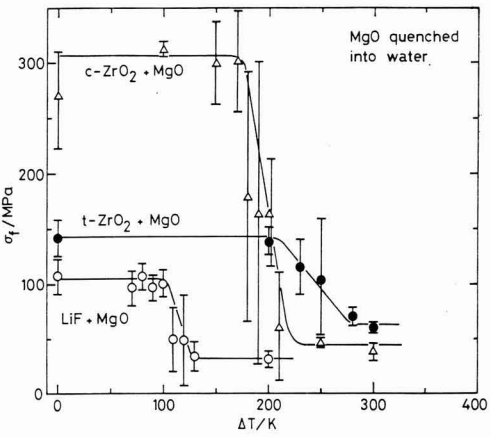

Fig. 1. Fracture stresses σ_f of MgO doped with LiF and MgO dispersed with ZrO_2 quenched from various temperatures into water at 18°C.

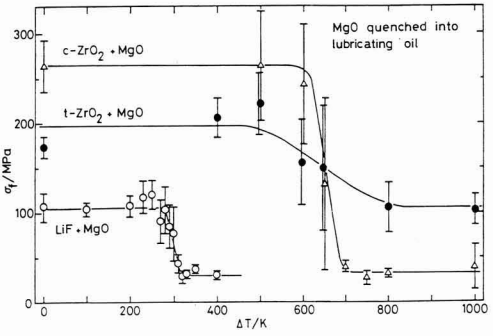

Fig. 2. Fracture stresses σ_f of MgO doped with LiF and MgO dispersed with ZrO_2 quenched from various temperatures into lubricating oil at 28°C.

not decreased by thermal shock, fracture stresses were not in the same values as those given in Fig.1, but we assume that their differences remain within the limit of experimental error (we mean the human error in specimen preparation). Critical temperature differences ΔT_c are observed (Fig.2) to be higher than those in Fig.1, where the specimens were quenched into a different cooling medium (water). As observed in Fig.2, ΔT_c is about 300K, 620K and 650K in the respective specimens of MgO doped with LiF, MgO dispersed with t-ZrO_2 and MgO dispersed with c-ZrO_2. All three of these ΔT_c values are about 3 times as high as the corresponding values of the specimens quenched into water. In the case of MgO dispersed with t-ZrO_2, it is seen that fracture stress decreases gently in the ΔT range around ΔT_c, and that, when thermal shock of higher than ΔT_c is given, fracture stress can remain at a certain high level. Summarizing Figs. 1 and 2, we can understand that dispersion of ZrO_2 in MgO can effectively improve the σ_f and ΔT_c of MgO ceramics.

Damage to the specimens caused by thermal shock was observed by a fluorescent dye penetration flaw detection technique, the results of which are shown in Fig.3. In the case of MgO doped with LiF, fluorescent emission started on the whole surface of specimen at around ΔT = 120K, which was close to ΔT_c. This phenomenon tends to indicate that a great number of fine cracks were generated by thermal shock on the entire surface of the specimen. In SEM photographs (Fig.4) of the fracture surfaces of MgO doped with LiF at ΔT = 0K as well as at ΔT = 130K which is a little higher than ΔT_c, individual grains can be clearly observed showing contours. This indicates the grain boundaries were selectively fractured, and agrees with the results obtained by the fluorescent dye penetration flaw detection technique. In the photographs of the specimen surfaces of MgO dispersed with t-ZrO_2 and MgO dispersed with c-ZrO_2 (Fig.3), crack generations are clearly observed to have taken place respectively at ΔT = 250K which is close the ΔT_c of the former

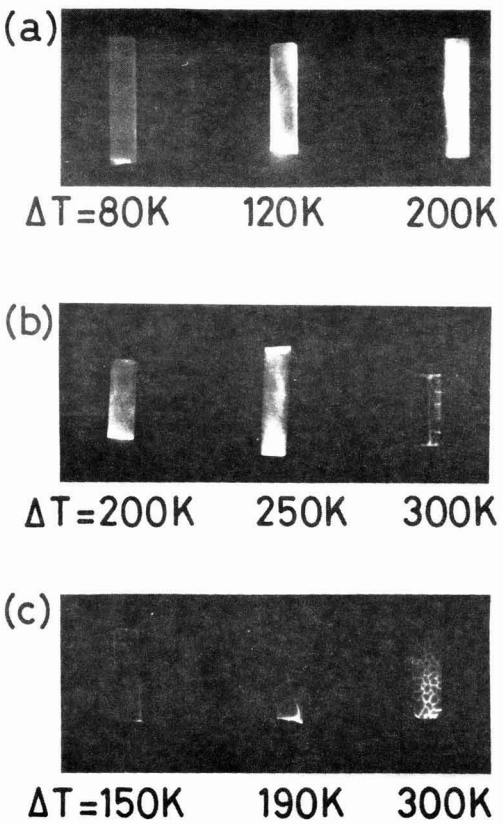

Fig. 3. Appearance of specimens after the thermal shock tests. Cracks are made visible by penetrated with a fluorescent dye: (a) MgO doped with LiF, (b) MgO dispersed with t-ZrO_2, and (c) MgO dispersed with c-ZrO_2.

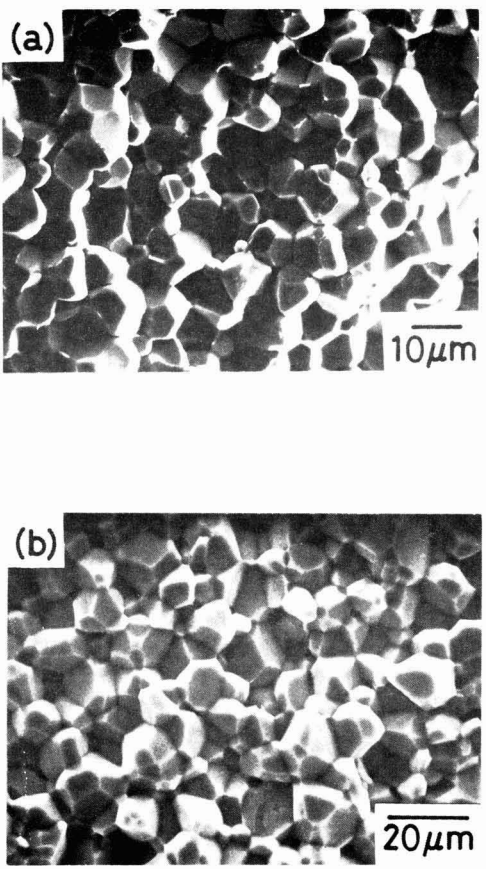

Fig. 4. Scanning electron micrographs of fracture surface of MgO doped with LiF: (a) ΔT=0K, and (b) ΔT=130K.

specimen, and at ΔT higher than 190K in the latter specimen, and more precisely, cracks are observed to be generated more finely in MgO dispersed with c-ZrO_2 than in MgO dispersed with t-ZrO_2.

According to the SEM photographs of the fractured surfaces of MgO dispersed with c-ZrO_2 (Fig.5), fractures are generated inside the grain in both cases of ΔT =0K and 300K (see Fig.5(b)), which is a completely different behavior from that of MgO doped with LiF. According to the SEM photographs of fracture surfaces of MgO dispersed with t-ZrO_2 (Fig.6), fractures are generated in both cases of ΔT = 0°K and 300K in an intermediate condition between the above two cases of MgO doped with LiF and MgO dispersed with c-ZrO_2. This indicates the co-existence of both fractures inside the grain and at the grain boundaries. All kinds of specimens were respectively confirmed not to show different behaviors in crack generation on the fracture surface between the specimen quenched at ΔT higher than ΔT_c. These behaviors suggested that there was no difference between fractures caused by thermal stress and those caused by external stress. When lubricating oil was used as the cooling medium, the
fracture surface of the specimen was too heavily stained to be observed by SEM.

4. Discussion

The ΔT_c of MgO was previously reported by Davidge and Tappin,[1] which they obtained by a thermal shock test using water as the cooling medium. This value was

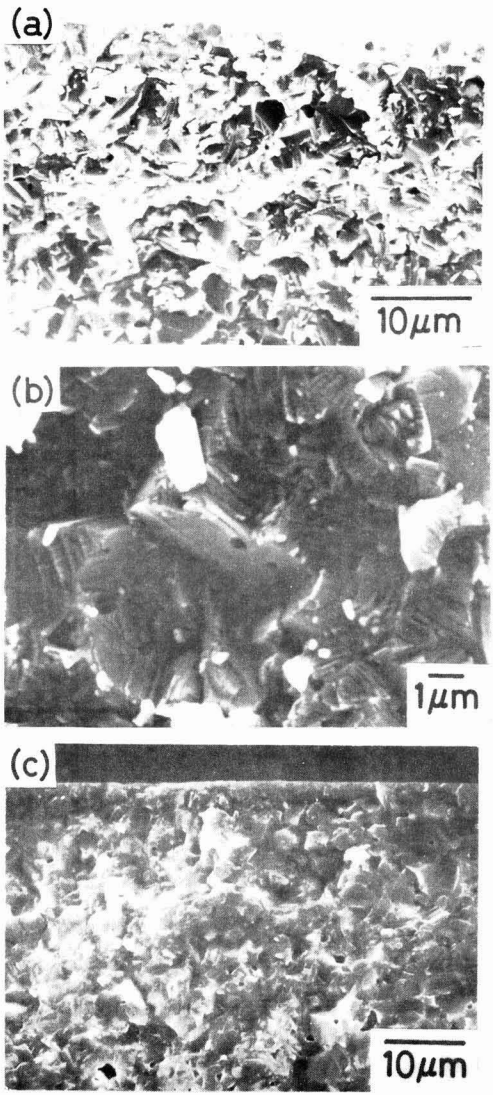

Fig. 5. Scanning electron micrographs of fracture surface of MgO dispersed with c-ZrO_2: (a) ΔT=0K, (b) ΔT=0K, and (c) ΔT=300K.

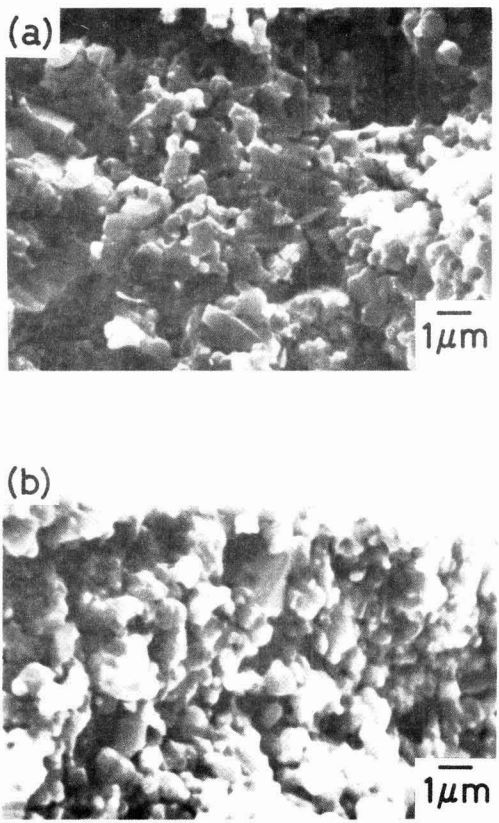

Fig. 6. Scanning electron micrographs of fracture surface of MgO dispersed with t-ZrO_2: (a) ΔT=0K, and (b) ΔT=300K.

115K, which agrees well with our experimental results using the specimen of MgO doped with LiF. However, it was lower than 150K,[2] which was the ΔT_c of MgO formed by a hot press process. Although thermal shock test results depend on the experimental procedures,[7] we think the ΔT_c value of MgO doped with LiF we obtained is in the same order as previous (published) data. Fracture stress of MgO ceramics of 150 to 200MPa has been reported.[2-8] The fracture stress of MgO doped with LiF obtained in our current study was rather low. Fractures in MgO generally include about 5% of transgranular fractures, but there were almost no transgranular fractures in MgO doped with LiF. This suggests, therefore, that the grain boundaries were weakened in our specimen of MgO doped with LiF. Such weakened grain boundaries are assumed to have been the reason for the slightly lower fracture stress σ_f of MgO doped with LiF. We doped LiF into MgO with the original intention of obtaining a higher density sintered body of MgO, but it appeared to result in weakened bonding at the grain boundary. In the case of MgO dispersed with t-ZrO_2, σ_f obtained closely corresponds to the bibliographic data. In the case of MgO dispersed with c-ZrO_2, σ_f obtained was as high as 300MPa, which is a significantly high value in MgO-based ceramics. Since almost all grains showed transgranular fractures in the case of MgO dispersed with c-ZrO_2, it is suggested that the bonding at the grain boundary was strong. Smaller grain size in MgO dispersed with c-ZrO_2 or t-ZrO_2 is assumed to be an additional cause for the higher fracture stress of these MgO-based materials than MgO doped with LiF.

Specimens of MgO dispersed with t-ZrO_2 showed a gentle decrease of fracture stress in the range around ΔT_c which was different from the behavior of other specimens. This difference in behavior can be explained by a thermal shock theory proposed by Hasselman.[9] As previously described in Section 2 under experimental procedure, MgO dispersed with t-ZrO_2 contains m-ZrO_2 and t-ZrO_2 in nearly equal content, thereby, it is reasonably assumed that microcracks were already generated in the specimen.[4] According to the theory by Hasselman, if these initial cracks were large in size and the experimental conditions were in quasi-static crack propagation,[9] the decrease of fracture stress is predicted to be slackened when ΔT exceeds ΔT_c. Our experimental results agree with this prediction. MgO dispersed with c-ZrO_2 has a higher density than MgO dispersed with t-ZrO_2, and the presence of microcracks in the former material has not been suggested in any investigation. Therefore, initial cracks generated in MgO dispersed with c-ZrO_2 are expected to be smaller in size than those generated in MgO dispersed with t-ZrO_2. In the case of MgO dispersed with c-ZrO_2, experimental conditions are assumed to be within a region of crack stability,[9] and the cracks are only extended kinetically by thermal shock, therefore, fracture stress is expected to decrease discontinuously in the ΔT range beyond ΔT_c, and our experimental results obtained concur. The same assumption applied to the case of MgO dispersed with c-ZrO_2 is also applicable to the case of MgO doped with LiF.

In the case of MgO dispersed with t-ZrO_2, especially when quenched into lubricating oil, residual fracture stress in the ΔT range far beyond ΔT_c is higher than that in the case of MgO dispersed with c-ZrO_2. According to the theory by Hasselman, when initial cracks in the material are small in size, the cracks in an unstable region are extended acceleratedly to reach a final crack length l_f, which is expressed below.

$$l_f = \left\{ \frac{3(1-2\nu)\sigma^2}{4\pi N \gamma E_0} \right\}^{1/2} \quad \cdots\cdots (1)$$

Here, ν is Poisson's ratio, N is crack concentration, γ is fracture energy, and E_o is Young's modulus of the material not containing cracks. This equation predicts that the higher the initial fracture stress of the material, the longer the cracks are extended by thermal shock and the lower the residual fracture stress becomes. Thereby, residual fracture stress is assumed to have become higher in the case of MgO dispersed with t-ZrO_2 which has a lower initial fracture stress than in the case of MgO dispersed with c-ZrO_2 which has a higher initial fracture stress. Strictly speaking, however, this equation is applicable only when initial cracks are small in size, and not applicable to MgO dispersed with t-ZrO_2 which has large initial cracks. Moreover, the experimental results obtained with MgO doped with LiF are not explained by this reasoning. In the study on thermal shock resistance characteristic of Mg-PSZ which contained t-ZrO_2,[10,11] high residual fracture stresses were reported in the ΔT range higher than ΔT_c, and they were attributed to the presence of t-ZrO_2 particles in the material.[10] The specimens of MgO dispersed with t-ZrO_2 used in our experiments contain m-ZrO_2 in addition to t-ZrO_2 and have a relative density less than 100%, therefore, their initial fracture stress is not as high as expected from the presence of t-ZrO_2, but the presence of t-ZrO_2 is supposed to be one of the causes for the increased residual fracture stress.

The relation between critical temperature difference ΔT_c, which is the highest temperature difference at which cracks are not generated in the specimen by thermal shock, and fracture stress σ_f of the specimen is expressed by the following equation.[12]

$$\Delta T_c = \frac{\sigma_f(1-\nu)}{E\alpha}\left(1.5+\frac{6K_s}{hd}\right) \quad \cdots\cdots (2)$$

Here, E is Young's modulus, α is the linear expansion coefficient, K_s is the thermal conductivity of specimen, d is the representative length of specimen, and h is the film heat transfer coefficient. $hd/K_s = \beta$ is called the Biot coefficient, which is a dimensionless index for expressing the degree of thermal shock.

By applying σ_f = 110MPa which was obtained with MgO doped with LiF, we calculate ΔT_c of MgO under conditions of water quenching. When a beam specimen was dropped into water in a vertical posture, it turned to a horizontal posture immediately after entering the water and then sank. Therefore, we considered it as a columnar specimen horizontally placed on the liquid,[13] and, based on this we calculated Nusselt number,[7] from which we calculated h. The descending rate of specimen in the liquid was measured as approximately 0.29m/s. By assuming $c_p = 4.22\times10^3 JK^{-1}kg^{-1}$, $\mu_1 = 2.82\times10^{-4}$Pas, and $K_1 = 0.682 Wm^{-1}K^{-1}$, we obtained Reynolds number R_e = 2600 and the film heat transfer coefficient $h = 8.70\times10^3 W/m^2K$. Then we calculated ΔT_c

of MgO as 400K by applying K_s = 43.1$Wm^{-1}K^{-1}$, E = 210GPa, α = 13.5×$10^{-6}K^{-1}$ and ν = 0.187, which were characteristic data of MgO. The ΔT_c value was measured in our experiments as 115K, which corresponds to the above calculated one, but did not agree with it as well as it did in the case of Y-TZP.[14] When the cross section of rod specimen is square instead of round, h is modified, and ΔT_c calculated with this modified h value becomes larger. Then, the difference between the calculated ΔT_c and the measured ΔT_c is reasoned as follows. R_e = 2600 was obtained in our experiments, which indicates our experiments were carried out in the region of laminar flow. However, the specimen temperature before quenching was higher than 100°C, thereby, quenching liquid is supposed to have been partially boiled and the interface between specimen and liquid was put into disorder. In such a disordered condition, the h value generally increases, becoming larger than the value above mentioned. The neglection of such an increase of h in our calculation is supposed to be one of the reasons for the different ΔT_c between the measured results and the calculated ones. Since the specimen was in a vertical posture at the moment when it entered into the liquid, a larger value of R_e should be applied at this moment that applied above. Even though the rod specimen turned to a horizontal posture soon after that, the h value as above calculated is assumed to have been evaluated smaller due to this change in posture.

The h value changes relatively widely when lubricating oil is used as a cooling medium compared to that when water is used. By applying C_p=0.36×$10^3JK^{-1}kg^{-1}$, μ_l = 9×10^{-3}Pas and k_l = 0.200$Wm^{-1}K^{-1}$ for the case of oil quenching, h = 1.02×$10^3Wm^{-2}K^{-1}$ was obtained, from which ΔT_c = 3100K was subsequently obtained. Therefore, ΔT_c in the case of using lubricating oil as a cooling medium is expected to become larger than ΔT_c in the case of using water. In our experiments, a much larger ΔT value was certainly obtained in the case of lubricating oil than in the case of water, and the difference between the two values was almost a magnitude of ten.

According to Eq. (2), ΔT_c is proportional to σ_f. Since no big differences of h values are assumed to be obtained in our experiments among the various specimens of MgO doped with LiF, MgO dispersed with t-ZrO_2 and MgO dispersed with c-ZrO_2, as far as the same cooling medium is used, the differences of ΔT_c among these three specimens are assumed to simply be due to the differences in σ_f among them. Based on the measured results of σ_f of MgO doped with LiF, we will estimate the ΔT_c values of the other specimens. When water was used as a cooling medium, σ_f values of MgO dispersed with t-ZrO_2 and MgO dispersed with c-ZrO_2 were respectively 1.3 times and 2.8 times as high as that of MgO doped with LiF, therefore, ΔT_c values are estimated as 150K and 300K respectively. These were experimentally obtained as 250K and 200K respectively, which qualitatively agreed with the above-mentioned expectation in the sense that both MgO dispersed with t-ZrO_2 and MgO dispersed with c-ZrO_2 showed larger ΔT_c than MgO doped with LiF. The reason why ΔT_c value of MgO dispersed with c-ZrO_2 was estimated to be larger than that of MgO dispersed with t-ZrO_2, contrary to the experimental results that the former was smaller than the latter, is assumed to be due to the extended cracks due to the coexistence of m-ZrO_2 in MgO dispersed with t-ZrO_2. According to the theory by Hasselman, Eq. (2) does not suitably apply in this case, and different equation which takes into account such factors as number of cracks, etc. is required for the calculation of ΔT_c. Different mechanisms are involved in the respective determination of ΔT_c of MgO dispersed with t-ZrO_2, which are assumed to have caused the contrary relation as mentioned above between the ΔT_c values obtained by estimation and measurement.

5. Conclusions

The authors prepared sintered MgO either doped with LiF or dispersed with ZrO_2 and investigated their behavior in thermal shock fracture, obtaining the following results. When water was used as a cooling medium, the critical temperature difference ΔT_c obtained was 250K and 200K in the respective cases of MgO dispersed with t-ZrO_2 and MgO dispersed with c-ZrO_2, both of which were higher than the ΔT_c of 115K in the case of MgO doped with LiF. When lubricating oil was used as a cooling medium, ΔT_c obtained was 620K and 650K in the respective cases of MgO dispersed with t-ZrO_2 and MgO dispersed with c-ZrO_2, both of which were higher than the ΔT_c of 300K in the case of MgO doped with LiF, as in the case of cooling medium of water. The decreasing rate of fracture stress σ_f in the range of temperature difference around the critical temperature difference ΔT_c was gentle. This gentle decreasing rate was assumed to have been caused by microcracks which were caused by the presence of the m-ZrO_2 phase, and was explained by the theory proposed by Hasselman. Residual fracture stress in the ΔT range higher than ΔT_c obtained was comparatively high in the case of MgO dispersed with t-ZrO_2. We assume that this high residual fracture stress was caused not only by microcracks but also by the presence of the t-ZrO_2 phase.

The reasons for the higher ΔT_c in MgO dispersed with ZrO_2 than in MgO doped with LiF were mostly explained by the increased σ_f in the former, but the mechanism involved in the determination of ΔT_c was found to be different in the cases of MgO dispersed with t-ZrO_2 and MgO dispersed with c-ZrO_2. From the calculated h values, ΔT_c was predicted to be higher in the case of cooling medium of water than in the case of that of lubricating oil, but the prediction did not agree quantitatively. Fractures in MgO doped with LiF were generated only at the grain boundaries, but those in MgO dispersed with c-ZrO_2 were generated inside the grains, and those in MgO dispersed with t-ZrO_2 were generated both at grain boundaries and inside the grains.

References:

1) R. W. Davidge and G. Tappin, Trans. Br. Ceram. Soc., 66(8) 405-22(1967).
2) C. I. Helgesson and S. Persson, Sci. Ceram., 7, 47-70(1973).

3) Y. Ikuma, A. Yoshimura, K. Ishida, and W. Komatsu, Mater. Sci. Res., 20, 295-304(1986).
4) R. Mikami, Y. Ikuma and W. Komatsu, Sekko-To-Sekkai, No.209, 27-32 (1987).
5) R. C. Garvie and P. S. Nicholson, J. Am. Ceram. Soc., 55(6) 303-305(1972).
6) E. M. Levin and H. F. McMurdie, Fig. 4339 in "Phase Diagrams for Ceramists, 1975 Supplement", Am. Ceram. Soc.(1975).
7) J. P. Singh, J. R. Thomas, D. P. H. Hasselman, J. Am. Ceram. Soc., 63(3-4) 140-144(1980).
8) A. G. Evans, D. Gilling, R. W. Davidge, J. Mater. Sci., 5, 187-97(1970).
9) D. P. H. Hasselman, J. Am. Ceram. Soc., 52(11) 600-604 (1969).
10) A. H. Heuer and L. H. Schoenlein, J. Mater, Sci., 20, 3421-27(1985).
11) T. Shiono, Y. Urata, Y. Okamoto, T. Nishida and T. Nishikawa, Proceedings, Autumn Symposium, Nippon Ceramics Kyokai, p.353-4(1988).
12) Edited by M. Kunugi, Muki-Zairyo-Kagaku, p.288, published by Seibundo-Shinkosha (1972).
13) R. H. Perry and C. H. Chilton, p.10-13 in Chemical Engineers' Handbook, 5th ed., McGraw-Hill, New York (1973).
14) T. Sato, T. Fukushima, T. Endo, M. Shimada, J. Mater. Sci. Lett., 6, 1287-90(1987).

This article is a full translation of the article which appeared in Nippon Seramikkusu Kyokai Gakujutsu Ronbunshi (Japanese version), Vol.97, No.8, 1989.

On Quartz in Amakusa Pottery Stone

Masaki Yasuoka, Kenji Nonobe,† Kiyoshi Okada and Nozomu Otsuka

Department of Inorganic Materials, Faculty of Engineering, Tokyo Institute of Technology
12-1, O-okayama 2-chome, Meguro-ku, Tokyo 152, Japan
† Now with INAX Co., 3-6, Koiehon-machi, Tokoname-shi, Aichi 479, Japan

Quartz in Amakusa pottery stones was characterized by various methods. Two specimens were collected from Tsurugasako-ko in Sarayama-vein and Kadonosako in Kaigan-vein among the Amakusa pottery stone deposits. They were crushed and classified into six fractions. Quartz was extracted from the classified pottery stones by chemical treatment using phosphoric acid and fluoric acid. The following anomalies were observed for quartz in the pottery stones. (1) Lattice constants of quartz in Tsurugasako-ko were larger than those in synthetic rock crystal up to 0.0029Å in a-axis and 0.0051Å in c-axis, and those in Kadonosako were up to 0.0038Å in a-axis and 0.0026Å in c-axis. (2) Lattice strains were 2-17x10^{-4} in Tsurugasako-ko and 7-24x10^{-4} in Kadonosako, and increased with decreasing grain size. (3) The temperature of the endothermic peak due to α-β phase inversion was slightly lower than 573°C, the inversion temperature of normal quartz. The peak was broader than that for normal quartz, and asymmetric in large grains. Double peaks were observed in small-grained specimens. (4) The content of Al_2O_3 analyzed was from 0.5 to 0.9 wt% and increased with decreasing grain size. These anomalies can be understood assuming substitution of Al ions into quartz. The transition temperature from quartz to cristobalite in pottery stones was lower than that in synthetic rock crystal, and was dependent on the localities.

[Received February 20, 1989; Accepted May 16, 1989]

Key-words: Quartz, Amakusa pottery stone, Substitution of Al_2O_3, Lattice constant, Lattice strain, α-β inversion

1. Introduction

Pottery stones are widely used raw materials for pottery manufacturing in Japan, because they can be formed and fired by themselves only after crushing. Among the various kinds of pottery stones in Japan, Amakusa pottery stone in Kumamoto prefecture has various properties such as excellent formability, excellent coloring after firing, and high strength of the fired body. Therefore, it is the most important mineral resource in the pottery industry. Hence, there are many reports available regarding the origin of these mineral deposits,[1-4] as well as the detailed constituent minerals.[5-6] The main constituent minerals consist of quartz, sericite and kaolinite, accompanied by minor amounts of mixed-layer clay minerals, feldspar, calcite, etc.

In his report [7] on the quartz contained in Amakusa pottery stone using powder X-ray diffraction analysis (XRD) and a polarizing microscope, Hamano confirmed that the quartz had a slightly longer a-axis lattice constant and a lower crystallinity, and that the phase transition temperature from quartz to cristobalite was more than 100°C lower in comparison to normal quartz. He assumed that these anomalies of quartz greatly contributed to the high strength of sintered bodies. In a recent report by Nakagawa,[8] the quartz in Amakusa pottery stone was investigated in terms of lattice constant, minor constituents and phase transition temperature. He confirmed several anomalies described below in comparison to normal quartz. (1) Lattice constants were obtained as a = 4.9137 to 4.9155Å and c = 5.4047 to 5.4057Å, both of which were a little longer than those of normal quartz, (2) most of the quartz specimens contained 0.1 to 1wt% of Al_2O_3, and (3) the phase transition temperature from quartz to cristobalite was 2° to 12°C lower.

In whiteware, fine quartz grains are mostly fused to form a glassy phase during firing, while coarse quartz grains remain unreacted as a whole, or remain unreacted inside the grain with a partial transition from quartz to cristobalite caused in the surface layer of grain, and they act as dispersion phase in a ceramics matrix. Therefore, quartz plays a very important role in whiteware. Because of the different behaviors of quartz, depending on the physical and chemical anomalies of the quartz, it is essential to characterize the quartz thoroughly. In the preparation of quartz specimens used in our study from Amakusa pottery stone, the authors crushed the raw materials and classified them in size fractions, and, from each classified material, separated and refined quartz specimens by chemical treatment. With these quartz specimens in respective sizes, we measured lattice constant, crystallite size and lattice strain by XRD, morphology of grain and composition analysis by a scanning electron microscope (SEM) which was combined with an energy dispersive X-ray detector (EDX), α-β inversion temperature by a differential thermal analyzer (DTA). We also examined the change from quartz to cristobalite during heating. Especially, the different characteristics of quartz caused by grain size were characterized.

2. Experimental Procedure

There are three major veins in the deposits of Amakusa pottery stones, which are called the Sarayama

vein, Murayama vein and Kaigan vein.[5] Two specimens were chosen among various deposits. One was from Tsurugasako-ko in the Sarayama vein which was as a typical pottery stone highly altered, and the other was from Kadonosako in the Kaigan vein as a typical one mildly altered. A dry stamp mill was used to crush the specimens which were then classified in 6 size fractions of >105, 37 to 105, 10 to 37, 5 to 10, 2 to 5 and <2μm. Mesh screens were used to classify larger sizes than 37μm, and an elutriation technique was used to classify smaller sizes than that. Classified specimens contained foreign minerals other than quartz, which were removed by dissolution with phosphoric acid.[9] Silicate gels which were generated in the process of phosphoric acid treatment were removed by dissolving with hydrofluoric acid. Quartz specimens as above refined were used as the starting materials in the experiments. In the case of classified samples of >105μm, a hand picking method under a microscope was used to separate quartz phenocryst from other minerals, which was used as the test specimen. Synthetic rock crystal was used as a standard reference material. In the heating test for the investigation of transition reaction from quartz to cristobalite, both Kawai pottery stone produced in Ishikawa prefecture and Tobe pottery stone produced in Ehime prefecture were tested, in addition to Amakusa pottery stones, and a comparison made.

A powder X-ray diffractometer (model Geigerflex) made by Rigaku Co. was used. For the measurement of lattice constants, Si (640a, NBS) was used as an internal standard, and 18 reflections were measured in the 2θ range of 20 to 100° using CuKα radiation. From these results, the lattice constants were calculated by the least squares method.[10] 15 reflections were precisely measured as well to obtain the crystallite size and lattice strain by the method of Hall[11] given in Eq. (1) below. To correct the broadening of the diffractometer, synthetic rock crystals were used which were especially prepared by classifying to 10 to 37μm and by annealing at 800°C for 5h.

$$\beta\cos\theta/\lambda = 2\eta\sin\theta/\lambda + K/\epsilon \quad \ldots\ldots\ldots (1)$$

Here, β is the true broadening of the reflection, θ is the diffraction angle, λ is the X-ray wavelength used, η is lattice strain, K is a constant, and ϵ is crystallite size.

To measure the phase transition temperature of quartz, a differential scanning calorimeter (model DSC-TG) made by Rigaku Co. was used. 20mg of specimen and 10°C/min temperature heating and cooling rates were used.

To measure Al_2O_3 content in the quartz grain, a SEM (model S-405) made by Hitachi Corp., and an EDX (model Kevex-7000) made by Kevex Co. were used. The standard reference materials for this measurement were two kinds of glasses of the SiO_2-Al_2O_3-K_2O system prepared in respective mole ratios of 94 : 6 : 30 and 91 : 9 : 30, as well as synthetic rock crystals (Al_2O_3 = 2 to 3ppm). The Al_2O_3 content in quartz specimens was obtained by an working curve method. An acceleration voltage of 25kV was used for the SEM. EDX analysis was carried out by spot analysis by a constant time method of 100sec using 20 grains randomly chosen under a microscope.

In the heating experiments specimens classified to 10 to 37μm, using an electric furnace equipped with $MoSi_2$ heating elements, were heated at the rate of 10°C/min to the desired temperature in the range of 1300° to 1500°C, held at that temperature for 1h, and cooled at the rate of 10°C/min. The ratios of cristobalite and quartz in the sample were respectively determined by a working curve method, based on integrated intensity ratios of the 101 reflections of respective crystalline phases, and, assuming that the total of the two phases was 100%, the respective ratios of the two phases were calculated. The minor elements contained in the pottery stone samples, Li, Na and K, were analyzed by flame spectrochemical analysis (model FPF-2 made by Hiranuma Sangyo Co.), and Al was analyzed by ICP emission spectrochemical analysis (model SBS-1100H made by Seiko Denshi Kogyo Co.). The specific surface area of each sample was determined by the BET method (model 2100-A made by Shimadzu Seisakusho Co.)

3. Results

3-1. Preparation of Specimens

XRD analyses showed that the quartz specimen from Tsurugasako-ko pottery stone contained quartz, sericite, kaolinite and calcite, while that from Kadonosako pottery stone contained the same minerals and in addition albite. Quartz content was higher than 60% in the quartz specimen with coarse grain sizes larger than 10μm, but it decreased rapidly to less than 30% in fine grain sizes, and it tended to decrease with finer grain size. The changes in residual minerals after the respective chemical treatments were investigated by SEM photographs, XRD patterns and DTA patterns. By the chemical treatments using phosphoric acid and hydrofluoric acid, clay minerals of sericite and kaolinite, and calcite were removed by dissolving, but albite contained in the quartz specimen from Kadonosako was not completely removed.

3-2. Lattice Constant

Figures 1(a) and (b) show the lattice constants of each classified quartz specimen from Tsurugasako-ko and Kadonosako. Lattice constants of synthetic rock crystal were obtained as a = 4.9129(2)Å and c = 5.4039(4)Å, which approximately agreed with those of a = 4.91300 (8)Å and c = 5.40473(9)Å,[12] which were obtained by a pattern fitting method. (Figures given in parentheses indicate the standard deviation of the data.) In the case of the quartz specimen from Tsurugasako-ko, all of the specimens with various grain sizes showed distributed lattice constant values in the range of a = 4.9142(2) to 4.9158(2)Å and c = 5.4041(4) to 5.4090(11)Å, both a and c values of which were longer than those of synthetic rock crystal, and the quartz specimens of smaller grain size especially tended to have longer values along the c-axis. On the other hand, in the case of quartz specimens from Kadonosako, lattice constants were obtained in the distribution range of a = 4.9126(3) to 4.9167(8)Å and c = 5.4040(5) to 5.4065(10)Å, among which coarse quartz grains larger than 5μm had similar

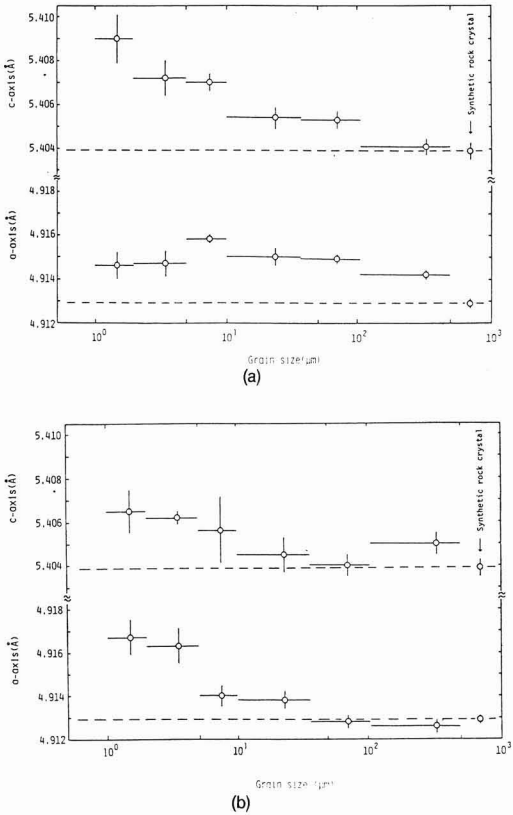

Fig. 1. Lattice constant of each classified quartz specimen. (a): Tsurugasako-ko, (b): Kadonosako.

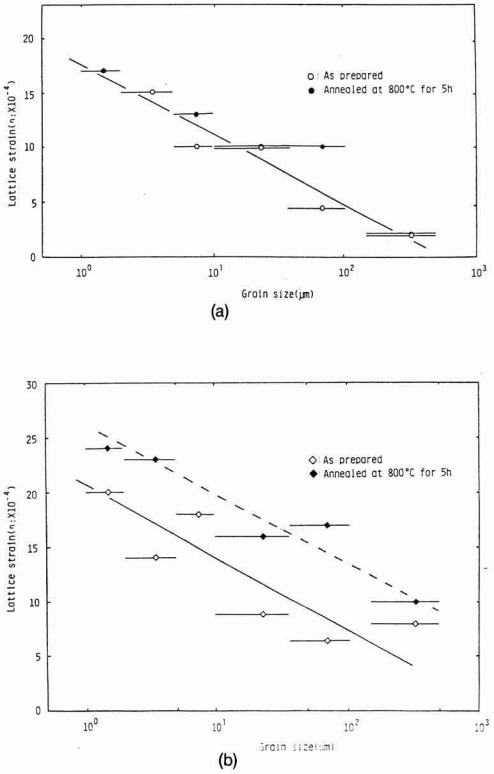

Fig. 2. Lattice strain of each classified quartz specimen. (a): Tsurugasako-ko, (b): Kadonosako.

lattice constant values to synthetic rock crystal, but fine grains smaller than that apparently had larger values than synthetic rock crystal, especially along the a-axis.

3-3. Crystallite Size and Lattice Strain

According to the method proposed by Hall, the crystallite size and lattice strain of each classified quartz specimen were calculated. Crystallite sizes obtained were as large as several thousand Å in any specimen, which were large enough for accurate results. Lattice strains obtained were distributed in a wide range of 2 to 24 x 10^{-4}, which included fairly large values. Figures 2(a) and (b) show the relationship between grain size and lattice strain of each classified quartz specimen. In both quartz specimens from Tsurugasako-ko and Kadonosako, the lattice strain apparently increased with the decreased grain size. When the specimens with the same grain size were compared, the quartz from Kadonosako had a larger lattice strain. When the specimens were annealed at 800°C for 5h, the lattice strain did not change at all, or rather increased. This behavior suggested that lattice strain was not introduced during the preparation of the specimen, but originated from the quartz itself. The reasons why lattice strain increased by annealing have not been clarified, but is possibly related to the same behavior reported by Iwai et al.[13]

3-4. Phase Transition

Figures 3(a) and (b) show the DTA curve and phase transition temperature of each classified quartz specimen respectively prepared from Tsurugasako-ko and Kadonosako. In the case of specimens from Tsurugasako-ko, the quartz phenocryst specimen of >105μm size had a sharp endothermic peak as did the synthetic rock crystal, but all other quartz specimens had a broad endothermic peak at a separate position shifted towards lower temperatures from the sharp peak position, in addition to a sharp one. This additional endothermic peak appeared more clearly with finer grain size quartz specimens. In the quartz specimen which had double endothermic peaks, the transition temperature was apparently observed to be a little lower than those of synthetic rock crystal and quartz phenocryst, as observed in Fig.3(a). In the case of quartz spe-

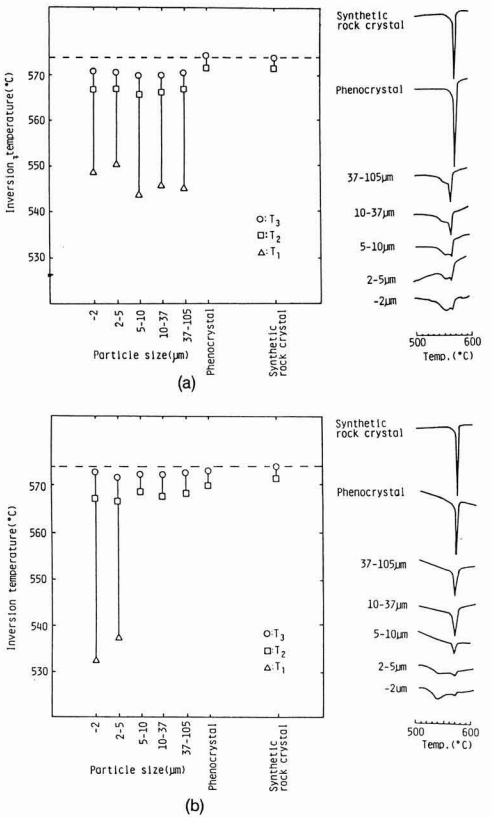

Fig. 3. DTA curve and inversion temperature of each classified quartz specimen. T_1 and T_2 represent starting temperature of first and second endothermic peaks, respectively. T_3 represents peak temperature of endothermic peak. (a): Tsurugasako-ko, (b): Kadonosako.

cimens from Kadonosako with grain sizes larger than 5μm, the endothermic peak because only a little broader and the transition temperature decrease was less. However, in the case of quartz specimens from the same Kadonosako with grain sizes smaller than 5μm, another endothermic peak appeared at a separate position around 530° to 540°C. These endothermic peaks appearing in DTA curves were observed to behave reversibly when heating and cooling cycles were repeated, therefore, it was assumed that these additional endothermic peaks corresponded to the phase transition of quartz from the low temperature type to high temperature type. Similar phenomena were reported in the case of quartz, especially fine crystalline quartz, in sedimentary rock.[14, 15]

3-5. Al_2O_3 Content

Figure 4 shows the relationship between the Al_2O_3 content and grain size of each classified quartz specimen from Tsurugasako-ko. Although the Al_2O_3 contents analyzed vary widely, the mean values show a comparatively systematic change. In the case of coarse grains larger than 10μm in size, the mean Al_2O_3 contents were nearly fixed at around 0.5wt%, but in the case of fine grains smaller than that, the mean Al_2O_3 content increased with the decreased grain size, reaching about 0.9wt% in the case of grain sizes smaller than 2μm. However, since a part of the impurity elements are possibly contained in the coarse grains in the form of liquid inclusions, we could not decide whether all of the Al_2O_3 content here determined is contained in the quartz grains in the state of a solid solution or not. The causes of the wide distribution of Al_2O_3 contents found are partly assumed to be that the Al_2O_3 contents were close to the limit of detection of the analytical instrument used, but mainly that the actual Al_2O_3 contents differed in different quartz grains, as reported by Nakagawa.[8]

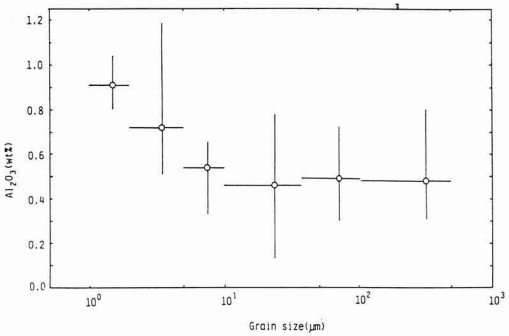

Fig. 4. Amount of Al_2O_3 in each classified quartz specimen of Tsurugasako-ko.

3-6. Formation Reaction of Cristobalite

Figure 5 shows the relationship between firing temperature and formation ratio of cristobalite from quartz in various localities in pottery stones. Table 1 shows contents of impurity elements of Li, Na, K and Al and specific surface area of various pottery stone specimens, both of which are supposed to affect the formation reaction from quartz to cristobalite. In the particular cases of pottery stones of Kadonosako and Tobe, the contents of Na, K and Al are supposed to have been higher, because albite or potassium feldspar contained in small amounts in the respective original minerals were not completely removed. Amakusa pottery stones are reported to contain various kinds of impurities in liquid inclusion,[6] so those inclusions are also supposed to have affected the analysis results given in Table 1. The temperature at which 50% of quartz was changed to cristobalite was compared for various pottery stone specimens, being obtained in the order shown below.

Synthetic rock crystal > Tsurugasako-ko > Kadonosako ≥ Kawai > Tobe.

The temperature was about 200°C lower for the spe-

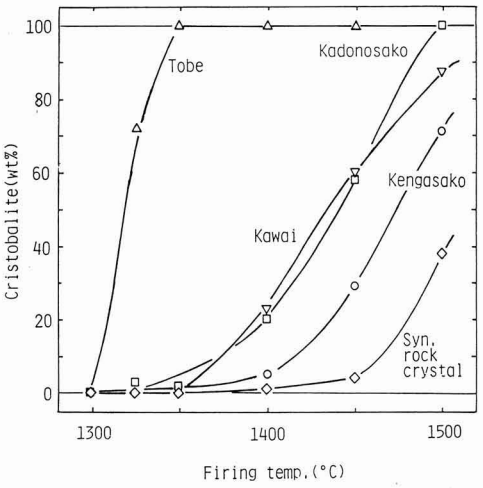

Fig. 5. Formation rate curves of cristobalite from quartz in various localities of pottery stones in 10-37μm size by firing each temperature for 1 h.

cimen from Tobe than for that of synthetic rock crystal.

4. Discussion

Our experimental results revealed that the fine grain quartz specimens prepared from both Amakusa pottery stones of Tsurugasako-ko showed peculiar behaviors different from those of normal quartz. Various anomalies observed in our study are basically the same as those reported by Nakagawa,[8] and can be explained by assuming the solid solubility of Al_2O_3 into quartz. The assumption implies that the lattice constants of quartz were extended by the solid solution of Al_2O_3 in quartz, and lattice strains were increased accordingly. If we assume that the Al_2O_3 content in the state of solid solution in quartz differs in grains, and that there are two kinds of quartz grains, one with high Al_2O_3 content and the other low and close to normal quartz, we can explain the double endothermic peaks appearing in the DTA curve by using the assumed phase diagram shown in Fig.6, which was proposed by Keith and Tuttle.[14] When we measured the DTA curves with the specimens after holding for various times up to 3000h at 850°C, which is in the stable temperature region of high temperature type of quartz, we observed that the two endothermic peaks tended to gradually become sharper with the increased holding time and to finally combine together into one. This result can be interpreted as being caused by the progress of homogenization of compositions between two quartz grains which contained different Al_2O_3 contents in the state of solid solution.

Table 1 Some impurity elements and surface area of each specimen in grain size of 10-37μm

	Tsuruga sako-ko	Kadonosako	Kawai	Tobe	Syn. rock crystal
Al_2O_3	5000	7500	3100	6000	2-3
Li_2O	220	90	20	170	
Na_2O	1100	3900	750	200	20-30
K_2O	1500	950	1200	1900	
Surface area (m^2/g)	0.29	0.43	0.20	0.41	0.42

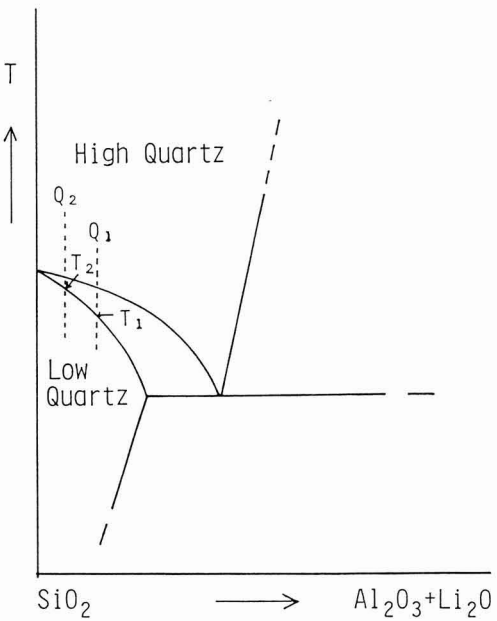

Fig. 6. Assumed phase diagram for Li_2O-Al_2O_3-SiO_2 system[16].

When heated, quartz is generally expected to make a phase transition to cristobalite via tridymite, however, it is known that quartz can make a direct transition from quartz to cristobalite when mineralizers such as Na ion and others are present.[17] It is also known that the transition from tridymite to cristobalite is strongly influenced by the presence of ions, and, according to the report by Suzuki and Arahori,[18] Al_2O_3 acts as a mineralizer for the remarkable acceleration of transition reactions from tridymite to cristobalite. In the pottery stones examined in our current study, the contents of alkali metals and Al_2O_3 were determined to be of the order of several thousand ppm, which should be a large enough content of coexisting composition to cause substantial changes in the phase transition temperature.

We assume that the effect of coexisting compositions caused the decrease of transition temperature from quartz to cristobalite in all quartz specimens as confirmed in our experiments, in comparison to the transition temperature of synthetic rock crystal. However, we could not clarify which among several coexisting compositions had most influence on the result.

5. Conclusions

In this study, the authors prepared quartz specimens from Amakusa pottery stones by a series of processes of crushing, classification into 6 size fractions and extraction by chemical treatment, and investigated their various characteristics, obtaining the following results.

1) Quartz specimens prepared from Amakusa pottery stone tended to have an increased lattice constant with decreased grain size.

2) The same quartz specimens tended to have increased lattice strain with decreased grain size, and this relationship was assumed to reflect the different chemical compositions in different grain sizes.

3) Double endothermic peaks were observed in the DTA curves for the quartz specimens with fine grain sizes, and both peaks were assumed to correspond to the phase transitions from low temperature type quartz to the high temperature type.

4) Higher Al_2O_3 contents were formed in the quartz specimens with fine grain sizes than in those with coarse grain sizes.

5) Quartz specimens prepared from various localities of pottery stone had the phase transition temperature from quartz to cristobalite about 50° to 200°C lower than that of high purity synthetic rock crystal, and this transition temperature differed widely depending on the locality of the pottery stone.

Acknowledgments

The authors should like to thank the respective parties listed below for their assistance to our study: to Ueda Pottery Stone Co. for the supply of pottery stone samples, to the Ceramic Experimental Station of Saga Prefecture for the loan of a stamp mill, to Daimon Laboratory in the Department of Inorganic Materials, Faculty of Engineering, Tokyo Institute of Technology for assistance with the thermal analysis, to Aoki Laboratory in the Medical Materials Laboratory, Tokyo Medical and Dental College, and Permeleck Electrode Co. for assistance with the chemical analysis, and to Fukushima Toyo Tsushinki Co. for the supply of synthetic rock crystal used as a standard reference material.

References:

1) M. Ueno, Chicho-Geppo, 3, 405-20 (1952),
2) K. Nakamura and H. Matsumura, Res. Rept. Faculty of Eng. Kumamoto Univ., 6, 36-44 (1958),
3) H. Takeshi and Y. Shiraki, "The Clay of Japan" ed. S. Iwao, Geol. Surv. Japan (1969) pp. 89-94.
4) Y. Togashi, Chicho-Geppo, 25, 491-508 (1974),
5) Z. Nakagawa, T. Hamano, H. Takeshi and Y. Uno, Nendo-Kagaku, 22, 179-91 (1982),
6) M. Nakagawa, Nendo-Kagaku, 28, 11-29 (1988),
7) T. Hamano, "Amakusa-Tooseki no Tokuchoo to Gyokai-Shindan ni kanrenshite", Kumamoto Chusho-kigyo Sogo-Shidosho (1974),
8) M. Nakagawa, Miner. J., 14, 37-47 (1988),
9) M. Tsunashima, H. Hayashi, R. Nakao and K. Fujimori, Akita-University-Kozan-Kenkyu-Hookoku, 4, 97-101 (1983),
10) T. Sakurai, "UNICS-Kessho-Kaiseki-Program", Nippon Kessho-Gakkai (1967),
11) W. H. Hall, Proc. Phy. Soc. (London), 61, 382-91 (1949).
12) H. Toraya, private communication (1986).
13) S. Iwai, J. Ossaka and H. Morikawa, Yogyo-Kyokai-Shi, 77, 172-8 (1969),
14) K. Nagasawa, J. Earth Sci. Nagoya Univ., 1, 156-76 (1953),
15) W. Smykatz-Kloss, "Differential Thermal Analysis" Springer-Verlag (1974) pp. 139-58,
16) M. L. Keith and O. F. Tuttle, Am. J. Sci., Bowen Issue, 203-80 (1952),
17) S. Udagawa, H. Yanagida and G. Sudo, "Fain-Kemikaruzu-toshiteno-Muki-Keiso-Kagoobutsu", Kodansha-Saientifiku, (1982), 111-2,
18) T. Suzuki and T. Arahori, Yogyo-Kyokai-Shi, 88, 637-42 (1981).

This article is a full translation of the article which appeared in Nippon Seramikkusu Kyokai Gakujutsu Ronbunshi (Japanese version), Vol.97, No.8, 1989.

DTA Studies for Thermochromism and Thermal Bleaching in Reduced Phosphate Glasses

Kouichi Kawashima, Jinzhu Ding, Hideo Hosono and Yoshihiro Abe

Department of Materials Science and Engineering,
Nagoya Institute of Technology
Gokiso-cho, Showa-ku, Nagoya 466, Japan

Thermally induced coloring and bleaching in reduced phosphate glasses were investigated by means of DTA. As-quenched glasses prepared under reducing conditions are transparent and colorless. On reheating at around the softening temperature of the glasses, they turn red ("striking"). The struck glasses become almost transparent and colorless ("bleaching") when they are heated above 580°C and quenched subsequently. The resultant glasses (PTC-RP glass) exhibit red-coloring by reheating above 200°C and/or light irradiation. It was explained in terms of transformation of colloidal phosphorus in the PTC-RP glasses that the endotherms at about 60°C and 580°C in the DTA curves are due to melting of white and red phosphorus, respectively, and that the exotherm at about 270°C is due to transformation of liquid phosphorus to amorphous red phosphorus, i.e., to ring opening polymerization of P_4 molecules.
[Received March 3, 1989; Accepted May 16, 1989]

1. Introduction

Various kinds of glasses have been reported[1-3] which undergo coloring and bleaching induced by reheating or by light irradiation. Most of them are silicate glasses doped with photoactive substances such as heavy and noble metals and halogen. Some kinds of non-silicate glasses have been reported, too,[4] which belong to a binary system of CaO-Al_2O_3 and exhibit photosensitivity based on a new mechanism.

The authors previously reported various unique characteristics exhibited by phosphate glasses. They can be, for instance, crystallization at around glass transition temperature[5] and protonic conduction,[6] coloring and bleaching induced by reheating or by light irradiation of phosphate glasses prepared by melting under reducing conditions.[7,8]

The phenomena of coloring and bleaching of these reduced phosphate glasses are different from those of previously mentioned photosensitive glasses. When phosphate glasses are melted under reducing conditions and quenched, transparent and colorless phosphate glasses are obtained. By heat treatment in a suitable temperature region (around glass softening temperature), these glasses turn red (striking). The struck glasses become transparent and colorless again when reheated to a temperature higher than about 580°C; the transparency and colorlessness are maintained after subsequent quenching. These glasses are both photochromic and thermochromic, and are called as PTC-RP glass (Photo- and Thermo-Colorizable Reduced Phosphate Glass).[8] PTC-RP glasses are colored by either light irradiation or reheating at a temperature beyond 200°C, and maintain the color when cooled to room temperature. When these colored glasses are reheated to a temperature higher than 580°C and quenched, they return to the transparent and colorless states. Such changes of coloring and bleaching can be repeated reversibly.

We have so far assumed[8] that the mechanism of such coloring and bleaching mentioned above is attributed to phase transformation of colloidal phosphorus formed in the glass matrices in the manner described below. Firstly, the elemental phosphorus is formed in glass matrices during melting in reduced conditions. By reheating the glass, this phosphorus associates to form a red phosphorus colloid (striking). Then by reheating to and holding at a temperature over 580°C, red colloidal phosphorus depolymerizes to become liquid phosphorus and the glass is bleached back. By quenching this liquid phosphorus, it becomes supercooled liquid or white phosphorus, and near-transparent and colorless PTC-RP glass is obtained. Therefore, we have assumed[8] that, in either case of photochromism or thermochroism, PTC-RP glass is colored by transformation of transparent liquid phosphorus or white phosphorus to red colloidal phosphorus.

It is generally very difficult to detect endothermic and exothermic reactions which correspond to certain kinds of phosphorus transformation, because white phosphorus and liquid phosphorus are quickly oxidized during ordinary DTA measurement in air because of their extremely high activity. Hence, there are few reports available on DTA measurements concerning transformation of phosphorus itself.

In this study, we investigated the DTA of PTC-RP glasses in detail and compared the results with the changes of state of elemental phosphorus. Based on those results, we examined the suitability of our previously mentioned assumption concerning the mechanism of striking and bleaching of PTC-RP glasses.

2. Experimental Procedure

We prepared PTC-RP glasses in four different compositions as shown in Table 1 by mixing raw materials in respective ratios. For example, in Table 1, "+2Si", means 2 moles of silicon powder added to 100 moles of glass. Silicon was added as the reducing reagent in the melting of glass. The mixed raw materials in an alumina crucibles were melted at 1300°C to 1350°C for 1h in air, and quenched by casting on a stainless steel plate to obtain transparent and colorless glasses.

These quenched glasses were heat-treated under the respective conditions shown in Table 1 for striking.

From the glasses turned red by heat treatment i.e., struck glasses, thin plate-like specimens of about 0.3mm thick were prepared by cutting and bleached by maintaining them at a temperature higher than 600°C. Transparent and colorless PTC-RP glasses were subsequently obtained by quenching.

In addition to the compositions and striking conditions of the glasses, Table 1 shows some thermal properties of the glasses such as the glass transition temperature (T_g) and dilatometric softening temperature (T_s). The specimen numbers used in the following sections in this report are also indicated.

DTA measurements were carried out at a heating rate of 10°C/min using the thin PTC-RP glass specimens (approximately 30mg) which were prepared by cutting the thin plate-like specimens into several mm square size.

Figure 1 shows the preparation method of PTC-RP glasses and the relationship between striking and bleaching of the glass specimens.

Table 1. Glass compositions, striking conditions and thermal properties.

Glass	I	II	III	IV
Composition (mol%)	$50P_2O_5 \cdot 50CaO$ (+6.5 Si)	$47P_2O_5 \cdot 52CaO$ Al_2O_3 (+3.5 Si)	$50P_2O_5 \cdot 33CaO$ $17Al_2O_3$ (+3.5 Si)	$69P_2O_5 \cdot 16Al_2O_3$ $12B_2O_3 \cdot 3K_2O$ (+2 Si)
Glass Transition Temperature (T_g)	530°C	550°C	340°C	660°C
Dilatometric Softening Point (T_s)	570°C	590°C	390°C	750°C
Striking Condition	580°C 30 h	580°C 50 h	400°C 50 h	720°C 24 h

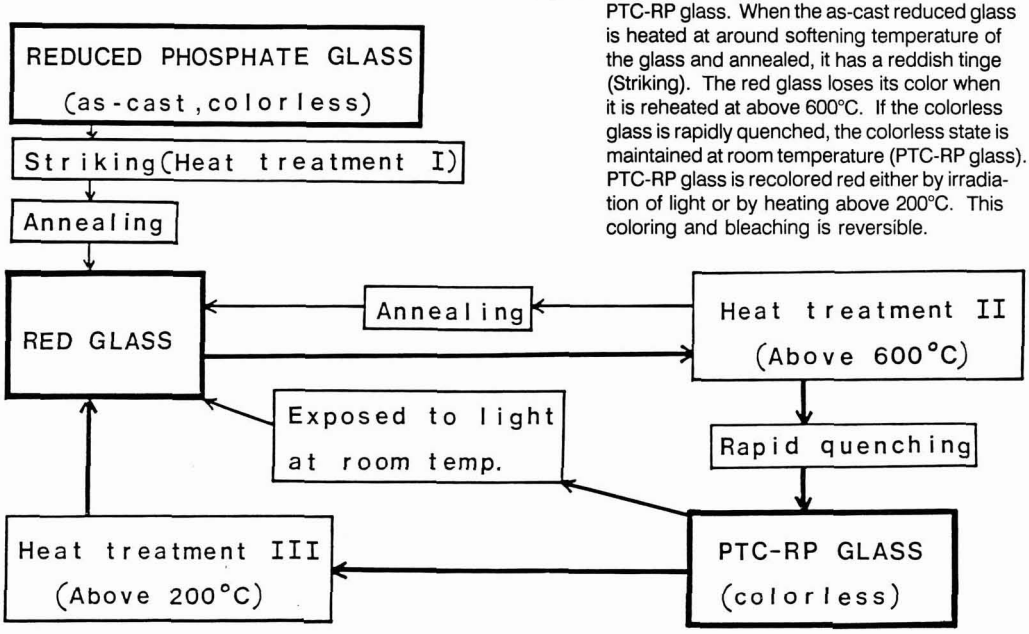

Fig. 1. Preparation method and coloring method of PTC-RP glass. When the as-cast reduced glass is heated at around softening temperature of the glass and annealed, it has a reddish tinge (Striking). The red glass loses its color when it is reheated at above 600°C. If the colorless glass is rapidly quenched, the colorless state is maintained at room temperature (PTC-RP glass). PTC-RP glass is recolored red either by irradiation of light or by heating above 200°C. This coloring and bleaching is reversible.

3. Results and Discussion

Figure 2 shows DTA curves of glass specimen I. Curve (a) is for glass specimen quenched from the molten state (as-cast), curve (b) is for fully struck (colored) glass specimen obtained by reheating the as-cast specimen at 580°C for 30h, and curve (c) is for the bleached glass specimen (PTC-RP glass) obtained by quenching the struck glass specimen after holding at 640°C for 5min. Curve (d) is for the oxidized glass specimen (oxidized glass), which was prepared by using the same raw materials as for the glass specimen of curve (a), except that SiO_2 was added in place of Si. All specimens exhibited an endothermic peak at the glass transition temperature of around 560°C. Additionally, curve (b) shows another endothermic peak at around 600°C, and curve (c) showed another endothermic peak at around 60°C and an exothermic peak at around 260°C. Considering the facts that those additional peaks were not observed in the glass specimens of curves (a) and (d), it was assumed that the additional peaks were related to the striking and the bleaching which are peculiar to PTC-RP glasses, but not related to the glass composition itself. We accordingly investigated the endothermic and exothermic reactions in more detail by using PTC-RP glasses with different compositions.

Figure 3 shows the DTA curve for a PTC-RP glass prepared from glass II. This PTC-RP glass was prepared by heating glass II (striking) at 580°C for 50h, subsequently bleaching it by holding at 620°C for 10min, and quenching. A sharp exothermic peak was observed at around 290°C.

Figure 4 shows the plots of $\lambda_{1/2}$ vs temperature of three kinds of PTC-RP glasses, which were prepared from glasses I, II and IV of different respective compositions. They were measured by placing a plate-like specimen in a furnace set in a given place in a spectrophotometer, and spectral changes were observed during heating at a constant rate. α indicates a coloring parameter, which is calculated using equation (1).

$$\alpha = \frac{\lambda_{1/2} \cdot t - \lambda_{1/2} \cdot i}{\lambda_{1/2} \cdot s - \lambda_{1/2} \cdot i} \quad \cdots\cdots (1)$$

The coloring of PTC-RP glasses by heat treatment is not due to formation of new absorption bands in the

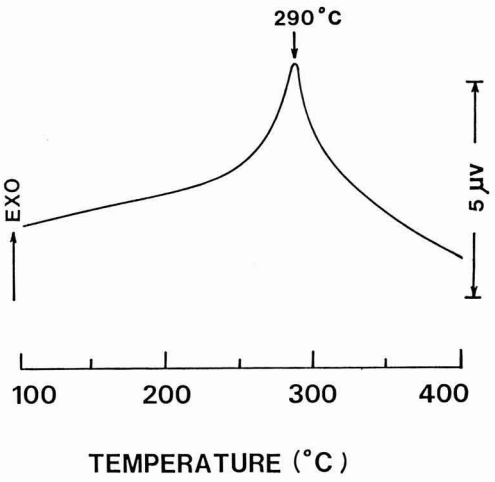

Fig. 3. DTA curves of bleached glass II at heating rate of 10°C/min in air.

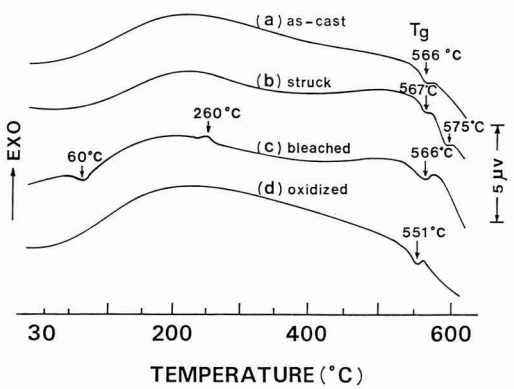

Fig. 2. DTA curves of glass I at heating rate of 10°C/min in air.
(a) as-cast (reduced)
(b) colored (struck)
(c) bleached (PTC-RP glass)
(d) as-cast (oxidized)

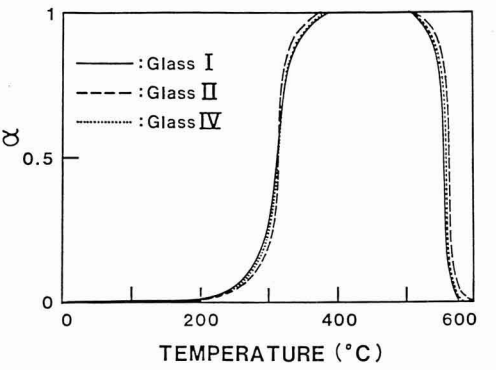

Fig. 4. Coloring and bleaching of PTC-RP glass during heating (10°C/min) where α is a coloring parameter estimated from equation (1); $\alpha=0$ means initial state (colorless); $\alpha=1$ means saturated state(red).
——— : glass I
– – – : glass II
····· : glass IV

light transmission spectrum, but due to the shift of the absorption edge toward the longer wavelength side. However, since the position of the absorption edge is difficult to be experimentally determined accurately, we adopted $\lambda_{1/2}$ as a parameter to indicate the position. The value of $\lambda_{1/2}$ is defined as the wavelength corresponding to half the value of its maximum transmission.[8] In equation (1), $\lambda_{1/2,s}$ is the $\lambda_{1/2}$ for glass specimens which have been fully struck, $\lambda_{1/2,i}$ is the $\lambda_{1/2}$ for specimens before heat-treatment or in other works for colorless PTC-RP glass, and $\lambda_{1/2,t}$ is the $\lambda_{1/2}$ for specimens after the heat-treatment for t min. Therefore, $\alpha=1$ corresponds to a saturated state of coloring (red) and $\alpha=0$ corresponds to the colorless state, and the larger λ value represents a more advanced state of coloring.[8]

When heated up, PTC-RP glass starts a gradual coloring at around 200°C, turns to a rapid coloring at around 300°C, and the color is bleached suddenly at around 570°C. The phenomena of these changes were confirmed to be independent of the glass composition.

In our previous report,[8] it was confirmed that the activation energy in the coloring reaction of PTC-RP glasses at around 200 to 300°C agreed with that of transformation of white phosphorus to red phosphorus. The exothermic peak temperature shown in Fig. 3 well agrees with the temperature at which α value starts to rise as shown in Fig. 4. These agreements suggest[10] that the exothermic peak shown in Fig. 3 corresponds to the transformation of liquid phosphorus or white phosphorus (P_4), which was formed in PTC-RP glass, to red phosphorus, or in other words, it corresponds to the ring-opening polymerization.

Although Fig. 4 shows abrupt decrease in α at around 550°C, no change was detected in the DTA curves of glass I and II at the corresponding temperatures (550°C). Weak endothermic and exothermic reactions were thought to be difficult to be detected in this temperature region because of the presence of various changes superimposed by such characteristics as T_g and T_s of the glass structure itself. Therefore, we investigated further to detect those weak reactions by using glass IV which has a high T_g of 660°C.

In Fig. 5, (a) is the DTA curve of glass IV which was colored by striking (at 720°C for 24h), and (b) is the DTA curve of the same glass which was heat-treated at 540°C for 330h after struck. Both specimens (a) and (b) showed the same degree of coloring. No peak was observed in (a), but an endothermic peak was observed at around 570°C in (b). The temperature of this endothermic reaction agrees with the temperature at which α abruptly decreased in Fig. 4, and we assume that it corresponds to depolymerization of red phosphorus to liquid phosphorus.[10]

The reasons why an endothermic reaction did not appear in the case of (a) are suggested as follows. Since the heat treatment temperature of 720°C is higher than melting point of red phosphorus (585°C),[11] red phosphorus forms in the specimen during the coloring. However, owing to the low crystallinity or broad molecular distribution of the red phosphorus, the endothermic peak in DTA curve[9] was not detected. As for (b), the specimen was heat-treated at 540°C for a long enough time to form crystalline red phosphorus in high crystallinity, (amorphous red phosphorus has been reported to be crystallized when heat-treated for long time in this temperature region, i.e., around 540°C) therefore, an endothermic peak corresponding to the melting of crystalline red phosphorus is assumed to have been present in the DTA curve.

Next, let us discuss endothermic peaks at around 60°C.

Figure 6 shows the DTA curves of glass III. Curve (a) indicates the PTC-RP glasses and curve (b) indicates a fully struck glass. It is seen that the endothermic

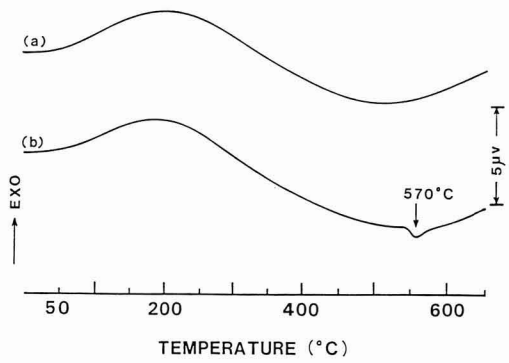

Fig. 5. DTA curves of glass IV at heating rate of 10°C/min in air (colored glass).
(a) 720°C 24h and annealed.
(b) 720°C 24h, subsequently 540°C for 330h and annealed.

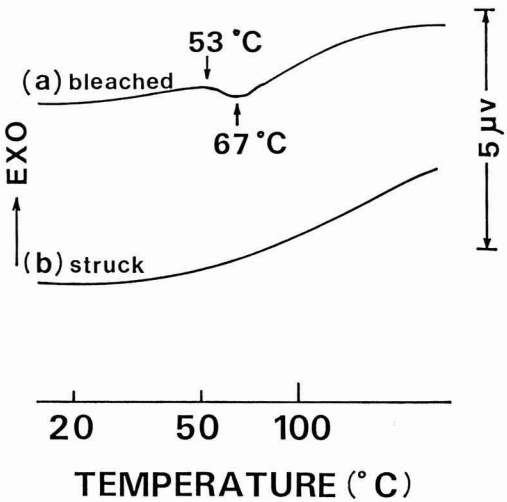

Fig. 6. DTA curves of glass III at heating rate of 10°C/min in air.
(a): bleached
(b): colored

reaction at 60 to 70°C is a phenomenon peculiar to PTC-RP glass or bleached glass.

The melting point of white phosphorus is 44.1°C.[11] Phosphorus precipitated in the glass matrices must be either white phosphorus or liquid phosphorus, because PTC-RP glass is transparent. Therefore, this endothermic reaction likely corresponds to the melting of white phosphorus, namely, the transformation of white phosphorus to liquid phosphorus.

Figure 7 shows the DTA curves of glass IV. Unlike glasses I and II, an endothermic peak was not detected at around 60°C in the DTA curve (b) of the bleached specimen obtained by quenching from 640°C. While, it was detected in the DTA curve (a) of the bleached specimen obtained by quenching from 780°C (5min). These results indicate that all of the endothermic peaks at around 60°C were observed only when the specimens were bleached by heat treatment at a temperature higher than T_s.

The heat treatment temperature of 640°C applied to glass IV is lower than the T_g, hence, the viscosity of the glass was too high ($>10^{14}$ poise) to deform the glass. This leads us to assume that colloidal phosphorus expands very little when heated in the bleaching treatment, in other words, the particle size of the colloid does not change at the bleaching temperature and liquid phosphorus and a small amount of phosphorus vapor become in an equilibrium state under high pressure. On the other hand, 780°C is higher than the T_s and phosphorus vapor pressure at this temperature is about 70 atm.[12] Because of the decreased viscosity of glass in this temperature region, the glass in the surrounding neighborhood of the colloid becomes fluidized owing to the high phosphorus gas pressure. Thus, the colloidal phosphorus becomes expandable, and liquid phosphorus and phosphorus vapor are not in an equilibrium state. It is therefore reasonable to assume that phosphorus vapor occupies a larger fraction in the colloid when the bleaching temperature is higher than T_s.

Liquid phosphorus is apt to be supercooled.[10] While, white phosphorus is formed when phosphorus vapor (P_4) is cooled.[10] Therefore, we suppose that, when PTC-RP glass was obtained by quenching from a temperature lower than T_g, supercooled liquid phosphorus came to exist, but very little white phosphorus was formed. On the other hand, when PTC-RP glass was obtained by quenching from a temperature higher than T_s, at which glass matrices were in a low viscosity state, we assume that white phosphorus was preferentially formed because the phosphorus vapor was cooled, and consequently the melting of white phosphorus was detected in the form of an endothermic peak in DTA curve.

Based on the results described above, thermal phase transformations of phosphorus that took place in the PTC-RP glasses are summarized in Fig. 8. It is noted that the exotherm due to the crystallization of amorphous red phosphorus were not detected in the present DTA experiments. Since the rate of this crystallization is generally considered to be extremely low,[9] we therefore assume that an exothermic reaction due to this crystallization was not able to be detected in the DTA curves during the process of heating. However, we experimentally confirmed in our previous study[13] that crystalline red phosphorus forms when the glasses were heat-treated for sufficiently long times.

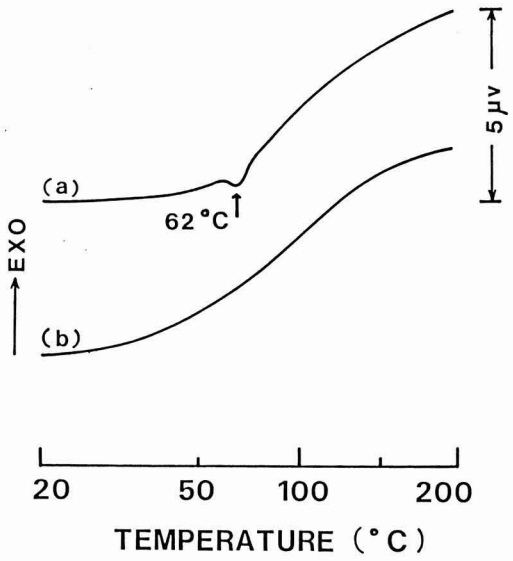

Fig. 7. DTA curves of glass IV at heating rate of 10°C/min in air (PTC-RP glass).
(a) bleached at 780°C for 5 min and quenched.
(b) bleached at 640°C for 10 min and quenched.

4. Summary

By means of DTA, the mechanism of thermally induced coloring and bleaching of reduced phosphate glasses (PTC-RP glass) was discussed.

Coloring of the glass in the temperature range of 200 to 300°C is caused by the transformation of liquid phosphorus (colorless) formed in the glass to red phosphorus (assumed to be amorphous); the coloring is accompanied by exothermic reaction in the DTA curve.

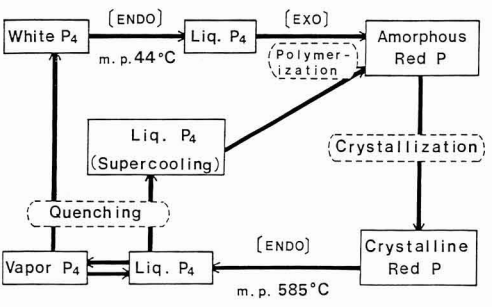

Fig. 8. The phase transformations of phosphorus in PTC-RP glass.

Bleaching of the glass at around 570°C is caused by the depolymerization of red phosphorus. However, the endothermic reaction due to the melting of red phosphorus is observed in DTA only when the crystallinity of red phosphorus is increased by a long enough heat treatment at 540°C.

Phosphorus in the bleached glass takes the state of either white phosphorus or liquid phosphorus. When the viscosity of the bleaching temperature is high, liquid phosphorus is mainly formed, while, when the viscosity is low, white phosphorus is mainly formed. In the latter case, therefore, an endothermic reaction due to the melting of white phosphorus is observed in the DTA curve.

From the experimental results of PTC-RP glasses obtained by means of DTA and from considerations of the changes of the state of elemental state phosphorus as described above, we concluded that colloidal phosphorus forms in PTC-RP glass, and that the phase transformation of colloidal phosphorus causes the coloring and the bleaching of PTC-RP glass.

Acknowledgments

This work was supported in part by a Grant-in-Aid (No. 62470062) for scientific research from Japanese Ministry of Education, Science and Culture.

References:

1) T.P. Seward III, J. Appl. Phys., 46[2]689-94 (1975).
2) A.J. Cohen and H.L. Smith, Science, 137, 981 (1962).
3) W.H. Armistead and S.D. Stookey, U.S. Pat., No.3208860, 1965.
4) H. Hosono, K. Yamazaki and Y. Abe, J. Am. Ceram. Soc., 68(1985)C-304.
5) Y. Abe, Nature (London), 282[5734]55-56(1979).
6) Y. Abe, H. Hosono, Y. Ohta and L.L. Hench, Phys. Rev. B, 38, 10166-69 (1988).
7) Y. Abe, R. Ebisawa and A. Naruse, J. Am. Ceram. Soc., 59[9-10], 453-54(1976).
8) Y. Abe, K. Kawashima and S. Suzuki, J. Am. Ceram. Soc., 69,2881(1947).
9) W.L. Roth, T.W. DeWitt and A.J. Smith, J. Am. Chem. Soc., 69,2881 (1947).
10) J.R.V. Wazer, "Phosphorus and Its Compound", Vol.1; Chap. 4. Interscience, New York, 1958.
11) J.C. Ballar, H.J. Emeleus, "Comprehensive Inorganic Chemistry", Vol.2, pp394, Pergamon Press(1973).
12) B.D. Melnik, E.B. Melnikov, "Technology of Inorganic Compounds", Chemical Engineer's Handbook, pp115, Wiener Bindery Ltd.(197).
13) H. Hosono, T. Satake, M. Hosoe and Y. Abe, J. Am. Ceram. Soc. 68[1]7-9(1985).

This article is a full translation of the article which appeared in Nippon Seramikkusu Kyokai Gakujutsu Ronbunshi (Japanese version), Vol.97, No.8, 1989.

Mechanical Properties of SiC-Matrix Ceramic Composite Reinforced with Dispersed Graphite Microcrystals

Satoshi Sodeoka, Kazuo Ueno and Kazuhisa Ueno*

Government Industrial Research Institute, Osaka
1-8-31, Midorigaoka, Ikeda, Osaka 563, Japan
* Osaka Electronics Communication University
18-8, Hatsu-cho, Neyagawa, Osaka 572, Japan

Silicon carbide containing 5 - 15 wt% graphite was fabricated by hot-pressing at 2000° - 2300°C using carbon black as a starting carbon material. B_4C of 1 wt% was doped in SiC as a sintering aid before mixing with carbon black. X-ray diffractometry and SEM revealed that the grain growth of SiC was suppressed by the carbon addition, and that carbon black changed to graphite microcrystals. Carbon addition increased the flexural strength of the composite appreciably. The composite with 10% graphite had the average strength of 820MPa and the maximum value of 1000MPa. The fracture toughness of 4.5MPa $\sqrt{m}$ for the 10% graphite composite was obtained, as compared with 3.3MPa $\sqrt{m}$ for monolithic SiC.

[Received March 3, 1989; Accepted May 5, 1989]

Key-words: Silicon carbide, Carbon black, Graphite, Composite, Grain growth, Flexural strength, Fracture toughness

1. Introduction

Silicon carbide ceramics, although having excellent heat and wear resistance and hardness, have poor toughness. A number of researchers therefore are attempting to develop SiC-base composite materials, in order to improve the fracture toughness of SiC. Several processes for making the composite materials including chemical vapor infiltration (CVI)[1,2] and whisker dispersion[3] for fiber-reinforced composites, and the addition of TiC[4] and TiB_2[5] for composites reinforced with dispersed grains, are studied.

Carbon is known to be one of good sintering aids for carbide-base ceramics. The authors have recently found that carbon black, when added to TiC in a much larger quantity (5 to 15%) than normally used for promoting sintering (1 to 3%), is transformed into graphite during the sintering process, and that the graphite microcrystals dispersed in the TiC matrix enhance the strength and the fracture toughness of the composite.[6] The graphite microcrystals also improve the wear resistance of TiC.[7]

In this study, SiC-matrix composite with the dispersed graphite microcrystals derived by above-mentioned transformation was fabricated, and the composite structures and effects of sintering conditions and the carbon content on the mechanical properties of the sintered composites.

2. Experimental Procedure

The starting SiC was β-type fine powder (ultrafine grade, supplied by Ibiden), 98% pure and having an average particle size of 0.27μm. Prior to the mixing of SiC with carbon black, boron carbide sintering aid was added to SiC at 1 wt%, by means of a ball milling with SiC balls in a polyethylene pot for 24h. The B_4C used (BCN-06, supplied by Hakusui Kagaku Kogyo) was 99% pure and had an average particle size of 0.13μm. Carbon black (supplied by Asahi Carbon) was furnace-processed, having an average particle size of about 0.2μm, as determined by electron microscopic analysis.

The starting carbon black was added to the B_4C-containing SiC at 5, 10 or 15 wt%, by means of a ball milling in a similar manner as mentioned above. The ball-milled mixture was granulated through a 500μm mesh, after having been filtered and dried. It was then hot-pressed at 2000° - 2300°C under 30MPa for 30 min. The hot-pressing mold was of graphite lined with powdered BN. The mold was covered with graphite powder during the hot-pressing in order to protect the mold against oxidation and get heat-insulation. Therefore, the atmosphere around the sample is assumed to be CO- and CO_2-rich air.

The specific gravity of the sintered body was measured by the Archimedean method (JIS R2205) after grinding with a #200 diamond wheel.

The sintered body was cut into about 3×4×40mm specimens for the 3-point bending test, which was performed under the conditions of span 20mm and crosshead speed 0.5mm/min (JIS R1601), at room temperature and 1300°C in air. Four to eight specimens were tested, and the mean bending strength was reported. The tensile surface was lap-finished with #800 diamond paste.

Fracture toughness was determined by the indentation method using a Vickers hardness tester, where an indenter was forced into the mirror-ground surface under a load of 5 to 10kg for 30 sec. The indentation pattern was not stable, frequently damaged by chipping. In such a case, no measurement was made, and indentation was attempted at another place. The Niihara's equation,[8] derived for radial cracks, was used to calculate fracture toughness value. Vickers hardness and fracture toughness measurements were performed simultaneously. Fracture toughness and Vickers hardness were measured for 8 to 20 indentations, and the mean values were reported.

The samples were analyzed by X-ray diffractiometry,

to identify the formed phases. The fracture surfaces of the specimens after the bending test were observed by an electron microscope.

3. Results and Discussion

3-1. X-Ray Diffractiometry

Figure 1 shows the X-ray diffraction patterns of the SiC and the C-SiC composites containing carbon black of 5, 10 or 15 wt% prepared at 2300°C (these samples are referred to as 5-, 10- or 15C-SiC respectively).

The X-ray diffraction pattern of the monolithic SiC (sample) were mostly attributed to the starting β-SiC, and to α-SiC to a lesser extent. The carbon-containing samples, on the other hand, had a peak at $2\theta=26°$, which were not found with the monolithic SiC and increased in height as the carbon content increased.

Figure 2 shows the effects of the sintering temperature on the interplanar spacing and integral width of this peak, observed with the 10C-SiC where the diffraction line for the SiC (111) lattice plane was used as an internal standard. The interplanar spacing decreased as the sintering temperature increased, and was constant at d=3.356Å above 2200°C. This value was very close to d=3.354Å for the graphite (002) lattice plane and the peak intensity increased with the carbon content. These facts indicate that the diffraction line corresponds to the graphite (002) lattice plane.

The presence of graphite in the composite, as was the case with the TiC-C system, indicated that carbon black added to the SiC matrix was transformed into graphite during the sintering process.

The interplanar distance of the 15C-SiC was d=3.354Å, i.e., fairly coincident with the distance of the graphite (002) lattice plane, at 2200°C and above, while that of the 5C-SiC sample was d=3.370Å even when formed at 2300°C. This means that the sample with lower carbon content had graphites with lower crystallinity. The crystallinity of graphite is known to be proportional to the degree of the graphitization. It is considered therefore that when the carbon content is small, the graphitization did not proceed enough even when fabricated at higher temperatures.

The integral width of the graphite (002) diffraction line decreased as sintering temperature increased, as shown in Fig. 2, which indicated that the crystals corresponding to the laminated graphite structures grew as the sintering temperature increased, assuming that the lattice strain of each system was almost the same.

α-SiC was clearly identified in the 5C-SiC sample, as was the case with the single SiC sample. The diffraction lines corresponding to α-SiC were also observed with the other samples, but to a much smaller extent. This suggested that increasing carbon content surpressed the transformation of β-SiC into the α phase.

3-2. Electron Microscopic Analysis

Figures 3(a), (b), (c) and (d) show the SEM photographs of the fracture surfaces of the monolithic SiC,

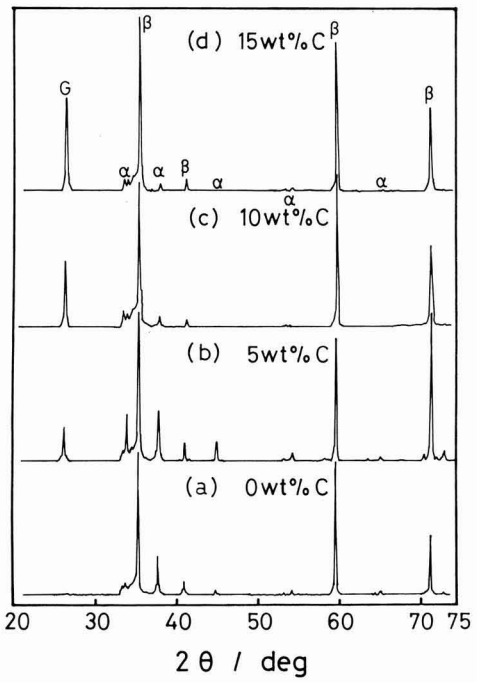

Fig. 1. X-ray diffraction pattern for (a) monolithic SiC, (b) 5 wt%, (c) 10 wt%, and (d) 15 wt% graphite-SiC composite, hot-pressed at 2300°C. G=grahite, $\alpha,\beta=\alpha$-, β-type SiC.

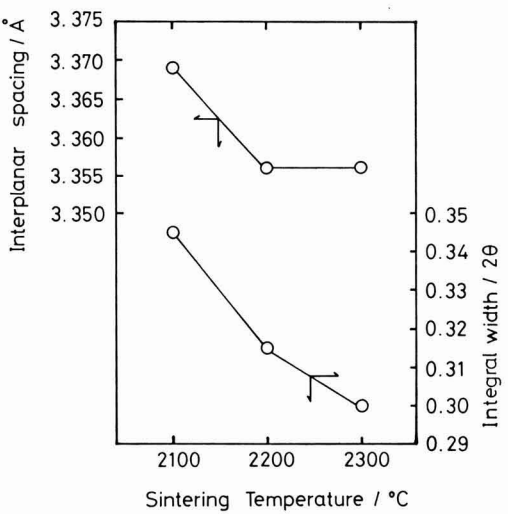

Fig. 2. Effect of sintering temperature on interplanar spacing and integral width of graphite (002) diffraction peak, observed for 10 wt% graphite-SiC composite.

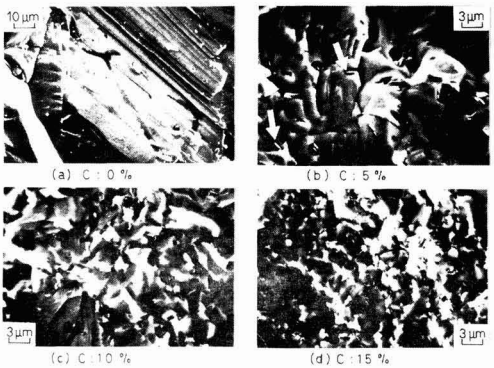

Fig. 3. Scanning electron microphotos for fracture surface of (a) monolithic SiC, (b) 5 wt%, (c) 10 wt%, and (d) 15 wt% graphite-SiC composite, hot-pressed at 2300°C.

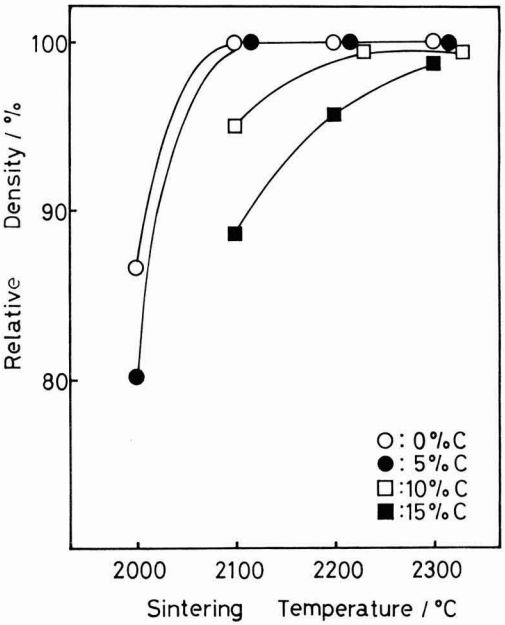

Fig. 4. Effect of sintering temperature on the relative density of (a) monolithic SiC, (b) 5 wt%, (c) 10 wt%, and (d) 15 wt% graphite-SiC composite.

and the 5C-, 10C- and 15C-SiC samples, all of which were sintered at 2300°C. The intragrain fracture in the monolithic SiC made it difficult to determine the grain shape and size.

It is reported that heating SiC up to 2200°C or above generally causes secondary recrystallization, to form very large plate-shape grains,[10] suggesting that the grain size of the monolithic SiC considered here was very large.

On the other hand, the constituent grains could be observed with the carbon-containing samples. Intragrain fracture was found with most of the grains in the 5C-SiC sample, and the grain boundaries were not observed clearly. The proportion of intergrain fracture to intragrain fracture increased as the carbon content increased, allowing the grain size to be observed more clearly. It was also found that size of the SiC grains decreased as the carbon content increased. These results led to the conclusion that carbon black hindered the growth of the SiC grains.

The SEM photographs of the carbon-containing samples show black-colored circular or elliptical images in places in the grain structures, and plate-shape grains (indicated by an arrow in Fig. 3(b)) were frequently observed in the black-colored images. The results with the TiC-C systems, coupled with the X-ray diffractiometry results, suggest that the plate-shape structures can be attributed to the graphite grains. It is assumed that the black-colored images corresponds to spaces formed around the graphite grains.

As discussed above, these results have indicated that carbon black added to the starting material is transformed, during the sintering process, into graphite microcrystals with the size of several micrometers, which are dispersed fairly uniformly in the grains and the grain boundaries. Crystallization of carbon black rarely occurs at below the hot-pressing temperature adopted in this study, i.e., 2300°C. Various materials, such as Si, Ti and Fe, are known to promote graphitization.[9] It is considered that SiC provides some material transfer routes to accelerate the graphitization of carbon black.

3-3. Sintering Behavior

Figure 4 shows the effects of sintering temperature on relative density of each sintered body. The relative density based means the ratio of bulk density to theoretical density where it was assumed that carbon black was completely transformed into graphite (d = 2.25g/cm^3).

The monolithic SiC and 5C-SiC were fully densified, when sintered at 2100°C. On the other hand, an increase in the carbon content degraded sinterability; the temperature required to densify the 10C-SiC sample was 2200°C, and for the 15C-SiC sample was 2300°C. The 15C-SiC sample had a relative density of 98.7% even when sintered at 2300°C, unlike the others which had densities of 99% or more. It has been suggested that carbon as sintering aid for SiC has two effects; one is to surpress the grain growth of SiC during the initial stage of sintering through migrating to the SiC particle surfaces, thereby retaining the sintering driving force up to a high temperature,[10] the other is to remove the surface oxide layers which may prevent the sintering of SiC.[11] It has also been suggested that the presence of carbon in excess of C/Si=1.0, i.e., the composition corresponding to the SiC+C phase in the phase diagram, prevents densification significantly by the actions of

free carbon.[12] This probably results from the effects of carbon which hinders not only surface diffusion on the SiC grain during the initial stage of sintering but also grain boundary diffusion at high temperatures. These phenomena might occur in the systems studied here.

All the samples prepared in this study contained 1 wt% of B_4C sintering aid, which should present in the grain boundaries to promote the diffusion of Si. It seems that B_4C may not work effectively as a sintering aid for the system with a large quantity of carbon. The presence of carbon black, whose bulk density is very low (d=1.86 to 2.04g/cm^3), will lower the green density unavoidably, even when the green compact is pressed prior to the sintering. Furthermore, an increase in carbon content is accompanied by a large shrinkage during the sintering, which also prevents the densification.

3-4. Mechanical Properties

Figure 5 shows the effects of sintering temperature on flexural strength at room temperature of the monolithic SiC and the 5C-, 10C- and 15C-SiC composites. Figure 6 shows the effects of sintering temperature on the flexural strength at 1300°C. For the monolithic SiC, flexural strength decreased as sintering temperature increased, with the highest level attained at a sintering temperature of 2100°C. The monolithic SiC was almost completely densified at 2100°C, as shown in Fig. 4, and a higher temperature might cause secondary recrystallization, causing the strength degradation by the formed larger grains.

The 5C-SiC sample was also densified at 2100°C, and the strength decreased when sintered at a higher temperature, because of the excessive growth of the grains, as was the case with the monolithic SiC. The sample prepared at 2100°C had a higher strength (800MPa or higher on average, and 1GPa at the highest) at room temperature than the monolithic SiC. This might result partly from the decreased grain size due to the presence of carbon, and a higher fracture toughness than that of the monolithic SiC, to be discussed later.

The effects of sintering temperature on the strength of the 10C- and 15C-SiC samples were more complicated than those for the monolithic SiC and the 5C-SiC samples. The 10C-SiC composite prepared at 2100°C had the highest strength, in spite of incomplete densification. The strength of the sample prepared at 2200°C is lower than that of the sample at 2100°C, but the strength increased slightly when prepared at 2300°C. Such a trend was also observed with strength measured at high temperature. Room temperature strength of the 15C-SiC sample was nearly constant, irrespective of the sintering temperature. For high-temperature strength, on the other hand, the sample prepared at 2200°C tended to show the lowest strength, as was the case with the 10C-SiC sample.

The porosity of the 10C- and 15C-SiC samples prepared at 2100°C were 5% and 10% or more, respectively, judging from their relative density levels. The relative density was estimated, as mentioned earlier, based on the assumption that the added carbon black was completely transformed into graphite. However, X-ray diffractiometry indicated that graphitization proceeded to only a small extent at 2100°C, and carbon black mostly remained amorphous between the SiC grains. It is therefore considered that the pore remained not so much as to degrade its mechanical strength.

Figure 7 shows the effects of sintering temperature on the fracture toughness of the monolithic SiC and 5C-, 10C- and 15C-SiC samples. Fracture toughness of the monolithic SiC was in a range from 3 to 3.3MPa·m$^{1/2}$, tending to decrease as sintering temperature increased. Fracture toughness of the carbon-containing samples generally increased with the carbon content, although varying differently with the sintered temperature sample by sample. In particular, the 15C-SiC sample sintered at 2300°C had an average fracture toughness of 4.7MPa·m$^{1/2}$ (5.5MPa·m$^{1/2}$ at the highest), which was more than 1.5 times higher than that of the monolithic SiC.

Two reasons can be considered for the increased fracture toughness caused by carbon: First, carbon surpressed the growth of the SiC grains, forming a sinter structure consisting of finer grains. As a result,

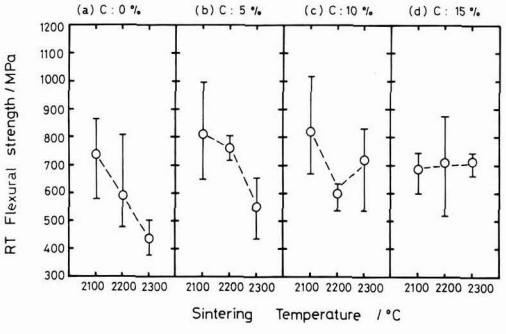

Fig. 5. Flexural strength at room temperature vs. sintering temperature for (a) monolithic SiC, (b) 5 wt%, (c) 10 wt%, and (d) 15 wt% graphite-SiC composite.

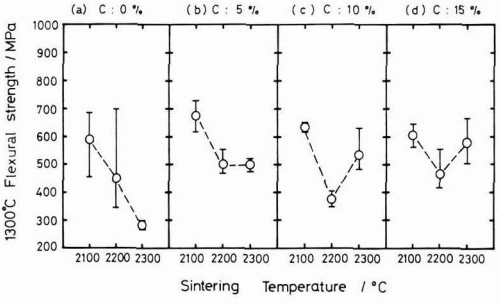

Fig. 6. Flexural strength at 1300°C vs. sintering temperature for (a) monolithic SiC, (b) 5 wt%, (c) 10 wt%, and (d) 15 wt% graphite-SiC composite.

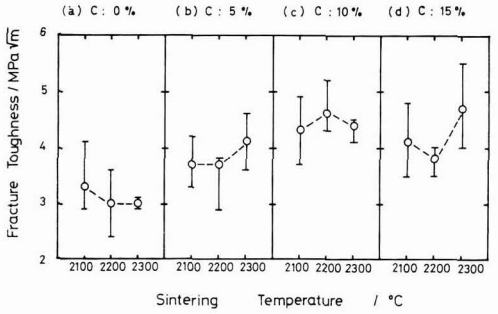

Fig. 7. Fracture toughness vs. sintering temperature for (a) monolithic SiC, (b) 5 wt%, (c) 10 wt%, and (d) 15 wt% graphite-SiC composite.

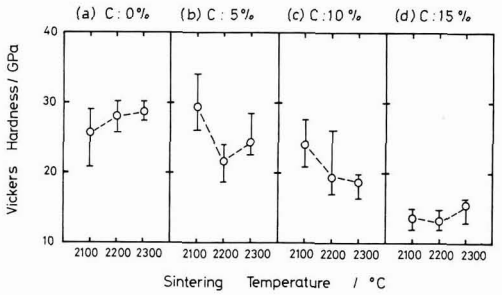

Fig. 8. Vicker's hardness vs. sintering temperature for (a) monolithic SiC, (b) 5 wt%, (c) 10 wt%, and (d) 15 wt% graphite-SiC composite.

fracture along the grain boundaries prevailed, making the fracture surfaces more complex, i.e., providing frequent deflections for crack propagation. The other reason is the contribution of the graphite particles dispersed in the sintered body. Graphite layers will delaminate easily at near the crack front, deflecting the propagation direction and, at the same time, absorbing crack energy.

Figure 8 shows the effects of the sintering temperature on Vickers hardness of the monolithic SiC and the 5C-, 10C- and 15C-SiC samples. The hardness of the monolithic SiC samples increased as sintering temperature increased, and that of the carbon-containing samples generally decreased with the carbon content, varying differently with temperature sample by sample. The decreased hardness with increased carbon content results from the low hardness of graphite (H_v = 300MPa).

4. Conclusions

The authors prepared monolithic SiC and SiC-C composites by hot-pressing, where the composites contained 5, 10 or 15% of carbon black dispersed uniformly in the structure. It was found that the added carbon black was transformed into graphite during the sintering process, and that the crystallinity of graphite tends to increase as the sintering temperature increases. The added carbon black hindered the growth of the SiC grains, increasing flexural strength and fracture toughness (1.8 times at maximum). The increased fracture toughness is considered to result from the prevailing fracture at the grain boundaries and delamination of the graphite layers at near crack front.

References:

1) E. Fitzer and R. Gadow, Am. Cer. Soc. Bull., 65 [2], 326-35 (1986).
2) D.P. Stinton, A.J. Caputo and R.A. Lowden, ibid, 65 [2], 347 - 50 (1986).
3) K. Sodeoka and K. Ueno, Proc. of 6th High-temperature Materials Basic Seminar, p. 83 - 87 (1986).
4) G.C. Wei and P.F. Becher, J. Am. Cer. Soc., 67 [8], 571 - 74 (1984).
5) M.A. Janney, Am. Cer. Soc. Bull., 66 [2], 322 - 24 (1987).
6) K. Ueno, K. Sodeoka and M. Yano, Seramikkusu Ronbunshi, 97, 507-12 (1989).
7) K. Ueno, M. Yano and S. Sodeoka, Proc. of Annual Meeting of Japan Ceramic Society, p.89 (1986).
8) T. Hase, H. Suzuki and H. Ueda, Yogyo-Kyokai-shi, 87 (10), 522 - 28 (1979).
9) Edited by Research Group of the Carbonic Materials, Tanso Zairyo Nyuumon, p.32 (1972).
10) H. Suzuki and T. Hase, Proc. Int. Sympo. on Factors in Densification and Sintering of Oxide and Non-oxide Ceramics, Edited by S. Somiya and S. Saito, Gakujutsubunken Fukyu-kai, p. 345 - 381 (1979).
11) S. Prochazka, Special Ceramics 6, Edited by P. Popper, Brit. Ceram. Assoc., p. 171 - 182 (1975).
12) A. Kato, "High-Temperature Ceramic Materials," edited by H. Suzuki, Nikkan Kogyo Shimmbun, p.76-83 (1985).

This article is a full translation of the article which appeared in Nippon Seramikkusu Kyokai Gakujutsu Ronbunshi (Japanese version), Vol.97, No.8, 1989.

Effects of Composition and Additives on Water Durability in V_2O_5-P_2O_5 Glass System

Takashi Naitoh, Takashi Namekawa, Seiichi Yamada and Kunihiro Maeda

Hitachi Research Laboratory, Hitachi, Ltd.
3-1-1, Saiwai-cho, Hitachi 317, Japan

V_2O_5-P_2O_5 glasses containing large amounts of V_2O_5 are known to have relatively low transformation and deformation temperatures, in spite of their low thermal expansion coefficients. However, poor water durability and strong devitrifying tendency prevent these glasses from being used as bonding glass. To improve these properties, the effects of composition and additives on the glass properties were studied, and the following results were obtained.

(1) An increase in P_2O_5 content improved the water durability and restrained the tendency of devitrification, while the transformation and deformation temperatures increased.

(2) On the other hand, addition of a small amount of Sb_2O_3 or PbO improved the water durability without affecting other properties of glasses.

(3) Infrared spectrum analysis confirmed that the glass was transformed from layered into network structures with increasing P_2O_5 content or by addition of Sb_2O_3 or PbO. The improved water durability was explained by the network structure which prohibits the water penetration into glasses.

[Received March 13, 1989; Accepted May 16, 1989]

Key-words: V_2O_5-P_2O_5 glass, Water durability, Devitrification, Bonding glass, Sb_2O_3, PbO, Layered structure, Network structure

1. Introduction

V_2O_5-P_2O_5 glasses, commonly known as electrically conductive glasses[1,5] are also considered to be glasses with low softening temperatures because of their low transformation and deformation temperatures.[4,5] PbO-B_2O_3 glasses have been chiefly used for airtight bonding materials with low softening temperatures,[6,8] but V_2O_5-P_2O_5 glasses are considered to be suitable as bonding glasses for materials with relatively low thermal expansion coefficients due to the lower thermal expansion coefficients of V_2O_5-P_2O_5 than those of PbO-B_2O_3 glasses.[4,5] However, their poor water resistance presents a great problem. Also, good flowability cannot be obtained due to devitrification resulting from crystallization taking place before softening. So, they have not been utilized as airtight bonding glasses with low softening temperatures.

In this study, to improve the above properties of V_2O_5-P_2O_5 glasses, the effects of composition and additive on the glass properties, in particular, water resistance, are examined. Furthermore, the relationship between the water resistance and structures of the glasses was studied.

2. Experimental Procedure

2-1. Preparation of Glasses

Guaranteed reagents manufactured by Wako Junyaku Kogyo K.K. were used as the raw materials. About 100g of a mixture containing the required amounts of the raw materials was put in an alumina crucible and melted in an electric furnace at 1050°C in air for 2 hours. To homogenize the glasses, the molten mixture was agitated thoroughly with an alumina bar and poured into a black lead mold kept at 150° - 200°C, forming glass blocks in sizes of 60×20×20mm. Next, the blocks were further heated at 270° - 470°C after being air-cooled and then straightened by annealing. To determine vitrification, the homogeneity was observed with an optical microscope and SEM, and it was also confirmed by X-ray diffraction that there was no diffraction peak.

2-2. Method of Measurement

2-2-1. Crystallization

The crystallization of the glasses was examined by differential thermal analysis (DTA). Using an 8002 differential thermal analysis system manufactured by Rigaku Electric Co., Ltd., glass powder milled to tens of μm was heated at a temperature rise rate of 10°C/min. For the standard, α-Al_2O_3 was used.

2-2-2. Transformation and Deformation Temperatures and Thermal Expansion Coefficients

Using a 2S-TMA-5 two-sample instrumental analysis system manufactured by Rigaku Electric, Co., Ltd., transformation and deformation temperatures and thermal expansion coefficients were measured. The temperature rise rate was 5°C/min. For the sample to be measured, a processed glass cylinder 5mm in diameter and 30mm in length was used and a quartz glass sample of the same size used as the standard material. The thermal expansion coefficients were obtained by measuring the average expansion at temperatures from 50°C to 30°C below the transformation temperature.

2-2-3. Water Resistance

Water resistance was evaluated by weight loss and the water erosion of the glass surface of a processed glass cube of 5×5×5mm size after soaking in 40cm^3 of distilled water at 70°C for half an hour and drying at 100°C in a constant temperature bath for 8 hours. The conditions of the surface were observed with a SEM. The elements dissolved into the water were measured by chemical analysis. Specifically, vanadium (V) was analyzed by the ICP emission analysis method and phosphorus (P) by the ICP emission analysis method or

the molybdenum blue absorptiometric method.

2-2-4. Hardness

Hardness was measured for a polished glass surface, using a MVK-E Vickers microhardness meter manufactured by Akashi Co., Ltd. Measuring conditions were set at a 100g load and a 15 seconds loading time.

2-2-5. Analysis of Glass Structures

To examine the relationship between water durability and glass structures, the infrared absorption spectrum was measured. The transmission method was used, using measurement samples prepared by the KBr disc method and a 170SX Fourier-transform infrared spectroscope manufactured by Nicolet.

3. Results and Discussion

3-1. Properties of V_2O_5-P_2O_5 Glasses

V_2O_5-P_2O_5 glasses are known to be obtained with a composition containing more than 5mol% of vitriformed oxide P_2O_5.[1-4] Glasses were prepared with compositions containing V_2O_5 in the range of 50 - 95mol% (P_2O_5 50 -5mol%). With compositions containing more than 90mol% of V_2O_5 (P_2O_5 less than 10mol%), however, the amounts of deposited V_2O_5 crystals were very large and no vitrification took place. The cause of the narrowed range of vitrification as above, compared with that recorded in the documents, seems to be the difference in the conditions of preparing glasses. In preparing the glasses used for this study, the glass casting molds were preheated in order to obtain relatively large glass blocks. This seems to have relatively slowed the cooling of the glasses, making their vitrification difficult. Using the vitrified samples, the relationship between composition and properties was studied.

Figure 1 shows the DTA curves of the prepared glasses. Exothermic peaks were observed at 420°C and 490°C on the curve of $80V_2O_5 \cdot 20P_2O_5$ glass and at 420°C on that of $75V_2O_5 \cdot 25P_2O_5$ glass. The X-ray analysis of the samples prepared by a similar heat treatment showed deposited V_2O_5 crystals. Thus, the exothermic peaks seem to result from the deposition of V_2O_5 crystals. Also, even if the glasses were heated, fluidity good enough for crystallization could not be obtained. With other glasses, such exothermic peaks were not observed and with the compositions of below 70mol% V_2O_5 (more than 30mol% P_2O_5) the fluidity was found to be good enough to reduce crystallization or devitrification. The large peaks in the range from 200°C to 500°C are based on the glass transformation, indicating that the glasses with higher V_2O_5 mol% deform at lower temperatures. Of the glasses prepared, the one having good fluidity at the lowest temperature was $70V_2O_5 \cdot 30P_2O_5$ glass which did not vitrify and had an endothermic peak in the lowest temperature range.

Figure 2 shows the relationship between the compositions and properties of the prepared glasses. Both the transformation and deformation temperatures and the hardness of the glasses decreased with increased V_2O_5 contents and the rate of decrease was low in the

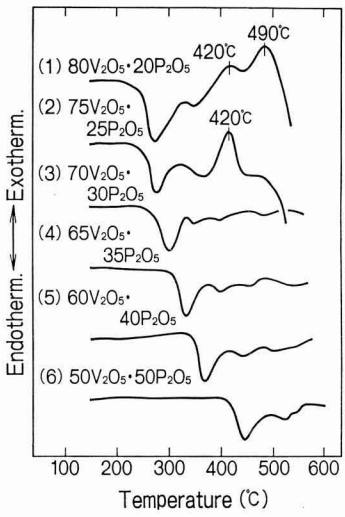

Fig. 1. DTA curves of V_2O_5-P_2O_5 glasses.

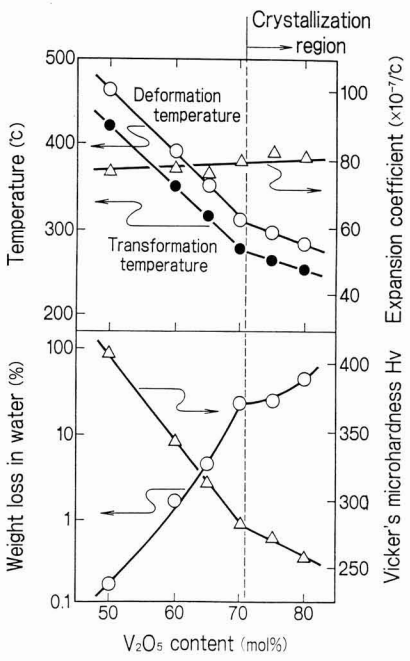

Fig. 2. Composition dependence of properties in V_2O_5-P_2O_5 glass system.

region of crystallization compositions above 70mol%. The changes in thermal expansion coefficients with composition were small, almost constant at about 80×10^{-7}/°C. In general, glasses with lower transforma-

tion and deformation temperatures tend to have larger thermal expansion coefficients. In contrast, for the V_2O_5-P_2O_5 glasses, as stated also in the reports by Hirashima et al.,[4,5] even if the transformation and deformation temperatures are lowered the change in the thermal expansion coefficients is small. This property is a very singular one for a glass, and its cause has not been identified. The weight loss in water increases with the increase of V_2O_5 contents, and particularly in or near the region of crystallization composition, the water resistance is very poor. This is also clearly seen from photos of glass surfaces eroded by water shown in Fig. 3. In the photos of the surfaces of glasses with higher V_2O_5 contents, cracked films can be seen and the surface is eroded flat and smooth while in the photos of glasses with low V_2O_5 contents polishing flaws are seen to remain although dents are observed at some spots, indicating that amounts dissolved into water are small. Since such cracks were not recognized before drying, they seem to arise from water vaporizing from within the glasses. In other words, as the V_2O_5 content increases, it becomes easier for water to penetrate into the glasses and for thick hydration layers to be formed. The analysis of the mole ratios (V/P) of the V and P in the cracked films showed that they are larger than those in the parent glasses. The amounts of V and P dissolved into water were analyzed, and the results are shown in Fig. 4. As shown in the figure, the amounts of dissolved V and P increase with the increase in V_2O_5 content (the decrease of P_2O_5 content). This corresponds well with the decrease of weight loss in water shown in Fig. 2. Regarding the amounts of V and P dissolved into water, the mole ratios of V/P were obtained and compared with those of the parent glass. As shown in Fig. 5, the mole ratios V/P of the dissolved elements into water are smaller than those of the parent glass and the difference between the two groups of the ratios widens with the increase in V_2O_5 content. Consequently, the V/P ratios in the cracked films become larger than those in the parent glass. For the compositions with V_2O_5 mole ratios below 70mol% (above 30mol% of P_2O_5) the ratio of the amount of dissolved elements into water V/P is almost constant at about 1, indicating that within this range of compositions, V and P dissolve into water at 1 to 1 regardless of the composition. On the other hand, for the compositions with V_2O_5 of above 70mol%, the V/P ratios of the elements dissolved into water slightly

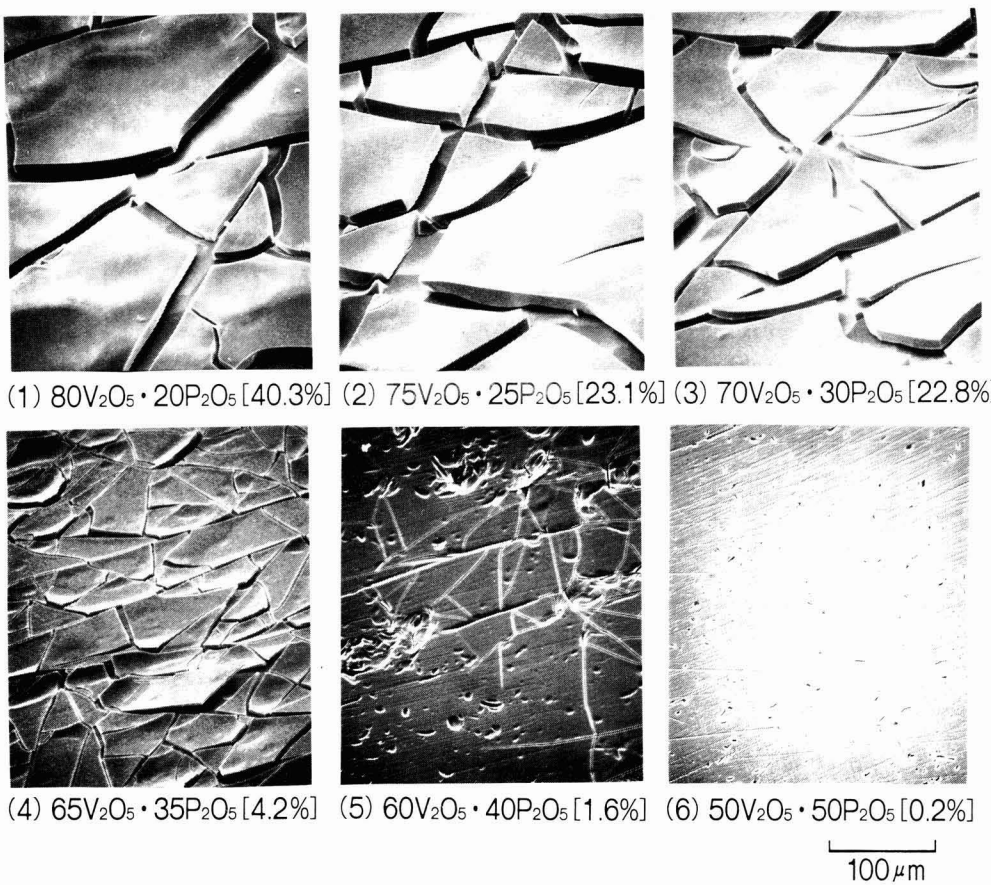

Fig. 3. Surfaces of V_2O_5-P_2O_5 glasses eroded by water.
[ ]: Weight loss in water

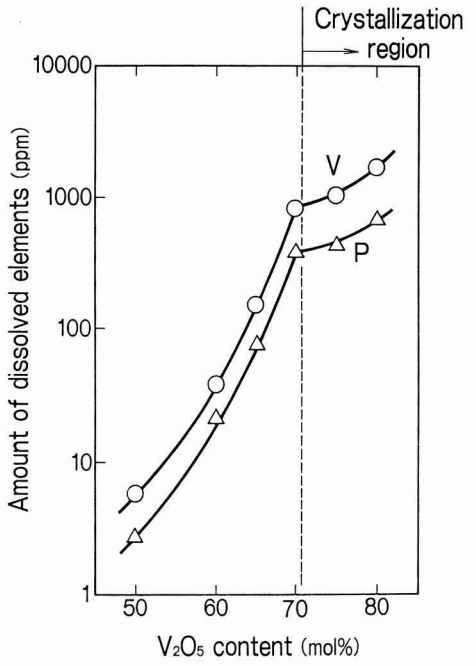

Fig. 4. Composition dependence of the amount of dissolved elements into water in V_2O_5-P_2O_5 glass system.

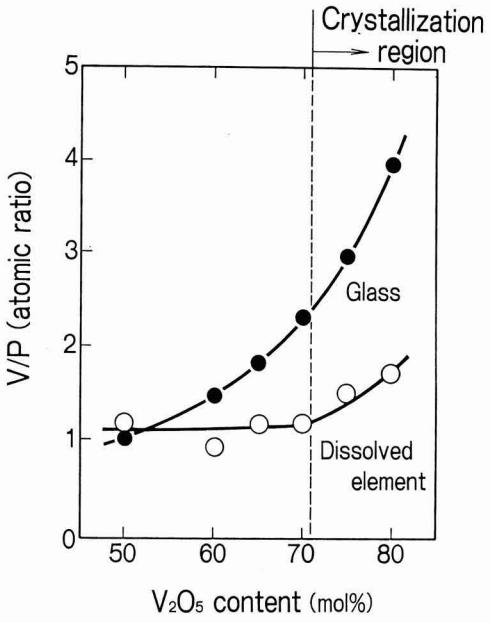

Fig. 5. Composition dependence of V/P atomic ratio of dissolved elements into water in V_2O_5-P_2O_5 glass system.

increase with the increase of V_2O_5 contents, which seems to have some relationship with the deposition of V_2O_5 within this range of compositions. As the above results indicate, since the conditions of erosion by water vary in accordance with glass compositions, we examined the transformation of glass structures due to the change in composition in order to find the causes as below.

3-2. Structures of V_2O_5-P_2O_5 Glasses and Mechanism of Erosion by Water

Figure 6 shows the infrared absorption spectrum of the glasses prepared. It also shows those of amorphous V_2O_5, β-$VOPO_4$ and $(VO)_2P_2O_7$ crystals. In the absorption spectrum of V_2O_5, it is assumed that the absorption of about 1020cm^{-1} is due to the stretching vibration of the V=O bond, that of about 820cm^{-1} to the stretching vibration of the V-O bond with a distance of about 1.8Å and that of about 600cm^{-1} to the stretching vibration of the V-O bond with a distance of about 2.0Å.[9,10] In the absorption spectrum of β-$VOPO_4$, it is known that the absorptions of about 1150cm^{-1}, about 1050cm^{-1} and about 940cm^{-1} are due to the asymmetrical stretching vibration of the P-O bonds and the absorption of about 1000cm^{-1} is due to the V=O bond.[11-13] In the absorption spectrum of $(VO)_2P_2O_7$, it is reported that the absorptions in the range of 1300 - 1100cm^{-1} are due to the asymmetrical stretching

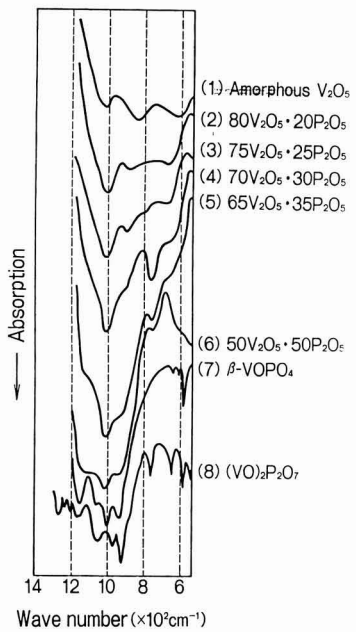

Fig. 6. IR absorption spectra of V_2O_5-P_2O_5 glasses, amorphous V_2O_5, β-$VOPO_4$ and $(VO)_2P_2O_7$.

vibration of the PO_3 bond, that of about 1050cm^{-1} to the symmetrical stretching vibration of the PO_3 bond, that of about 980cm^{-1} to the stretching vibration of the V=O bond, that of about 930cm^{-1} to the asymmetrical stretching vibration of the P-O-P bond,[12,13] and that of about 740cm^{-1} to the symmetrical stretching vibration of the P-O-P bond. $80V_2O_5 \cdot 20P_2O_5$ and $75V_2O_5 \cdot 25P_2O_5$ glasses seem to have the same structures, as have both spectrums similar to that of amorphous V_2O_5. Also, the absorption of about 820cm^{-1} and about 600cm^{-1} shift to higher wavenumbers, suggesting that their V-O bonds are strengthened by the presence of P_2O_5. Further, if the V_2O_5 content is reduced with the increase in P_2O_5 content, their absorption spectrums show great changes. Specifically, for $70V_2O_5 \cdot 30P_2O_5$ glass, a new large absorption appears at about 750cm^{-2}. Based on the comparison with the absorption spectrum of $(VO)_2P_2O_7$, it is assumed that this absorption is due to the asymmetrical stretching vibration of the P-O-P bond. The P-O-P bond can be broken easily by hydrolysis into P-OH and HO-P.[14] For $65V_2O_5 \cdot 35P_2O_5$ glass, the absorption of about 750cm^{-1} became smaller, while a new absorption started appearing at about 1150cm^{-1} and 920cm^{-1}. For $50V_2O_5 \cdot 50P_2O_5$ glass, the absorption at about 750cm^{-1} became smaller, and the absorptions at about 1150cm^{-1} and 920cm^{-1} became larger and similar to the absorption spectrum of β-$VOPO_4$. These results suggest that the structures of $V_2O_5 \cdot P_2O_5$ glasses became closer to that of β-$VOPO_4$ as P_2O_5 content increases as shown in the case of $50V_2O_5 \cdot 50P_2O_5$ glass.

It is known that amorphous V_2O_5 has a layered structure with spaces wide enough for water to penetrate and that if water penetrates into these spaces between layers, the structure is destroyed with the V_2O_5 layers separating, as if peeled off, and dissolved into water.[9,15-17] Therefore, from the results of the above infrared absorption spectrum measurement, it is assumed that also in the case of $80V_2O_5 \cdot 20P_2O_5$ and $75V_2O_5 \cdot 25P_2O_5$ glasses which are thought to have the same structure with amorphous V_2O_5, water penetrates into the glass structure with a similar mechanism forming large cracked films as shown in Fig. 3. Also, it can be explained that since amorphous V_2O_5 tends to crystallize, glasses with similar structures tend to crystallize. It is assumed that the change in the infrared absorption spectrum with the increase of P_2O_5 content indicates that a structure similar to that of amorphous V_2O_5 was transformed to one similar to that of β-$VOPO_4$. Since β-$VOPO_4$ has a network structure,[11] the glass is not easily penetrated by water. Thus, the water resistance seems to be improved with the increases in P_2O_5 content, as shown in Fig. 3. The reason for the small change in thermal expansion coefficients with glass compositions seems to be related to this structural transformation.

As stated above, the water resistance of these glasses can be improved by selecting the composition of V_2O_5 and P_2O_5. However, the increase in P_2O_5 content presents the problem of raising the transformation and deformation temperatures, as shown in Fig. 2. It is desirable for a glass with a low softening temperature for use as an airtight bonding material to have the lowest possible transformation and deformation temperatures without crystallizing or devitrifying. $70V_2O_5 \cdot 30P_2O_5$ glass is the most desirable of the prepared glasses in this respect. But the water resistance of the glass is not sufficient. The glass is assumed to maintain in some degree a similar layered structure to that of amorphous V_2O_5, as it showed similar erosion conditions to those of $80V_2O_5 \cdot 20P_2O_5$ and $75V_2O_5 \cdot 25P_2O_5$ glasses as shown in Fig. 3. Also, it seems to have many P-O-P bonds which are hydrolysed, as the absorption at about 750cm^{-1} in the infrared absorption spectrum of Fig. 6 is large. Therefore, in order to improve the water resistance of the glass, the authors considered trying to cause a similar structural transformation to that in the case of the increased P_2O_5 content by adding small amounts of a third element.

3-3. Effects of Additives on Water Resistance of Glass

For the additive, Fe_2O_3 was used which has been reported to be a water resistance promoting substance for V_2O_5-P_2O_5 glasses, water resistance promoting substance for other types of glass[18,19] a substance that forms glass in combination with V_2O_5[20] and a substance that effectively decreases the amount of water absorption.[21,22] The additive concentrations were set at 1mol% in the base glass in order to keep increases in the transformation and deformation temperatures as low as possible. For the base glass, $70V_2O_5 \cdot 30P_2O_5$ glass which has good fluidity at the lowest temperature of the prepared glasses was used. Table 1 shows the rates of weight loss in water of the glass containing various

Table 1. Water durability of $70V_2O_5 \cdot 30P_2O_5$ glasses containing 1mol% of various additives.

Additive	Weight loss in water (%)
None	22.8
PbO	2.8
Sb_2O_3	4.2
Bi_2O_3	5.1
BaO	5.7
Fe_2O_3	6.0
TiO_2	6.8
ZnO	7.3
CdO	7.5
MgO	7.6
Al_2O_3	7.7
SnO	8.8
TeO_2	10.3
ZrO_2	11.1
B_2O_3	12.9
GeO_2	15.6

additives. All the additives studied had the effect of decreased of weight losses in water. In particular, PbO, Sb_2O_3, Bi_2O_3 and BaO were noted as more effective additives than Fe_2O_3. Further studies were made on the effects of these additives on water resistance by increasing the additive concentrations. As shown in Fig. 7, the weight loss in water decreased with increases in the additive concentrations, indicating that their effects were in the order of Sb_2O_3 > PbO > Bi_2O_3 > BaO, and the addition of Sb_2O_3 or PbO was found to be particularly effective in improving water resistance. Adding 7mol% of Sb_2O_3 and 19mol% of PbO reduced the weight loss in water to almost zero. Also, no water erosion on the surface of these glasses was observed. Next, properties of the glasses other than water resistance were investigated in relation to the effects of Sb_2O_3 and PbO addition.

Figure 8 shows the DTA curves of $70V_2O_5 \cdot 30P_2O_5$ glasses with 7mol% of Sb_2O_3 or 19mol% of PbO added. The exothermic peak resulting from crystallization was observed at 500°C for the $70V_2O_5 \cdot 30P_2O_5$ glass with 7mol% of Sb_2O_3 added. Although Sb_2O_3 promoted crystallization, as above, the glass underwent no crystallization below 450°C and good fluidity was obtained within this range of temperatures. But, for the $70V_2O_5 \cdot 30P_2O_5$ glass with 19mol% of PbO added no exothermic peak was observed. Since PbO forms glass in combination with V_2O_5, PbO addition seems to hinder crystallization.

Figure 9 shows the effects of the concentration of added Sb_2O_3 on the deformation temperature and ther-

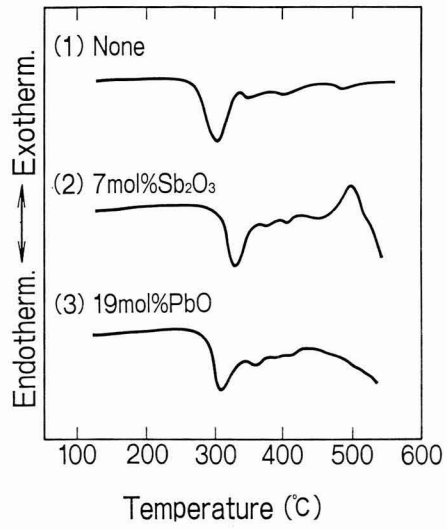

Fig. 8. DTA curves of $70V_2O_5 \cdot 30P_2O_5$ glasses containing Sb_2O_3 or PbO.

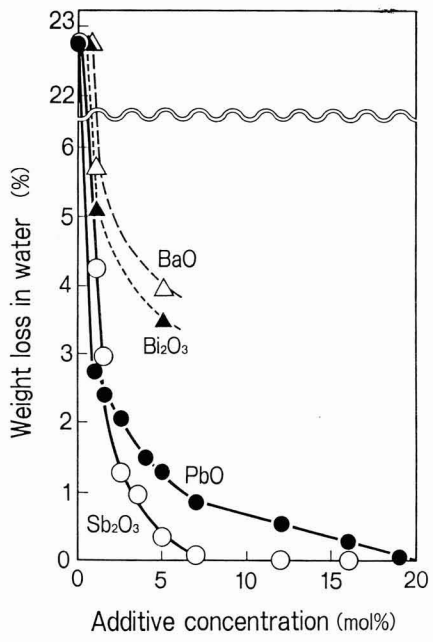

Fig. 7. Effect of additive concentration on water durability of $70V_2O_5 \cdot 30P_2O_5$ glass.

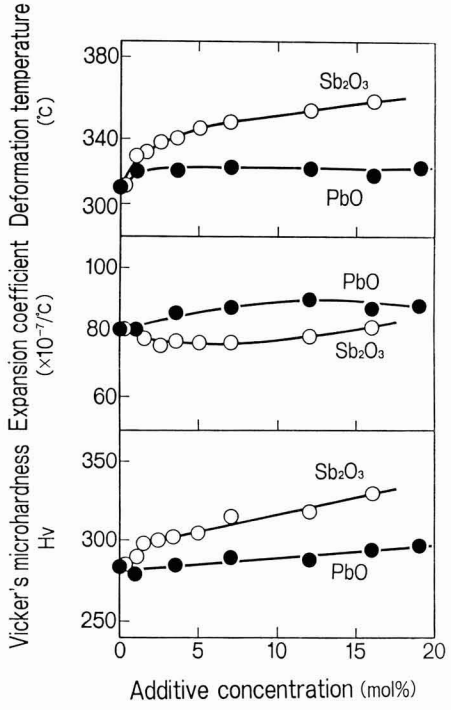

Fig. 9. Effects of additive concentration on deformation temperature, expansion coefficient and vicker's microhardness of $70V_2O_5 \cdot 30P_2O_5$ glass.

mal expansion coefficient of $70V_2O_5 \cdot 30P_2O_5$ glasses. When Sb_2O_3 is added, the change in the thermal expansion coefficients is small but the deformation temperature and hardness increase with the increase of additive concentration. However, the deformation temperature increases in a relatively narrow range, rising to 54°C even when 16mol% is added, making the glass suitable for use as a glass with a low softening temperature. On the other hand, in the case of adding PbO, the changes in these properties are small, but the thermal expansion coefficients are larger than when adding Sb_2O_3. The cause of the difference in properties arising from using either Sb_2O_3 or PbO may be that the addition of Sb_2O_3 tends to increase interatomic bonding more than PbO because the absolute value of the free energy is 3 to 4 times larger than that of PbO.

3-4. Effects of Adding Sb_2O_3 or PbO on the Glass Structure

Figures 10 and 11 show the infrared absorption spectrums of the $70V_2O_5 \cdot 30P_2O_5$ glasses with Sb_2O_3 or PbO added, respectively. The absorption decreases at about 750cm^{-1} and increases at about 1150cm^{-1} and 920cm^{-1} as the additive concentration increases. This is similar to the results where P_2O_5 content was increased as shown in Fig. 6. In other words, it is assumed that P-O-P bonds which are hydrolysed decrease in number with the addition of Sb_2O_3 or PbO, while a network structure similar to that of β-$VOPO_4$ is formed. As a result, it is harder for water to penetrate the glass and since Sb_2O_3 or PbO with a water resistance better than that of P_2O_5 is present in the glass, the water resistance seems to have been very much improved. As stated previously, since Sb_2O_3 promotes better bonding than PbO in a glass structure, the effects of improving water resistance are thought to be greater. The broadening of the infrared absorption with the addition of PbO seems to indicate that the glass is stabilized more by adding the PbO.

4. Conclusions

The effects of composition and additive on the properties and structure in V_2O_5-P_2O_5 glasses were studied and the following results obtained.

1) Glasses with a higher V_2O_5 contents have low transformation and deformation temperatures and a poorer water resistance and tend to undergo crystallization (devitrification). On the other hand, the thermal expansion coefficients change little with composition in a narrow range of about 80×10^7/°C.

2) The glass is transformed from a layered structure similar to amorphous V_2O_5 to a glass network similar to β-$VOPO_4$ with increasing P_2O_5 content (or decreasing V_2O_5 content). This structural transformation made the glass harder to penetrate for water, improving the water resistance.

3) The addition of Sb_2O_3 or PbO is very effective in improving the water resistance. When 7mol% of Sb_2O_3 or 19mol% of PbO is added to $70V_2O_5 \cdot 30P_2O_5$ glass with a poor water resistance, no erosion by water is observed. In this case, the changes in glass properties

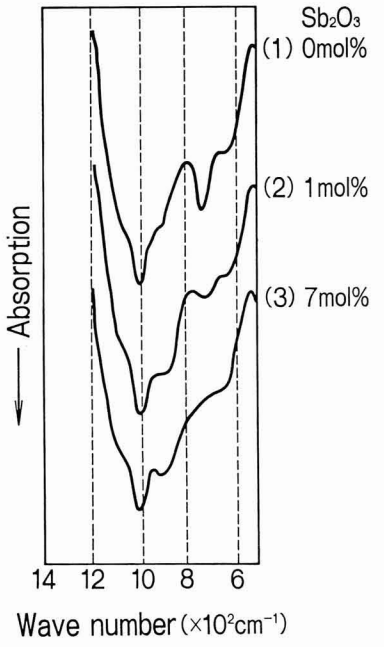

Fig. 10. IR absorption spectra of $70V_2O_5 \cdot 30P_2O_5$ glasses containing Sb_2O_3.

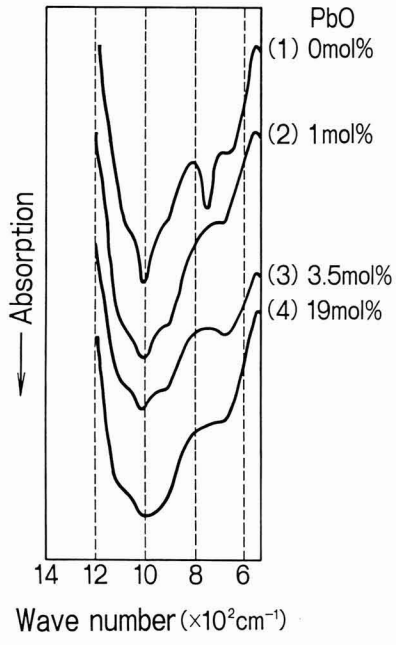

Fig. 11. IR absorption spectra of $70V_2O_5 \cdot 30P_2O_5$ glasses containing PbO.

such as the deformation temperature, the thermal expansion coefficient and hardness are small.

4) The additions of Sb_2O_3 and PbO bring about a structural transformation of the glass similar to that of increasing P_2O_5 content.

References:

1) P.L. Baynton, H. Rawson and J.E. Stanworth, Nature, 173, 1030-32 (1954).
2) P.L. Baynton, H. Rawson and J.E. Stanworth, J. Electrochem. Soc., 104, 207-40 (1957).
3) G.S. Linseley, J. Non-Cryst. Solids, 4, 208-19 (1970).
4) S. Hirajima, M. Mitsuhashi, T. Yoshida, Ceram. Soc., 90, 411-19.
5) H. Hirashima, K. Nishi and T. Yoshida, J. Am. Ceram. Soc., 66, 704-08 (1983).
6) H.R. Daton, J. Am. Ceram. Soc., 39, 109-12 (1956).
7) J. Gallup and A.G.F. Dingwall, Ceram. Bull., 36, 153-55 (1958).
8) K. Takagi, "Glass Engineering Handbook" Comp. by Moriya, Naruse, Kato, Tashiro, Asakura-shoten (1963) p. 507-48.
9) L. Rivoalen, A. Revcolevschi, J. Livage and R. Collongues, J. Non-Cryst. Solids, 21, 171-79 (1976).
10) S. Hirashima, T. Koyama, T. Yoshida, Ceram. Soc., 93, 554-60.
11) R.N. Bhargava and R.A. Condrate, Appl. Spectrosc., 31, 230-36 (1977).
12) T.P. Moser and G.L. Schrader, J. Catalysis, 92, 216-31 (1985).
13) E. Bordes and P. Courtine, J. Catalysis, 57, 236-52 (1979).
14) F.A. Cotton and G. Wilkinson, "Inorganic chemistry (Book 1)," Trans. by Nakahara, Baifukan (1979) p. 452.
15) J. Livage, P. Pineau, M.C. Leroy and M. Mickaud, Phys. Status Solidi A, 39, 73-8 (1977).
16) A.C. Wright, Philos. Mag. B, 30, L23-28 (1984).
17) J. Livage, Mat. Res. Soc. Sym. Proc., 32, 125-34 (1984).
18) S. Dobashi, "Chemistry of Glass," Kodansha (1982) p.85.
19) S. Dobashi, "Physics and Chemistry of Glass Surface," Kodansha, (1986) p.145 - 237.
20) S. Dobashi, "Chemistry of Glass," Kodansha (1982) p.90.

This article is a full translation of the article which appeared in Nippon Seramikkusu Kyokai Gakujutsu Ronbunshi (Japanese version), Vol.97, No.8, 1989.

Preparation and Properties of SiO_2 from Rice Hulls

Yoshinori Nakata, Masaaki Suzuki, Takeshi Okutani, Masanobu Kikuchi* and Takeo Akiyama**

Government Industrial Development Laboratory, Hokkaido
2-17 Tsukisamu-Higashi, Toyohira-ku, Sapporo 004, Japan
*IMC, 145-213, Aza-Yuufutu, Tomakomai 059-13, Japan
**Ikeda Bussan Ltd., 771, Kozono, Ayase 252, Japan

Dry rice hull contains 13-29wt% inorganic matter depending on the species, climate and geographic location. The inorganic matter is composed of silica (87-97wt%) with small amounts of alkali and other trace elements. Properties of ash obtained by combustion of between 400 and 1500°C were investigated. The SiO_2 in the rice hull was localized in the outer and inner epidermis of rice hull. The SiO_2 in rice hull ash formed by combustion below 800°C of rice hull powder with a particle size below 152μm was amorphous. Particles of the ash having an average diameter of 20μm were aggregates of small particles with a diameter of 2-5μm. At combustion temperatures above 900°C, the SiO_2 in rice hull ash consisted of cristobalite and small amount of tridymite. The surface of ash particles melted and the particles bonded to each other. The particle size was 40-60μm. It was found that potassium contained in the rice hull ash caused surface melting of SiO_2 particles and accelerated the crystallization of amorphous SiO_2 to cristobalite.
[Received March 20, 1989; Accepted May 16, 1989]

Key-words: Rice hull, Rice hull ash, SiO_2, K-Si-O system, Amorphous silica, Cristobalite

1. Introduction

Si is an element with a Clarke Number (composition ratio of element on the earth) of 25.8%, and is the second most common element after oxygen on the surface of the earth. Accordingly, Si is found in many forms in nature. In many cases Si is mixed with other minerals in a rock or forms a solid solution with other minerals. Tridymite, quartz and agate are pure minerals consisting of SiO_2 only.

SiO_2 is also contained in some plants as well as minerals. Typical organisms containing SiO_2 are diatoms, rice, and horsetails which are generally called the siliceous plants. Among these, rice is cultivated in Asian countries such as China, India, Thailand and Japan, supplying the basic staple. In rice hulls, which are by-products from rice production, 13 - 29wt% of inorganic matter is present, of which 87 - 97wt% is SiO_2.

It is difficult to use rice hulls in agriculture in the form of compost, because of the high resistance to breakdown, so at present no good use can be made of rice hulls, except for some usage in agricultural materials. In contrast to quartz and quartzite, however, the good reactivity of SiO_2 from rice hulls has been used in studies on the production of silicon tetrachloride used for making artificial quartz glass,[5,6] SiC whiskers[2,3] and metallic silicon.[4] Recently, as an example of the use of biomass, there have been many attempts to obtain a heat source or to generate electric power by burning organic matter such as the cellulose contained in rice hulls at 71 - 87wt%. As a result, a large amount of ash (SiO_2) is discharged. In order to obtain some basic information about the uses of SiO_2 in rice hulls, we examined the relationship between the combustion temperature and such factors as chemical composition, crystal phase, surface area, shape and properties of ashes from which all organic matter such as the cellulose contained at 71 - 87wt% in rice hulls is removed by combustion. In addition, the products were compared with a commercial SiO_2 reagent.

2. Experimental

2-1. Preparation and Analysis of Rice Hull Powder Sample

A powder with particle sizes below 152μm was used as the rice hull sample. Rice hull was compressed with a rice hull compressive crusher (Mizuho Thermal Apparatus Mfg. Co., Ltd.) at 200° - 300°C and a pressure of 100±50ton/cm^2 to form a solid mass of rice hulls. Then the solid matter was crushed to obtain a rice hull powder with particle sizes below 152μm. The water content of the powder obtained was 6.8wt%, and the SiO_2 content was 30.4wt% in the rice hull powder obtained after drying in a vacuum at 107°C for an hour.

The shape of the rice hulls before fracture was examined using a scanning electron microscope and the distribution of the SiO_2 in rice hulls using an X-ray micro-analyzer (JEOL Ltd. JXA-8600M).

2-2. Preparation of Pyrolyzed Rice Hulls

When rice hulls were heated in an air flow, starting from room temperature, the temperature rises rapidly at over 250°C, up to about 1000°C, depending upon the amount of rice hull powder. This is due to the speedy combustion of low molecular weight flammable matter generated from the pyrolysis of organic matter such as cellulose. (When rice hulls are pyrolyzed in an inert gas, if the temperature exceeds 300°C, gas and liquid matter generated by the pyrolysis of organic matter, that is the volatile contents, were observed.) After the speedy combustion the fixed carbon with a low combustion rate and high molecular weight began to burn. In order to control the rapid temperature rise due to the combustion of the volatile component in the early stage and to

examine the change in phase of SiO_2 in rice hulls according to temperature, pyrolyzed rice hulls (PRH) were prepared by the following process, removing the volatile contents, from the rice hulls. Rice hull ash was prepared by combustion at 400° - 1500°C and the properties examined.

The preparation of PRH was carried out by placing 100g of rice hull powder into a vessel made of quartz glass of 5cm inner diameter. The vessel was placed in a vertical type electric furnace. The rice hull powder were heated in Ar flowing at 300ml/min and heated to 500°C at a heating rate of 13.3°C/min, and the sample retained for an hour then cooled to room temperature. 56.5g PRH was obtained. The SiO_2 content of the PRH was 53.8wt%.

2-3. Combustion of PRH

1g PRH was placed in a combustion boat made of mullite and put into the center of a silicon carbide heater electric furnace provided with a mullite tube of 3cm inner diameter. The PRH was heated in air flowing at 100ml/min at a heating rate of 5°C/min up to the prescribed temperature between 400° - 1500°C. Then the PRH was kept at that temperature for an hour to obtain rice hull ash.

2-4. Analysis of Product

The analysis of both PRH and rice hull ashes generated by combustion of PRH was performed using a powder X-ray diffractometer (CuKα) (Rigaku Denki Mfg. Co. Geigerflex RAD-3C Type). The determination of SiO_2 both in PRH and rice hull ashes was performed as follows. The sample was dissolved in nitric acid and perchloric acid, precipitating SiO_2, the SiO_2 was filtered and heated to find the weight of SiO_2. In addition, K_2O, Na_2O, CaO, MgO, MnO, Fe_2O_3, Al_2O_3 and soluble SiO_2 were determined by atomic absorption analysis of the filtrate obtained from the quantitative analysis of SiO_2 (Hitachi Ltd. Z-8000). The carbon remaining in the rice hull ashes was determined using a chromatic C Type VK-1D (Horiba Mfg. Co.). The shape and size of the ashes was examined using a scanning electron microscope (JEOL Ltd. JSM-T330A) The surface area of the ash was measured using a Quantasorb (Quantachrome Ltd.). The thermal analysis of both PRH and ashes was carried out using a TG-DTA (MAC Science TG-DTA2000).

2-5. Comparison of Rice Hull Ashes with Commercial SiO_2

SiO_2 reagent (below 300 mesh, purity 99.999% produced by Furuuchi Mfg. Co.) after undergoing the heat treatment described in paragraph 2-3 was compared with rice hull ashes. The analysis of powder after heat treatment was performed as described in paragraph 2-4, when required.

3. Results and Discussion

3-1. Distribution of SiO_2 in Rice Hulls

Scanning electron micrographs of the outer epidermis of rice hulls (a) and of the inner epidermis contacting the rice grain (b) are shown in Fig. 1.

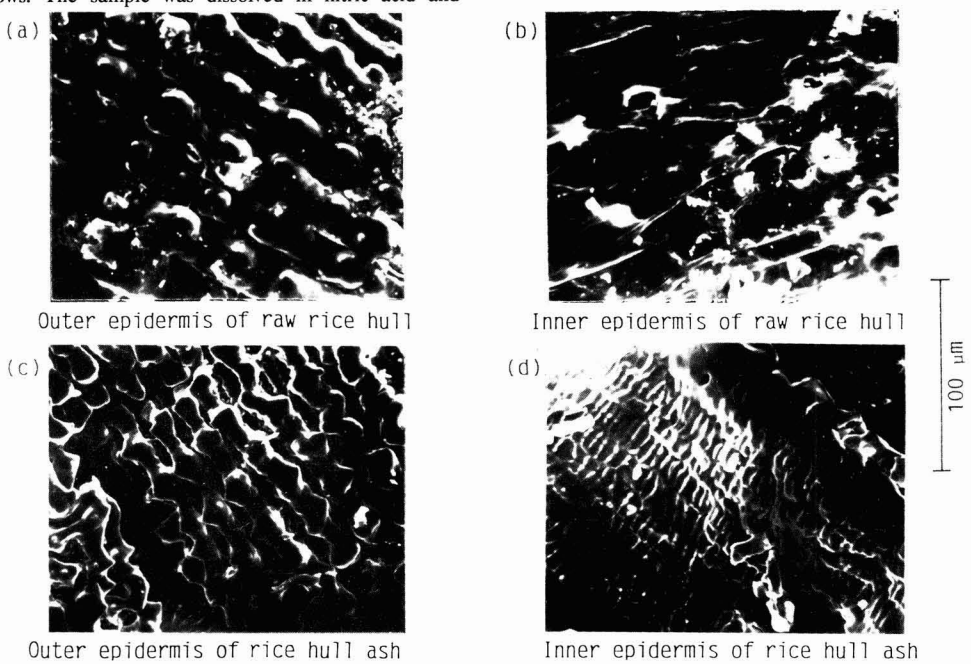

Fig. 1. Scanning electron micrographs of outer and inner epidermis of raw rice hull and rice hull ash.

The half-spherical projection on the surface of the outer epidermis is 15 -20μm in diameter and arranged regularly along the long axis of the rice hull. Approaching both ends, the diameter of the projection becomes smaller and the interval also becomes smaller. The inner epidermis is flatter than the outer one. The shape of ash particles obtained after the treatment of one uncrushed rice hull at 900°C in an air flow of 100ml/min for an hour is shown in Fig. 1(c) and (d). The outer epidermis of the rice hull ash is somewhat shrunk, retaining the pattern of half-spherical projections. In the micrograph of the inner epidermis (d) the cell wall can be observed. The composition of the ashes is shown in Table 1.

The SiO_2 content was 96.5wt%. Micrographs (c) and (d) are thought to show the SiO_2 distribution.

The electron image and SiKα X-ray image of the cross section of the rice hull are shown in Fig. 2.

The cross section through the projection arranged regularly along the long axis of the rice hull is shown in micrograph (a) and the cross section along the projection line in micrograph (b). Sharma et al.[3] have reported that the outer epidermis contains more Si with a weight ratio of 2.4:1 than the inner epidermis. In the present work a trend similar to this was observed.

3-2. Thermal Behavior of Rice Hull Powder

The thermal behavior of rice hull powder in air and argon was examined using a TG-DTA. The TG-DTA curve of the rice hulls measured in air flowing at 50ml/min at a heating rate of 10°C/min is shown in Fig. 3. The weight loss in the range from room temperature to 100°C is due to adsorbed water. Two exothermic

Table 1. Composition of rice hull ash produced from fluidized rotational furnace (wt%).

SiO_2	96.5
Na_2O	0.07
K_2O	0.90
MgO	0.04
CaO	0.13
Al_2O_3	0.63
Fe_2O_3	0.23
C	1.30

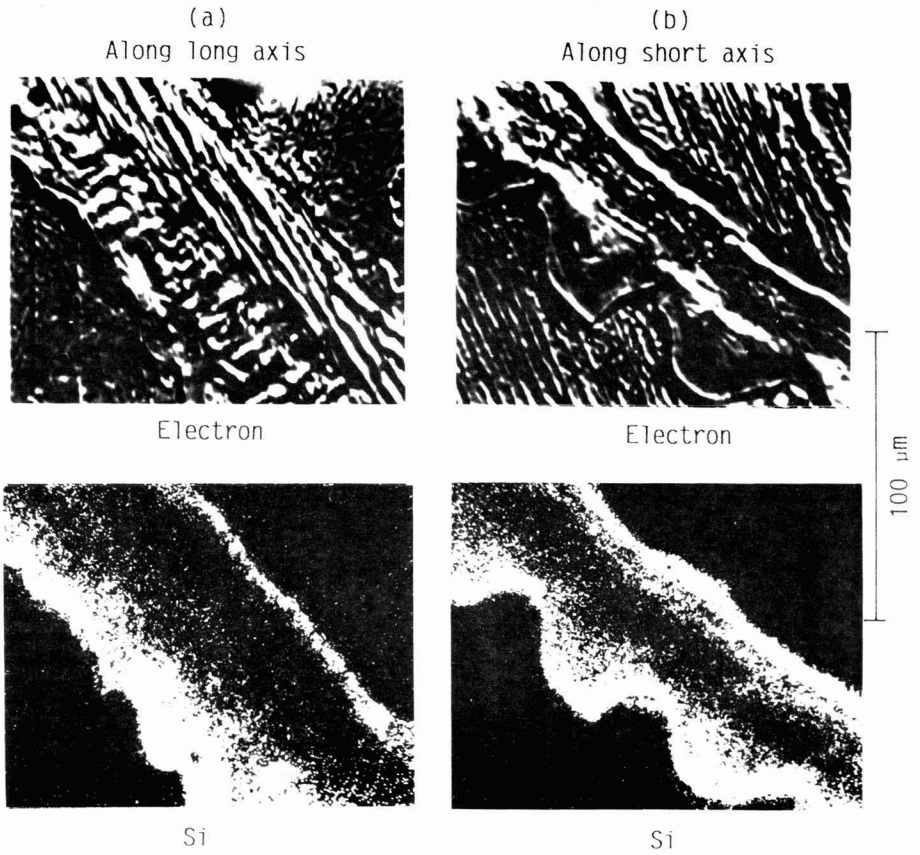

Fig. 2. Electron microprobe X-ray images of cross section of rice hull.

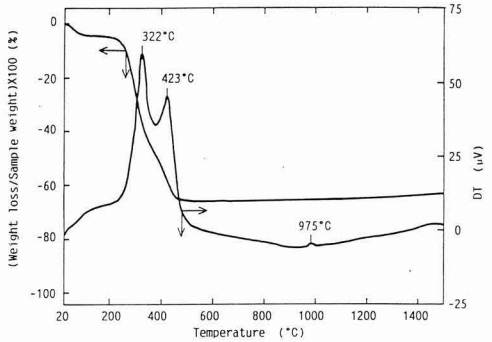

Fig. 3. TG and DTA curve of rice hull powder in air flowing at 50ml/min.
Sample weight: 7.19mg, Heating rate: 10°C/min, Thermocouple, Pt-PtRh13%.

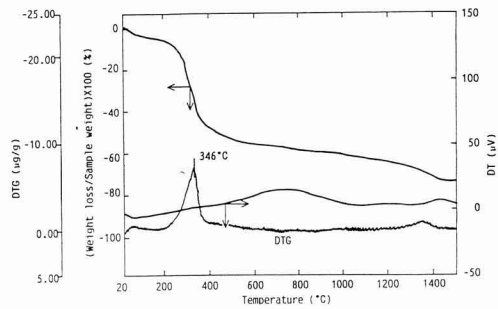

Fig. 4. TG, DTA and DTG curve of rice hull powder in Ar flowing at 50ml/min.
Sample weight: 7.8mg, Heating rate: 10°C/min, Thermocouple: Pt-PtRh13%.

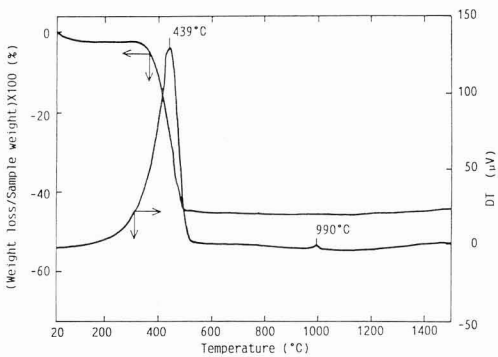

Fig. 5. TG and DTA curve of pyrolyzed rice hull (PRH) in air flowing at 50ml/min.
Sample weight: 7.79mg, Heating rate: 10°C/min, Thermocouple: Pt-PtRh13%.

peaks were observed at 322°C and 423°C. The peaks are due to the combustion of organic matter such as cellulose.

The TG-DTA curve of rice hull powder measured in argon gas flowing at 50ml/min are shown in Fig. 4. The weight loss began about 200°C, and the largest weight loss can be seen at 346°C (position of DTG peak). At over 500°C a gradual decrease can be seen. In the rapid weight loss range from 200° to 400°C, white smoke and yellow gas (volatile components) were generated. Presumably this is due to low molecular weight substances generated from the pyrolysis of organic matter such as cellulose.

The TG-DTA curve of PRH, which was prepared by the pyrolysis of rice hull powder in argon at 500°C for an hour, measured in air flowing is shown in Fig.5.

One exothermic peak only can be seen at 439°C, so we assume that this is due to the combustion of the carbon which remains after pyrolysis.

Based on the above observation, we concluded that the exothermic peak at 322°C in Fig. 3 is due to the combustion of low molecular weight substances generated by the pyrolysis of organic matter such as cellulose contained in rice hulls and that the exothermic peak at 423°C is due to the combustion of the pyrolysis residue or the combustion of unpyrolyzed carbon or the combustion of so called fixed carbon.

Regarding the TG-DTA curves in Figs.3 and 5, an exothermic peak can be seen near 990°C. Near the peak no change in weight was observed. Presumably then the peak is due to the crystallization from amorphous SiO_2 to cristobalite, based on the result of X-ray diffraction.

3-3. SiO_2 Formed from Combustion of PRH

When rice hulls are subjected to combustion, a few percent of carbon remains. This carbon cannot be removed even if combustion is carried out at 1300°C in air or oxygen. When the rice hulls were subjected to combustion without special treatment, a higher temperature was achieved due to the combustion of substances generated by the pyrolysis of the rice hulls (volatile contents). (If 100g rice hulls was heated up to 250°C, with sufficient air, the volatile contents began to burn and the combustion temperature rose to 1000°C). 0.90wt% of potassium oxide was present in the ashes as shown in Table 1. The potassium reacted with SiO_2 at high temperature, became molten and the unburnt carbon dissolved into the melt. The carbon remained, because contact with oxygen was hindered. The SEM photograph of the rice hull ashes produced from a fluidized rotational furnace (Hokuto Engineering Co. furnace type WHB-450-M, amount of supplied rice hulls 450g/hr, temperature 900±100°C, retention time 4 hours) is shown in Fig. 6. It can be seen that the surface of the ash particle is molten and caked.

In order to check the runaway combustion temperature due to pyrolyzed products from the rice hulls and to follow exactly the behavior of the SiO_2 in the rice hulls depending on the combustion temperature, rice hull ashes were obtained from a horizontal type electric furnace, oxidizing fixed carbon contained in 1g PRH at temperatures from 400° to 1500°C. The properties of the SiO_2 in the ashes thus obtained are shown in Table 2.

Heating rate means the rate from room temperature to

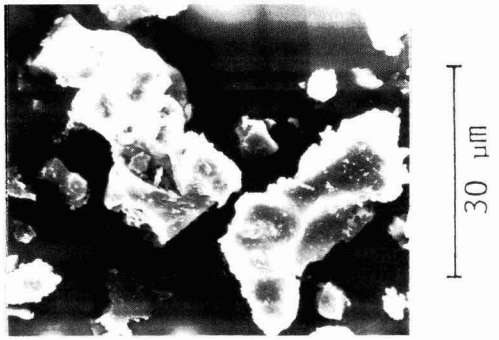

Fig. 6. SEM photograph of rice hull ash produced from fluidized rotational furnace.

Table 2. Properties of ash prepared by combustion of PRH in air flowing (100ml/min) at various temperature for 1hr.

Exp. no.	Combustion temp. (°C)	SiO_2 content (wt%)	C content (wt%)	Crystalline of SiO_2	Surface area (m^2/g)	Color
1	400	89.5	0.65	Amorphous	146.7	Black
2	500	87.0	0.46	〃	130.6	〃
3	600	92.5	0.25	〃	66.6	Grey
4	650	93.2	0.20	〃	45.9	Greyish white
5	700	94.0	0.06	〃	18.7	Pink white
6	800	97.0	0.02	〃	5.3	〃
7	900	96.2	0	C, T	0.8	〃
8	1000	96.6	0	〃, 〃	0.7	〃
9	1100	99.3	0	〃, 〃	0.6	〃
10	1200	99.0	0	〃, 〃	0.6	〃
11	1300	96.9	0	〃, 〃	0.6	〃
12	1400	99.7	0	〃, 〃	0.5	〃
13	1500	99.9	0	〃, 〃	0.4	〃

* PRHs were heated from room temperature to the combustion temperature at the heating rate of 5°C/min in air flowing.
+ Crystalline of SiO_2; C:Cristobalite, T:tridymite.

Table 3. Effect of various heating rate up to 1000°C from room temperature in air flowing of 100ml/min for properties of SiO_2 prepared from PRH.

Exp. no.	Heating rate (°C/min)	SiO_2 content (wt%)	C content (wt%)	Crystalline of SiO_2	Surface area (m^2/g)	Color
8	5	96.6	0.00	C, T	0.7	Pink white
14	10	96.8	0.09	〃, 〃	0.7	Grey white
15	15	96.8	0.13	〃, 〃	0.8	White grey
16	20	96.2	0.41	〃, 〃	0.9	Black grey

* Crystalline of SiO_2 ; C: Cristobalite, T: Tridymite.

the prescribed temperature. The content of SiO_2 in the rice hull ashes increased with an increase in temperature. The color of the ashes became white mixed with pink at temperatures over 700°C. The carbon content was 0wt% at temperatures over 900°C. According to the X-ray diffraction analysis of the ashes, amorphous SiO_2 was present at temperatures below 800°C of which X-ray diffraction line was broad, peaking at 4.1 - 4.2Å of d value. At temperatures over 900°C diffraction peaks of heating rate the more carbon was incorporated into the ashes.

The SEM photographs of the particle surface of rice hull ashes prepared by combustion of PRH in the range of temperature 600° - 1500°C are shown in Fig. 7. Ash particles prepared below 800°C were aggregates of small particles with diameters of 2 - 5μm forming a secondary particle with an average diameter of 20μm. A large primary particle with a diameter of 40μm was observed among the particles. There were few large primary particles at temperatures near 800°C. The small particles with a diameter of 2 - 5μm were aggregated to form a secondary particle with a diameter of 40μm. Over 900°C, the small particles with a diameter of 2 - 5μm began to melt, at higher temperatures more particles melted. The average diameter of the particles is as follows: 48μm at 900°C, 60μm at 1100°C, 40μm at 1300°C and 40μm at 1500°C. At 900°C and 1000°C the contact face of the small particles was molten, and the aggregated secondary particle contained many voids. At 1300°C and 1500°C, the whole particle was molten to form a single large particle. The shape of the particle heated at a heating rate 5°C/min up to the prescribed temperature is shown in Fig. 7. When the heating rate was 10, 15 and 20°C/min, the melting process of the particle surface was accelerated, with an increase in the heating rate. The SiO_2 reagent was heated by the same process as PRH, but it did not show the same behavior as SiO_2 from rice hull ashes. Neither a change in the surface shape of the particle (with an average diameter 30μm) nor melting of the particle even at 1500°C were observed.

The surface area was $5m^2/g$ at 800°C and it increased with a decrease in temperature. It was $146.7m^2/g$ at 400°C. At over 900°C it was in a range from 0.8 to $0.4m^2/g$. The trend of decreasing surface area with an increase in combustion temperature agrees well with the observation that the particle surface was molten and aggregated. Regarding the commercial SiO_2, the surface area was 0.2 - $0.3m^2/g$ at temperatures 400° cristobalite and only max, peak of tridymite could be observed. The max. diffraction line of tridymite became larger with an increase in temperature. In the DTA measurement of the ashes obtained in the range of 400° - 800°C, an exothermic peak was observed between 981° - 991°C. This peak is due to the crystallization from amorphous SiO_2 to cristobalite, based upon the X-ray diffraction patterns before and after peak. The exothermic peak could not be observed in the ashes obtained by combustion over 900°C where the SiO_2 was cristobalite. The crystallization from amorphous SiO_2 to cristobalite was observed at 1500°C, using commercial SiO_2 reagent. SiO_2 in rice hull ashes was crystallized at a temperature 600°C lower than commercial SiO_2.

The change in the properties of SiO_2, by changing the heating rate up to 1000°C, is shown in Table 3. No difference was observed in the SiO_2 content, SiO_2 crystalline phase and surface area, compared with the case when the heating rate was 5°C/min (Fig. 2). The carbon content increased with an increase in the heating rate. The color of the rice hull ashes changed from white mixed with pink into black gray. The higher the - 1500°C, and no change with temperature could be observed.

The result of determination of the chemical composi-

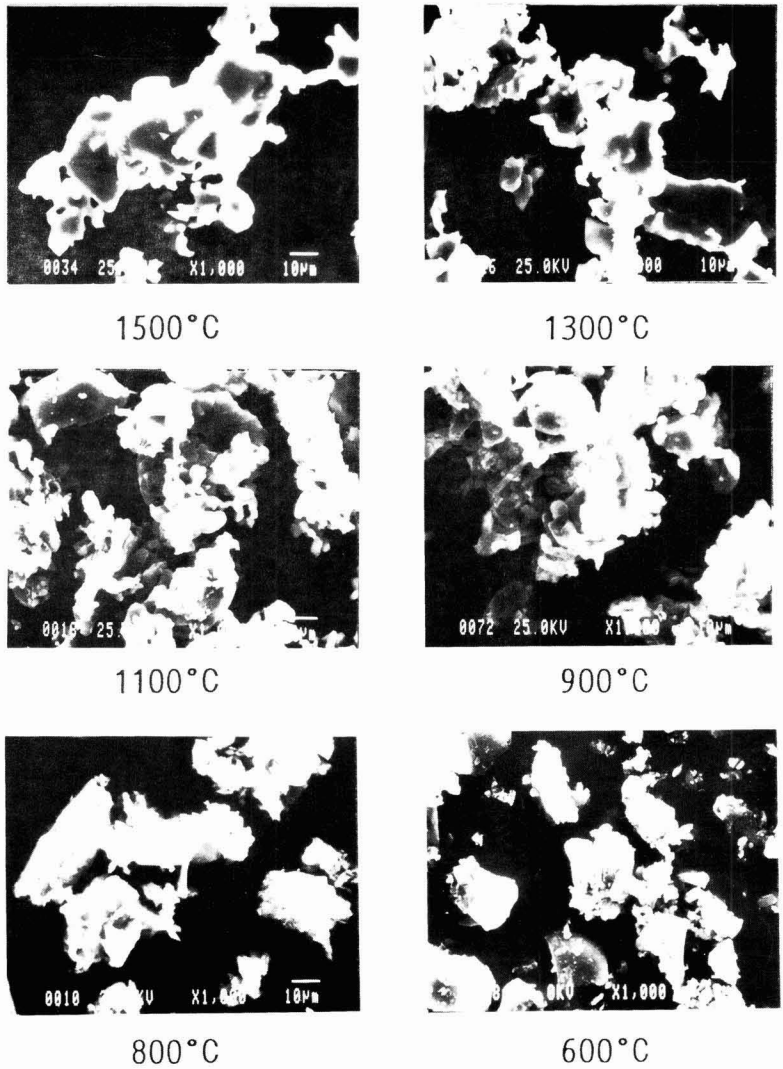

Fig. 7. SEM photographs of particle surface of rice hull ashes prepared by combustion of PRH at various temperatures for 1hr. Heating rate up to prescribed temperature: 5°C/min.

tion such as K_2O and Na_2O contained in the rice hull ashes prepared at various temperatures is shown in Table 4.

The rice hull ashes prepared at temperatures over 1000°C was over 99% SiO_2, summing the SiO_2 contents shown in Table 2 and 3, and the soluble SiO_2 shown in Table 4. The K_2O originating from fertilizer and the CaO, MgO, Al_2O_3 from the soil are impurities in the rice hull ashes. K_2O, Na_2O, CaO, MnO, MgO and Fe_2O_3 contents decrease with an increase in combustion temperature, but the Al_2O_3 did not change. Experiments No.14, 15 and 16 show the cases with different heating rates but at the same combustion temperature of 1000°C. When the heating rate was high, there was no decrease in K_2O content. This is due to the fact that K was diffused into SiO_2 by the reaction of K_2O and SiO_2 before the K_2O is vaporized by the rapid heating rate, so more K remained. Na_2O is also to be thought to have the same behavior as K_2O but the trend is not clear, because of the low content. When the heating rate was high, more K remained in the ashes. Potassium polysilicate with a melting point at a lower temperature ($K_2Si_nO_{2n+1}$ thought to be a potassium polysilicate with a large n value based upon the contents of K) was formed by reaction of SiO_2 and K, which included carbon causing the ashes to melt, and the color of the ashes changed to gray or black.

In order to examine the function of K, 1 or 2wt% of

Table 4. Chemical composition of rice hull ashes prepared by combustion of PRH at various temperatures.

Exp. no.	Combustion temp. (°C)	Na_2O	K_2O	MgO	CaO	Al_2O_3	MnO	Fe_2O_3	Soluble SiO_2	Ignition loss
		(wt%)								
PRH	-	0.04	1.11	0.13	0.25	0.34	0.05	0.27	1.15	46.5
1	400	0.03	1.95	0.30	0.42	0.34	0.06	0.22	2.59	3.6
2	500	0.03	1.77	0.26	0.42	0.40	0.10	0.31	4.66	2.4
3	600	0.03	1.77	0.28	0.36	0.30	0.14	0.29	1.71	1.6
4	650	0.05	1.43	0.22	0.34	0.45	0.12	0.36	3.06	1.6
5	700	0.01	1.11	0.15	0.24	0.26	0.06	0.22	0.66	1.5
6	800	0.03	0.48	0.16	0.27	0.43	0.03	0.14	0.66	0.9
7	900	0.01	0.40	0.10	0.25	0.34	0.01	0.08	0.56	0.5
8	1000	0.01	0.23	0.02	0.22	0.32	0.01	0.07	0.63	0.4
9	1100	0.03	0.13	0.02	0.17	0.30	0.00	0.06	0.45	0.2
10	1200	0.01	0.06	0.00	0.07	0.32	0.00	0.06	0.63	0.4
11	1300	0.01	0.04	0.00	0.03	0.36	0.00	0.11	0.45	0.3
12	1400	0.01	0.05	0.00	0.01	0.36	0.00	0.07	0.60	0.4
13	1500	0.01	0.01	0.00	0.03	0.30	0.00	0.12	0.45	0.3
14	1000	0.01	1.77	0.02	0.25	0.25	0.00	0.07	0.36	0.5
15	1000	0.01	1.77	0.02	0.27	0.36	0.00	0.10	0.30	0.6
16	1000	0.03	1.43	0.02	0.29	0.32	0.01	0.11	0.53	0.6

* Exp. nos. correspond to those in Table 2 and 3.

KCl and KOH were added to SiO_2 reagent, and the same heat treatment performed as for PRH. The surface melting of the SiO_2 particle was observed during heat treatment at 1100°C for an hour. In the case of rice hull ashes the surface melting of the particle was observed at 900°C. The above temperature was higher by 200°C. This is due to the melting of the potassium polysilicate generated by the reaction of a potassium salt and SiO_2.

The effect of K was investigated using TG-DTA. No DTA peak was observed in the TG-DTA measurement using SiO_2 reagent only, but when KCl was added to the SiO_2 reagent, an exothermic peak was observed between 1270°C and 1330°C. When KOH was added to the SiO_2 reagent, the exothermic peak was observed between 905°C and 978°C. Based on the results of X-ray diffraction analysis, the peak was due to the crystallization of amorphous SiO_2 to cristobalite. SiO_2 was crystallized to cristobalite from amorphous SiO_2 by heat treatment in air for an hour at 1100°C in the case of KCl and at 900°C in the case of KOH. The diffraction line of tridymite was not observed. The decrease of the crystallization temperature was caused by the effect of the potassium compound added.

4. Conclusions

The residue of the rice hull powder pyrolyzed in an inert gas was heated in air in the range of temperatures from 400°C to 1500°C. The following results were obtained by examining the properties of the SiO_2 obtained.

1) The SiO_2 in rice hulls is localized in the outer and inner epidermis. In the combustion of rice hulls, first the oxidization reaction (combustion) of vapor and liquid components (volatile) generated by the pyrolysis of organic matter such as cellulose occurs and the combustion of fixed carbon follows. The rate of the combustion reaction of the volatile component in the early stage is fast and it is not easy to control the combustion temperature but it is easy to control the combustion temperature of the fixed carbon.

2) In the combustion experiments with pyrolyzed rice hulls (PRH), more carbon is incorporated into the SiO_2 with an increase in the heating rate from room temperature to the prescribed temperature. Presumably more carbon is incorporated because the potassium compound contained in the rice hulls reacts with SiO_2 and becomes molten. In the case of a low heating rate, because potassium is volatilized, the potassium content decreases and the melting is checked, so ashes containing no carbon of a white mixed pink color are obtained.

3) The SiO_2 contained in rice hulls is amorphous. When it is retained at 900°C for an hour, crystallization to cristobalite occurs. Tridymite is detected in small amounts only and the X-ray diffraction peak became larger with an increase in combustion temperature. However, the amorphous SiO_2 reagent was crystallized to cristobalite at 1500°C.

4) When rice hulls are heated at temperatures below 800°C, the small primary particles with diameters of 2-5μm aggregated to form a secondary particle. At temperatures over 900°C, fusion between primary particles was observed and the melting advanced with an increase in temperature. The surface area was $5m^2/g$ at 800°C, became larger with a decrease in temperature and was $147m^2/g$ at 400°C and 0.8 - $0.4m^2/g$ at over 900°C. The shape of particle surface agreed well with the above trend.

5) K_2O, CaO, MgO, Al_2O_3 and so on were contained in PRH ashes. K_2O, Na_2O, CaO, MgO, MnO and Fe_2O_3 were volatilized with an increase in combustion temperature and the contents decreased but there was no change in Al_2O_3.

6) Potassium contained in the PRH ashes accelerated both the melting of particles and the crystallization of amorphous SiO_2 to cristobalite.

References:

1) T. Okutani, Fine Ceramics, 7, 24-32 (1986).
2) J.-G. Lee and I.B. Cutler, Am. Ceram. Soc. Bull., 54, 195-198 (1975).
3) N.K. Sharma, W.S. Williams and A. Zangvil, J. Am. Ceram. Soc., 67, 715-720 (1984).
4) L.P. Hunt, J.P. Dismukes, J.A. Amick, A. Schei and K. Larsen, J. Electrochem. So., 131, 1683-1686 (1984).
5) P.K. Basu, C.J. King and S. Lynn, AIChE Journal 19, 439-445 (1973).
6) T. Okutani and Y. Nakata, "High Tech Ceramics," Edited by P. Vincenzini, Elsevier (1987) pp.511-516.

This article is a full translation of the article which appeared in Nippon Seramikkusu Kyokai Gakujutsu Ronbunshi (Japanese version), Vol.97, No.8, 1989.

Influence of Powder Properties on Sintering Behavior of Silicon Carbide

Osami Abe, Takaaki Nagaoka, Masataka Yamamoto*, Norohiro Ohtake* and Mamoru Asuwa*

Government Industrial Research Institute, Nagoya
1-1 Hirate-cho, Kita-ku, Nagoya 462, Japan
*Showa Denko, 1 Soga, Shiojiri 399-64, Japan

Two kinds of silicon carbide powders prepared through different synthesizing processes were classified and decarbonated to investigate the particle size dependence of powder properties. Influence of the particle size on the sintering behavior was studied by dilatometry and microstructural observations. A powder synthesized from metallic silicon and carbon in solid state has a broad primary particle size distribution. This powder was also characteristic in having large amounts of unreacted carbon and impurity oxygen contained in the fine component of classified powder. The densification with boron and carbon additives progressed initially with equiaxial grain growth, and then, with formation of plate-like grains at high temperatures. The free carbon contained in the fine component promoted the densification remarkably at the initial stage sintering, while the coarse component reduced the densification rates. Inhomogeneous sintered bodies were obtained from the powder consisted of the fine component with the large amount of free carbon and poorly sinterable coarse component. On the contrary, the other powder synthesized from tetrachlorosilane and heavy oil in gas phase had a narrow size distribution. In this case, the classified and decarbonated components showed almost the same densification behavior producing sintered bodies with homogeneous microstructure. The starting powder have to be homogeneous in chemical composition especially in fine components in addition to the reduced component of coarse particles.
[Received March 27, 1989; Accepted May 16, 1989]

Key-words: Silicon carbide, Sintering behavior, Chemical composition, Particle size, Homogeneity

1. Introduction

Silicon carbide ceramics are now attracting interest for use as high-temperature structural materials because of the high strength and excellent corrosion resistance even at 1300°C or higher where the strength of a sintered silicon nitride degrades greatly.[1,2] However, the room-temperature strength and fracture toughness are less than those of silicon nitride ceramics. It is desirable to control their microstructure more closely in an attempt to improve these properties.[3] Another problem in manufacture is that the sintering temperature of silicon carbide is over 1900°C, but temperatures exceeding 2100°C generate feather which tends to lower its strength, thus limiting the range of optimum heating conditions. Consequently, it is important to study the relationship between the properties of starting powder materials and the sintering behavior and the resultant microstructure of the sintered bodies.

The authors investigated the influence of characteristics of several commercial powders on the temperature dependence of shrinking rate, β-α transition, microstructure, etc., and reported the following results: (1) when the growth of plate-like grains occurred in the early stage of sintering, a structure interlocked by the plate-like grains disturbed the further densification; and (2) not only the size of primary particles but powder agglomeration, the presence of free carbon, and powder morphology greatly affect the sinterability.[4,5] One whether to represent powder characteristics with average values. Especially, in the case of powder manufactured by solid-phase synthesis including milling process, inhomogeneity in chemical composition and crystallinity will be caused depending on particle size, obscuring any correlation between sinterability and powder characteristics.

In this study, powder samples manufactured by a solid-phase method including milling process and by a sort of gas-phase synthesis were classified to examine the inhomogeneity of chemical composition depending on particle size, as well as to investigate the influence on sintering behavior and the microstructure of sintered bodies.

2. Experimental Method

The following two kinds of silicon carbide were used: Powder L (Showa Denko) and M (Mitsui Toatsu Chemicals, MSC-20). The former was obtained by milling after a solid-phase reaction between metallic silicon and carbon black,[6] while the latter was synthesized from silicon tetrachloride and a heavy oil.[7,8] They were dispersed in distilled water for centrifugal classification. The classified powder materials were further subjected to decarbonation and acid cleaning (decarbonation) to prepare 8 kinds of powder as shown in Table 1. The powders LF, LC, MF, and MC were fine powder components (F) and coarse powder components (C) after classifying the powders L and M. The powders LFD, LCD, MFD, and MCD were obtained by the decarbonation of the classified powder. The decarbonation was conducted in air at 650°C for 2 hours. In the acid cleaning, hydrofluoric acid (10%) was used to dissolve silica while agitating the powders at room temperature, followed by rinsing thoroughly with distilled water. They were fully dried at 150°C under vacuum.

Phenol resin (as Carbon source, Showa Polymer, 6.2wt%) and amorphous boron (H. C. Starck, 0.37wt%) were added to the powder samples, mixed with a ball

Table 1. Characteristics of original and classified powders.

	Specific surface area / $m^2 \cdot g^{-1}$	Free carbon content / wt%	Oxygen content / wt%	Free SiO_2 content / wt%	Particle size / μm a*1	Particle size / μm b*2	Metallic impurity / ppm Al	Fe	total
L	17.9	0.80	0.84	0.27	0.10	0.05-1.00	19	57	141
M	20.2	0.28	0.89	0.26	0.09	0.08-0.45	20	116	229
LF	29.6	2.33	2.48	0.88	0.06	0.06-0.27			
LC	11.5	0.46	0.61	0.21	0.16	0.15-1.05			
LFD	31.4	1.42	1.13	0.16	0.06	0.06-0.26			
LCD	10.1	0.23	0.30	0.06	0.19	0.15-1.10			
MF	22.6	0.52	1.52	0.49	0.08	0.06-0.28			
MC	14.4	0.25	0.80	0.25	0.13	0.13-0.45			
MFD	23.7	0.37	0.97	0.11	0.08	0.05-0.29			
MCD	12.2	0.23	0.72	0.09	0.15	0.18-0.43			

*1 calculated from specific surface area and theoretical density of SiC (3.21 $g \cdot cm^{-3}$).
*2 observed in SEM photographs.

mill in acetone for 40 hours and dried in a nitrogen gas flow and then under vacuum at 150°C. The mixed powder (5g) was sieved (60 mesh) for granulation, molded into compacts 40×9×9mm in size under a pressure of 5MPa, and CIP-ed at 500MPa. The green density was 1.96 - 2.02$g \cdot cm^{-3}$.

The shrinking rate of the green compacts was measured using the high-temperature dilatometer described in previous paper.[9] The measurement was carried out up to 2100°C (holding time: 60min) in an argon atmosphere (3.0MPa), with a heating rate of 5.0$K \cdot min^{-1}$ and a load of 10g. The bulk density and porosity of the sintered bodies obtained were measured by an Archimedean method. The microstructure were observed with a scanning electron microscope (SEM) (Model S-800, Hitachi, Ltd.). The crystalline phases were identified by powder X-ray diffractometry (XRD) (Model RAD-B, Rigaku Denki) with CuKα radiation at 30kV and 15mA. The amounts of polytypes of SiC were determined from the XRD intensity according to the method of Iseki et al.[10] In order to examine the microstructural difference during the sintering process, other samples were prepared at 1700°, 1800°, 1900°, and 2000°C (20s) for the same procedure. The cooling rate to 1300°C for these samples was 75$K \cdot min^{-1}$.

3. Results

3-1. Properties of Silicon Carbide Powder

Figure 1 shows the primary particle size distribution of silicon carbide powder before classification. In determining the primary particle size, the major axis (l) and minor axis (d) of 800 particles were measured after random sampling from SEM photos of powder particles to calculate two-axis average diameters ((l+d)/2). The powder L produced by the solid-phase method had a broad particle size distribution and contained many

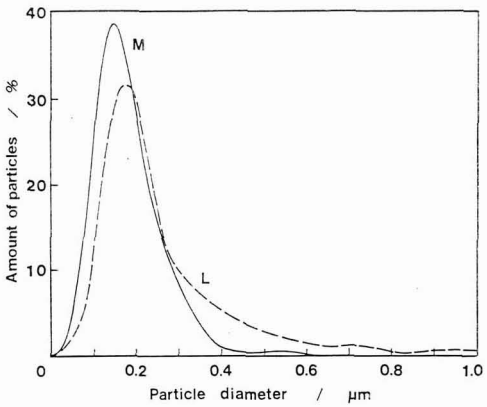

Fig. 1. Numerical size distribution of primary particles of unclassified silicon carbide powders.

coarse particles over 0.25μm in size. By contrast, that of the powder M was nearly a normal distribution, with most particles of less than 0.4μm.

The powder morphology was also affected by the synthesizing methods: the classified sample prepared from the powder L consisted of particles with indefinite shape, while that obtained from the powder M had particles with round shape close to spherical and ellipsoid. Decarbonated powders had almost the same particle diameter and morphology as classified powders before decarbonation. In the case of the powders LF, MF and MC as well as their decarbonated forms, the values of the sphere-equivalent diameters calculated from the specific surface area (Table 1) and the theoretical density of the silicon carbide (3.21$g \cdot cm^{-3}$) almost agreed with the particle sizes shown in the SEM photos

Fig. 2. SEM photographs of classified powders.

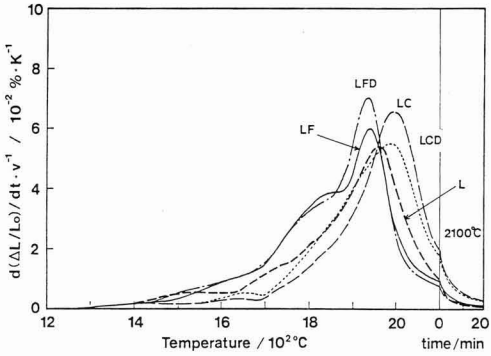

Fig. 3. Temperature dependence of shrinking rate for powder L and the derived powders. Additives: 6.2wt% phenol and 0.37wt% amorphous boron, Heating rate: 5K·min^{-1}, Atmosphere: Ar (0.3MPa), Gas flow rate: 500cm^3·min^{-1}, Load: 10g.

(Fig. 2). However, the particle sizes of the powders LC and LCD were considerably greater than the sphere-equivalent diameters. This indicates that the powders LC and LCD were composed of particles with many defects such as cracks.

Assuming that the specific surface area of the unclassified powder can be obtained by mixing fine and coarse powder components, the average volume and average surface area of the particles were calculated from the specific surface area of coarse and fine powder components presented in Table 1, and the proportions of the coarse powder components were computed as 9.67% and 9.68% for powders L and M respectively. Comparing these values with the particle size distribution in Fig. 1, the powder L is considered to be classified at a primary particle size of 0.47μm and the powder M at 0.28μm.

3-2. Temperature Dependence of Shrinking Rate

Figure 3 shows the temperature dependence of the shrinking rate of powders L and LF-LCD. The difference in green density among the specimens was as small as ±0.03g·cm^{-3} so that the shrinking rate provided a good way to compare sinterability. A distinct difference in shrinking behavior was detected between fine (LF and LFD) and coarse powder (LC and LCD) components. In spite of containing only 9.7% of a coarse powder component, the shrinking rate of the unclassified powder L decreased greatly compared with the powder LF. As in Fig. 2, when a sample contains particles as large as 5 times the primary particle size, sinterability is substantially lowered even if the content of coarse powder is low. In the comparison of the powder component LF with LFD, the shrinking rate became greater over 1850°-1950°C after decarbonation which reduced the amount of oxygen and free carbon. In the case of the coarse powder component, the powder LCD after decarbonation had also high sinterability at 1700-1950°C.

Figure 4 presents shrinking rate curves for the powders M and MF-MCD. It shows that among classified powders with a small difference in particle size, the difference between shrinking rate curves becomes small

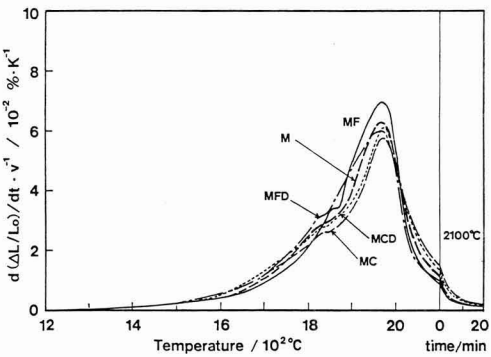

Fig. 4. Temperature dependence of shrinking rate for powder M and the derived powders. Additives: 6.2wt% phenol and 0.37wt% amorphous boron, Heating rate: 5K·min^{-1}, Gas flow rate: 500cm^3·min^{-1}, Atmosphere: Ar (0.3MPa), Load: 10g.

as well. As in Table 1 showing powder properties, only the powder MF contained much free carbon and oxygen. The others had quite a small difference between these values. This suggests that the difference in shrinking rate at 1800°-1900°C in the case of the powders MFD and MCD (and MC) strongly reflects only the influence of particle size. An increase in the shrinking rate of MF over 1850°C in the comparison of MF with MFD as well as the low shrinking rate of MF at less than that temperature is probably due to the effects of free carbon and oxygen.

3-3. Temperature Dependence of Bulk Density and Closed Porosity

Figure 5 gives the temperature dependence of bulk density and closed porosity for classified and decarbonated powder. In the case of the classified and decarbonated components of the powder L (Fig. 5 top), the densification of the fine powder components LF and LFD advanced rapidly over 1700°C, reaching a bulk density of 2.9-3.0g·cm^{-3} even at 2000°C. By contrast, that of the coarse components LC and LCD was slow, and the bulk density remained at 3.0g·cm^{-3} even after sintering at 2100°C for 60 minutes. The bulk density of the unclassified powder L was 3.14g·cm^{-3} (at 2100°C for 60 minutes) close to that of the fine powder component (3.15-3.17g·cm^{-3}). These results show a good agreement with the temperature dependence of the shrinking rate in Figs. 2 and 3.

In the classified and decarbonated components of the powder M (Fig. 5 bottom), little difference was detected in bulk density up to 1900°C. Nevertheless, at 2000°C, the bulk density increased in the order of MF > MFD > MC > MCD. This order means the positive influence of fine particle size and decarbonation on the sinterability.

The closed porosity of all the powder samples increased at 1900°-2000°C, and then decreased again as sintering proceeded. In the case of the powder components LC and LCD, closed pores once generated were hard to remove even after sintering at 2100°C for 60 minutes.

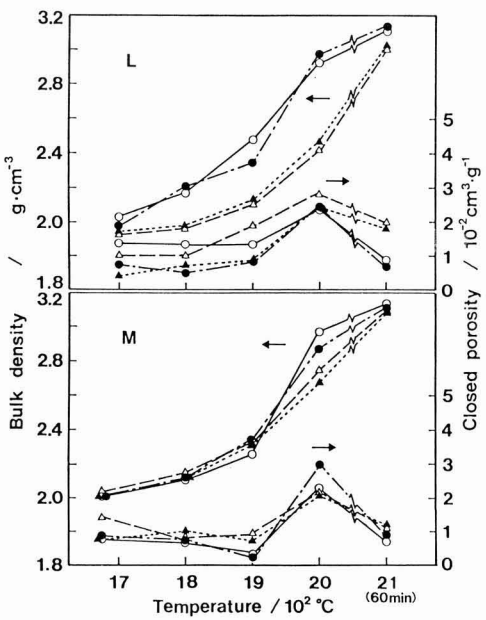

Fig. 5. Temperature dependence of bulk density and closed porosity.
○: LF, MF, △: LC, MC, ●: LFD, MFD, ▲: MCD, MCD

3-4. Microstructure and Crystalline Phases of Sintered Bodies

Figure 6 presents SEM photos of polished and etched surfaces of samples sintered at 2100°C for 60 minutes. There was a distinct difference in microstructures between the fine powder components (LF, LFD) and coarse powder components (LC, LCD) of the powder L, in contrast to the small difference in the case of the powder M. In the former four samples, numerous plate-like grains were generated especially in the coarse components. On the other hand, in the latter four, the number of plate-like grains was less than that of the former, and they grew by extension through shapeless grains.

Figures 7 and 8 show microstructural difference during sintering for samples prepared from the powders L and M. In the case of the powders LF and LFC, many plate-like grains were already formed at 2000°C, while in LC and LCD particles still remained indeterminate even at 2000°C. For the powders LC and LCD, plate-like grains grew rapidly in the course of densification over 2000°C. In the classified and decarbonated samples of the powder M, grain growth resulted in nearly spherical grains at 1900°C. These samples, at 2000°C, formed shapeless, dense structures containing relatively small amount of plate-like grains, the volume ratios of which were less than those of the powders LF or LFD.

Figure 9 shows the temperature dependence of the residual β-SiC content. Most of the α-SiC grains generated below 2000°C were 6H polytype. At 2100°C (60min), 15R and 4H polytypes appeared as well as 6H. The β-SiC content of the powder LF-LCD (Fig. 9 top) gradually decreased over 1700°C, dropping sharply at 2000°C in the fine powder component. As for coarse powder components, the decrease in the β-SiC content was greater in the decarbonated powder LCD. In the case of the powder MF-MFD (Fig. 9 bottom) almost no β→α transformation of silicon carbide was encountered below 1900°C, with a slight decrease in the β-SiC content of coarse powder components at 2000°C. After sintering at 2100°C, the β-SiC content of each sample decreased with that of the decarbonated powder less than that of the nondecarbonated. With regard to the powder LF-LCD, the plate-like grains were more likely to grow as the β-SiC content decreased. By contrast, the powder MF-MCD did not show such a distinct correlation.

4. Discussion

4-1. Relationship of Properties and Particle Diameter of Silicon Carbide Powder

As listed in Table 1, no substantial difference was detected between the characteristics of the unclassified powders L and M except for the amount of free carbon. The comparison of characteristics of classified powder shows notable differences in the amounts of free carbon and silica as well as oxygen content between fine and coarse powder components. Unreacted fine carbon is considered to remain in the powder L synthesized by solid-phase reactions. In this study, changes in proper-

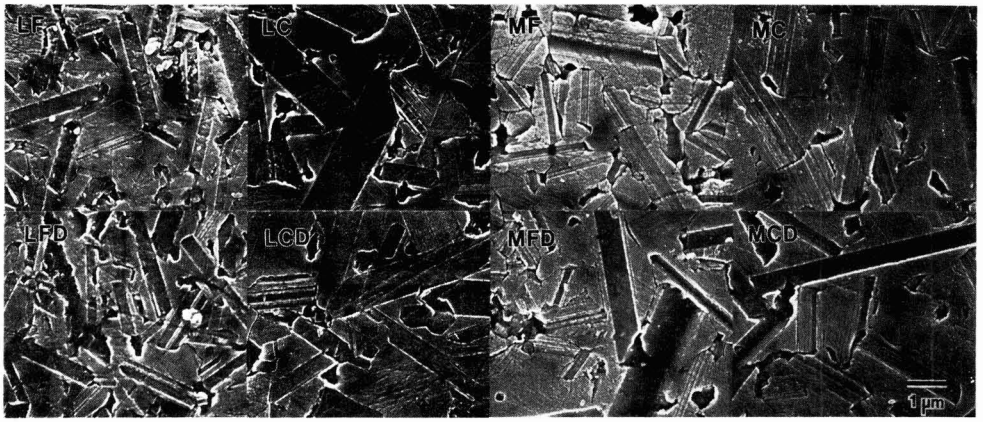

Fig. 6. Microstructure of sintered bodies prepared at 2100°C for 60min.

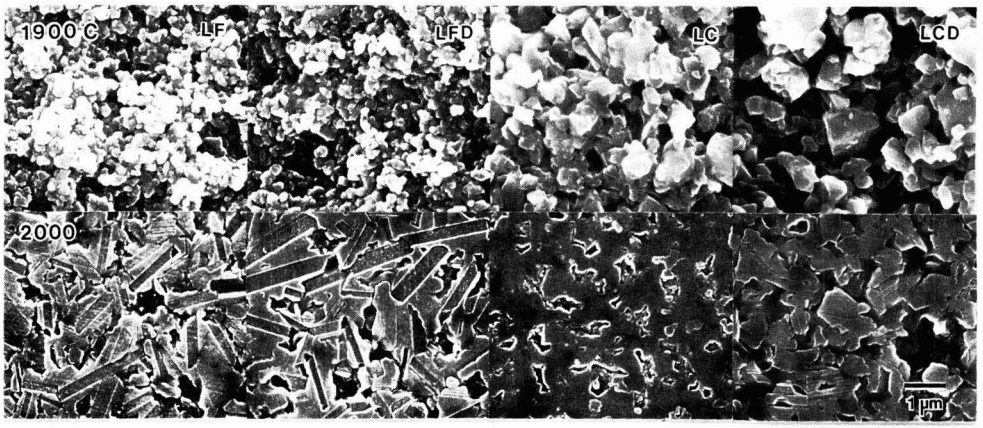

Fig. 7. Microstructure of sintered bodies for classified and decarbonated powders from powder L at 1900° and 2000°C.

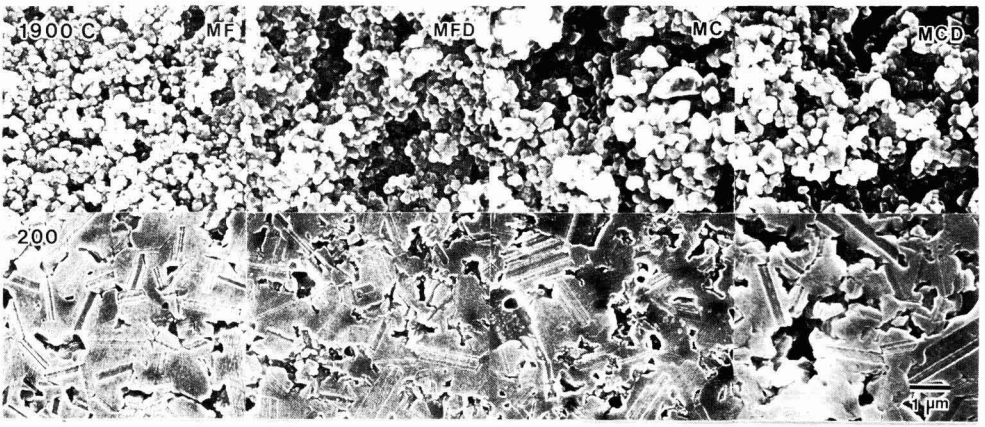

Fig. 8. Microstructure of sintered bodies for classified and decarbonated powders from powder M at 1900° and 2000°C.

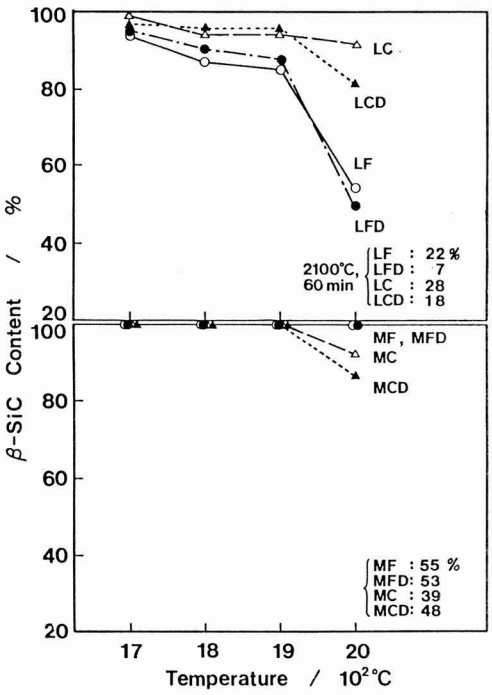

Fig. 9. Temperature dependence of beta-silicon carbide content.
○: LF, MF, △: LC, MC, ●: LFD, MFD, ▲: MCD, MCD.

ties were investigated with only two powder samples prepared by a solid-phase method and a gas-phase method. However, it is generally acceptable that the powder by the solid-phase method was liable to have an inhomogeneous composition depending on the particle size.

Table 1 also indicates that the oxygen content was high in fine powder components. It was expected that the powder L obtained by the solid-phase method where milling was one of the major production processes would show a remarkable decrease in oxygen content by decarbonation and acid treatment, whereas the powder M by the gas-phase method was not affected much by the same treatment, so that in the former an oxygen impurity present on the surface was easy to remove while in the latter it was mainly inside the particles. The amount of free silica was greatly decreased by decarbonation and acid treatment in both samples, suggesting that it was present on the powder surface. From the above results, the powder by the solid-phase method could be characterized not only by a broad particle size distribution and indefinite shape of particles but also by much unreacted carbon especially in fine powder components and oxygen on the surface. On the other hand, the powder by the gas-phase method had a similar particle size and roundish shape along with low free carbon content. The oxygen contained inside the powder particles as an impurity was hard to remove.

4-2. Relationship Between Powder Characteristics and Sintering Behavior

In the case of the powder L having fine and coarse powder components with great differences in particle size and composition, as in Fig. 3, a substantial difference was noticed in the sintering behavior between a classified sample and a decarbonated one. Because of the great difference in particle size between fine and coarse powder components, the powder L contained as much as 33% in volume of the coarse powder, even with a proportion of 9.7%. The great difference in particle size coupled with the high volume content of the coarse powder enhanced the decrease in the sinterability of the unclassified powder L compared with the fine powder component. In the powder M, a difference in particle size between fine and coarse powder components was about twice and the volume content of the coarse powder was 13%, which is considered to have resulted in a small difference in sinterability between powder samples.

In the comparison of shrinking rate curves between the powder L and M, their peak temperatures clearly shifted to higher temperatures with an increase in particle size in the order of LC, LCD > MF, MFD > = MC, MCD > LF, LFD. Especially, the shift in peak temperature was remarkable for the powders LC and LCD. The sinterability was considered to show a substantial decrease when the primary particle size increased more than 0.5μm.

The fine powder components of the powder L was characterized by a high shrinking rate in the range of 1700°-1850°C. The shrinking rate curve of the powder MF-MFD with smaller primary particle sizes than that of the powder LC and LCD had a region at 1800°-1850°C where the shrinking rate was high. This trend was more notable in the powder containing much free carbon and oxygen. It is generally believed that in sintering silicon carbide with boron and carbon, the presence of oxygen (silica) in a powder material reduces its sinterability by the generation of carbon dioxide, etc. Consequently, this high shrinking rate at low temperatures can be interpreted as the powder containing much free carbon which also acts as a sintering aid. To confirm this point, 10wt% of phenol resin and 0.4% of amorphous boron was added to the powder M, and the shrinking rate was measured under the same conditions as in Fig. 4. Figure 10 shows the shrinking rate curve obtained. It resembles the shrinking behavior of the powders LF and LFD (Fig. 3) rather than the powder M (Fig. 4). It is clear that a high carbon content increased the shrinking rate at temperatures below 1800°C.

Decarbonation and acid treatment leads to a decrease in oxygen content as well as free carbon content, so that no distinct trend was detected in the effect of oxygen on the shrinking rate. However, the poor sinterability of the powder LC than that of LCD will be caused by impurity oxygen.

In the comparison of microstructures with shrinking rate curves, the sintering processes of the powders LF, LFD, and MF-MCD at relatively low temperatures below 1900°C were not accompanied by the growth of plate-like grains and generated little α-SiC. The shrinking rate curves of these samples show that the sintering

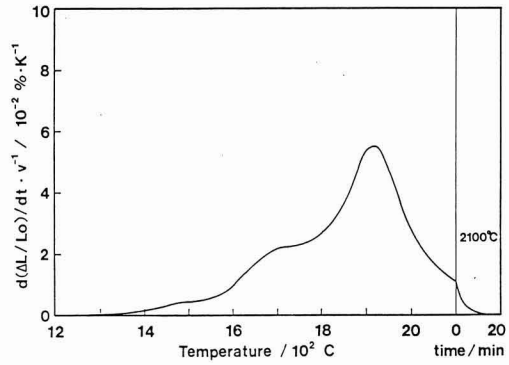

Fig. 10. Temperature dependence of shrinking rate of powder M with 10wt% phenol and 0.4wt% amorphous boron.
Heating rate: 5K·min^{-1}, Atmosphere: Ar (0.3MPa), Gas flow rate: 500cm^3·min^{-1}, Load: 10g.

proceeds through two characteristic stages below and over 1850°C. The first sintering stage at low temperature was accompanied by equiaxial grain growth, and densification was substantially promoted by a high content of free or added carbon. The second sintering stage at high temperature indicates densification with the growth of plate-like grains, and the shrinking rate is considered to increase in the case of high carbon content. However, if the shrinking much progressed in the first sintering stage, the shrinkage in the second stage naturally becomes smaller, so that the shrinking rate is apparently lowered. This shrinking behavior with two stages is probably caused by the mechanism of densification advancing in the first sintering stage, particle diameter becoming larger and the particle shape changing from equiaxial (indeterminate) to plate-like, thus controlling the rate of mass transfer required for densification. At higher temperatures, even such conditions are considered to allow sufficient mass transfer to regain the shrinking rate. In the case where a sample has large particle size and relatively low shrinking rate in the first sintering stage such as the powders LC and LCD, only a single peak appeared in the shrinking rate curve.

No significant correlation was detected between the shrinking behavior stated above and $\beta \rightarrow \alpha$ transformation of silicon carbide. Hase et al. reported that plate-like grains include not only various polytypes of α-SiC but also β-SiC, which confirms the lack of a correlation.[11]

As has been described above, the sintering of silicon carbide proceeds with the effect of inhomogeneous composition depending on particle size as well as particle size itself. In the case where boron and carbon were added, free carbon contained mainly in the fine powder component acted as a sintering aid to promote densification, while the use of other sintering aids such as alumina may reduce sinterability instead. Additionally, if the sinterability of the powder changes according to particle size, boron-carbon aids are predicted to harm the microstructural homogeneity of sintered bodies. Hence, it will be necessary to pay attention to powder characteristics of the fine powder component, especially the homogeneity of composition, as well as the reduction of coarse powder content.

Acknowledgments

The authors wish to thank Mr. A. Tsuge, Chemical Dept., Government Industrial Research Institute, Nagoya, for his assistance in the measurement of free carbon content and others. This study was conducted as part of the R & D Project of Basic Technology for Future Industries, Ministry of Industrial Trade and Industry.

References:

1) K. Kobayashi, K. Kishi, S. Umebayashi and K. Miyazaki, Proc. 1st. Int. Symp. on Ceram. Components for Engines, 449 - 456 (1983).
2) H. Suzuki and K. Kijima, ibid., p. 490 - 504.
3) W.D. Boecker, C.H. McMaurty, S.G. Seshadri and M. Srinivsan, Proc. 2nd. Int. Symp. on Ceram. Mater. and Components for Engines p. 697 - 712 (1986).
4) O. Abe, M. Yamamoto, Y. Samejima and T. Sugeno, "Fine Ceramics - Jisedai-Kenkyu-no-Ayumi," Edited by Engineering Research Association for High Performance Ceramics, 426-440 (1988).
5) O. Abe, M. Yamamoto, M. Ohashi, T. Nagaoka, and S. Kanzaki, Reports of the Governmental Industrial Research Institute, Nagoya, 37, 247 - 255 (1988).
6) M. Yamamoto, Preprint for 3rd Symp. of Jisedai R & D Project (Fine Ceramics) 1 - 11 (1985).
7) S. Aoki, A. Hagimura, H. Miyashita, M. Nakajima and N. Murakawa, "Sintering '87," ed. by S. Somiya, M. Shimada, M. Yoshimura and R. Watanabe, Elsevier Sci. Plublishers, London, 1070 - 1075 (1987).
8) N. Murakawa, N. Nakajima, N. Maruyama, K. Isogaya and K. Yoshida, "High Tech Ceramics," ed. by P. Vincenzini, Elsevier Sci. Publishers, London, 501 - 509 (1987).
9) O. Abe and S. Kanzaki, Seramikkusu Ronbun-Shi, 97, 187-191 (1989).
10) T. Maruyama, H. Kitamura, and T. Iseki, Yogyo-Kyokai-Shi, 94, 790 - 794 (1986).
11) T. Hase, T. Egashira, T. Iseki, and H. Suzuki, Yogyo-Kyokai-Shi, 88, 106 - 107 (1980).

This article is a full translation of the article which appeared in Nippon Seramikkusu Kyokai Gakujutsu Ronbunshi (Japanese version), Vol.97, No.8, 1989.

Effect of Fluoride Addition on Crystal Growth of MgO

Mitsuo Shimbo, Zenbe-e Nakagawa, Yutaka Ohya and Kenya Hamano*

Research Laboratory of Engineering Materials, Tokyo Institute of Technology
4259, Nagatsuta, Midori-ku, Yokohama 227, Japan
* Faculty of Engineering, Kanagawa University
3-27-1, Rokkakubashi, Kanagawa-ku, Yokohama 221, Japan

Crystal growth of MgO doped with AlF_3 and MgF_2 has been studied by BET method and X-ray powder diffractometry. The fluorides were hydrolyzed by the water contained in MgO powder above 500°C and generated HF gas, which was adsorbed on the surface of MgO. Fluorides inhibited crystal growth of MgO below 900°C, but accelerated the growth above 1000°C, because of evaporation of adsorbed HF. Departure of HF from the surface increases the surface energy of MgO and/or forms active points on the surface, and then migration of MgO between grains, mainly through evaporation and condensation, is promoted and would result in rapid crystal growth. MgF_2 crystallized again at 1000°C for MgO doped with MgF_2 in dry air.

The HF coverage of MgO grains in a specimen containing 2 mol% MgF_2 (evaluated as monolayer) was constant up to 1000°C and decreased above 1100°C. It was inferred that crystal growth of MgO proceeded so as to maintain the balance of surface energy for the evaporation of HF from the surface at 1000°C and that the crystal growth couldn't follow because of the rapid evaporation of HF above 1100°C.

[Received April 6, 1989; Accepted May 16, 1989]

Key-words: MgO, Crystal growth, Fluorine addition, HF adsorption, HF coverage

1. Introduction

Negative ion, in contrast to positive ion, can be dispersed in air by decomposition and evaporation during heating. Taking advantage of these properties, a sintered body with high density and purity was produced, using halogen ion, a representative negative ion, as the calcining agent of MgO.[1]

Ikegami et al.[2,3] reported that, in the calcination of $Mg(OH)_2$ powder treated with hydrochloric acid or hydrofluoric acid solution, Cl^- promotes the crystal growth of MgO powder, F^- inhibits the crystal growth below 900°C and promotes it above 1000°C and F^- has a promotion effect on sintering. Hamano et al. investigated the nature and sintering properties of $Mg(OH)_2$ calcined powder doped with various chemical compounds, and found that $CaCl_2$[4] promotes periclase crystal growth during calcination and the early stage of sintering, CaF_2[4] promotes MgO sintering in a low temperature range according to decomposition and $MgCl_2$[5] causes the materials to lose relics of $Mg(OH)_2$ during calcination, forming round periclase grains and results in the promotion of sintering.

The authors have reported that, when $Mg(OH)_2$ powder is doped with AlF_3 or treated with fluoric acid, HF is absorbed on the surface of $Mg(OH)_2$ and the thermal decomposition is retarded.[6] In the present work, the effect of fluoride after the decomposition of $Mg(OH)_2$ was investigated, in other words, the effect of fluoride addition on the crystal growth of MgO. MgO powder prepared by the calcination of Mg(OH) was used as the starting material, and fluoride was added. In the previous report, it was clear that the vapor was related to fluoride decomposition,[6] so the experiments were performed under controlled partial vapor pressure to examine the effect of the amount of fluoride added.

2. Experimental Method

The $Mg(OH)_2$ and fluoride were the same as used in the previous report. MgO powder was produced from $Mg(OH)_2$ by calcining for an hour at 500°C and stored in a dryer at 150°C to prevent absorption of water vapor. MgF_2 or AlF_3 was added at 2 mol% to the MgO and wet mixed in a resin ball mill with ethanol for 4 hours.

A sample (3g) was put into a platinum boat and heated in a horizontal pipe type furnace, in an air flow of 150 ml/min at a heating rate of 6°C/min up to the required temperature (500°C - 1200°C) and retained at this temperature for an hour. The partial vapor pressure in air was controlled from the pressure under a liquid nitrogen trap (dew point −196°C) to around 100mmHg. The resultant powder was stored in a desiccator containing P_2O_5 as drying agent after the furnace was cooled.

Another sample was also made using $Mg(OH)_2$ instead of MgO. In this case the specimen was heated at 500°C - 1100°C for an hour.

The quantitative analysis of the crystalline phase, crystallite size and lattice constant of periclase in the heated specimen was performed by X-ray powder diffraction using CuKα radiation (Rigaku Denki RU-200). The crystallite size was obtained from the 420 diffraction line, using electromelted magnesia powder as a reference. The specific surface area of specimens was obtained by the BET method using nitrogen gas, and the calcined powders were observed with a transmission type electron microscope (TEM) (JEOL Ltd. JEM-2000EX). The analysis of the fluorine content was obtained using alizarin complex absorptiometry.

Table 1. Crystalline phases of calcined $Mg(OH)_2$ with and without fluorides.

Temp.(°C)	No add.	MgF_2 add.	AlF_3 add.
500	P	P	P
600	〃	〃	〃
700	〃	〃	〃,C**
900	〃	〃	〃,SP*,C**
1000	〃	〃	〃,SP*,MgF_2*
1100	〃	〃,MgF_2**	〃,SP

P : MgO * weak peak
C : α-Al_2O_3 ** very weak peak
SP : $MgAl_2O_4$

Table 2. Effect of water vapor pressure of calcined MgO with MgF_2.

Temp. (°C)	P_{H2O} (mmHg) 0	20	100
500		P,MgF_2**	P
800	P	P	〃
900	〃	〃	〃
1000	〃,MgF_2**	〃	〃
1100	〃,MgF_2**	〃	〃
1200	〃,MgF_2**	〃	

** very weak peak

Table 3. Effect of water vapor pressure of calcined MgO with AlF_3.

Temp. (°C)	P_{H2O} (mmHg) 0	20	100
500			P
800	P,C**	P,C**	P
900	〃,SP**	〃,SP**	P,SP**
1000	〃,SP*,MgF_2*	〃,SP*	〃,SP*
1100	〃,SP*,MgF_2	〃,SP*	〃,SP*
1200	〃,SP*,MgF_2	〃,SP*	

C : α-Al_2O_3 * weak peak
SP : $MgAl_2O_4$ ** very weak peak

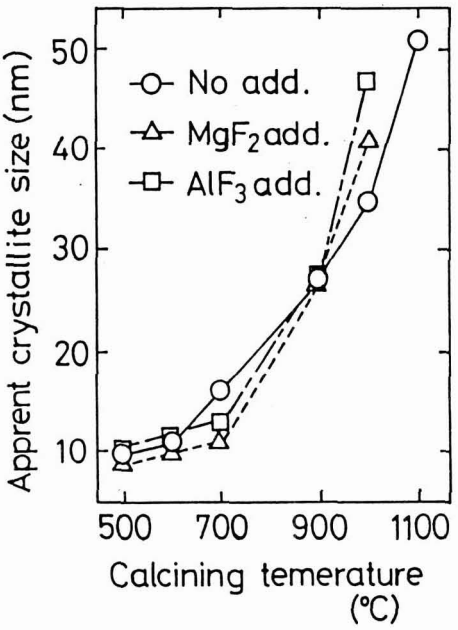

Fig. 1. Apparent crystalline size of fluoride added MgO calcined for 1hr. in air.

3. Results and Discussion

3-1. Thermal Change of $Mg(OH)_2$ Containing Fluoride

The crystalline phases of each specimen are shown in Table 1. The main crystalline phase was periclase, and no fluoride was detected at 500°C in the specimen with fluoride added. Corundum and spinel were generated above 700°C in the specimens containing AlF_3. A small amount of MgF_2 was detected when the specimen containing MgF_2 was heated at 1100°C, and when the specimen containing AlF_3 was heated at 1000°C. The authors previously reported that when MgF_2 or AlF_3 is hydrolyzed, an amorphous or poorly-crystallized decomposition product and HF gas are formed by the effect of vapor generated from the thermal decomposition of $Mg(OH)_2$. It is inferred that in the present work the HF gas generated was adsorbed on the grain surface of MgO. The adsorbed fluorine was segregated at high temperature, a Mg-F crystalline lattice formed and the MgF_2 detected by X-ray diffraction.

The change in crystallite size of periclase according to the heating temperature is shown in Fig. 1. The crystallite size of the specimen containing fluoride was smaller than that without fluoride at 700°C, but the specimen containing fluoride had a considerably larger crystallite size above 1000°C.

3-2. Properties of MgO Containing Fluoride

3-2-1. Effect of Vapor

The changes in the crystalline phase of the heated specimen with the partial vapor pressure are shown in Table 2 (with MgF_2 added) and in Table 3 (with AlF_3

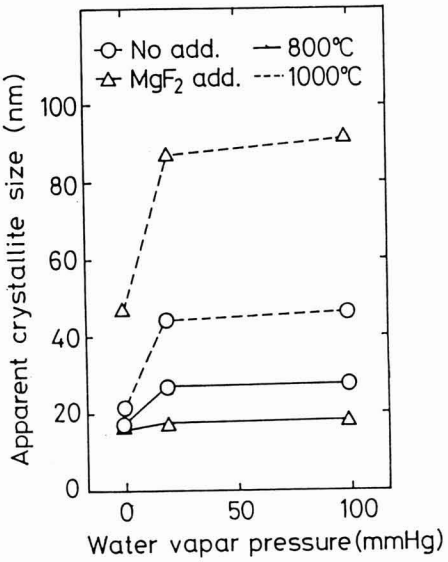

Fig. 2. Water vapor pressure and apparent crystallite size of MgO calcined in air flow.

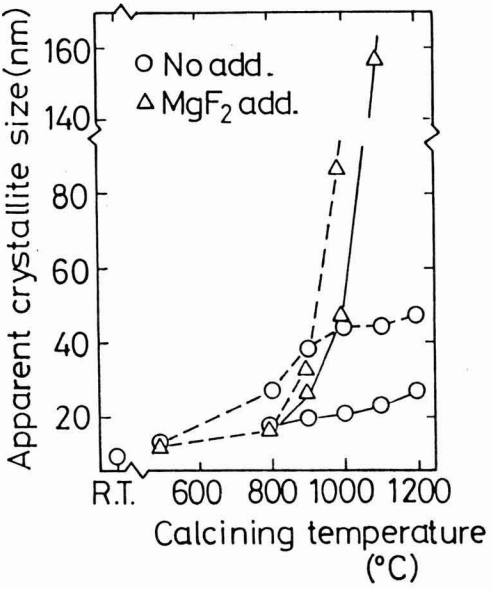

Fig. 3. Apparent crystallite size of MgO with and without MgF_2 calcined in air flow.
—— : dehydrated by liquid nitrogen
------ : wet air (PH_2O = 20mmHg)

added).

A small amount of MgF_2 was detected in the specimen heated under a partial vapor pressure of 20mmHg at 500°C and in the specimen heated in dry air above 1000°C. The hydrolysis of MgF_2 proceeded insufficiently at a partial vapor pressure below 20mmHg at 500°C. When the specimen was heated in dry air at 800°C and 900°C, MgF_2 was not detected, periclase was single phase and the added MgF_2 decomposed. When MgO powder without additive was heated in air up to 700°C, it decreased in weight by 4.2%. The decrease is thought to be due to the evaporation of water contained in the MgO powder. As the amount of vapor produced is about 4 times as large as the water required to hydrolyze the added MgF_2, the MgF_2 is thought to be completely hydrolyzed by this vapor. It is inferred that the HF gas generated by the decomposition of MgF_2 was chemically adsorbed on the surface of the MgO grains. Because fluorine tends to concentrate on the surface,[7] MgF_2 is formed by the concentrated fluorine at about 1000°C. There was no change in the IR and ESCA spectra with different heating temperatures, so no information about bonding was obtained.

In the specimen containing AlF_3, the main crystalline phase was periclase, MgF_2 detected in dry air above 1000°C, corundum detected in the specimen under a partial vapor pressure below 20mmHg at 800°C and spinel detected in the specimen heated above 900°C. AlF_3 was not detected in any case. It has been shown that AlF_3 is hydrolyzed easily by vapor at 500°C,[6] so AlF_3 was hydrolyzed by the water vaporized from the MgO powder during heating. Judging from the above results, in any case of MgF_2 addition or AlF_3 addition, HF gas generated by the decomposition of fluoride was adsorbed chemically on the surface of the MgO grains and the MgF_2 deposited above 1000°C. Presumably the effect of HF on the crystal growth of MgO can be examined by the study of MgF_2 addition and so experiments continued on this sample.

The effect of partial vapor pressure in air at 800°C and 1000°C on the periclase crystal growth is shown in Fig. 2. In the range from dry air to a partial vapor pressure of 20mmHg, the crystallite size in all specimens became larger, and was almost constant above 20mmHg. Judging from these data, the effect of vapor was complete at 20mmHg. In the following experiments, the effect on crystal growth in dry air and at partial vapor pressure 20mmHg (vapor air) was studied. The crystallite size of MgO heated in dry air and in wet air is shown in Fig. 3. Regarding the specimens heated in dry air above 800°C, the specimen with MgF_2 added had a larger crystallite size than that with no addition. Regarding the specimens heated in wet air below 900°C the specimen with MgF_2 added had a smaller crystallite size than that with no addition. Regarding the specimens heated in wet air above 1000°C, the specimen with MgF_2 added had, on the contrary, a larger crystallite size than that with no addition. The micrographs of the specimens heated in wet air are shown in Fig. 4. The specimen heated at 800°C remains as in the original

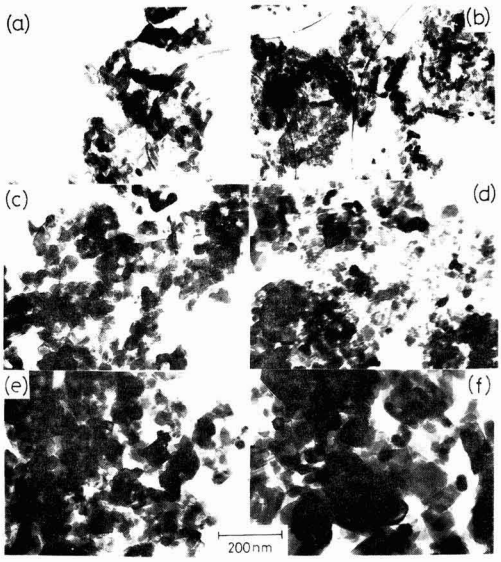

Fig. 4. TEM photographs of calcined materials in wet air flow.
(a) No add. 800°C, (b) MgF_2 add. 800°C
(c) No add. 900°C, (d) MgF_2 add. 900°C
(e) No add. 1000°C, (f) MgF_2 add. 1000°C

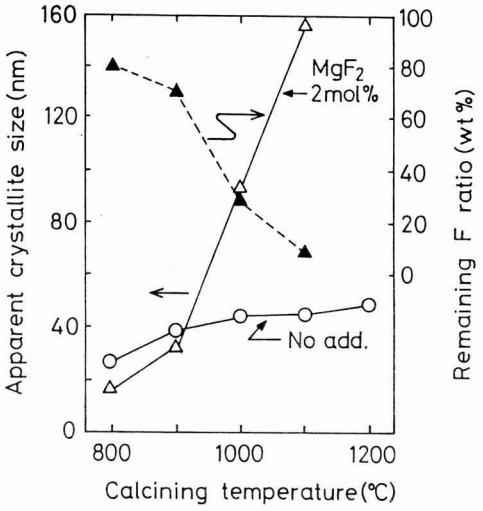

Fig. 5. Remaining fluorine and apparent crystallite sizes of calcined MgO.

image, the size of primary grain with MgF_2 added is 10 - 20nm and the one with no addition is 20 - 30nm. At 900°C, both specimens formed aggregates of primary grains of the same size. At 1000°C the specimen with MgF_2 added had round primary grains of 50 - 150nm and the specimen with no addition was the same as that at 900°C. The aggregates were observed to become smaller with the addition of MgF_2. Judging from above results, the crystal growth of MgO is promoted by vapor, checked below 800°C with added fluoride, but promoted above 1000°C and the aggregates of grains becomes smaller.

Analyzing the fluorine amount remaining in the powder after the specimen containing MgF_2 was heated in wet air, the relationship between the remaining fluorine and crystallite size is shown in Fig. 5. The ratio of remaining fluorine plotted on the vertical axis is based on the amount of fluorine originally added to MgF_2 being 100%. At 800 - 900°C the remaining fluorine decreased from 80 to 70%. The crystallite size became a little larger but smaller compared to that with no addition. Above 900°C the amount of fluorine decreased rapidly at the same time as crystallite size became larger with an increase in temperature. However, the crystal growth according to the temperature rise in the specimen with no addition was small.

The fact that the periclase crystal growth was checked by adsorption of HF is due to the following causes. The chemical adsorption of HF gas on the MgO grain surface was concentrated on Mg^{2+} which is highly electro-negative. The ionic diffusion coefficient in single crystal MgO at 1500°C for Mg^{2+} is $3.4\times10^{-10}cm^2/s$, and for O^{2-} is $5.1\times10^{-14}cm^2/s$.[8] However, the surface diffusion coefficient is $9.8\times10^{-10}cm^2/s$. There is a rapid diffusion on the surface. Because the diffusion on the MgO surface is checked by adsorption of HF, migration decreases to check MgO crystal growth. Related to the above, because HF with a strong bond is adsorbed in Mg^{2+}, the surface energy of the MgO grain decreases and thus helps to check periclase crystal growth.

The powder calcined above 1000°C has, if there is no addition, strong aggregates, if MgF_2 is added, weak aggregates and is easily fractured. This means that the calcined powder has, if MgF_2 is added, a small contact area between the grains. Because above 1000°C MgO crystal growth did not proceed if there was no additive and it proceeded rapidly if MgF_2 was added, there was no strong correlation between the crystal growth and the strength of contact between the grains. Accordingly, it is unlikely that MgO crystal growth is only caused by surface diffusion, so we suppose that there is another transport through the vapor phase than through surface diffusion. This suggestion is supported by the following observations. The MgO vapor pressure at 1300°C is comparatively high, about 10^{-15} atm[10] and evaporation/condensation on the MgO surface contributes to MgO crystal growth.[11] If MgF_2 is added, the fact that MgO crystal growth is promoted considerably above 1000°C is due to the following. When the temperature increases to the co-melting point of MgO and MgF_2 (1214°C)[12], HF adsorbed on the MgO surface is liable to evaporate. When HF is evaporated the MgO surface energy is increased rapidly or active points are generated. By this change MgO is evaporated alone or with HF, so the migration between grains is promoted and rapid crystal growth occurs.

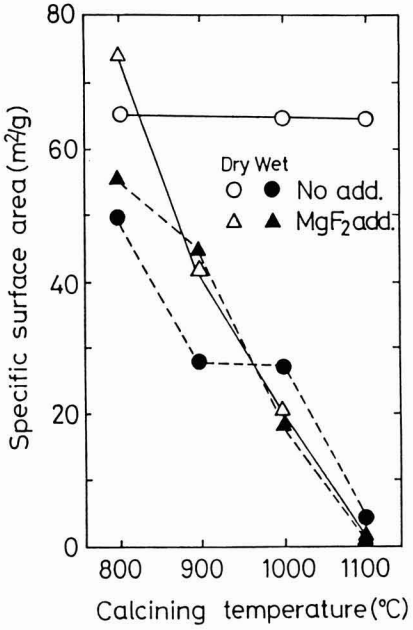

Fig. 6. Specific surface area of calcined materials.

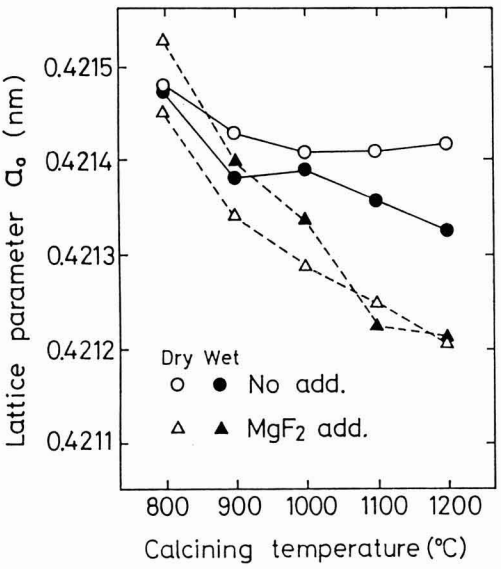

Fig. 7. Water vapor pressure and lattice parameters of MgO with and without fluorides.

Table 4.Grain size ratio of calcined materials.

	No add.		MgF_2 add.	
Calcining temp.(°C)	800	1000	800	1000
Part.size/Cryst.size	1.26	1.41	1.76	1.07

Part.size : evaluated from surface area
Cryst.size : measured using X-ray diffractometry

3-2-2. Specific Surface Area and Lattice Parameter

The specific surface area of the heated powders is shown in Fig. 6. When a specimen with no additive was heated in dry air, the specific surface area did little change. When it was heated in wet air, the specific surface area decreased remarkably with an increase in temperature. Regarding the specimen with fluoride added, the specimen heated in dry air at 800°C had a larger specific surface area than that heated in wet air. Both specimens had almost same specific surface area above 800°C. The ratio of the grain size obtained from the specific surface area of specimen heated in wet air to the crystallite size obtained from X-ray diffraction is shown in Table 4. This value represents the degree of aggregation of MgO powder and compaction during heating. At 800°C the specimen with MgF_2 added had larger value than that with no addition, but at 1000°C the specimen with MgF_2 added had a smaller value. These data shows that when MgF_2 was added, the specimen was MgO powder with strong aggregation at 800°C and that above 1000°C the crystal growth occurred and the specimen was MgO powder with weak aggregation. Lattice parameter of periclase in each heated powder is shown in Fig. 7. The periclase with MgF_2 added had a larger value than the one with no addition below 900°C, but above 1000°C the periclase with MgF_2 added had a smaller value than that with no addition and at 1200°C both periclases in dry air and in wet air had the value of about 0.42112nm reported in the literature.[13] In other words MgO crystal growth was promoted by the desorption of HF, and then MgO could be obtained with high crystallinity.

3-3. Effect of Amount of Additive

The effect of the amount of MgF_2 added, was investigated by changing the amount from 0.1 mol% to 8 mol% and after heating the specimen in wet air in the range from 800°C to 1100°C, the change in crystallite size of MgO was measured. The main crystalline phase was periclase. When the amount of MgF_2 was above 4 mol% at 900°C and 1000°C, a small amount of MgF_2 was detected. The relationship between the amount added and the crystallite size is shown in Fig. 8. At 800°C, the specimen with no additive had the largest value of crystallite size and the value decreased with an increase in the amount of additive. At 900°C, when 0.1 mol% was added, the crystallite size decreased rapidly, when

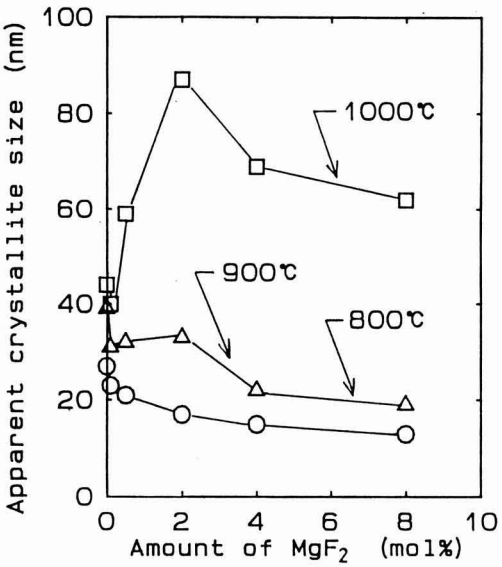

Fig. 8. Amount of magnesium fluoride addition and apparent crystallite sizes of calcined materials.

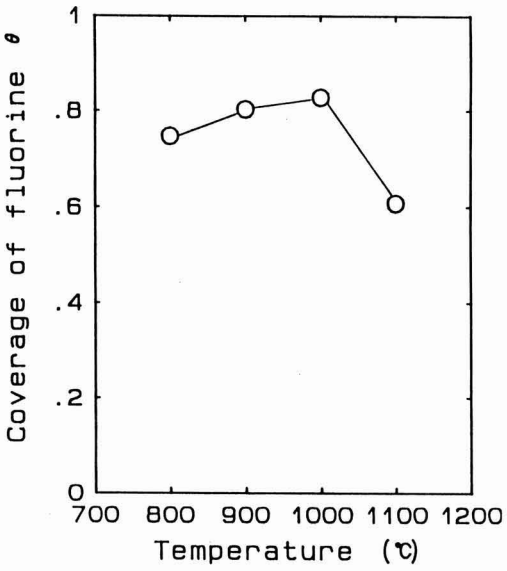

Fig. 9. Coverage of hydrogen fluoride of calcined MgO in wet air flow.

0.1 - 2 mol% was added, the crystallite size became almost constant and when above 2 mol% was added, crystallite size decreased with an increase in the amount of additive. At 1000°C, when 0 - 2 mol% was added the crystallite size increased, and when more was added, the crystallite size decreased. As mentioned in the previous paragraph, when HF was adsorbed on the surface of MgO, the crystal growth was checked and when HF was desorbed from the MgO surface, the crystal growth was promoted. At 800°C, more HF was adsorbed with an increase in the additive and the crystal growth were inhibited strongly. At 1000°C, the desorption of HF became rapid, so crystal growth was promoted. At 1000°C, when the amount of additive was above 4 mol%, because the amount of remaining HF was large, crystal growth was checked.

3-4. HF Coverage and Crystal Growth

In order to clarify the relationship between MgO crystal growth and the adsorption of HF, the HF coverage from the adsorbed amount was estimated and the change with heating temperature was investigated. When HF was adsorbed on Mg^{2+} in the MgO surface and formed a monolayer, the expression below relates the specific surface area, S(m^2/g) of MgO (a_0 = 0.42112nm), and the remaining fluorine in MgO, x_0 (wt%),

$$x_0 = 3.56 \times 10^{-2} S \text{ (where coverage } \theta = 1) \quad \ldots\ldots (1)$$

The coverage was obtained, using the actual fluorine contents x (wt%) by Eq.(2).

$$\theta = x / x_0 \quad \ldots\ldots (2)$$

Substituting Eq.(1) into Eq.(2),

$$\theta = x / (3.56 \times 10^{-2} S) \quad \ldots\ldots (3)$$

The specific surface area of MgO powder heated in wet air with 2 mol% MgF_2 and the value of chemical analysis of fluorine were substituted into Eq.(3) to obtain coverage θ. The result is shown in Fig. 9. The coverage is almost constant below 1000°C, and decreases at 1100°C. Because MgO surface energy is increased rapidly and MgO becomes unstable by evaporation of HF up to 1000°C, crystal growth proceeds with desorption of HF, in order to maintain the HF coverage constant, in other words, to retain the balance of MgO surface energy. At 1100°C HF is desorbed rapidly and the coverage decreases because crystal growth can not follow to maintain it constant. This could inhibit the promotion effect of crystal growth of HF.

4. Conclusions

The outline of the effect of fluoride addition on MgO crystal growth is as follows:

1) The added fluoride was hydrolyzed, with the evaporation of water contained in the MgO powder. The HF gas generated was adsorbed on the surface of the MgO

grain.

2) MgO crystal growth proceeds more rapidly in wet air, partial vapor pressure 20mmHg, than in dry air. Even if the partial vapor pressure was increased, moreover there was no change.

3) When fluoride was added to MgO, below 900°C the MgO crystal growth was checked by the adsorption of HF, above 900°C the crystal growth was promoted with an increase in HF desorption. Presumably the promotion of crystal growth was due to the evaporation/condensation process through the increase in surface energy of MgO.

4) Regarding the shape of the MgO grains, the specimen with no additive had aggregates of primary grains. When the specimen containing MgF_2 was heated above 1000°C, primary grains with little aggregation were obtained.

5) Regarding the effect of added MgF_2, below 900°C the crystal growth is checked with an increase in additive, at 1000°C crystal growth was promoted when the addition was below 2 mol%, but when the addition is above 4 mol%, crystal growth was checked with an increase in additive.

6) The coverage by fluorine of MgO grain with 2 mol% MgF_2 was constant up to 1000°C and decreased above 1000°C.

Acknowledgments

We thank Mr. T. Sato, Analysis Center Co. for the chemical analysis of fluorine. We thank Dr. N. Asaga, Daimon Research Lab., Inorganic Materials Dept., faculty of Engineering, Tokyo Institute of Technology, who gave us useful advice about the measurement of specific surface area.

References:

1) K. Hamano, Refractory, 37, 124 - 34 (1985).
2) T. Ikegami, S. Matsuda and H. Suzuki, Ceramics Japan, 86, 97 - 101 (1978).
3) T. Ikegami, M. Tsutsumi, S. Matsuda, S. Shirasaki and H. Suzuki, J. Appl. Phys., 49, 4238 - 41 (1978).
4) K. Hamano, K. Muroyama, Z. Nakagawa and K. Saito, Ceramics Japan, 87, 474 - 82 (1979).
5) K. Hamano, Z. Nakagawa and H. Watanabe, "Structure and Properties of MgO and Al_2O_3 Ceramics", Advances in Ceramics, Vol. 10, Edited by W.D. Kingery, American Ceramic Soc. (1984), pp. 610 - 18.
6) M. Shimbo, Y. Ooya, Z. Nakagawa and K. Hamano Ceramics Japan, 97, 640 - 44 (1989).
7) W.C. Jhonson, D.F. Stein and R.W. Rice, J. Am. Ceram. Soc., 57, 342 - 44 (1974).
8) Chemical Society of Japan, "Inorganic Reaction of Solid," Academic Publish Center (1975), pp. 46.
9) J. Henney and J.W.S. Johnes, J. Mat. Sci., 3, 158 - 64 (1968)
10) V.L.K. Lou, T.E. Mitchell and A.H. Heuer, J. Am. Ceram. Soc., 68, 49 - 58 (1985).
11) Y. Kotera, T. Saito and M. Terada, Bull. Chem. Soc. Jap. 36, 195 - 99 (1963).
12) W. Hinz and P.O. Kunth, Am. Mineral., 45, 1198 - 210 (1960).
13) Fine Ceramics Dictionary Compilation Commission, "Fine Ceramics Dictionary," Gihodo (1987), pp. 498.

This article is a full translation of the article which appeared in Nippon Seramikkusu Kyokai Gakujutsu Ronbunshi (Japanese version), Vol.97, No.8, 1989.

Shape of AlN Powders Prepared by Vapor Phase Reaction of $AlCl_3$ NH_3-NH_3-N_2 System

Takanori Watari, Toshihiko Akizuki, Hiroshi Ikeda†, Toshio Torikai and Ohsaku Matsuda

Saga University, Faculty of Science and Engineering Applied Chemistry
1, Honjo, Saga
† Now with Fukuryo Semicon Engineering Co., Ltd.

AlN powders were prepared by vapor phase reaction of $AlCl_3 \cdot NH_3$-NH_3-N_2 system. $AlCl_3 \cdot NH_3$ was prepared by the evaporation and decomposition of $AlCl_3 \cdot nNH_3$ (n = 1.7 - 1.8) at 430°C. The shape of AlN particles varied with the molar ratio $[NH_3]/[AlCl_3 \cdot NH_3]$ (X) or the synthesis temperature (T_R). At T_R = 1400°C, AlN particles had columnar crystals at X≤7, but had smooth surface at X≥9. However, at T_R = 1000°C, AlN particles had smooth surface even at X = 4.2.
[Received January 17, 1989; Accepted May 16, 1989]

Key-words: AlN powder, $AlCl_3 \cdot NH_3$, Vapor Phase Reaction, Morphology

1. Introduction

Aluminum nitride (AlN) is very suitable for use as a material for optical elements, semiconductors and melting of metals, because of its high transparency in a wide range from infrared to ultraviolet regions, high thermal conductivity and resistance to corrosion.[1] The AlN-base materials for these devices are generally produced by sintering AlN powder, of which the sinterability increases as the particle size decreases.[2]

The synthesis of fine AlN particles by the vapor-phase process has been discussed for the $Al(i\text{-}Bu)_3$-NH_3 and $AlCl_3$-NH_3 systems,[3,4] but not for the system where $AlCl_3 \cdot NH_3$ is used as the starting material.

In this study, the authors synthesized AlN powder by vapor-phase reactions of the $AlCl_3 \cdot NH_3$-NH_3-N_2 system, to investigate the effects of synthesis conditions on the particle shape.

2. Experimental Procedure

$AlCl_3$ reacts with NH_3 to form $AlCl_3 \cdot nNH_3$, where n = 1 to 14. Those compounds with n > 1 liberate NH_3 when heated to 350°C, being transformed into $AlCl_3 \cdot NH_3$.[5] In this study, $AlCl_3$ (special grade, supplied by Katayama Kagaku) was reacted with NH_3 (99.99%, supplied by Seitetsu Kagaku Kogyo) at 180°C to form $AlCl_3 \cdot nNH_3$ (n = 1.7–1.8), which was heat treated at 430°C in a nitrogen atmosphere to form $AlCl_3 \cdot NH_3$ by the evolution of excess NH_3. Nitrogen was treated with activated copper to remove oxygen, and dried with liquid nitrogen. NH_3 was dried with potassium hydroxide. The product composition was $AlCl_3$:NH_3 = 1:1.00 to 1.04 (this compound is referred to as the adduct).

Figure 1 illustrates the apparatus used for the preparation of AlN, consisting of an adduct evaporation section and reaction section, which were heated by a Kanthal and SiC heater respectively. The adduct was placed on an alumina boat evaporated in the evaporation section and then passed to the reaction section. NH_3 was supplied to the reaction section through an alumina tube. The temperature at which NH_3 emerged into the reaction section is referred to as the mixing temperature, which was varied by changing the NH_3 nozzle position, and was determined by the temperature profile across the reaction section. The feed adduct concentration was determined by the reaction time and weight change before and after the reaction. The product powder was recovered on a filter paper. The phases formed were identified by X-ray diffractiometry (CuKα), and the powder morphologies were observed with a transmission electron microscope. The surface area was determined by the BET method using liquid nitrogen.

The synthesis conditions were: $AlCl_3 \cdot NH_3$ concentration; 1.3 to 8.9vol%, NH_3 concentration; 8 to 20vol%, total flow rate; 1000cc/min., synthesis temperature (T_R); 800 to 1400°C, and mixing temperature (T_M); 600 to 1000°C. The mixing temperature was set at least 200°C lower than the synthesis temperature.

The product powder was collected on the filter paper, contaminated with NH_4Cl, and heat-treated at 400°C for 2h in a nitrogen atmosphere, to remove the impurity.

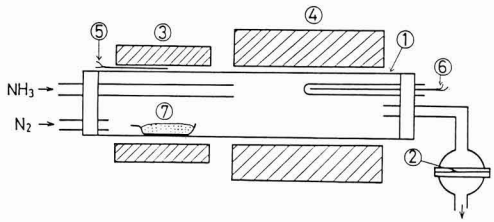

Fig. 1. Apparatus for preparation of AlN.
1: Alumina tube, 2: Filter paper, 3: Kanthal heater, 4: SiC heater, 5: C.A. thermocouple, 6: Pt/Pt-Rh (13%) thermocouple, 7: $AlCl_3 \cdot NH_3$

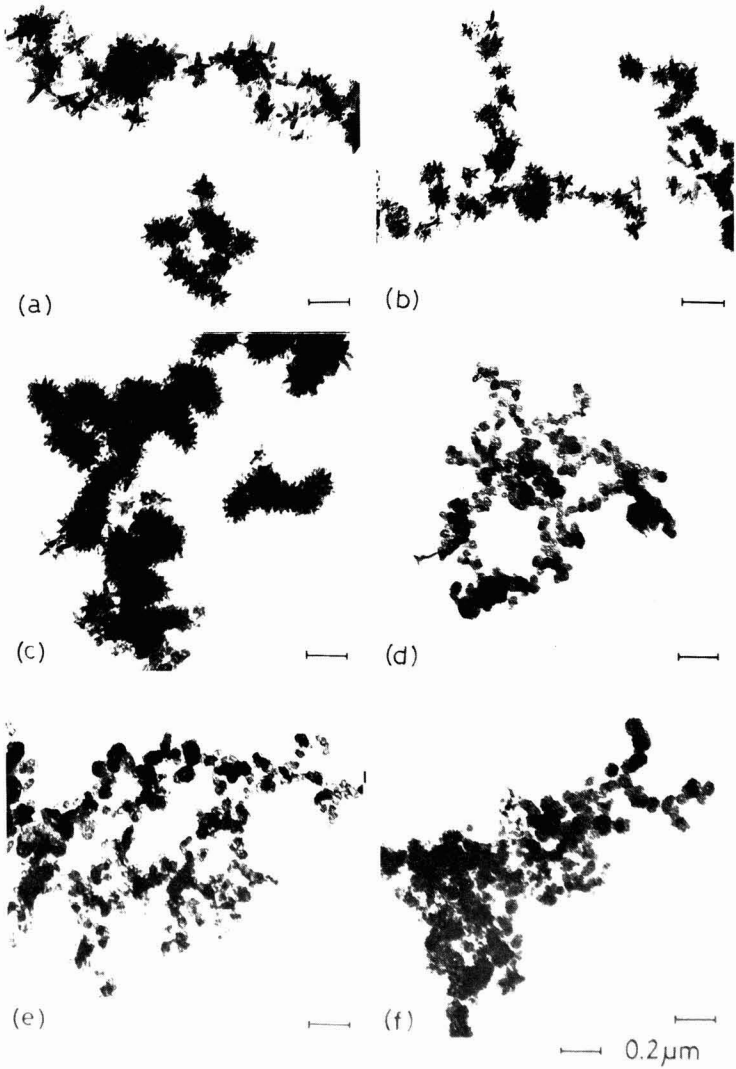

Fig. 2. Transmission electron micrographs of AlN particles.

3. Results and Discussion

The product powder shape varied with the operating conditions of the feed ratio ($[NH_3]/[AlCl_3 \cdot NH_3]$, X) and synthesis temperature. Figure 2 shows representative transmission electron micrographs of the product particles prepared at 1400°C. The columnar grains growing radially and the grains with projections on the surfaces were formed at a low X level ($X \leq 7$), but the particles formed at a high X level ($X \geq 9$) were rarely columnar, usually relatively spherical with smooth surfaces. The radially growing particles were considered to be columnar grains growing over the AlN microparticles, while those particles with projections on the surfaces were columnar grains growing over AlN particles of relatively large size. On the other hand, Figs. 2(a), (c), (e) and (f) indicated that the particle shape was little affected by the adduct concentration and synthesis temperature. Figure 3 shows the relationship between specific surface area and feed ratio ($NH_3/AlCl_3 \cdot NH_3$). The specific surface area increased as the feed ratio increased, or as the columnar grains were replaced by grains with smooth surfaces.

The product powder was amorphous when prepared at 800°C, but formation of the AlN crystal was observed when the synthesis temperature was increased to 1000°C to 1400°C. Figure 4 shows the effects of synthesis temperature on AlN particle shape and specific surface area. The product particles prepared at 1000°C had

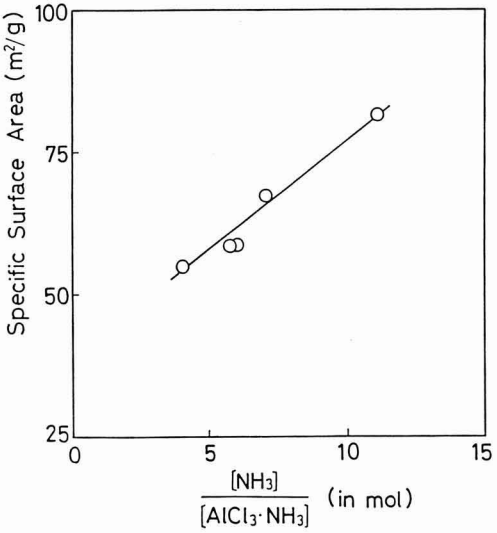

Fig. 3. Relation between specific surface area and $[NH_3]/[AlCl_3 \cdot NH_3]$.
T_R: 1400°C, T_M: 800°C, $[AlCl_3 \cdot NH_3]$ = 1.3-2.9 vol%

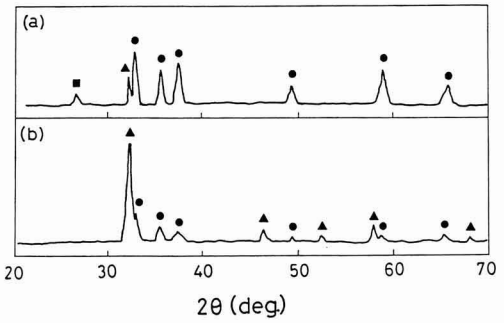

Fig. 5. X-ray diffraction patterns of reaction products of (a) $AlCl_3 \cdot NH_3$-N_2 and (b) $AlCl_3 \cdot NH_3$-NH_3-N_2 systems.
●: AlN, ▲: NH_4Cl, ■ : $AlCl_3 \cdot NH_3$
(a) T_R: 1400°C, $[AlCl_3 \cdot NH_3]$ = 1.7 vol%, N_2: 400 cc/min
(b) T_R: 1400°C, T_M: 800°C, $[AlCl_3 \cdot NH_3]$ = 4.8 vol%, $[NH_3]$ = 20 vol%, Total flow rate: 1000 cc/min

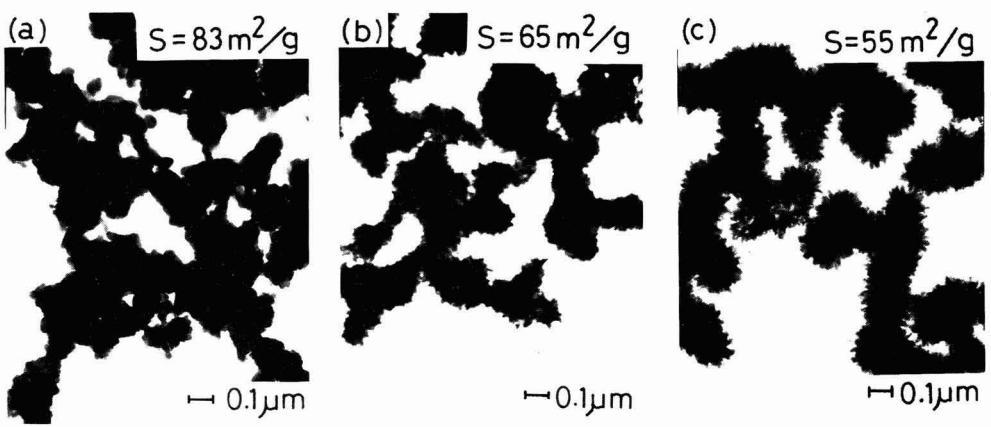

Fig. 4. Effect of synthesis temperature on shape of AlN particles.
T_M: 800°C, $[AlCl_3 \cdot NH_3]$ = 2.7 - 2.9 vol%, $[NH_3]/[AlCl_3 \cdot NH_3]$ = 4.1 - 4.3
T_R: (a) 1000°C, (b) 1200°C, (c) 1400°C

smooth surfaces, but the columnar particles increased both in number and size as the synthesis temperature increased to 1200°C and further to 1400°C. The particles synthesized at 1000°C, shown in Fig. 4(a), were secondary particles consisting of primary ones, because their size determined from their specific surface area was about 230Å.

Figure 5 shows the X-ray diffraction patterns of the particles synthesized by the vapor-phase reactions of the $AlCl_3 \cdot NH_3$-N_2 and $AlCl_3 \cdot NH_3$-NH_3-N_2 systems. These results were obtained with particles prior to the removal of NH_4Cl. The particles were measured in a nitrogen atmosphere, so that they were not contacted with air. Those particles prepared in the absence of

NH_3 contained AlN, NH_4Cl and $AlCl_3 \cdot NH_3$, and deliquesced rapidly in air, releasing an offensive odor. On the other hand, the powder synthesized in a flow of NH_3 at an X ratio of 2 released an offensive odor, resulting from the hydrolysis of the adduct, but those synthesized at X>3, consisting of AlN and NH_4Cl as far as the X-ray diffractiometry results showed, underwent no deliquescence in air and released no odor associated with the adduct hydrolysis. These results indicated that NH_3 eliminated HCl from the adduct.

It has been observed that when a metallic chloride is reacted with NH_3 in the vapor-phase process while being mixed in an electrical oven center to form a nitride powder, the size of the product chloride particles tends to decrease as the synthesis temperature increases, because of the accelerated nucleation.[4,6] However, the results in Fig. 4 show the opposite trend, since the specific surface area decreased as the synthesis temperature increased. In this study, the starting materials (aluminum chloride and the adduct) were mixed with NH_3 about 15cm away from the oven center, and hence the AlN particles were already formed before they were heated to the given synthesis temperature at the oven center. This might cause the apparent result that the nucleation rate was not affected much by the synthesis temperature. Kimura et al. suggested that the powder deposited in the $AlCl_3$-NH_3 mixing zone of the vapor-phase $AlCl_3$-NH_3-N_2 system consisted of a number of columnar grains extending in the radial direction.[4] They are considered to be formed by heterogeneous nucleation on the AlN particles deposited in the mixing zone. The columnar grains shown in Fig. 4 might be formed in a similar manner. Elimination of HCl from the adduct proceeded to only a limited extent at a low X level, with the result that the adduct starting material remained until it reached the oven center, where the elimination was accelerated to form the columnar grains over the AlN particles. They grew faster as the temperature increased, showing clearer columnar shapes. At a high X ratio, on the other hand, the elimination of HCl from the adduct occurred fast enough to prevent the adduct from reaching the oven center, thus forming particles with smooth surfaces, even at 1400°C, as shown in Fig. 4(d), (e) and (f).

(This article was presented to the 33rd Artificial Minerals Seminar, October, 1988)

References:

1) M. Iwata, Electrochemistry, 39, 173 - 77 (1971).
2) K. Komeya and H. Inoue, J. Mater. Sci., 4, 1045 - 50 (1969).
3) K. Tsuchida, Y. Takeshita, A. Yamane and A. Kato, Yogyo-Kyokai-shi, 95, 1198 - 201 (1987).
4) I. Kimura, K. Hotta, H. Nukui, N. Saito and S. Yasukawa, Seramikkusu, 96, 206 - 10 (1988).
5) V.T. Renner, Z. Anorg. Allg. Chem., 298, 23 - 33 (1959).
6) A. Kato, M. Iwata, J. Hojo and M. Nagano, Yogyo-Kyokai-shi, 83, 453 - 59 (1975).

This article is a full translation of the article which appeared in Nippon Seramikkusu Kyokai Gakujutsu Ronbunshi (Japanese version), Vol.97, No.8, 1989.

Fabrication of Polycrystalline Ruby from High Purity Metal Salts

Koichi Hayashi and Kenji Morinaga*

R&D Division, TOTO Ltd.
1-1, Nakashima 2-chome, Kokurakita-ku, Kitakyushu-city, Fukuoka 802, Japan
* Department of Materials Science and Technology,
Graduate School of Engineering Sciences, Kyushu University
6-1, Kasugakouen, Kasuga-shi, Fukuoka 816, Japan

Polycrystalline ruby was prepared using high purity oxides derived from metal salts by HIPing at 1250°C under 1000 atm Ar for 8 hrs after normal sintering at 1250°C for 4 hrs. The in-line optical transmission of the obtained ruby was about 70% from 650 to 2500nm over a wide range of wave length. The translucence was higher than polycrystalline ruby prepared by the ordinary method or translucent alumina, and almost comparable to single crystal ruby.
[Received March 3, 1989; Accepted June 23, 1989]

Key-words: Metal salts, High purity oxides, Translucence, Polycrystalline ruby

1. Introduction

Artificial ruby is excellent in respect of its hardness, corrosion resistance and translucent compared to other materials, and is used for precision products, such as watch parts, etc.

Historically, main current of artificial ruby was single crystal which was made by Verneuil's method,[1] but recently, polycrystalline rubies were produced by the development of sintering technique. These polycrystalline rubies are used for the substitution of single crystal rubies in the fields of precision products, such as bonding tools for joining IC chips to lead frames with a gold wire, optical connectors, or in the field of ornamental jewelry.

Some methods[2] are reported for producing polycrystalline ruby, where aluminum oxide and chromium oxide are mixed with the addition of magnesium oxide as a sintering additive, and sintered in hydrogen atmosphere after forming, or other methods of sintering in vacuum of 10^{-1} Torr or higher. However, the polycrystalline rubies obtained by these methods are inferior in characteristics compared to single crystal rubies: that is, they do not always show homogeneity of structure, and their average grain size is so large as to exceed 10μm.

The present authors have established a method to synthesize polycrystalline ruby which has almost equivalent characteristics to single crystal rubies.

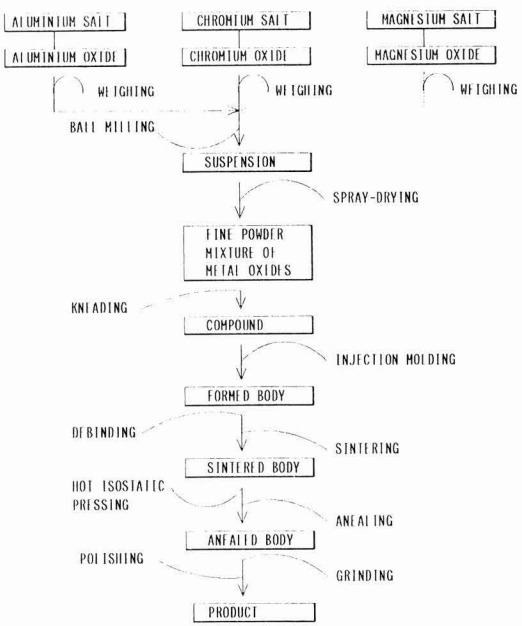

Fig. 1. Flow sheet of fabrication of polycrystalline ruby

2. Experimental

2-1. Raw Materials

Fine powders of aluminum oxide, chromium oxide and magnesium oxide with purities higher than 99.99% which were obtained by thermal decomposition of aluminum salt ($NH_4AlCO_3(OH)_2$), chromium salt ($NH_4CrCO_3(OH)_2$) and magnesium salt ($Mg(NO_3)_3 \cdot 6H_2O$) were used.

As organic binders, composite material of Ceramo IB-27B (Daiichi Kogyo Seiyaku) the main constituent of which is resin of acryl group, Bee Wax (Chukyo Yushi) and Atactic Polypropylene (Chiba Chemical), were used.

2-2. Production

Producing flow sheet of specimen was shown in Fig.1. Desired compositions of polycrystalline ruby are A: chromium oxide 1.2wt%, and B: 1.2wt% chromium oxide and 0.5wt% magnesium oxide. The aluminum salt was calcined at 1200°C for 2 hrs, the chromium salt at 1230°C for 2 hrs and the magnesium salt at 1200°C for 1 hr. These oxide powders were mixed for 24 hrs in a nylon ball mill using acetone as solvent. In order to keep the homogeneity of powder after mixing, spray

granulation method was applied. After adding organic binder so as to make weight ratio 5:1, the molding compound was made by pressure mixing with a kneader.

Injection molding method which is particularly excellent in homogeneity, was employed for forming.[3] Using a forming machine of Type JC12SA2 (Nihon Seikosho), sample blocks of 5×4×60mm were formed under the conditions of injection pressure of 1200kg/cm^2 and injection temperature at 213°C. Organic binder was removed out by thermal decomposition by heating up to 450°C in N_2 atmosphere of 8 atm with debinding furnace (TJ-400, Tokai Konetsu), and then heating in air up to 900°C with the rate of 150°C/hr. The specimen was sintered in a Kanthal electric furnace at 1250°C for 4 hrs using the aluminum oxide with purity of 99.99%, and then HIPed in Ar atmosphere of 1000 atm, at 1250°C for 8 hrs with a HIP apparatus (Dr. HIP, Kobe Seikosho), where temperature and pressure were simultaneously raised. The specimen was annealed under a vacuum of 10^{-4} Torr at 1150°C for 2 hrs after the HIP treatment. Specimens obtained were finished with a grinding and polishing machine (Ecomet Type 4, Buhler Co.).

2-3. Evaluation

Obtained polycrystalline rubies were evaluated by bulk density, Vickers hardness, bending strength at room temperature, translucence for visible radiation and SEM observation. The bulk density was measured by Archimedes' method. The Vickers hardness was measured with AKASI MVK-E tester. The strength at room temperature was measured with a three points bending tester (type OSS-5000, Shimadzu Seisakusho) by JIS-R1601 method. The in-line optical transmission was measured with type U-3410 (Hitachi Seisakusho). The SEM observation was carried out with type S-800 (Hitachi Seisakusho).

3. Results and Discussion

Properties of the polycrystalline ruby produced in this study were compared to those of polycrystalline ruby produced by ordinary methods, translucent alumina and single crystal ruby. As shown in Table 1, our polycrystalline ruby has superior properties to polycrystalline ruby produced by ordinary methods or translucent alumina. Its bending strength and Vickers hardness are nearly equivalent with single crystal ruby.

Figure 2 shows the result of the in-line optical transmission for a single crystal ruby and A polycrystalline ruby with the thickness of 1mm. The A polycrystalline ruby had above 70% transmission over a wide range of wave length from 650 to 2500nm, which is comparable to a single crystal ruby. Two characteristic absorption bands for the rubies existed at about 400 and 550nm.

Figure 3 shows the specimens with the thickness of 1mm described in Table 1. The polycrystalline ruby has higher translucency to read the letters than the polycrystalline ruby prepared by ordinary methods or translucent alumina.

Figure 4 shows the result of SEM observation of the polycrystalline ruby produced in this study. The specimen was completely densified without any addition of

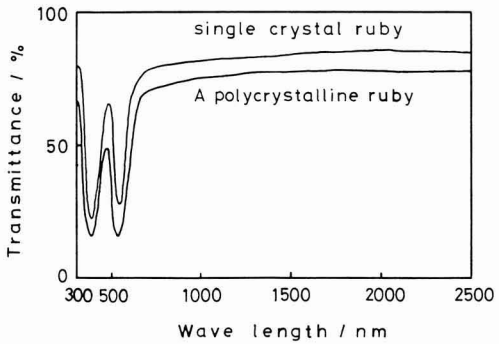

Fig. 2. Transmittance of single crystal ruby and A polycrystalline ruby

Table 1. Evaluation

	A polycrystalline artificial ruby	B polycrystalline artificial ruby	Ordinal polycrystalline artificial ruby	Translucent aluminium oxide	Ordinal single crystal artificial ruby
Chemical composition	1.20%Cr2O3	1.20%Cr2O3 0.05%MgO	1.20%Cr2O3 0.05%MgO	0.05%MgO	1.00%Cr2O3
Color	red	red	red	white	red
Bulk density	4.00	4.00	3.98	3.97	3.99
Hardness	2106Hv	2102Hv	2059Hv	1911Hv	2101Hv
Strength	72.4kg/mm2	73.8kg/mm2	43.6kg/mm2	37.7kg/mm2	74.0kg/mm2→ 13.5kg/mm2↑
Translucence	◎	◎	△	○	◎

For bulk density, hardness and strength in room temperature, averaged values were listed, and ordinary polycrystalline rubies and translucent alumina, data which were traced based on references 2), 6) were listed, for ordinary single crystal rubies, data which were in the market.

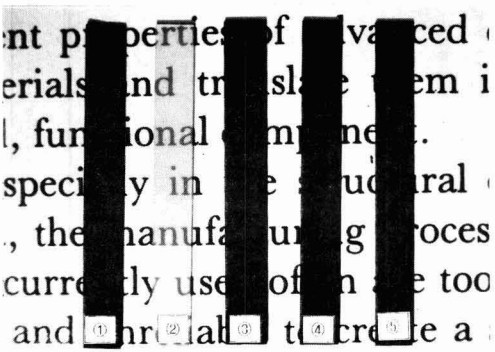

Fig. 3. Photographs of translucence
1 Ordinary single crystal ruby
2 Translucent alumina
3 Ordinary polycrystalline ruby
4 A polycrystalline ruby
5 B polycrystalline ruby

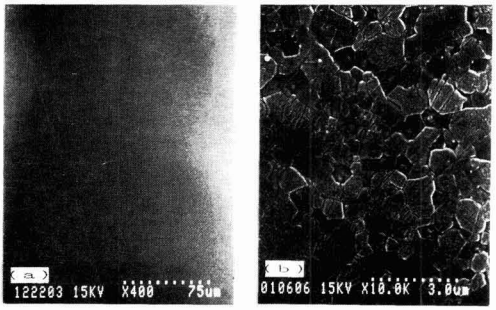

Fig. 4. SEM photographs of polycrystalline ruby
(a) SEM photograph of polished surface of the polycrystalline ruby: 1.2wt% CR_2O_3
(b) SEM photograph of surface of the polycrystalline ruby: 1.2wt% Cr_2O_3, after etching chemically by KOH liquids

MgO, and it consisted of fine grains of about 2μm without second phase in grain boundaries.

The translucency of oxide ceramics are influenced by two factors, i.e. one is the optical properties of the material itself, and the other is controlled by microstructural inhomogeneity, which includes second phases in grain boundaries as impurities or additives, and pores or defects in grains.[4] The high translucency of the artificial ruby in the present work reveals its excellent microstructure without such defects. The excellent microstructure[5] also refers to the excellent strength of this ceramic as shown in Table 1.

The polycrystalline ruby can be produced from homogeneous oxide powders with higher purity than 99.99% obtained by thermal decomposition of metal salts. Since these powders have high reactivities, dense and homogeneous microstructures without extraordinary grain growth, sintered body can be obtained without MgO additive as a sintering aid. Moreover, the HIP treatment removed pores or defects remained in sintered body in small amount. As the result, properties such as translucency, strength, hardness, etc. of obtained polycrystalline ruby in this study, are to be considerably improved.

4. Summary

Polycrystalline ruby was prepared using high purity oxides synthesized from metal salts. Polycrystalline ruby, which is equivalent to a single crystal ruby in various properties, was developed. Detailed method of production and result of analyses will be reported later on.

References:

1) Y. Nakazumi, Refractory, 39, 220 - 224 (1987).
2) T. Ikegami, Japanese Patent Application Laid Open, Print No.97572 (1984).
3) K. Saito, "Fainseramikkusu no Shashutsuseikeigijutsu" Nikkan Kogyo Shinbunsha (1987) p.6 - 11.
4) N. Kimura, Abstract of 8th HIP Seminar, 108 - 113 (1988).
5) K. Hamano, "Fine Ceramics Handbook" Asakura Shoten, (1984) p.459 - 466.
6) K. Nakano, Electronics, 30, 43 - 49 (1985).

This article is a full translation of the article which appeared in Nippon Seramikkusu Kyokai Gakujutsu Ronbunshi (Japanese version), Vol.97, No.8, 1989.

High Strength Si_3N_4 Ceramics

Yoshio Ukyo and Shigetaka Wada

Toyota Central Research & Development Labs., Inc.
Nagakute-cho, Aichi-gun, Aichi 480-11, Japan

Si_3N_4 ceramics composed of fine-grained α'-Si_3N_4 and β'-Si_3N_4 were fabricated by hot-pressing mixtures of Si_3N_4, Y_2O_3 and AlN powders. The Si_3N_4 ceramics showed a very high strength (about 1.3 GPa at room temperature and 1.0 GPa at 1400°C) and a high fracture toughness (about 7.0MPa·m$^{1/2}$).
[Received May 26, 1989; Accepted June 23, 1989]

Key-words: Silicon nitride, Aluminum nitride, Yttria, Hot-pressing, Strength, Fracture toughness

1. Introduction

Si_3N_4 ceramics as well as SiC ceramics, with strong covalent bonds, have attracted much attention as high temperature structural materials because of their excellent high temperature mechanical properties. Dense Si_3N_4 can only be obtained by using MgO, Al_2O_3, Y_3O_3 and other oxides as additives. The sintering with these additives is based on liquid phase sintering. However, the liquid phase remains a glass phase in the sintered Si_3N_4, affecting its high temperature characteristics such as high temperature strength and creep resistance.

It is very important to decrease the amount of the glass phase for improving the strength of Si_3N_4 ceramics, especially at high temperatures. The possible ways are (1) to use high purity Si_3N_4 powder, (2) to reduce or eliminate the use of additives, or (3) to devitrify the glass phase.

Richerson[1] pointed out that the high temperature strength of Si_3N_4 ceramics was influenced by the kinds and amounts of impurities contained in raw materials, and was significantly improved by decreasing the impurities.

HIPing is very effective to sinter Si_3N_4 powder with small amounts of additives or without additives. For example, Homma et al.[2] obtained dense Si_3N_4 ceramics by HIPing pure Si_3N_4 powder without additives at 1900°-2000°C under a pressure of 150MPa. The 3-point bending strength was about 650MPa at room temperature and about 750MPa at 1400°C. In this case, the amount of the liquid phase formed during sintering was little and no grains with high aspect ratios were obtained. Therefore, the fracture toughness value is very low[3] in spite of its high strength at elevated temperatures.

Tsuge et al.[4] obtained hot-pressed Si_3N_4 with a crystalline grain boundary phase, formed as a consequence of high temperature presintering heat treatment in AlN powder. The 3-point bending strength was about 80kg/mm^2 at 1300°C. Shimamori et al.[5] nitrided Si powder containing Y_2O_3 and then hot-pressed the nitrided body. The 3-point bending strength was about 900MPa at room temperature and at 1300°C, but the fracture toughness value was also low.

For increasing the strength of ceramics, it is necessary to increase the fracture toughness value and to restrain the defects as small as possible. Thus, a Si_3N_4-SiC whisker composite with a high fracture toughness value was developed.[6] In many cases, however, an increase in fracture toughness value did not lead to an increase in strength because other defects were induced due to the difficulty in whisker dispersing.

The influence of the grain size on the strength will become important when large defects associated with fabrication processes are eliminated from the materials by progress in the fabrication process. Lange[7] reported that prismatic grain structure with an average grain size of <5μm would be most desirable for high strength.

Recently, Ishizawa et al.[8] and Komatsu et al.[9] have obtained Si_3N_4 ceramics composed of β-Si_3N_4 and α'-Si_3N_4. Komatsu et al.[9] fabricated Si_3N_4 ceramics composed of β-Si_3N_4 and α'-Si_3N_4 by hot-pressing the mixture of Si_3N_4, Y_2O_3, HfO_2 and AlN powders. The 3-point bending strength was about 100kg/mm^2 at room temperature and about 125kg/mm^2 at 1300°C. The fracture toughness value was about 6.9MPam$^{1/2}$.

These results suggest that the Si_3N_4 ceramics with a high strength both at room and high temperatures, and with a high fracture toughness value will be realized by controlling the microstructure.

We have fabricated Si_3N_4 ceramics composed of α'-Si_3N_4 and β'-Si_3N_4 by hot-pressing mixtures of Si_3N_4, Y_2O_3 and AlN powders. The sintering reaction was carefully controlled to suppress the grain growth. The Si_3N_4 ceramics obtained were composed of very fine α'-Si_3N_4 and β'-Si_3N_4 grains. Figure 1 shows the microstructure of the Si_3N_4 ceramics observed by TEM. As shown in Fig.1, the Si_3N_4 ceramics obtained were mainly composed of very fine prismatic grains smaller than 1μm even in longer axis. The space between β'-Si_3N_4 grains was filled with finer, round shape grains of about 0.1 to 0.3μm. STEM/EDS analysis revealed that the prismatic and the finer, round shape grain were β'-Si_3N_4 and α'-Si_3N_4, respectively. Moreover, the observation by TEM with high magnification revealed that there were only very small triple points and a small amount of grain boundary phase.

Figure 2 shows the 4-point bending strength of the Si_3N_4 ceramics up to 1400°C. The bending strength was about 1.3GPa at room temperature and about 1.0GPa at 1400°C. These values are extremely high compared with those of ordinary Si_3N_4 ceramics. This fact seems to be attributed to the microstructure revealed by TEM observation. The fracture toughness value measured by indentation fracture method was about 7.0 to 7.5MPam$^{1/2}$. This value is comparable with that of the sintered Si_3N_4. The strength of Si_3N_4 ceramics is considered to be increased with decreasing grain size as described above. On the other hand, the fracture toughness value increases with grain size.[10] From the

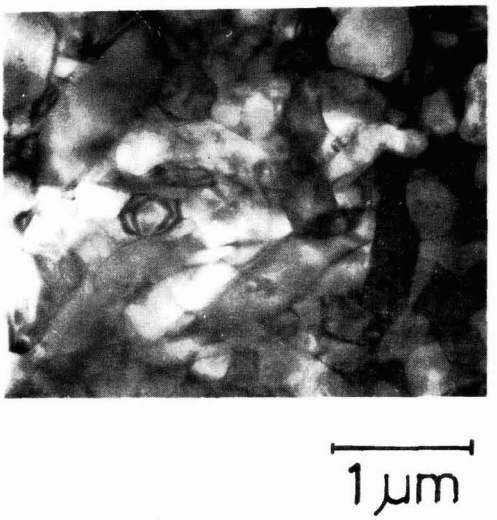

Fig. 1. Microstructure observed by TEM.

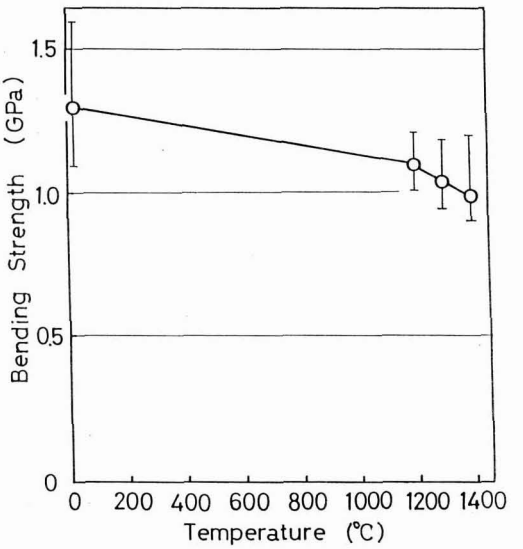

Fig. 2. Dependence of bending strength on temperature.

point of microstructure, the increase in strength and fracture toughness values is inconsistent. However, the strength and fracture toughness of the Si_3N_4 ceramics obtained are high, and these characteristics seem to be different from those of usual sintered Si_3N_4 ceramics. Although the reason for this has not yet been clarified, we consider it to be closely related to the microstructure in which very fine α'-Si_3N_4 grains exist between fine prismatic β'-Si_3N_4 grains.

The Si_3N_4 ceramics with a very high strength (1.3GPa at room temperature and 1.0GPa at 1400°C) and a high fracture toughness value were developed as described above. Since oxidation resistance and creep resistance are important, the evaluation of these properties are now being conducted.

References:

1) D.W. Richerson, Amer. Ceram. Soc. Bull., 52, 560-69 (1973).
2) K. Homma, H. Ikada, T. Fujikawa and T. Tatsuno, Yogyo-Kyokai-Shi, 95, 229-34 (1987).
3) K. Nezuka, Y. Miyamoto and M. Koizumi "Proc. Int. Conf. on Hot Isostatic Pressing", CENTEK publishers (1987) pp. 359-65.
4) A. Tsuge, K. Nisida and Ml. Komatsu, J. Amer. Ceram. Soc., 58, 323-26 (1975).
5) Y. Shimamori, T. Kato and Y. Matsuo, "Fine Ceramics Jisedai-Kenkyu-no-Ayumi (Progress of Fine Ceramics for Future Industries)", Engineering Research Association for High Performance Ceramics (1988) pp. 115-29.
6) T. Kandori, Y. Ukyo and S. Wada, "Proc. Int. Conf. on Whisker- and Fiber-Toughened Ceramics", ASM International (1988) pp. 125-29.
7) F.F. Lange, J. Amer. Ceram. Soc., 56, 518-22 (1973).
8) K. Ishizawa, N. Ayuzawa, A. Shiranita, M. Takai, N. Uchida and M. Mitomo, "Ceramic materials and Components for Engines" (1986) pp. 511-18.
9) M. Komatsu, T. Kameda, Y. Goto and K. Komeya, "Abstract Book of the Annual Meeting of Ceramic Society of Japan", (1987) pp. 301-2.
10) E. Tani, S. Umebayashi, K. Kishi and K. Kobayashi, J. Mater. Sci. Lett., 4, 1454-1456 (1985).

This article appeared in English in Nippon Seramikkusu Kyokai Gakujutsu Ronbunshi (Japanese version), Vol. 97, No.8, 1989.

Far Infrared Reflection and Raman Spectra of Complex Perovskite-Type Compounds, $Ba(Mn_{1/3}Ta_{2(1-x)/3}Nb_{2x/3})O_3$

Kunio Tochi, Tomiyasu Ohgaku, Nozomu Takeuchi and Shuichi Emura*

Faculty of Technology, Kanazawa University
2-40-20, Kodatsuno, Kanazawa 920, Japan
*The Institute of Scientific and Industrial Research, Osaka University
8-1, Mihogaoka, Ibaraki-shi, Osaka 567, Japan

Infrared reflection and Raman spectra of the complex perovskite-type compounds, $Ba(Mn_{1/3}Ta_{2(1-x)/3}Nb_{2x/3})O_3$ have been measured at x=0.0, 0.1, 0.3, 0.5, 0.7, 0.9, and 1.0. Two mode behavior was observed for both end-members and all the solid-solution in the vibration of BO_6-type octahedrons, where B indicates Mn, Ta and Nb ions. The coexistence of TaO_6 and NbO_6 octahedrons in solid solutions, however, resulted in one-mode behavior, instead of two-mode one. That is, these two octahedrons represent one-mode behavior.
[Received May 29, 1989; Accepted June 23, 1989]

Key-words: Complex perovskite-type solid solution ceramics, Far infrared reflection spectra, Raman spectra, Two-mode behavior, One-mode

1. Introduction

In the previous report,[1] we measured the infrared reflection and Raman spectra for two complex perovskite ceramic compounds, $Ba(Mn_{1/3}Ta_{2/3})O_3$ and $Ba(Ni_{1/3}Ta_{2/3})O_3$, and found that there are two-mode behaviors in the inner vibrations of the BO_6-type octahedrons, where B indicates Mn, Ta, and Ni ions. In the present investigation we further study the effect of the replacement of Ta^{5+} ions in $Ba(Mn_{1/3}Ta_{2/3})O_3$ by Nb^{5+} ions partially or completely by making the solid-solutions.

2. Experimental Procedure

2-1. Sample Preparation

Samples were made from the starting materials of reagent-grade $BaCO_3$, $MnCO_3$, Ta_2O_5, and Nb_2O_5. They were mixed in the mole ratio to form $Ba(Mn_{1/3}Ta_{2(1-x)/3}Nb_{2x/3})O_3$ for x=0.0, 0.1, 0.3, 0.5, 0.7, 0.9, and 1.0. The mixtures were ball-milled in pure water. After dried, they were heated at 1100°C for 4h, cooled to room temperature and ground in pure water for 48h. After they were again dried, they were pressed at 1×10^8 Pa into disks 14mm in diameter and 2mm thick and heated at 1600°C for 2h in air. The heating rate was 270°C/h. Finally they were cooled to room temperature within 24h. Sample faces were polished to a mirror state.

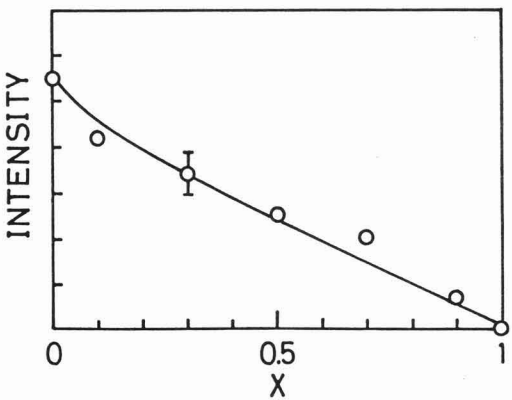

Fig. 1. Intensity of the (100)* reflection line for $Ba(Mn_{1/3}Ta_{2(1-x)/3}Nb_{2x/3})O_3$. This shows the formation of the D_{3d} hexagonal superstructure.

2-2. XRD Analysis

XRD patterns were measured at room temperature. Figure 1 shows the intensity of the (100)* reflection line in the D_{3d} hexagonal structure[2] as a function of x-value. It is seen that the intensity decreases with the increasing x-value. This indicates that the hexagonal superstructure of the solid-solution is gradually lost with increasing x-value.

2-3. Infrared Reflection Spectra

IR reflection spectra were measured by using a Fourier Transform IR monochormator at room temperature. Figure 2 shows the results for the solid-solutions from x=0.0 to 1.0. All the reflection peaks were numbered from 1 to 6. Remarkable changes were hardly observed by changing the x-value, except that the peak numbered-6 grows with increasing x-value.

The reflection spectra were analyzed using the Kramers-Kronig relation.[3] TO-phonon frequencies were estimated from the positions of the maxima in the imaginary part, $\mathrm{Im}(\epsilon)$, of the complex dielectric constant, $\epsilon=\epsilon'+i\epsilon''$, and LO-phonon frequencies were estimated from the maxima of $-\mathrm{Im}(1/\epsilon)$, where Im indi-

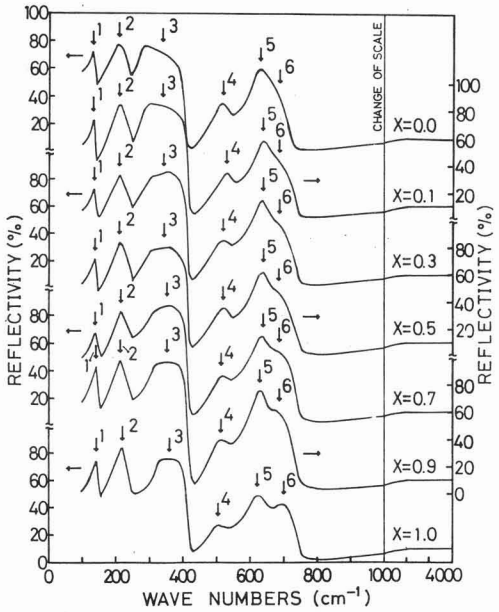

Fig. 2. Infrared reflection spectra for $Ba(Mn_{1/3}Ta_{2(1-x)/3}Nb_{2x/3})O_3$. Reflection bands are numbered from 1 to 6.

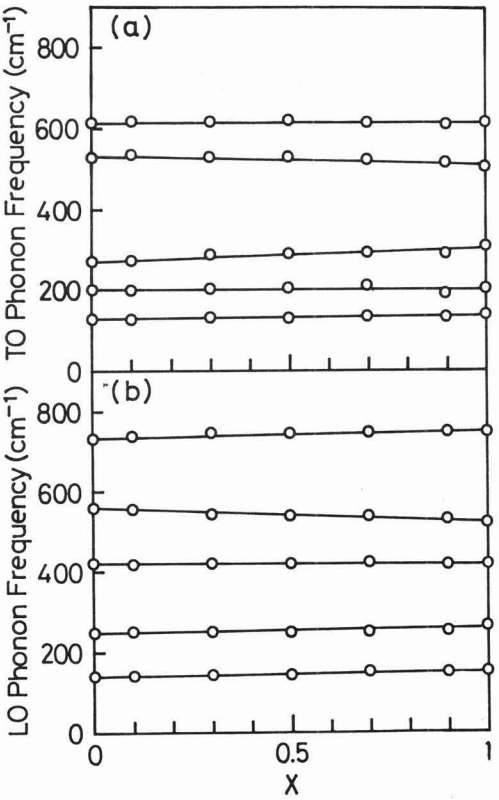

Fig. 3. Peaks for Im(ϵ) and -Im($1/\epsilon$) curves obtained by the Kramers-Kronig analysis of the reflection spectra, where $\epsilon = \epsilon' + i\epsilon''$ is the complex dielectric constant and Im indicates the imaginary part of the complex number. TO and LO phonon frequencies are shown by the peak frequencies of the Im(ϵ) and -Im($1/\epsilon$), respectively. They are shown in (a) and (b), respectively.

cates the imaginary part of the complex number. They are shown in Figs.3(a) and 3(b) as functions of x-value.

The oscillator strengths of different modes are in proportion to the areas under the ϵ''-curve. As an example Fig.4 shows the result of the Kramers-Kronig analysis for x=1, i.e., for $Ba(Mn_{1/3}Nb_{2/3})O_3$. It is seen from the figure, though the reflection peak numbered-6 and the corresponding LO-peak are remarkable, that the related oscillator strength and the TO-phonon peak are very weak.

2-4. Raman Spectra

Raman spectra were measured using an Ar laser at room temperature. As an example, Raman spectrum for $Ba(Mn_{1/3}Ta_{1/3}Nb_{1/3})O_3$ is shown in Fig.5. Figure 6 shows the peak positions of the spectra for all the solid solutions including the end-members. The results seem to be not very different from those in Fig.2, especially there are similarities between the TO-mode peak positions and the Raman peak positions. However, the lines of peaks around 800, 420, and 380cm^{-1} observed in Fig.5 for Raman spectra are lost in the TO-modes as well as in the LO-modes in Fig.2. It has been discussed that the 420 and 380cm^{-1} Raman peaks are due to the torsional vibrations of the BO_6-type octahedrons distorted into C_{4v}-symmetry.[1] The F_{2u}-mode in the O_h-symmetry splits into the B_1- and E-modes in the C_{4v}-symmetry, where the B_1-mode vibration is forbidden in the IR reflection spectra, while both the B_1- and E-modes are allowed in the Raman spectra. In addition, there is the experimental fact that the torsional E-mode is too weak to be detected in the reflection spectrum of a $BaTiO_3$, whose symmetry is C_{4v}.[4] Therefore, the absence of the torsional modes in the IR reflection spectra of the solid-solutions including the end-members, i.e., $Ba(Mn_{1/3}Ta_{2/3})O_3$ and $Ba(Mn_{1/3}Nb_{2/3})O_3$, can be understood in that these samples the BO_6-octahedrons are distorted from O_h-symmetry, or at least they are not in the symmetry having a center of inversion.

3. Discussion

It has been reported by Perry et al.[5] that the IR reflection spectra for perovskite compounds such as

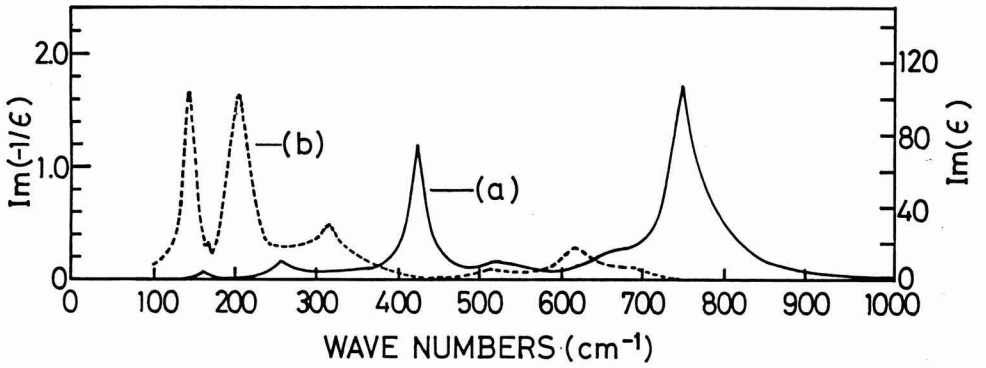

Fig. 4. An example of the Kramers-Kronig analysis for x=1, i.e., for $Ba(Mn_{1/3}Nb_{2/3})O_3$. Notice that Im(ε) is very weak around 700 - 800cm^{-1}, while -Im(1/ε) is remarkable.

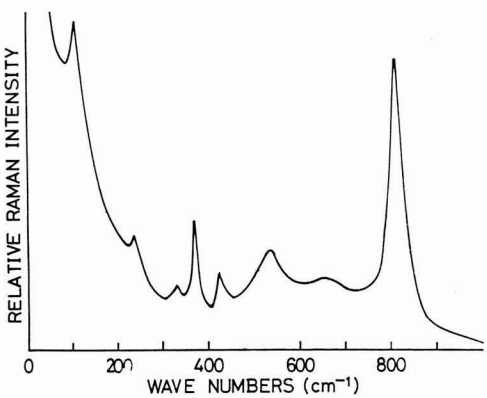

Fig. 5. An example of the Raman spectram for x=0.5, i.e., for $Ba(Mn_{1/3}Ta_{1/3}Nb_{1/3})O_3$.

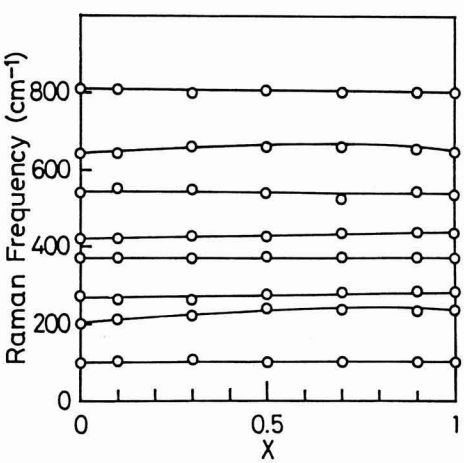

Fig. 6. Peak positions of the Raman spectra for $Ba(Mn_{1/3}Ta_{2(1-x)/3}Nb_{2x/3})O_3$.

$CaTiO_3$, $SrTiO_3$, $BaTiO_3$, $PbTiO_3$ or their corresponding zirconates should show three reststrahlen bands related with the three triply degenerate infrared active modes. However, when the compounds are in cubic O_h-symmetry, the torsional modes of the BO_6-octahedrons are not observed in both the IR and Raman spectra. When the octahedrons are distorted into, for instance, C_{4v}-symmetry, the torsional modes will be observed in the Raman,[6] and in some cases also in the IR reflection spectra.[5] Besides, there are cation-BO_3 lattice modes, which appear at the lowest frequencies of the spectra.[5] The spectra in Figs.2 and 4, or the lines in Figs. 3 and 6 are in agreement with the above statement. This situation is again clearly understood from Table 1, in which the data for the end-members are listed.

Table 1 shows that there are three groups of modes due to the inner vibrations of the BO_6-octahedrons, in which each group splits further into two modes: One is caused by the octahedron whose center is occupied by a Mn^{2+} ion, and the other is occupied by a Ta^{5+} or Nb^{5+} ion. It should be noted that there are no splittings into two-mode behaviors due to the two octahedrons whose centers are occupied by Ta^{5+} and Nb^{5+} ions as has been directly seen from Figs. 3 and 6 for solid-solutions. Therefore, it can be said that the octahedrons related with the Ta^{5+} and Nb^{5+} ions show one-mode behaviors in their inner vibrations when they are in the solid-solutions.

This difference in the mode behaviors should have been caused by the difference in their valencies between Mn^{2+} and Ta^{5+} or Nb^{5+} ions. The difference in the atomic masses of these ions should be less important for the mode behaviors. The atomic mass for Mn, Nb, and Ta are 54.94, 92.91, and 180.95 amu, respectively. It is seen that the relative mass ratio of Mn to Nb is smaller than that of Nb to Ta. Therefore, if the difference in the atomic masses is more important than that in the valencies, two-mode behaviors of the Ta- and Nb-octahedrons should appear taking the precedence of those of Mn- and Ta- as well as Mn- and Nb-octahedrons.

We may further assume that in the solid-solution the disorder between Ta^{5+} and Nb^{5+} ions happens easier than the disorder between Mn^{2+} and those pentavalent ions, i.e., Ta^{5+} and Nb^{5+} ions, though the latter disorder

Table 1. Infrared reflection and Raman data of Ba $(MN_{1/3}Ta_{2/3})O_3$ and $Ba(Mn_{1/3}Nb_{2/3})O_3$ complex perovskite ceramics.

	$Ba(Mn_{1/3}Ta_{2/3})O_3$			$Ba(Mn_{1/3}Nb_{2/3})O_3$		
	Infrared (cm^{-1})			Infrared (cm^{-1})		
Modes	(TO)	(LO)	Raman (cm^{-1})	(TO)	(LO)	Raman (cm^{-1})
Unknown			806			801
Stretching Mode	620	736	640	620	749	661
	530	540	540	512	527	526
Torsional Mode	silent	silent	421	silent	silent	436
	silent	silent	370	silent	silent	373
Bending Mode	276	418	270	312	422	283
	198		200	198	259	235
(Cation-BO_3 Lattice Mode)	130	146		138	154	
Unknown			100			105

may not completely be excluded.[7]

On the other hand, the XRD intensity for the (100)* shown in Fig.1 is caused by the formation of superstructures resulting from the ordered configuration of these Mn^{2+}, Ta^{5+}, and/or Nb^{5+} ions. One would expect the compound with Ta^{5+} ions, as opposed to Nb^{5+} ions, to have more of a tendency to show a true homogeneous crystal on an atomic scale because of a much larger mass difference between Mn and Ta than between Mn and Nb. We believe that the difference in the ionic radius between Ta^{5+} and Nb^{5+} is not so important, because the radii for Ta^{5+} and Nb^{5+} are 0.073 and 0.070nm, respectively. Therefore, the monotonous decrease of the intensity of the (100)* line in Fig.1 is in agreement with the above consideration of the mass difference that with increasing x-values, i.e., with increasing Nb^{5+} concentration, ordered configuration of the hexagonal superstructure disappears gradually.

It might be further considered that the disordering between the divalent Mn^{2+} and those pentavalent ions increases with increasing Nb^{5+} concentration, i.e., with increasing x-value because of the less difference in the mass ratio between Mn and Nb than Mn and Ta. The increase in the intensity of the reflection peak numbered-6 in Fig.2 might be related to the suggestion of Barker and Sievers[7] that weak structure in a mixed crystal spectrum might be a normally inactive mode made active by the disorder.

References:

1) K. Tochi, N. Takeuchi and S. Emura, J. Am. Ceram. Soc., 72, 158 -- 60 (1989).
2) H. Tamura, T. Konoike, Y. Sakabe and K. Wakino, J. Am. Ceram. Soc., 67, C59 -- 61.
3) F. Stern, "Solid State Physics Vol.15", ed. F. Seitz and D. Turnbell, Academic Press (1964) pp.327 -- 42.
4) W. Spitzer, R.C. Miller, D.A. Kleinmann and L.E. Wowarth, Phys. Rev., 126, 1710 -- 21 (1962).
5) C.H. Perry and McCarthy, Phys. Rev., 128, A1537 -- 38 (1965).
6) M. DiDomenico, Jr., S.H. Wemple and S.P.S. Porto, Phys. Rev., 174, pp.522 -- 30 (1968).
7) A.S. Barker, Jr., and A.J. Sievers, Rev. Mod. Phys. 47, Suppl. No.2, pp.1 -- 179 (1975).

This article appeared in English in Nippon Seramikkusu Kyokai Gakujutsu Ronbunshi (Japanese version), Vol. 97, No.8, 1989.

Synthesis of 2H-SiC Whiskers by Decomposition of Si_3N_4

Jian-bao Li, Gang Peng, Jian-gang Wu, Kunihito Koumoto* and Hiroaki Yanagida**

Tsinghua University
100084, Beijing, People's Republic of China
*Department of Industrial Chemistry, Faculty of Engineering, The University of Tokyo
7-3-1 Hongo, Bunkyo-ku, Tokyo 113, Japan
**Research Center for Advanced Science and Technology, The University of Tokyo
4-6-1 Komaba, Meguro-ku, Tokyo 153, Japan

Whiskers of 2H-SiC were synthesized by the decomposition of silicon nitride in a graphite reaction vessel at 1900°C under the nitrogen pressure of 1 MPa. The obtained long whiskers were typically ≈10mm long and 0.05-0.1mm in diameter and short whiskers were ≈0.1mm long and ≈10μm in diameter. Morphology observations suggested that they had grown by the spiral growth mechanism.

[Received June 6, 1989; Accepted June 23, 1989]

Key-words: Silicon carbide, Whisker, Synthesis, Morphology, Silicon nitride

1. Introduction

Silicon carbide whiskers have drawn much attention because of their usefulness for strengthening ceramics, metals and plastics in composites. Previously reported methods for synthesizing SiC whiskers are principally the carbothermal reduction of silica and the VLS (vapor-liquid-solid) technique in which Si-containing gases such as $SiCl_4+CH_4$ or $Si(CH_3)_3Cl$ are flown through a hot reaction zone.[1-3] SiC whiskers synthesized so far have been of cubic β-type and few reports on those of α-type have appeared in the literature. This short communication reports a new attempt to synthesize 2H-SiC (one of the α forms) whiskers by the decomposition of Si_3N_4 in a graphite reaction vessel.

2. Experimental

Silicon nitride powder was formed into a cylindrical compact 5cm in diameter and 5cm high. The green compact had 40-50% relative density. The employed starting powder was either commercially available or obtained by crushing waste ceramic parts such as ceramic rotors, ceramic gas turbine wheels, etc.[4] The green compact was placed in a graphite reaction vessel and heated up to 1900°C in a nitrogen atmosphere. The pressure of nitrogen was fixed to be 1 MPa in order to control the rate of decomposition of Si_3N_4. X-ray powder diffraction measurement, optical microscope and scanning electron microscope (SEM) observations were carried out on the obtained whiskers.

3. Results and Discussion

A photograph of the SiC whiskers grown around a Si_3N_4 compact is shown in Fig. 1. The whiskers were gray to green, long whiskers were typically ≈10mm long and 0.05-0.1mm in diameter, and short whiskers were ≈0.1mm long and ≈10μm in diameter. It was confirmed from the X-ray diffraction pattern of the crushed powder shown in Fig. 2 that the synthesized whiskers were almost completely composed of 2H-SiC (wurtzite structure).[5]

Observations of the morphologies of whiskers were further carried out with SEM. Micrographs are shown in Fig. 3, where it can be seen that a whisker usually becomes thinner as it grows and its top ends with a steeple head. When a whisker grows via the VLS mechanism, a solidified sphere, which is melted during whisker growth, is usually seen on the top end. However, no such spheres were found on the tops of the whiskers synthesized by the present method, suggesting that they had grown via the spiral growth mechanism. A number of growth stripes or grooves present on the

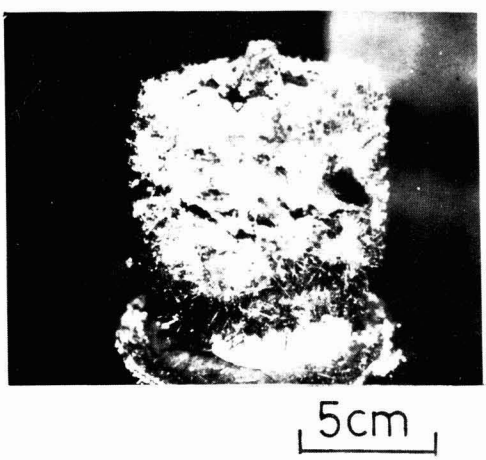

Fig. 1. SiC whiskers grown around a silicon nitride compact.

sides of the whiskers as seen in Fig. 3 must be associated with this growth mechanism.

Four types of shape regarding to the cross section of a whisker were recognized: rhombus, rectangle, hexagon and triangle. It should be pointed out that the shape of the cross section changed from hexagon to rectangle, and further to rhombus as the growth site became farther off the surface of a Si_3N_4 compact, while a small number of triangular cross sections were distributed randomly. This observation must be closely related to the difference in the degree of supersaturation of silicon in the surrounding vapor phase derived from the decomposition of Si_3N_4, though the detailed mechanism should be subject to further investigation.

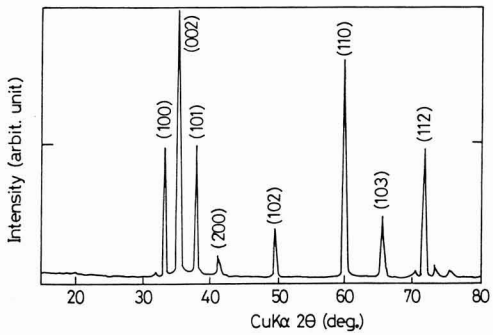

Fig. 2. Powder X-ray diffraction pattern of the synthesized whiskers. Miller indices of 2H-SiC are indicated.

References:

1) K. Ueno and Y. Toibata, J. Ceram. Soc. Jpn., 91, 491-497 (1983).
2) G.C. Wei, US Patent, 4,543,345(1985).
3) J.V. Milewski et al., J. Mater. Sci., 20, 1160-1166(1985).
4) G. Peng and J.B.Li, Proc. 2nd Chinese Youth Symp. Mater. Sci., in press.
5) JCPDS Card 29-1130 in Powder Diffraction File, Sects. 29-30 (Inorg. Vol.), International Centre for Diffraction Data (USA), 1987.

This article appeared in English in Nippon Seramikkusu Kyokai Gakujutsu Ronbunshi (Japanese version), Vol. 97, No.8, 1989.

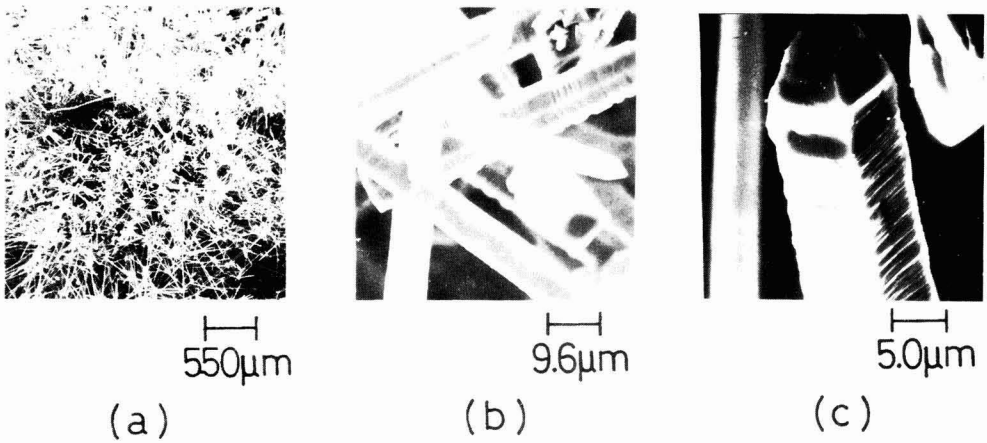

Fig. 3. Scanning electron micrographs of the whiskers.

Information & communications

Fall Meeting of the Ceramic Society of Japan, 1989

October 2-4, 1989, Kyoto

(Kyodai-Kaikan; 15-9, Yoshida-Kawaramachi, Sakyo-ku, Kyoto, Japan; tel. 075-751-8311)

Program

Abbreviations of Affiliations

GIRIN, GIRIO, GIRIK, GIRIT : Government Industrial Research Institute, Nagoya/Osaka/Kyushu/Tohoku
NCLI : National Chemical Laboratory for Industry
ETL : Electrotechnical Laboratory
NIRIM : National Institute for Research in Inorganic Materials
JFCC : Japan Fine Ceramics Center
TIT : Tokyo Institute of Technology
NIT : Nagoya Institute of Technology
Kyoto IT : Kyoto Institute of Technology
NUT : Nagaoka University of Technology
TUT : Toyohashi University of Technology
NDA : National Defense Academy

I : Institute (of)
T : Techn(ology/ological/ical)
R : Research
U : University (of)

[Dielectric Ceramics/Microwave Dielectric Ceramics]

5-1A01 Low-Temperature Properties of Microwave Dielectric Resonators, ○H Matsumoto · H Takagi · H Tamura · Y Sakabe (Murata Mfg Co Ltd)

5-1A02 The Influence of Ba Shortage on the Intensities of Superlattice Line of $Ba(Zn_{1/3}, Ta_{2/3})O_3$ Ceramics, ○M Tsurumi · K Endo · K Murakawa (Fuji Electrochemical Co Ltd)

5-1A03 Compositional and Microstructural Control of Complexed Low-Loss Dielectrics in the La-Ti-Sn-O System, ○J Takahashi · K Kageyama* (NIT · Sumitomo Special Metals Co Ltd*)

5-1A04 Microwave Dielectric Properties of $PbO-La_2O_3-TiO_2$ Systems, ○H Utaki · S Hirahara · N Fujikawa (Kyocera Corp)

[Dielectric Ceramics/Piezoelectric and Pyroelectric Ceramics]

5-1A05 Piezoelectric and Pyroelectric Properties of $(BiNa)_{1/2}TiO_3$-Based Solid Solution, ○T Takenaka · K Sakata (Science U Tokyo)

5-1A06 Microstructural Dependence of the Piezoelectric Properties in $PbTiO_3$ Ceramics, ○K Goda* · K Hiragushi* · M Kuwabara (Kyushu IT · Kurosaki Refractories Co Ltd*)

5-1A07 Composite Pyroelectric Ceramics, ○T Takenaka · H Komiya · K Sakata (Science U Tokyo)

5-1A08 Agglomerativity of PLZT Fine Powders from Aqueous Solutions, ○Y Yoshikawa · M Sato · S Sugiyama · K Tsuzuki (Nihon U)

5-1A09 Powder Compaction and Two Stage Sintering of Fine CP-PLZT Powder, ○M Sato · Y Yoshikawa · K Tsuzuki (Nihon U)

5-1A10 HIP of Strontium Barium Niobate ($Sr_{1-x}Ba_xNb_2O_6$), ○A Watanabe · H Haneda · Y Moriyoshi · S Shirasaki (NIRIM)

5-1A11 The Mixed Sintered Material with the High Dielectric Constant by the HIP, ○K Oonishi · S Tanaka · T Morohashi (Alps Electric Co Ltd)

5-1A12 Endurance to Compression Stress of PZT Based Ceramics, ○Y Kawamura · N Matsumoto · H Kamataki · K Mukae (Fuji Electric Co R&D Ltd)

5-1A13 Admittance Analysis of Piezoelectric Ceramics around Resonance Frequency, ○T Tsurumi · T Ichihara · K Asaga · M Daimon (TIT)

5-1A14 Synthesis of $ZnO-Bi_2O_3-BiF_3$ Varistor Using HIP, M Yoshimura · S-E Yoo · ○H Kimura* · M Hayashi* · N Ishizawa (TIT · Murata Mfg Co Ltd*)

5-1A15 Piezoelectric Phenomena and Applications of $Pb(SnSbNb)O_3-Pb(ZrTi)O_3$ Ceramic, ○H Taike · N Yokoe · T Horiuchi (Kyocera Corp)

[Dielectric Ceramics/Composite]

5-1A16 Properties of Ferroelectric-Ferrimagnetic Composites, ○M Miyamoto · T Yamasaki · Y Hikichi* (Kokushikan U · NIT*)

5-1A17 Piezoelectric Properties of Composite Structured Piezoelectric Ceramics, ○K Oonishi · S Tanaka · T Morohashi (Alps Electric Co Ltd)

5-1A18 Fabrication of Microwave Absorber (Ⅱ), S Chino · ○T Yamamoto · A Oshimoto* (NDA · Tokyo I Polytechnics*)

5-1A19 The Mixed Sintering of Mn-Zn Ferrite and Ni-Zn Ferrite, K Oonishi・T Morohashi・○M Kawarada (Alps Electric Co Ltd)

〔Surface Modification of Ceramics／Chemical Improvement〕

3-1B01 Improvement of ALC Properties by Inorganic Surface Coating, ○S Tsujii・M Nakamura・H Shiomi・T Kimura・K Inoue (Kyoto IT)

3-1B02 Phase Transition of Water on the Surface of Modified Silica : (Ⅱ) Investigation by Low Temperature DSC, ○S Yamaoka・M Nakamura・H Shiomi・T Kimura・K Inoue (Kyoto IT)

3-1B03 Ion-Exchange at the Surface of Porous Hydroxyapatite Ceramics, ○M Nagai・M Hibino・T Nishino (Musashi IT)

3-1B04 Modification of Porous Glass Surface with Specific Hydroxyl Groups, S Tsutsumi・○T Takei・M Chikazawa・T Kanazawa (Tokyo Metropolitan U)

3-1B05 Surface Charge of Ceramics Fine Particles in Aqueous Solutions, ○S Takeda・M Kurose・I Tari (Okayama U)

3-1B06 Effects of Organic Compounds Adsorption on Dispersion of Clay, ○E Watanabe・M Horio (GIRIN)

3-1B07 Stress Corrosion of Densified Borate Glass, K Hirao・○Z Zuyi・N Soga (Kyoto U)

3-1B08 Chemical Interaction between Fluoride Glasses and Melts or Solutions, T Yoko・○Y Kondo・S Sakka (Kyoto U)

〔Surface Modification of Ceramics／Ion Implantation〕

3-1B09 Formation of Silicon Oxynitride Layer into Silica Glass Using Ion Implantation, ○K Oyoshi・T Tagami・S Tanaka (Nippon Sheet Glass Co Ltd)

3-1B10 Structural Modification of Single Crystal Iron Films by Ion Implantation and Their Magnetic Properties, K Nakajima・S Okamoto (NUT)

3-1B11 Structure and Magnetic Properties of Co Thin Films Implantated with Nitrogen Ions, ○F Noguchi・K Nakajima・S Okamoto (NUT)

3-1B12 Ion-Implantation Effect in Intermetallic Compound Films, ○S Sato・K Nakajima・S Okamoto (NUT)

〔Surface Modification of Ceramics／Substrate〕

3-1B13 The Effect of Blocking SiO_2 Film for Na^+ Ion Diffusion, ○S Oono・T Yamaoka・K Morio・Y Kusuda・S Tanaka (Nippon Sheet Glass Co Ltd)

3-1B14 The Effect of Glass on the TFT (Ⅱ), ○S Oono・T Yamaoka・K Morio・Y Kusuda・S Tanaka (Nippon Sheet Glass Co Ltd)

3-1B15 Study on the Substrate Materials for High-T_c Superconducting Thin Films, ○Y Watanabe・T Ishihara・Y Takita (Oita U)

3-1B16 (Withdrawn)

〔Surface Modification of Ceramics／AlN〕

3-1B17 Selective Area Formation of Conductor Films by Laser Sublimating of Ceramics, ○N Morita・T Watanabe・Y Yoshida (Chiba U)

3-1B18 Effect of Plasma Sintering on AlN Surface, ○S Akimoto*・K Kijima・T Uetuki・K Tanaka (Kyoto IT・Murata Mfg Co Ltd*)

3-1B19 Relationship between AlN Surface Properties and Sintering Nitrogen-Pressure, ○N Takada・S Katube・M Komatu・T Takahashi (Toshiba Corp)

3-1B20 Microstructure of Boundary Layer of Metallized AlN, ○H Asai・F Ueno (Toshiba Corp)

〔Surface Modification of Ceramics／Structural Ceramics〕

3-1B21 (Withdrawn)

3-1B22 Formation of Lath-Like Si_3N_4 Crystals from Alkali-Assisted Oxidation of Hot-Pressed Si_3N_4 Surface, ○N Azuma・K Nakamura (GIRIN)

3-1B23 Activation Energy Measurement on Desorption and Evaluation of Silicon Nitride Powders, ○M Kawamoto・K Ishizaki・C Ishizaki (NUT)

3-1B24 Oxidation Behaviors of Structural Ceramics in Combustion Gas Flow, ○Y Furuse・T Tsuchiya・S Handa・N Takahashi (Tokyo Electric Power Co)

3-1B25 Fabrication of Al_2O_3/Al_2O_3 Fiber Composites with High Porosity, ○H Iwamura・M Hashiba・Y Nurishi (Gifu U)

3-1B26 Effect of Coating by Salt Bath Immersing Method on Friction and Wear of Si_3N_4 and SiC, T Arai・○H Oikawa (Toyota Central R&D Labs Inc)

3-1B27 Surface Modification of Y-TZP, ○T Yamamoto・R Shikata (Osaka Cement Co Ltd)

3-1B28 Sintering of SiC by Plasma Technique, ○M Kitamura・K Kijima・T Uetuki・K Tanaka (Kyoto IT)

〔Preparation of Ceramics from Liquid Phase／Sol-Gel Process〕

2-1C01 The Kinetic Study of the Hydrolysis and Condensation Reaction of the Silicon Tetraethoxides by NMR and Gas Chromatography, ○T Sasaki・I Ohara・H Maekawa・T Maekawa・T Yokokawa (Hokkaido U)

2-1C02 Effects of Solvents in the Preparation of SiO_2-P_2O_5 Wet Gel Prepared by the Sol-Gel Process, ○M Fukuoka*・A Makishima (NIRIM・U Tokyo・Olympus Optical Co Ltd*)

2-1C03 Phase Separation in Silica Sol Containing Organic Polymer I. Systems Containing Ionic Polymer, ○K Nakanishi・N Soga (Kyoto U)

2-1C04 Phase Separation in Silica Sol Containing Organic Polymer Ⅱ. Systems Containing Neutral Polymer, ○H Komura・K Nakanishi・N Soga (Kyoto U)

2-1C05 Molecular Orbital Analysis of Sol-Gel Process, ○N Uchida・K Uesaka・Z Kato・K Uematsu・K Saito (NUT)

2-1C06 Preparation of ZrO_2 Precursor by Metal Alkoxide, ○C Sakurai・T Fukui・M Okuyama (Colloid RI)

〔Preparation of Ceramics from Liquid Phase／Powder Synthesis (1)〕

2-1C07 Formation Mechanism of Monodispersed TiO_2 and ZrO_2 Particles, ○T Ogihara・M Ikeda・N Mizutani・M Kato (TIT)

2-1C08 Synthesis of Zircon Powder by Sol-Gel Method, ○T Takano・M Takada・H Kobayashi・T Mitamura・T Mori*

(Saitama U・Tosoh Corp*)

[Preparation of Ceramics from Liquid Phase/Powder Synthesis (2)]

2-1C09 Hydrothermal Synthesis of $SrZrO_3$ Fine Powders, ○H Yamanoi・S Uedaira (Sony Corp)

2-1C10 Hydrothermal Synthesis of $CaTiO_3$ Fine Powders, ○S Uedaira・H Yamnoi (Sony Corp)

2-1C11 Synthesis of Tin Oxide Powders by Homogeneous Precipitation, H Hayashi*・○Y Katatae・A Kato (Tosoh Corp*・Kyushu U)

2-1C12 Synthesis of $BaTiO_3$ by Spray Pyrolysis Method and Its Evaluation, ○K Nonaka・K Okada・N Otsuka・Yano (TIT)

2-1C13 Synthesis of High T_c Superconductor $BiSrCaCu_2O_x$ Powder from Metal Alkoxides (Ⅱ), Y Ozaki・K Tamura・○M Yoshimura (Seikei U)

2-1C14 Mechanochemical Effects for Synthesis of Oxide Superconductor, ○M Awano・Y Torii・H Takagi (GIRIN)

2-1C15 Effect of Ultrasound on Precipitation from Homogeneous Solution Using Urea, ○N Enomoto・Y Ohya・Z Nakagawa・Y Tomomasa* (TIT・Sumitomo Chemical Co Ltd*)

2-1C16 Synthesis of Acicular PZT Powder by Precipitation Mixing Method, ○A Takenaka・T Kimura・T Yamaguchi (Keio U)

2-1C17 Hydrothermal Synthesis of Needle-Like Mullite, K J Kim・M Yoshimura・K Hishinuma*・○T Kumaki*・S Sōmiya** (TIT・Chichibu Cement Co Ltd*・Teikyo U**)

2-1C18 Thermal Behavior and Pore-Structure of Silica-Containing Mixed-Oxide Gels Prepared through Wet Processes, ○S Kaneko・M Mikawa・S Yamagiwa* (Shizuoka U・Kyowa Chemical Ind Co Ltd*)

2-1C19 Preparation of Mullite/ZrO_2 Composite Ceramics by Colloidal Filtration, S Hirano・T Hayashi・○C Kato (Nagoya U)

2-1C20 Preparation of Cordierite Ceramics by Metal Alkoxide Method, ○T Fukui・C Sakurai・M Okuyama・M Sasaki (Colloid RI)

2-1C21 Sinterability of Hydroxyapatite Powders Prepared by Spray-Pyrolysis Technique, ○M Kobayashi・S Inoue (Kanto Chemical Co Inc)

2-1C22 Laser-Sintering of Alkoxy-Derived $BaTiO_3$-$CoFe_2O_4$ Composite Powder (Ⅱ), Y Ozaki・K Kawasaki・○K Oshima (Seikei U)

2-1C23 Preparation of Fine Particles of CaSe and CaS from $Ca(OC_2H_5)_2$, ○T Ishihara・H Matsui・G Hashizume (Ind RI Hyogo)

2-1C24 Post-Sintering of α-Si_3N_4 Whiskers Dispersed Apatite Ceramics from Fine Powders Synthesized Hydrothermally, ○K Ioku・N Ishizawa・T Noma・S Sōmiya・M Yoshimura (TIT)

[New Compounds, Potential Materials for New Applications]

Invited Talk Ⅰ Tetrapod-Like Crystal of ZnO, ○M Kitano・T Hamabe・S Maeda (Matsushita Ind Equipment Co Ltd)

[New Compounds, Potential Materials for New Applications/Oxide]

6-1D01 Metal-Semiconductor Transition in Ruthenates with Pyrochlore Structure, ○R Kanno・T Yamamoto・Y Takeda・O Yamamoto (Mie U)

6-1D02 Magnetic Property of $BaGd_2Mn_2O_7$, ○A Shimono・K Hayashi・N Kamegashira・S Kawano* (TUT・Kyoto U*)

6-1D03 Synthesis and Fluorescence Properties of $RE_2Te_4O_{11}$ (RE; Rare Earth Element), ○M Shimada・A Shibuya・T Endo・T Sato (Tohoku U)

6-1D04 Sol-Gel Synthesis and Electrical Properties of $PbTiO_3$-$MgTiO_3$ Solid Solutions, H Yoshioka (Ind RI Hyogo)

6-1D05 A Trial to Make an Expert System for the Formation of Perovskite-Type Mixed Oxides, ○Y Fujiwara・I Yasui (U Tokyo)

6-1D06 Anisotropic Crystal Growth of Hexaaluminates for Heat Resistant Fine Particles, ○M Machida・T Shiomitsu・K Eguchi・H Arai (Kyushu U)

6-1D07 Machinable Glass-Ceramics Containing Rare Earth Oxides, A Makishima・M Asami*・○A Mamiya* (NIRIM・U Tokyo・Sasaki Glass Co Ltd*)

6-1D08 Some Properties of Al_2TiO_5 Base Ceramics, ○T Kameda・K Komeya (Toshiba Corp)

6-1D09 Preparation of High-Purity Silica from Rice Husk, ○M Nakamura・Y Azuma・N Ohshima (Tokai U)

[New Compounds, Potential Materials for New Applications/Non-Oxide]

6-1D10 Development of Co-Fired Electro-Conductive/Resistive Near-Net-Shape Ceramics, ○Y Yasutomi・A Chiba・K Sonobe・M Sobue (Hitachi Ltd)

6-1D11 Development of Near-Net-Shape Electro-Conductive Reaction-Bonded TiN Ceramics, ○A Chiba・Y Yasutomi・M Sobue (Hitachi Ltd)

6-1D12 Formation Behaviour of Iron Carbides with High Saturated Magnetization, S Hirano・○S Tajima (Nagoya U)

6-1D13 Microstructure and Magnetic Properties of Sitered Metal-Ceramics Complexes, ○K Taki・K Nakajima・S Okamoto (NUT)

6-1D14 Synthesis and Sintering of Zr-Se System Compounds (Se/Zr Ratio=2.0-1.0), ○M Itakusu・K Tanaka・T Uetsuki・K Kijima (Kyoto IT)

6-1D15 Crystal Structure and Thermal Change in Hot-Pressing $Ti_{1.33}Se_2$, ○K Tanaka・M Onoda*・M Itakusu・T Uetsuki・K Kijima (Kyoto IT・NIRIM*)

6-1D16 Preparation and Densification of $PbSe_xTe_{1-x}$ by HIP Treatment, T Hattori・Y Iwadate・○T Sato (Chiba U)

6-1D17 Constitution of Lead Chalcohalide Glasses and Their Electrical and Optical Properties, ○K Ezaki・A Osaka・Y Miura・J Takada・K Oda (Okayama U)

Invited Talk Ⅱ Recent Topics of High T_c Superconductors Viewing from Solid State Physics, K Asayama (Osaka U)

[High Toughening Ceramics/Non-Oxide]

4-1E01 High Temperature Strength of HIPed β-Sialons, ○I Tanaka・G Pezzotti・K Matsushita・T Okamoto・Y Miyamoto

(Osaka U)

4-1E02 Evaluation of Mechanical Properties of Ceramics for Gas Turbine Component, Y Matsushita · ○N Takahashi · Y Furuse (Tokyo Electric Power Co)

4-1E03 Influence of the O′-Phase Ratio on the Mechanical Properties of β'-O′ Sialon Composites, ○K Yabuta · H Nishio (NKK)

4-1E04 Microstructure and Properties of Cr_3C_2 Sintered Body, ○K Isozaki · Y Hirashima · Y Imamura (Denki Kagaku Kogyo KK)

4-1E05 The Relationship between Tensile Strength and Flaw-Size of Silicon Carbide Filament, Y Matsuo · ○J Li · S Kimura (TIT)

4-1E06 Synthesis of SiC Whiskers under Pressure, J Oka · ○S Yamada · E Yasuda · H Yoneda · Y Tanabe (TIT)

4-1E07 Joining of BN Machinable Ceramics to Metals and Evaluation of Mechanical Properties, ○K Suganuma · T Fujita · K Niihara (NDA)

4-1E08 Electron Microscopic Observation of Crack in SiC, ○Y. Bando · H Tanaka · Y Inomata (NIRIM)

4-1E09 Friction and Wear of Silicon Nitride Ceramics, ○S Suyama · Y Abe · Y Fujimoto (Toshiba Corp)

〔High Toughening Ceramics／Whisker Reinforcement〕

4-1E10 Size Effect of SiC Whisker on Al_2O_3/SiC Whisker Composite Ceramics, ○E Maeda · T Funahashi · R Uchimura (Kawasaki Steel Corp)

4-1E11 Fracture Behavior of Polycrystalline Alumina with Various Grain Size, ○M Kaji · H Atari · S Kohsaka · K Koga (Kyocera Corp)

4-1E12 Fracture Toughness of Whisker Reinforced Al_2O_3, ○T Nose · M Ueki · T Fujii · H Kubo (Nippon Steel Corp)

4-1E13 Mechanical Properties of C-Coated SiC Whisker Reinforced Alumina, ○H Watanabe · A Nakahira* · T Hirano* · K Niihara*(Ashikaga IT · NDA*)

4-1E14 Hot Isostatic Pressing of Alumina-Silicon Carbide Whisker Composites, ○J-Y Kim · Z Kato · N Uchida · K Uematsu · K Saito (NUT)

4-1E15 Microstructure and Mechanical Property of Whisker Reinforced Ceramic Composite, Y Hirata · ○N Hamada · Y Ishihara · S Hori* (Kagoshima U · Kureha Chemical Ind Co*)

4-1E16 Mechanical Properties of Si_3N_4-SiC Whisker Composites, ○T Yonezawa · Y Goto · A Tsuge (Toshiba R&D Center)

4-1E17 Displacement Rate Dependence of High Temperature Tensile Strength of Whisker Reinforced Hot-Pressed Silicon Nitride, ○T Ohji · Y Yamauchi · W Kanematsu · S Ito (GIRIN)

4-1E18 Dispersion and Consolidation of β-Silicon Nitride Whisker Suspension, Y Hirata · ○S Nakagawa · Y Ishihara (Kagoshima U)

4-1E19 Fabrication of Si_3N_4 Whisker/Si_3N_4 Composite, ○K Hayashi · K Yoshino · T Ohhara · Y Okamoto · T Nishikawa (Kyoto IT)

4-1E20 Some Properties of Pressureless-Sintered SiC Whisker/Si_3N_4 Composite Fabricated by Slip Casting, ○S Saitoh · M Minamizawa · T Yonezawa · T Matsuda (Japan Metals & Chemicals Co)

4-1E21 Properties of β-Sialon/SiC Whisker Ceramic Composites, ○Y Goto · T Yonezawa · A Tsuge · M Komatsu (Toshiba Corp)

4-1E22 Effects of Length of Whisker on Toughening Mechanism of Whisker Reinforced Ceramics, ○T Kinoshita · T Wakabayashi · M Ueki · H Kubo (Nippon Steel Corp)

4-1E23 Study on Fabrication of SiC-Whisker/SiC Composites, ○K Miyahara · T Watanabe · M Ohno · S Koga · T Sasa (IHI Co Ltd)

4-1E24 Effects of Silicon Carbide Whisker Addition on Mechanical Properties of Boride Based Ceramics Composite, ○T Ogata · T Mori · H Kuwajima (Toray Ind Inc)

4-1E25 Effect of Sintering Aids on Mechanical Properties of Carbon Fiber Reinforced B_4C Ceramics, ○H Okuda · K Nakano* · A Kamiya* · Y Kanno** (Tokai Carbon Co Ltd · GIRIN* · Yamanashi U**)

〔Dielectric Ceramics／Dielectrics〕

5-2A01 Influence of Firing Atmosphere on the Cubic-Hexagonal Transition and the Chemical States of Titanium in $BaTiO_3$ with Additions of Various Oxides, N Takeuchi · ○H Tanaka · M Wakamatsu · S Ishida* (Kyoto IT · Chubu U*)

5-2A02 Oxygen Diffusion Coefficients of Ca-Doped Barium Titanate, ○S Kobayashi · H Takagi · Y Sakabe (Murata Mfg Co Ltd)

5-2A03 Diffuse Phase Transition in $BaTiO_3$ Type Ferroelectric Ceramics, ○T Yamamoto · T Sakuma (U Tokyo)

5-2A04 Effect of AC Field on Sintering of TiO_2, ○T Maruyama · T Watanabe · K Goto (TIT)

5-2A05 Crystal Structure of Y_3TaO_7, ○T Tanaka · F Marumo · H Morikawa · K Tanaka · M Yoshimura · Y Yokokawa (TIT)

5-2A06 Synthesis of $BaTiO_3$ Thin Film by Hydrothermal-Electrochemical Method, ○S-E Yoo · M Hayashi* · N Ishizawa · M Yoshimura (TIT · Murata Mfg Co Ltd*)

〔Dielectric Ceramics／Semiconductors〕

5-2A07 Electrical Properties of Grain and Grain Boundary of Sintered $BaTiO_3$ Prepared under Various Heating Conditions Using Some Oxide Insulators, ○H Sumino · N Wakiya · O Sakurai · K Shinozaki · N Mizutani · M Kato (TIT)

5-2A08 Effects of Oxygen Atmosphere Annealing on Electrical Properties of $SrTiO_3$ Ceramics, ○S Ueda · M Fujimoto (Taiyo Yuden Co Ltd)

5-2A09 Sintering of Strontium Titanate in the Presence of Lithium Fluoride, ○I Ueno · Y Wakahata · H Okinaka (Matsushita Electronic Components Co Ltd)

5-2A10 Twin of ZnO Varistor (Ⅰ), ○T Yamamoto · K Okazaki* (NDA · Sagami IT*)

5-2A11 Electrical Properties of Boron Carbide Composite Ceramics (2), ○T Kineri・R Kogiso・Y Kawaguchi (TDK Co Ltd)

〔Dielectric Ceramics/Perovskite-Type Complex〕

5-2A12 Synthesis and Characterization of Perovskite-Type Complex Oxide Compound $Pb(Mg_{1/3}, Nb_{2/3})O_3$, S Hirano・K Kikuta・○W Sakamoto (Nagoya U)

5-2A13 Preparation of Ferroelectric Ceramic Powder and Thin Film from Metal Alkoxides, ○K Okuwada・M Imai・K Kakuno* (Toshiba R&D Center・Yokohama Natl U*)

5-2A14 Reaction Mechanism and Dielectric Properties of Low-Firing Multilayer Capacitor Materials Including Pb $(Mg_{1/2}W_{1/2})O_3$, A Ochi・S Takahashi・K Utsumi・M Shirakata (NEC Corp)

5-2A15 Electric Properties of MLC Based on PLZT Dielectrics, H Tanidokoro (Mitsubishi Mining & Cement Co Ltd)

5-2A16 Preparation and the Dielectric Properties of BL Capacitors Using $Pb(Fe, W)O_3$, ○T Azuma・I Katayama・M Takeo・M Kuwabara (Kyushu IT)

〔Dielectric Ceramics/Low Temperature Fired Dielectrics〕

5-2A17 Dielectric and Insulated Characteristics of Low Fireable Dielectrics, ○Y Imanaka・S Aoki・N Kamehara・K Niwa (Fujitsu Labs Ltd)

5-2A18 Interaction between Glass and Ferroelectric Ceramics, ○H Ayaki・A Ishigami・T Yamaguchi (Keio U)

5-2A19 Investigation of the Properties of Glasses/Al_2O_3 Sintered Composites Containing Fluorides, ○B Ryu・I Yasui (U Tokyo)

5-2A20 Multilayer Ceramic Substrate Containing Dielectric Materials, ○H Takagi・Y Mori・H Tani・Y Sakabe (Murata Mfg Co Ltd)

5-2A21 Properties and Reliability of Capacitors Buried in Low Temperature Cofired Multilayer Ceramic Substrates, ○S Kawaminami・M Kubota・K Ogura (Nihon Cement Co Ltd)

〔Dielectric Ceramics/AlN Ceramics〕

5-2A22 Effects of Powder Characteristics and Shaping Method on Sintering of AlN, ○T Kanemaru・M Yokoi・M Kumagai・T Funahashi・R Uchimura (Kawasaki Steel Corp)

5-2A23 Effects of Sintering Atmosphere on Characteristics of AlN Ceramics, ○A Horiguchi・M Kasori・F Ueno・A Tsuge (Toshiba R&D Center)

5-2A24 Metallization of Aluminum Nitride with a Tungsten Conductor, ○M Tsukada・K Omote・H Yokoyama・N Kamehara・K Niwa (Fujitsu Labs Ltd)

5-2A25 Electric and Mechanical Characteristics of Thin Films on 170 W/mK AlN Substrate, ○N Nakagawa・T Yasumoto・N Iwase・T Nakai (Toshiba Corp)

5-2A26 Joining of AlN Substrate by Active Brazing Alloy, Y Kurokawa・W D Scott*・C Toy* (NEC Corp・U Washington*)

〔Preparation of Ceramics from Gas Phase/Powder〕

1-2B01 Propeties of Aluminum Nitride Synthesized by the Reduced Pressure CVD Technique——Effect of Aluminum Compounds as Starting Materials, ○K Sano・K Itatani・A Kishioka・M Kinoshita (Sophia U)

1-2B02 Synthesis of Composite Powder of AlN and Y-Compound by Fluidized Nitridation Technique, ○N Hotta・I Kimura・M Yoshida・T Aoyama・N Saito (Niigata U)

1-2B03 Synthesis of AlN-Si_3N_4 Composite Powder by Using Fluidized Nitridation Technique and Its Properties, ○N Hotta・I Kimura・M Yoshida・T Aoyama・N Saito (Niigata U)

1-2B04 Ultra Fine Si_3N_4 Powder Observed with a TEM, Y Moriyoshi・S Komatsu・T Ishigaki・S Matsumoto (NIRIM)

1-2B05 Microstructural Change of Amorphous Si-N Fine Powders with a Small Addition of Carbon at High Temperatures, T Amano・T Hirai*・K Izaki** (Sagami IT・Tohoku U*・Mitsubishi Gas Chemical Co Ltd**)

1-2B06 Crystallization and Sintering Behavior of Amorphous Si_3N_4-SiC Composite Particles Produced by Vapor Phase Reaction Method, ○J Hojo・H Shibato・A Kato (Kyushu U)

1-2B07 Preparation of SiC-Si_3N_4 Composite Fine Powders by RF Plasma Technique, ○M Suzuki・Y Nakata・T Okutani A Kato* (GIDL Hokkaido・Kyushu U*)

1-2B08 Synthesis of Ultrafine Tungsten Carbide Powders with RF Thermal Plasma and Their Properties, ○K Sakanaka・T Tsunoda・A Motoe・T Kameyama・K Fukuda (NCLI)

1-2B09 Synthesis of Mo Compounds by the Spray-ICP Technique, M Kagawa・○M Suzuki・T Hirai・Y Syono・T Kameyama*・T Tsunoda*・K Fukuda* (Tohoku U・NCLI*)

1-2B10 (Withdrawn)

〔Preparation of Ceramics from Gas Phase/Oxide Film〕

1-2B11 Formation of Oxide Thin Film by an Activated Reactive Evaporation Method (Part 1), ○H Asano・H Kitaguchi・K Oda・J Takada・A Osaka・Y Miura・T Terushima*・Y Bondo* (Okayama U・Kyoto U*)

1-2B12 Formation of Oxide Thin Film by an Activated Reactive Evaporation Method (Part 2), ○T Okamura・H Kitaguchi*・K Oda*・J Takada*・A Osaka*・Y Miura*・T Terashima**・Y Bando** (Tosoh Corp・Okayama U*・Kyoto U**)

1-2B13 Optical and Electrical Properties of Ceramic Films Doped with Transition-Metal Ions, ○A Takada・S Okamoto (NUT)

1-2B14 Thickness Dependence of Gas Sensor Properties in Tin Oxide Thin Films, ○T Suzuki・T Yamazaki・M Azumaya (Tokyo U Agric T)

1-2B15 Preparation and Characterization of ITO Thin Films 4 : Characterization of the Films Sputter-Deposited in a Water Vapor Atmosphere, ○Y Sawada・N Masuda・N Mizutani*・M Kato* (Tokyo I Polytechnics・TIT*)

1-2B16 Effects of Post-Annealing on the Calcium Phosphate Films Sputterred on Ceramics, ○K Yamashita・K Kitagaki・S Yamada・T Umegaki・T Kanazawa (Tokyo Metropolitan U)

1-2B17 Chemical Vapour Deposition of Ceramic Films Using Metal Alkoxide Compounds, ○T Omura · H Ichimura · K Kobayashi (RIMS Ltd)
1-2B18 (Withdrawn)
1-2B19 Effects of a Small Amount of Impurities on Viscosity of Silica Glass, ○K Maeda · Y Ota · H Nakajima · M Sugizaki (Asahi Glass Co Ltd)
1-2B20 The Relation between Internal Stress and Adhesion of Silicon Oxide Film Formed by Vacuum Vapor Deposition on Plastics, ○Y Fukumoto · T Tsutao · T Uehara (Sekisui Chemical Co Ltd)
1-2B21 Elastic Property of Rf-Sputtered Amorphous Films in the System Al_2O_3-SiO_2 and Al_2O_3-$AlPO_4$, ○T Hanada · Y Bessyo · N Soga (Kyoto U)

[Preparation of Ceramics from Gas Phase/Coating]

1-2B22 Ceramics Coating on C/C Composite for High Oxidation Resistance, ○C Kawai · T Igarashi (Sumitomo Electric Ind Ltd)
1-2B23 Growth Characteristics of CVD SiC/Si_3N_4, ○T Ohashi · E Toya · Y Itoh · M Sumiya (Toshiba Ceramics Co Ltd)
1-2B24 CVD-Silicon Nitride Coating on Sintered-Silicon Nitride Body, ○K Hayashi · A Miyazaki · M Tamura (Toshiba Ceramics Co Ltd)
1-2B25 CVD-Silicon Nitride Coating on Electro-Conductive Ceramics, ○A Miyazaki · K Hayashi · M Tamura · H Tashiro (Toshiba Ceramics Co Ltd)

[Preparation of Ceramics from Liquid Phase/Fiber]

2-2C01 Crystallization Processes in β-Alumina Fibers with Heating, ○T Maki · S Sakka (Kyoto U)
2-2C02 Porous Zirconia Filament from Metal Alkoxides (Ⅱ), Y Ozaki · ○K Kawasaki (Seikei U)
2-2C03 Preparation of Ceramic Fibers by Polymeric Precursor Method (1), ○T Nishio · Y Fujiki* (Unitika · NIRIM*)
2-2C04 *Preparation of Non-Oxide Ceramics Fibers from Metal Alkoxides*, ○M Sekine · H Ikoma · M Mitomo* (Colloid RI · NIRIM*)

[Preparation of Ceramics from Liquid Phase/Passive Coating Film]

2-2C05 Alkali Passivation Mechanism of TiO_2-SiO_2 Coating Films Prepared by the Sol-Gel Method, ○A Matsuda · Y Matsuno · S Katayama · T Tsuno (Nippon Sheet Glass Co Ltd)
2-2C06 Influence of the Alkyl Group on SiO_2 Coating on Steel Sheets, ○K Izumi · M Murakami · H Tanaka · T Deguchi · N Tohge* · T Minami* (Nisshin Steel Co Ltd · U Osaka Pref*)
2-2C07 Corrosion-Resistance of Steel Sheets Coated with SiO_2 by Sol-Gel Method, ○M Murakami · K Izumi · H Tanaka · T Deguchi · N Tohge* · T Minami* (Nisshin Steel Co Ltd · U Osaka Pref*)
2-2C08 Nitridation of Sol-Gel Derived TiO_2 Coating Films, ○M Nishijima · K Kamiya · K Tanaka (Mie U)
2-2C09 Preparation and Properties of SiO_2-ZnO Thin Films by the Sol-Gel Method, ○Y Katayama · T Kawaguchi (Asahi Glass Co Ltd)
2-2C10 Selective Area Formation of Ceramic Films from Liquid Phase by Laser Heating, ○N Morita · T Watanabe · Y Yoshida · H Hanagata* (*Chiba U · Dipsol Chemicals Co Ltd**)

[Preparation of Ceramics from Liquid Phase/Functional Coating Film (1)]

2-2C11 Preparation of Conductive Thin Film by Sol-Gel Method and Electrical Properties, T Tsuchiya · T Sei · ○T Yamauchi (Science U Tokyo)
2-2C12 Preparation and Properties of ITO Thin Films by Sol-Gel Method, ○T Furusaki · X Xueliang · K Kodaira (Hokkaido U)

[Preparation of Ceramics from Liquid Phase/Functional Coating Film (2)]

2-2C13 Electrochemical Synthesis of Complex Metal Oxide Films · ○Y Matsumoto · J Hombo (Kumamoto U)
2-2C14 Preparation and Properties of PZT Thin Films from Metal Alkoxides——DEA System, M Matsuki · Y Matsuda · ○T Suzuki · K Kobayashi · Y Takahashi* (Toray Ind Inc · Gifu U*)
2-2C15 Structure of Amorphous WO_3 Films Prepared in Liquid Phase, ○T Nanba · Y Nishiyama · I Yasui (U Tokyo)
2-2C16 Preparation of $Li_2B_4O_7$ Coating Films by Sol-Gel Method, ○H Yamashita · T Yoko · H Kozuka · S Sakka (Kyoto U)
2-2C17 Hydroxyapatite-Coating by Chemical Reaction of Glass with Aqueous Solution——*Effects of Solution*, T Kokubo · ○Y Abe* · T Yamamuro (Kyoto U · Murata Mfg Co Ltd*)
2-2C18 Preparation and Properties of RuO_2-Based Oxide Films Prepared by Alkoxide Process, Y Takahashi · ○S Nagata · K Takasuga · K Kuramasu* · S Saitoh* (Gifu U · Matsushita Electronic Co*)
2-2C19 *Preparation of Superconducting BYCO Films by the Dipping-Pyrolysis Process*, ○T Manabe · T Kumagai · H Minamiue* · W Kondo · S Mizuta (NCLI · Nihon Kagaku Sangyo*)
2-2C20 Preparation of Bi-Sr-Ca-Cu-O System Superconductor Thin Film Using Metal Alkoxides, ○S Katayama · M Sekine (Colloid RI)

[Preparation of Ceramics from Liquid Phase/Gel Composite (1)]

2-2C21 Sintering Silica Gels Prepared by Sol-Gel Method in the Presence of Organic Polymers, T Shimazaki · Y Machii · K Takei · ○F Hayashi (Hitachi Chemical Co Ltd)
2-2C22 Ammonolysis of Methyl-Group-Containing Silica Gels, ○H Unuma · Y Suzuki · S Sakka* (GIDL Hokkaido · Kyoto U*)
2-2C23 Effect of Titania Addition on Monolithics Silica Gel, ○Y Azuma · N Ohshima (Tokai U)
2-2C24 Effect of Metallic Salts Additives and Composition of Starting Powder on the Properties of Mullite Sintered Body by Sol-Gel Method, ○N Ishibashi · M Tokunaga · H Kobayashi · T Mitamura · T Akiba* (Saitama U · Chichibu Cement Co Ltd*)
2-2C25 Effects of the Partial Hydrolysis Conditions of TEOS on the Crystallization of Mullite Precursors Derived from

Alkoxides, ○H Suzuki・F Anzai・H Saito (Toyota TI)

2-2C26 Effects of Various Solvents on the Pore Size Distribution of Porous Silica by Sol-Gel Process, ○T Horiuchi・T Sugiyama・H Takashima (GIRIN)

2-2C27 Processing of Lightweight Cellular Ceramics by a Sol-Foaming Method, ○T Fujiu・G L Messing* (Nikon・Pennsylvania Stete U*)

〔New Compounds, Potential Materials for New Applications／Layered Compounds〕

6-2D01 Synthesis of Novel Trioctahedral Ni-Smectite, T Iwasaki・○K Torii (GIRIT)

6-2D02 Formation and Phase Transitions of Hydrated Layered Vanadium Oxides, ○Y Oka・N Yamamoto・T Ohtani* (Kyoto U・Okayama U Science*)

6-2D03 Thermal Dehydration and Rehydration Behavior of Adipate-Complexed Layered Calcium Phosphate, H Monma (NIRIM)

6-2D04 New Compounds in the System of Nb_2O_5-H_3PO_4-H_2O, ○N Kinomura・T Tanabe・N Kumada・F Muto (Yamanashi U)

6-2D05 Synthesis of New Type Graphite Intercalation Compounds with Ferric Chloride in Chloroform, ○Y Soneda・M Inagaki (TUT)

6-2D06 Alkali Metal Intercalation into Layer Structured Crystals ZrNX(X=Cl, Br, I), ○M Ohashi・S Yamanaka・M Hattori (Hiroshima U)

6-2D07 Formation Mechanism of $ZrNH_{0.6}$ from Layer Structured Crystal β-ZrNCl, M Ohashi・○H Yamamoto・S Yamanaka・M Hattori (Hiroshima U)

〔New Compounds, Potential Materials for New Applications／Superconductors〕

6-2D08 Superconducting Properties in the $Pb_2Sr_2Ca_{0.0}Y_{0.5}Cu_{3-x}Fe_xO_8$ System, H Niu・N Fukushima・K Ando (Toshiba Corp)

6-2D09 Electrical Properties of Bi-Sr-Ca-Re-Cu-O Systems, ○T Kawano・F Munakata・A Nozaki・H Yamauchi・S Tanaka (Superconductor R Lab)

6-2D10 Preparation of High T_c Superconductor Bi (Pb)-Sr-Ca-Cu-O by Acetate Precursor, ○M-C Kim*・H Haneda・I Tanaka・S-J Park*・S Shirasaki (NIRIM・Seoul Natl U*)

6-2D11 XPS Study of the High-T_c Superconductor in the Pb-Bi-Sr-Ca-Cu-O System, ○M Nagata・T Suenaga・Y Honda・**K Sakai* (Kumamoto Ind RI・Kumamoto IT*)**

6-2D12 Preparation and Evaluation of Bi-Pb-Sr-Ca-Cu-O Ceramics, ○H Yamanaka・M Matsuda・M Takata・T Yamashita・M Ishii* (NUT・Nihon Cement Co Ltd)

6-2D13 Reactivity of $YBa_2Cu_3O_{7-x}$ with Gas Species, M Yoshimura・○S Inoue・N Ishizawa・S Sōmiya (TIT)

6-2D14 Reaction between Superconductive $YBa_2Cu_3O_{7-x}$ and Environmental Gases, ○N Takeuchi・M Wakamatsu・Y Hoshiyama・S Ishida* (Kyoto IT・Chubu U*)

6-2D15 Microstructural Dependence of J_c in YBCO Ceramics, ○H Shimooka・I Katayama・T Inada・M Kuwabara (Kyushu IT)

6-2D16 Preparation of Superconductor $YBa_2Cu_3O_{7-y}$ by Hot Isostatic Press (Part Ⅳ), ○T Araki・Z Kato・N Uchida・K Uematsu・K Saito (NUT)

6-2D17 Fabrication of $Y_1Ba_2Cu_3O_{7-x}$ Ceramics and Composite with High Performance, ○T Yamamoto・G Terui・K Okazaki* (NDA・Sagami IT)

6-2D18 Effect of Extrusion Method for High Critical Current Density of Ceramic Superconductors, ○S Asada・M Takahashi・S Suzuki (NIT)

6-2D19 Microstructural Effects on the Superconductive Properties of Rapidly Quenched Amorphous Films in the Bi Containing Systems, M Yoshimura・○T-H Sung・Y Ohya・N Ishizawa・Z Nakagawa

6-2D20 Preparation of High T_c Superconducting Tapes by Pyrolysis of Organic Acid Salts, T Nakamoto・H Kobayashi・○M Fukushima・T Shiono・E Hosokawa・H Nasu* (Showa Electric Wire & Cable Co Ltd・Mie U*)

6-2D21 Preparation and Characteristics of High T_c Superconducting Film by Spray Pyrolysis Method, ○T Fujimura・M Matsuda・M Takata・T Yamashita・M Ishii* (NUT・Nihon Cement Co Ltd*)

6-2D22 Superconductivity of Bi-Pb-Sr-Ca-Cu-O Ceramics, ○M Matsuda・Y Mizutani・M Takata・T Yamashita*・M Ishii* (NUT・Nihon Cement Co Ltd*)

6-2D23 Fabrication and Evaluation of Y-Ba-Cu-O Superconducting Thick Films by a Doctor Blade Method, ○M Ishii*・M Matsuda・A Ito・M Takata・T Yamashita* (NUT・Nihon Cement Co Ltd*)

6-2D24 Microstructure and Suerconducting Properties of Ag-Sheathed Er-Ba-(K)-Cu-O Tape, ○K Nomura・F Hosono・A Nomoto・T Umezawa・M Seido・T Kamo* (Hitachi Cable Ltd・Hitachi Ltd*)

〔High Toughening Ceramics／Composite〕

4-2E01 Fracture Behaviour of MgO-Stainless Composite, T Nishida・T Shiono, ○H Fujioka・T Nishikawa (Kyoto IT)

4-2E02 Preparation and Properties of B_4C Based Composite (Ⅱ), ○T Yanai・K Niihara (NDA)

4-2E03 Fracture and Fiber Bridging of a 2D-C/C Composite, ○T Miyajima・M Sakai・M Inagaki (TUT)

4-2E04 Abnormality of Young's Modulus for Si_3N_4/SiC Nano-Composites, ○K Niihara・T Hirano・A Nakahira・K Izaki* (NDA・Mitsubishi Gas Chemical Co*)

4-2E05 High Temperature Strength of Si_3N_4-SiO_2 Ceramics, ○J Zeng・O Yamada*・I Tanaka・Y Miyamoto (Osaka U・Osaka Ind U*)

4-2E06 Fabrication and Mechanical Properties of TiB_2-(2 mol % Y_2O_3-ZrO_2)-SiC Sintered Material, ○S Torizuka・H Nishio (NKK)

4-2E07 Superplastic Finishing and Wear Properties in Fine-Grained Al_2O_3/ZrO_2 Composite, ○S Inoue・M Sasagawa・F Wakai* (Riken Corp・GIRIN*)

4-2E08 Synthesis and Properties of SiC-Y_2O_3-Al_2O_3 Composite, ○M Omori · T Hirai · K Nishiyama* (Tohoku U · Science U Tokyo*)

[High Toughening Ceramics/Fatigue]

4-2E09 Mechanical Properties of Mullite Ceramics, ○M Ashizuka · T Okuno · T Honda · Y Kubota* (Kyushu IT · Tosoh Corp*)

4-2E10 (Withdrawn)

4-2E11 Fatigue Behavior of Gas Pressure Sintered Si_3N_4 at Room Temperature, ○T Niwa · K Urashima · Y Tajima · M Watanabe · Y Matsuo (NGK Spark Plug Co Ltd)

4-2E12 Fatigue Behavior of Gas Pressure Sintered Si_3N_4 at High Temperature, ○K Urashima · Y Tajima · M Watanabe · Y Matsuo (NGK Spark Plug Co Ltd)

4-2E13 Effect of Heating Atmosphere on High-Temperature Oxidizing Rates of Sintered Si_3N_4, M Wakamatsu · ○M Ishikawa · S Shimizu · N Takeuchi · Y Nakano (Kyoto IT)

[High Toughening Ceramics/Toughening Mechanism and Evaluation]

4-2E14 An Analysis of Toughening Mechanism in Si_3N_4-SiC Composites, ○G Pezzotti · I Tanaka · T Okamoto · Y Miyamoto (Osaka U)

4-2E15 Toughening Mechanisms of Vapor Grown Carbon Fiber Ceramic Composites, ○T Uchiyama · Y Hoshi · M Endo* (Riken Corp · Shinshu U*)

4-2E16 A Consideration of the Indentation Load Dependence of K_{IC} Values Determined by ISB Technique, ○N Miyata · M Ogawa · H Tamada · H Jinno (Kyoto U)

4-2E17 Statistical Analysis of Carbon Fiber Strength, ○Y Tanabe · A R Bunsell* · M Inagaki** · M Sakai** · E Yasuda (TIT · ENS des Mine de Paris* · TUT**)

[High Toughening Ceramics/Strengthening by Particle Dispersion]

4-2E18 Crack Propagation Behavior of Ceramic Composites, ○T Shiono · T Nishida · M Asano · T Nishikawa (Kyoto IT)

4-2E19 Microstructure and Mehanical Properties of Fine Grained ZTA, ○K Hayashi · K Sakaue · H Konishi (Kyocera Corp)

4-2E20 Controlled Stress-Induced Phase Transformation in ZrO_2/Al_2O_3, ○K Nakane · M Hama (Sumitomo Chemical Co Ltd)

4-2E21 (Withdrawn)

4-2E22 O_2/Ar Gas HIPing and Mechanical Properties of Ce-TZP/Al_2O_3 Composites, T Sato · M Ishitsuka · T Endo · M Shimada (Tohoku U)

4-2E23 Grain-Size Dependence of Fracture Strength for Al_2O_3 Composites, ○A Nakahira · K Niihara (NDA)

4-2E24 Mechanical and Thermo-Mechanical Properties for the MgO/SiC Nano-Composites, ○K Niihara · A Nakahira · H Ueda* · H Sasaki* (NDA · Mitsubishi Mining & Cement Co Ltd*)

4-2E25 Effect of Grain Size on Mechanical Properties of Alumina Doped Polycrystalline Magnesia, K Yasuda · Y Tsuru · Y Matsuo · S Kimura (TIT)

4-2E26 Effects of Lanthanoide Oxide Addition on Sintering of High Purity Fine Mullite Powder, ○N Kosugi · T Mori · Y Kubota (Tosoh Cop)

4-2E27 Toughening of Selected Ceramics by SiC Particle Dispersion, Y Furuse · K Matsuhiro* (Tokyo Electric Power Co · NGK Insulators Ltd*)

4-2E28 Preparation of Zirconia-Toughened Bioactive Glass-Ceramics and Its Mechanical Properties, ○T Kasuga · K Nakajima · T Kasuga · M Yoshida (HOYA Corp)

4-2E29 Mechanical Properties of SiC-Boride Composites, ○S Kohsaka · K Koga (Kyocera Corp)

[Preparation of Ceramics from Gas Phase/Superconductors]

1-3A01 Preparation of Y- and Bi-Oxide-Superconducting Films by CVD and Their Properties, ○H Yamane · H Kurosawa* · A Suhara · T Hirai · K Watanabe · H Iwasaki · N Kobayashi · Y Muto (Tohoku U · Riken Co*)

1-3A02 Preparation of Metal Oxide Thin Films Relating to High-T_c Superconductor by Plasma CVD, ○M Yoshimoto · T Hashimoto* · T Kosaka · K Hukuda** · S Okazaki*** · M Kogoma*** · H Koinuma (TIT · U Tokyo* · Shi-Etsu Chemical Co Ltd** · Sophia U***)

1-3A03 Preparation of Superconducting Multilayered Thin Films by Sputtering, ○M Yoshimoto · T Asakawa* · T Shiraishi* · A Takano · H Nagata** · M Kawasaki*** · H Koinuma (TIT · Tokai U* · Sumitomo Cement Co Ltd** · U Tokyo***)

1-3A04 Preparation of Y- and Bi-oxide Superconducting Thin Films by ECR Plasma Sputtering, ○H Masumoto · T Goto · T Hirai (Tohoku U)

1-3A05 Preparation and Characterization of $YBa_2Cu_3O_x$ Films by Flame Pyrolysis, ○M Koguchi · Y Matsuda · E Kinoshita · K Hirabayashi (Furukawa Electric Co Ltd)

1-3A06 Formation Process of Fine Powders of Bismuth Oxide-Based Superconductors by the Spray-Pyrolysis, ○N Tohge · M Tatsumisago · T Minami · K Okuyama · K Arai · Y Kousaka (U Osaka Pref)

1-3A07 High Temperature Vaporizations of Components in Superconductor Oxides Ceramics, K Sakai · ○S Tashiro · T Sata · T Suenaga* (Kumamoto IT · Kumamoto Ind RI*)

1-3A08 Effects of Oxygen Partial Pressure and Temperature on Oxygen Contents in Superconductor Oxide Ceramics, ○K Sakai · H Fujii · T Sata (Kumamoto IT)

[Preparation of Ceramics from Gas Phase/Non-Oxide Film]

1-3A09 Preparation of SiC Films by ECR-Plasma CVD, ○T Inoue · T Yamamoto · N Hayashi · K Maruyama · K Kamata · I Tanabe (NUT)

1-3A10 Preparation of B_xC by Chemical Vapor Deposition and its Thermoelectric Properties, ○T Seki · C-H Pai · K

Koumoto · H Yanagida (U Tokyo)

1-3A11 Electronic Structure and Properties of B 1 Type $Mo_{1-x}M_xN$ (M=Nb, Ti) Thin Films, ○G-C Lai · M Takahashi · K Nobugai · F Kanamaru (Osaka U)

1-3A12 Crystal Structure and Electronic State of Cu_3N Thin Films Prepared by RF-Sputtering, ○S Izumi · M Takahashi · F Kanamaru (Osaka U)

1-3A13 Microstructure and Properties of AlN Thin Films Prepared by IVD Method, ○A Sawaguchi · K Toda · K Niihara (NDA)

1-3A14 Optical Property of Oxygen Added Reactive Sputtered AlN Thin-Film, ○N Morita · F Ueno · A Tsuge (Toshiba R&D Center)

1-3A15 TiN Deposition Using an Arc Ion Plating, ○H Ichimura · Y Chiba · S Yamamoto · A Kawana · T Omura (Sumitomo Metal Mining Co Ltd)

1-3A16 Adhesion of Arc Ion Plated TiN Film on Steel, ○S Yamamoto · A Kawana · Y Chiba · H Ichimura (Sumitomo Metal Mining Co Ltd)

1-3A17 Corrosion Coatings Using an Arc Ion Plating, ○A Kawana · S Yamamoto · Y Chiba · T Omura · H Ichimura (Sumitomo Metal Mining Co Ltd)

1-3A18 Preparation of TiN Film by Plasma CVD and Its Plasma Diagnostics, ○Y Ishii · T Shibata · H Ichimura · K Kobayashi (RIMS Ltd)

1-3A19 Preparation of Non-Stoichiometric TiN_x by CVD, ○C-C Jiang · T Goto · T Hirai (Tohoku U)

1-3A20 Properties of TiN Films Deposited from Vapor Phase, ○N Inoue · H Kawai* · K Ishima** · M Motoyama (Silver Alloy Co Ltd · Kansai Yushi Co Ltd* · Ind RI Hyogo**)

1-3A21 Synthesis of Boron Nitride Thin Films by CVD Method (Ⅱ), ○I Tamatani · K Kijima · T Uetsuki · K Tanaka (Kyoto IT)

1-3A22 Structure of BN Prepared by ECR Plasma CVD, ○T Tanaka* · T Goto · H Masumoto · T Hirai (Toyo Knife Co Ltd* · Tohoku U)

1-3A23 Synthesis of Cubic Boron Nitride by Microwave Plasma CVD, ○H Saito · N Hayash · K Kamata · I Tanabe (NUT)

1-3A24 Preparation and Characterization of Si-B-N Films by Plasma CVD Ⅱ, ○K Sameshima · N Hayashi · K Kamata · I Tanabe (NUT)

〔Preparation of Ceramics form Liquid Phase/Gel Composite (2)〕

2-3C01 Synthesis of Glasses in the $MgO-SiO_2$ System by a Sol-Gel Method, ○Y Kadogawa · S Shimada (U Kansai)

3-3C02 Synthesis and Some Properties of $Na_2O-ZrO_2-SiO_2$ Glasses by Sol-Gel Method, ○T Hara · S Uegaki · K Wada (Shinko-Pfaudler Co Ltd)

2-3C03 Thermal Treatment of Gibbsite in Glycol, ○M Inoue · Y Kondo · T Inui (Kyoto U)

2-3C04 A New Synthesis of Alumina for Catalyst Support, ○K Maeda · F Mizukami · M Watanabe · N Arai · S Niwa · M Tobe · K Shimizu (NCLI)

〔Preparation of Ceramics from Liquid Phase/Functional Material〕

2-3C05 Preperation of Nd Doped Glasses by Sol-Gel Method, ○T Fujiyama · M Hori (Colloid RI)

2-3C06 Precipitation of Lithium-Molybdenum Oxides from Aqueous Solutions, ○Y Nishikawa · M Inagaki (TUT)

2-3C07 Preparation of CdS Microcrystallite-Doped Silica Glasses by the Sol-Gel Process and Their Optical Properties, ○M Nogami · K Nagasaka (Aichi IT)

2-3C08 Crystallization and Characterization of Beta Alumina Synthesized by Sol-Gel Process, ○K Terabe · S Yamaguchi · A Imai* · Y Iguchi (NIT · Nagoya Muni Ind RI*)

2-3C09 Chemical Processing of Bi-Sr-Ca-Cu-O Superconductor, S Hirano · T Hayashi · ○H Tomonaga (Nagoya U)

2-3C10 Preparation of Bi-Sr-Ca-Cu-O System Superconductors through Sol · Gel Method, Y Masuda · ○T Tateishi* (Kobe Steel Co Ltd · Kobelco RI Inc*)

2-3C11 Synthesis of High T_c Superconductor $YBa_2Cu_3O_{7-y}$ from Metal Alkoxides (V), Y Ozaki · ○K Tamura (Seikei U)

2-3C12 Preparation of V_2O_5-GeO_2 Gels from Metal Alkoxides and Their Properties, K Sudo · ○H Hirashima (Keio U)

2-3C13 (Withdrawn)

〔Preparation of Ceramics from Liquid Phase/Preparation from Melt〕

2-3C14 Glass-Forming Behavior of a Mixed Alkali Silicate Melt Containing Three Kinds of Alkaline Ions, ○K Kawamura · R Ota · J Fukunaga · N Yoshida (Kyoto IT)

2-3C15 Properties of Li-Al-Si-O-N Oxynitride Glass Ceramics, ○H Unuma · Y Suzuki · T Furusaki* · A Miura* · K Kodaira* (GIDL Hokkaido · Hokkaido U*)

2-3C16 Effects of Polymerization Degree on the Electronic States of $Li_2O-P_2O_5$ Glasses, ○Y Kowada · H Adachi · T Minami* (Hyogo U · U Osaka Pref*)

2-3C17 Structure and Thermal Stability of an Oxyfluoride Borate Glass, ○W Kotani · J Fukunaga · R Ota · N Yoshida (Kyoto IT)

2-3C18 Crystallization Behavior of Fluoroaluminate Glasses, ○T Osuka · Y Dai · T Kawaguchi (Asahi Glass Co Ltd)

2-3C19 The Structure Analysis of Ag_3AsS_3 Glass, ○M Okuno · H Sugaya · T Matsumoto (Kanazawa U)

2-3C20 Microstructure of TiO_2 Sintered Body Formed by Self Combustion Method, ○K Urabe · M Koizumi · Y Miyamoto* (Ryukoku U · Osaka U*)

2-3C21 Preparation of NbB and Nb_3B_4 Crystals Using Molten Copper-Flux, ○S Okada · K Hamano · T Lundström* (U Kanagawa · Uppsala U*)

2-3C22 Synthesis of Amorphous Ferrite and Properties, T Tsuchiya · T Sei · ○M Nakamura (Science U Tokyo)

2-3C23 Bioactivity of Magnetite-Containing Glass-Ceramics, T Kokubo · ○Y Ebisawa* · K Oura · T Yamamuro (Kyoto U · Sumitomo Metal Ind*)

2-3C24 Ba-Mica-Containing Glass-Ceramics, ○T Kasuga・T Kasuga・K Nakajima (HOYA Corp)
2-3C25 Interaction of Bioactive Glass-Ceramic A-W with Simulated Body Fluids, ○C Ohtsuki・T Kokubo・T Yamamuro (Kyoto U)
2-3C26 Preparation of Rapidly Quenched Glasses in the System Ag_2O-V_2O_5 and Their Characteristics as Cathode Materials for All Solid State Silver Batteries, ○N Machida・H Handa・T Minami (U Osaka Pref)
2-3C27 Critical Current Densities of Bi-Based High T_c Superconducting Ceramics Prepared by the Melt Quenching Method, ○R Sato・H Meguro・T Komatsu・K Matsusita・T Yamashita (NUT)
2-3C28 Properties and Crystallization Process of Bi-(Pb)-Ca-Sr-Cu-O Glasses, ○N Tohge・S Tsuboi・Y Akamatsu・M Tatsumisago・T Minami (U Osaka Pref)

[High Toughening Ceramics/Sintering]

4-3E01 Effect of ZrO_2 Inclusion Particles on the Sintering, ○R Yazaki・T Kimura・T Yamaguchi (Keio U)
4-3E02 Kinetics of Sintering in Y Doped ZrO_2, ○S Matsuda・H Haneda・A Watanabe・S Shirasaki (NIRIM)
4-3E03 Heat Treatment of SiC Whiskers under N_2 Atmosphere (3), ○K Ichinoseki・K Iwafuchi・T Furuta (Toshiba Ceramics Co Ltd)
4-3E04 The Relation between Sintering and Grain Growth in Silicon Nitride, M Mitomo・○S Uenosono*・F Saito (NIRIM・Kawasaki Steel Corp*)
4-3E05 Sintering Behavior and Mechanical Properties of Silicon Nitride, ○K Tanaka・M Yoshida・K Koga (Kyocera Corp)
4-3E06 Dynamic Compaction of Non-Oxide Ceramic Powders Utilizing Exothermic Reaction, ○A Sawaoka・H Kunishige・Y Horie・T Akashi* (TIT・Sumitomo Coal Mining*)
4-3E07 Hot Isostatic Pressing of Zirconia Dispersed Apatite Ceramics, ○M Takagi・Z Kato・N Uchida・K Uematsu・K Saito (NUT)
4-3E08 Gas Pressure Combustion Sintering of TiB_2-Ni Composite Materials, ○T Takakura・I Tanaka・T Okamoto・Y Miyamoto (Osaka U)
4-3E09 Diamond Ceramics of Nanometer-Size Particles by Shock-Compaction Technique (Ⅲ), ○S Sawai・K Kondo (TIT)
4-3E10 Sintering of Shock-Synthesized Diamond Powder, ○S Sawai・K Kondo・M Akaishi*・N Yamaoka* (TIT・NIRIM*)
4-3E11 Shock Compaction of Ceramic Composites (Ⅱ), ○K Koshikawa・S Sawai・K Kondo (TIT)
4-3E12 Effects of Cr, Fe Additives on Sintering and Solution-Exsolution Phenomenon of Magnesia Ceramics, K Hamano・○T Fukuhara・K Ohmori・S Okada (U Kanagawa)

[High Toughening Ceramics/Oxide]

4-3E13 Preparation of Sinterable CaO-PSZ Fine Powders by Solid State Reaction, ○T Matsui・T Uetsuki・K Tanaka・K Kijima (Kyoto IT)
4-3E14 Properties of Electro-Conductive ZrO_2 Composites, ○Y Fujii・I Kameda・M Mouri・K Yamada (Sumitomo Chemical Co Ltd)
4-3E15 Tensile and Bending Strength of TZP, ○K Noguchi・Y Matsuda・M Oishi・T Masaki*・S Nakayama* (Toray R Center Inc・Toray Ind Inc*)
4-3E16 Phase Transformation of Arc-Melted R-TZP in High-Temperature- and High-Pressure-Water (R=Er, Y, ···), ○M Yashima・M Yoshimura・N Ishizawa・S Somiya (TIT)
4-3E17 The Development of FGM Pipe, ○S Miyazaki・E Tanaka・T Kawai (Yokogawa Electric Corp)
4-3E18 Effects of Heating Conditions on Properties of Magnesia Compacts (2), K Hamano・○T Nakazawa・S Okada (Kanagawa U)
4-3E19 Microstructure and Properties of Mullite Ceramics, ○Y Sawabe・Y Ohya・Z Nakagawa (TIT)
4-3E20 Thermal and Mechanical Properties of Zirconia Composites, ○T Sasaki・M Shiroyama・M Furukawa・T Masaki*・A Tokuda*・M Mizushina* (Nippon Tungsten Co Ltd・Toray Ind Inc*)
4-3E21 Effect of Annealing on the Oxygen Lattice Diffusion in Monoclinic ZrO_2 Doped with Y_2O_3 and MgO, ○Y Ikuma・A Ohtaki・Y Nakao (Kanagawa IT)
4-3E22 Non-Linear Fracture and Slow Crack Growth Observed in Chevron-Notched Bend Testing, Y Okamoto・H Hattori・Y Miyata・K Hayashi・T Nishikawa (Kyoto IT)
4-3E23 In-Situ Observation of Structural Changes of 2.5 mol % Y-TZP by X-Ray Diffraction, ○Y Kitano・Y Mori・A Ishitani・T Masaki*・A Tokuda* (Toray R Center Inc・Toray Ind Inc*)
4-3E24 Phase Relation in the System Al_2O_3-TiO_2, T Ochiai・Y Ohya・Z Nakagawa・M Nakamura* (TIT, Fuji Xerox Co Ltd*)
4-3E25 Fracture Behavior of Alumina Matrix Composite, M Kaji・○S Kohsaka・K Koga (Kyocera Corp)
4-3E26 Characterization of Flows and Their Effect on the Properties of Al_2O_3 Ceramics, ○M Sekiguchi・H Kurita・J-Y Kim・Z Kato・N Uchida・K Uematsu・K Saito (NUT)
4-3E27 Effect of Pressure Control of Slurry Dewatering in Slip Casting, ○S Uchimura・N Uzaki・M Takatsu* (Sinto Kogyo Ltd・NIT*)

News

Review of Fine Ceramics

MITI has reviewed fine ceramics and is to hold the first meeting of the basic problem council of the fine ceramics industry. The discussion items are the future directions of the fine ceramics industry, the issues for technological development, the development of industrial bases such as standardization and data bases, the promotion of regional industries and international cooperation. The environment surrounding the fine ceramics industry has been greatly changed and therefore a review will be made after five years. For the future, a new projection of demand will be made in line with the appearance of high temperature superconductive materials and far infrared ceramics and recent strategies for the development of new products by companies. High performance fine ceramics, new manufacturing processes, and development of the automotive gas turbine will be investigated as issues of new technology development. The fine ceramics industry is steadily growing with the production value of about 800 billion yen in FY1988. However, structural materials to be used for automobile engines and tooling machine parts have grown at a lower rate than expected. MITI plans to make clear measures to increase these materials.

Ceramic Engine

Isuzu Motors Ltd. has announced success in the development and commercialization of an adiabatic turbo compound engine using fully ceramic materials. The company has been developing ceramic adiabatic turbo compound engines with a dual fuel type of gasoline and diesel in order to increase energy efficiency and to have no cooling system and further the development of multi-fuel type engine to utilize methanol and fine coal powder. The engine for both gasoline and diesel can run at 150km/h at 7 to 8000rpm and the combustion efficiency has increased by nearly 30 to 50% over the current engine. The weight can also be reduced to one third. There is no generation of particulates which become a problem for the environment and the generation of nitrogen oxides is also reduced. It will be installed in a commercial car in two years. Multi-fuel type engines will be developed hopefully in three years.

Elucidation of Structure of Artificial Diamond Thin Film

Fujitsu Laboratories, Ltd. has found a method to elucidate the structure of artificial diamond thin film, which is expected to be applicable to electronic devices and optical devices in the future, utilizing nuclear magnetic resonance (NMR). Artificial diamond and natural diamond are given a magnetic field using the NMR method and when the data of absorption and emission of electro-magnetic waves have been measured and compared, the measured results for both samples have been found to differ slightly. It has been discovered from these results considering various models that carbon atoms in the artificial diamond crystal likely bond with several hydrogen atoms.

If measured data can be correlated to models, a method to elucidate the diamond structure will be established. If the structure of diamond crystal and the mechanism of crystal growth can be analyzed in detail, it will lead to the control of impurities and to the development of manufacturing technology for complete diamond crystal with fewer faults.

In-Liquid Granulation of Microsphere Ceramics

Hokkaido University, Muroran Institute of Technology and Showa Shell Sekiyu K.K. have jointly developed a method to manufacture effectively a microsphere ceramic using in-liquid granulation. In-liquid granulation obtains granules by aggregating and pressurizing in a liquid using a second liquid (cross-linking liquid) which does not dissolve in the suspending liquid. It has such features as easy separation of liquid and solid, formation of low-liquid content product, selective granulation and formation of spherical granules. A study group led by Hokkaido University has attempted to investigate the granulation condition in oil and in water with the object of manufacturing zirconia microspheres.

A sintered granule having 1.05 to 1.02 sphericity (ratio of maximum length and width of grain) and 170 to 480μm average size could be obtained by the in-oil granulation with no additive. The method will be utilized as a new granulation method for ceramics.

Indigenous Production of Silicon for Solar Battery

The New Energy and Industrial Technology Development Organization (NEDO) has announced the development of the NEDO direction reduction method to manufacture silicon for solar batteries (polycrystal silicon, 99.9999% purity) from domestic low grade silica sand by molten reduction. Two companies, Nippon Sheet Glass Co., Ltd. and Kawasaki Steel Corp., Ltd. have taken charge of the development. Low grade silica sand (96 to 97% purity) which is abundantly produced in Japan is used for the raw material to manufacture high purity silica (99.9999% purity) which is reduced to silicon of 99.9999% purity. The manufacturing technology for high purity silica from low grade silica sand, manufacturing technology for the reducing agent to make silicon from silica, the operation technology of high yield reducing furnaces and technology to eliminate impurities in silicon have been established. The cost is a half of the conventional method. Polycrystalline silicon solar batteries have been manufactured using silicon obtained by this process. The conversion rate has been tested showing a similar level to that of present solar batteries as high as 14 to 15%.

Short Time Production of Single Crystal of Barium Boride

A joint research group of Prof. F. Marumo of Tokyo Institute of Technology and NEC Corp. has developed technology to manufacture good quality barium boride single crystal, as a new type of non-linear optical material, in a short period of time. Tetra-hydrate of barium boride is molten at high temperature and put in a platinum crucible and the crystal seed is drawn up from the solution at 0.6mm/h with 20rpm. Thus, the production of single crystal having about 28mm total length and 7mm diameter can be achieved. There are two crystalline forms, one (low temperature

phase) showing non-linear pattern and another (high temperature phase) not showing the non-linearity. When the crystal is made directly from high temperature solution, it becomes the high temperature phase. In this case, the solution is made in a super-cooled state to take out the low temperature phase only. Barium boride has high transparency and an excellent property resistant to temperature change and it can shorten the wavelength of solid lasers to the ultraviolet zone. If a precise processing machine is commercialized utilizing this device, it will be possible to improve the integration degree and yield in the manufacturing process of super-LSI to a great extent. According to the Materials Development of NEC Corp., the growth rate of single crystal can be raised to several mm/h. This is more than ten times that of the conventional method enabling cost reductions. The current price level of several hundreds of thousand yen per unit can be reduced to a fifth to a tenth.

New Ceramic Scissors for Barbers

Koransha Co., Ltd. has started the aggressive marketing of new ceramic scissors for barbers with a combination of metal and zirconia. A thin zirconia edge is attached to one edge of metal scissors with an adhesive. The problems of conventional advanced ceramic scissors such as less elasticity which is inevitable for scissors, no soft sharpness and broken edges by the gearing of edges have been overcome. As the edge of zirconia is very hard, another metal edge is naturally sharpened by use retaining sharpness for a long period of time. Zirconia is manufactured by Koransha's own slip casting technology. It has the world's highest bending strength. There are 13 types of scissors depending on the size and shape. The price ranges from 80,000 to 150,000 yen per pair. It is slightly less than twice that of metal scissors.

Photo 1. Ceramic scissors, RANCERA

New Ceramic Turbo Rotor

NGK Insulators Ltd. has jointly with Nissan Motor Co., Ltd. developed a new type ceramic turbo rotor using a ball bearing with a reduced time lag by 10 to 20% over the conventional type and has enhanced high temperature strength. In a conventional ceramic turbo charger, the rotation shaft of turbine rotor contacts the bearing with lubricant. The new type has about half the friction by using a ball bearing. The diameter of the rotor blade is smaller from 55.5 to 51.3mm. The time lag (turbo lag) from stepping on the accelerator to starting the turbo is also reduced by 10 to 20%. A change in the silicon nitride composition of the material has increased the high temperature (1200°C) strength. The bonding part of the ceramics and metal has a stronger bond by changing the metal composition. As a result, it can withstand a temperature up to 1200°C. NGK calls the new type turbo rotor a "second generation ceramic turbo" and is to strengthen marketing activities.

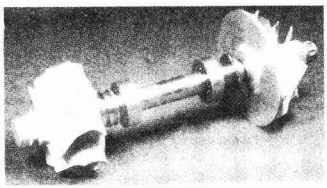

Photo 1. Ball bearing type ceramic turbo rotor

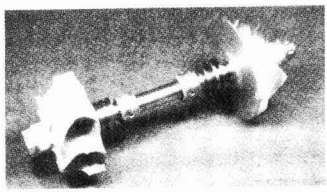

Photo 2. Floating metal type ceramic turbo rotor

Jet-Melt Powder for Strong Bonding of Metal and Ceramics

Nara Kikai Seisakusho Co., Ltd. jointly with the National Institute for Metals of Science and Technology Agency has for the first time succeeded in developing a jet-melt powder which strongly bonds metal and ceramics. The jet-melt powder is manufactured by bonding 50μm aluminum powders with 5μm yttrium powders by static electricity to adhere the yttrium powder on the surface of the aluminum powder. Then the yttrium powder is fixed inside the aluminum powder by mechanical shock. The powder has about 50μm size and is almost spherical. The coefficient of thermal expansion of the jet-melt powder is similar to that of metal and ceramics. Therefore it is suitable for bonding of metal and ceramics. A product using the jet-melt powder for an intermediate layer has withstood thermal shock more than 2000 times. This composite fine powder has improved the contact between metal and ceramics by more than 7 times. It is expected to have uses in the manufacturing of structural parts which require thermal resistance such as car engine parts and turbine engine parts of aircraft.

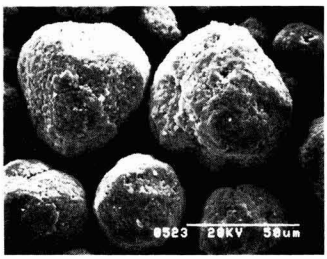

Photo 1. Newly developed jet-melt powders

Spherical Diamond Fine Powder

The National Institute for Research in Inorganic Materials, Science and Technology Agency, has succeeded in synthesizing spherical diamond fine powder using a microwave plasma CVD method which is a popular process for diamond manufacturing and is utilized for making diamond thin film. The methane concentration and the substrate temperature differ from the conventional method. The methane concentration is as high as 10 to 50% using methane gas as a raw material. The substrate temperature at which diamond is deposited is 400° to 600°C which is 400°C lower than usual. The particle size varies with the substrate temperature within less than 1μm. About 0.5μm diamond fine particles are made at 400° to 500°C substrate temperature.

Photo 1. Spherical diamond fine powders

Thrust Power Measurement Using 5.5kVA Superconducting Linear Induction Motor

Prof. O. Tsukamoto, Yokohama National University has developed a prototype 5.5kVA superconducting induction motor using AC NbTi alloy superconducting wire to measure thrust power at room temperature. It was a joint study with The Furukawa Electric Co., Ltd. and Nippon Steel Corp. on the development of AC superconducting equipment. It was the world's first demonstration of an AC superconductor linear motor. It will have a radical impact on the design of transportation systems used for conveyer systems, trucks and other linear motor systems when system control technology, superconducting AC coil designing technology motor design technology, cooling technology, etc., are developed. The test device developed was composed of an AC superconducting coil at the primary side and a metallic plate at secondary side to make a linear induction motor. A 50Hz 3 phases AC current was applied, and the professor measured the thrust power of the AC linear motor when copper, aluminum and stainless steel plates of 1mm thick were used. The thrust power measured was 5.3g at 310A for a copper plate secondary winding. This value is equivalent to 100 times the current and 2500 times the thrust power of ordinary conducting linear motors.

Tunnel Junction Using BSCCO System

Assoc. Prof. Y. Okabe, The University of Tokyo, has, jointly with Assoc. Prof. A. Nakayama, Kanagawa University, succeeded in forming a tunnel junction using the BSCCO system. They have also succeeded in forming a tunnel junction using the yttrium system. For the BSCCO system tunnel junction, bulk BSCCO was used as the substrate or lower electrode on which a gold layer 7nm thick, a 10nm thick magnesium oxide insulator film, and a 200nm thicken niobium upper electrode were evaporated sequentially. The gold film is used to prevent formation of a metamorphic layer caused by diffusion of oxygen from a 10nm deep layer in the surface of the high temperature superconductor. The method to prevent the generation of the metamorphic layer using a precious metal was developed by Prof. Okabe. The gold layer is incorporated with the high temperature superconductor to have superconductivity by the proximity effect. The yttrium system was formed using sputtering. Hystersis peculiar to tunnel junctions and a superconducting Josephson current were observed in experiment at liquid helium temperature. He also observed Schapiro stepping when the junction was irradiated by microwaves. Since a high temperature oxide superconductor has a larger gap voltage when compared with metallic superconductors, the tunnel junction of the BSCCO system permits 10 times faster motion than metallic junctions in principle. The performance of the tunnel junction made by Prof. Dkabe is far from the switching speed expected in theory, however, the experiment demonstrated the possibility of applying oxide superconductors to electronic elements.

New Rolling Process Suitable for Oxide Superconductors

The Metallic Plasticity Processing Laboratory has developed new rolling technology called repeated crossing rolling, which permits fine rolling of oxide superconductors. In this process, the lower roller of a pair vibrates in a fan shape for which the center of the roller is the fulcrum. With this mechanism, the oxide superconductor is ground into a fine powder to allow formation of a high density superconducting wire. The working of oxide superconductor wire uses a oxide superconductor contained in silver or copper tubes. After rolling, these oxides contained in metallic tubes are sintered. The new method rolls the tube while the roller rolls the tube repeatedly to make oxide fine particles.

Progress of R&D on High T_c Superconductors

Publication of R&D results about oxide superconductor has decreased remarkably. There are two kinds of comments on the phenomenon; (1) Companies have begun to control information released; (2) R&D activities have approached a new phase of practical applications.

At the spring meeting of the Japanese Society of Applied Physics, a research leader of The Furukawa Electric Co., Ltd. suggested in an invitation lecture that it had become clear that oxide superconduction would prove its characteristics to be equivalent to those of metallic superconductors now in industrial use. He added also that oxide superconductors would be applied in many fields by the mid-1990s, and designers should begin preparation to design applications for practical use. Since the company has long experience of applying superconductivity to industrial uses, his opinion had a strong impact. His position reflected the recent progress in

H_c and J_c. However, there is no indication that private companies have begun control of the release of information. Many say that the R&D results of basic studies should be evaluated by specialists openly. It is a precompetitive phase, and there is no interest in concealing results of R&D even from the view point of application technology. But R&D is progressing steadily.

Development of an Evaluation System for Oxide Superconductors

Nippon Kokan K. K. has, jointly with Yokogawa Hewlett Packard, Ltd., developed a superconductor characteristic evaluation system. It can measure J_c, H_c, and T_c, ten times faster than the conventional method. It is composed of a cylindrical measurement device 35cm in diameter and 1m high, and a 16-bit microcomputer. The inside of the stainless steel tube of the measurement equipment is a vacuum to prevent convection of heat. It holds the sample container in the center and is supported in liquid nitrogen. A powerful magnet and heater are installed around the sample holder. The current is measured while the magnetic field is gradually changed. The cycle of change in the magnetic field intensity is 20 seconds.

Bench Scale Roller for Oxide Superconductors

Dowa Mining Co., Ltd. has developed a bench scale roller which can be used for the manufacture of oxide superconductor wire. The roller can roll silver or copper tubes of 4 to 8mm in diameter.

Neodium System Oxide Superconductor Does Not Change Its T_c Under High Pressure

Prof. N. Moori, the University of Tokyo, has found that the T_c of a neodium system superconductor does not increase under high pressure, a unique characteristic. He suggested that the neodium system superconductor might have a peculiar crystalline structure causing the characteristic phenomena. In an experiment under 2.5GPa, neodium cerium and copper oxide had a T_c of 22K and no change in the T_c. However, with strontium added the T_c increased by 7K when the pressure went up to 2.5GPa.

Abstracts of Articles on Ceramics from the Selected Journals of the Learned Societies

Funtaikogaku-Kaishi
Vol. 26, No. 3, (1989)
pp. 146 - 150

Preparation of Fine Particles of Superconducting Oxides by Aerosol Reactor

Kikuo OKUYAMA,[†1] Motoaki ADACHI,[†2] Kouji ARAI,[†1] Yasuo KOUSAKA[†1]
Noboru TOHGE,[†3] Masahiro TATSUMISAGO[†3] and Tsutomu MINAMI[†3]

A new process for preparing particles of superconducting oxides is developed by using the aerosol flow reactor in which aqueous solutions of corresponding metal nitrates or acetates are atomized and their droplets are evaporated and thermally decomposed. For Y−Ba−Cu−O system, the particles having orthorhombic $YBa_2Cu_3O_{7-x}$ phase can be formed directly at the decomposition temperatures from 900℃ to 1000℃. The particles obtained are spherical and their size can be changed by changing the concentration of the aqueous solutions. The bodies sintered from these particles show the off-set temperature of superconducting transition at 84 K. For the Bi−Ca−Sr−Cu−O system, the produced particles of the $BiC\text{-}a\ SrCu_2O_x$ composition differ from either 80 K or 110 K phase, whereas the sintered bodies show the X−ray diffraction of the 80 K phase with the on-set temperatures of superconducting transition at 87 K and 110 K.

Key Words : Superconductor, Fine Powder, Aerosol Reactor, $YBa_2Cu_3O_{7-x}$, $BiCaSrCu_2O_x$

Funtaikogaku-Kaishi
Vol. 26, No. 3, (1989)
pp. 151 - 156

The In-situ Measurments of Ultra-Fine Oxide Particles Formed in a Flame

Korekazu UEYAMA,[†1] Keizo TANAKA,[†2] Hideyo KAWAZOE[†3]
Akira IINO,[†3] Yoshikazu MATSUDA[†3] and Shintaro FURUSAKI[†2]

$SiCl_4$ and / or $GeCl_4$ were oxidized in an oxygen-hydrogen flame, and in-situ measurements of oxide particles in the flame were performed by using an Ar^+ ion laser. The following results were obtained : 1) When only $SiCl_4$ was fed into the system, silica particles were formed just above the top of a burner, and the particles were ascending keeping the mean particle size almost constant at 50～60nm in a narrow path without spreading laterally. 2) When only $GeCl_4$ was fed, germania particles formed just above the burner top were vaporized due to the increase in flame temperature, diffused laterally as gaseous molecules, and condensed again to particles as the flame temperature decreased. 3) In the system when both $SiCl_4$ and $GeCl_4$ were simultaneously fed into the flame, the vaporization of Ge decreased considerably.

Key Words : In-situ Measurement, Ultra Fine Particles, Argon Ion Laser, Dynamic Light Scattering, Nucleation

Funtaikogaku-Kaishi
Vol. 26, No. 3, (1989)
pp. 157 - 162

Submicron Ceramic Powder Synthesis by a Fluidized Bed of Microcontainer Particles

Mayumi TSUKADA,[†1] Jun NAITO,[†2] Takako MASUDA[†3]
and Masayuki HORIO[†1]

The concept of a fluidized bed of microcontainer particles is proposed. Although conventional fluidized beds are not good at handling cohesive submicron particles, the use of microcontainer particles enables us to produce and process them in fluidized beds. To examine the proposed concept, the syntheses of nitrogen ceramic powders (Si_3N_4, TiN and AlN) through carbothermal reduction and nitridation were performed in a thin fixed bed and a fluidized bed at 1300～1550℃. In every case, submicron powders were successfully obtained. For Si_3N_4 synthesis, the SiO(g) loss from the fixed bed and the degrees of silica reduction and nitridation were determined as functions of time and temperature. Though the deposition of SiO vapor increased the stickiness of the bed, the bed was fluidized with no problems when the gas flow rate was sufficiently high for bubbling. The SiO vapor deposition in the freeboard was found to be controllable by adjusting particle size and the gas flow rate.

Key Words : Fluidized Bed, Submicron Powder, Microcontainer Particles, Silicon Nitride, Nitrogen Ceramics

Funtaikogaku-Kaishi
Vol. 26, No. 3, (1989)
pp. 169 - 173

Electrostatic Formation of a Ceramic Membrane with Fine Pores

Hideo YAMAMOTO,† Tsuyoshi NOMURA†
and Sen-ichi MASUDA†

A new method for forming a cermamic membrane was devised. Ultrafine particles synthesized by thermally activated CVD(Chemical Vapor Deposition) were deposited on the surface of a porous ceramic supporter by electrostatic force and sintered in an inert gas atmosphere. The ceramic membrane made by this method is available for ultrafiltration because it has very fine pores of about 0.04 micro-meter in diameter but a large porosity.

Key Words : Electrostatic Formation, Ceramic Membrane, CVD, Ultrafine Particle

Funtaikogaku-Kaishi
Vol. 26, No. 3, (1989)
pp. 174 - 178

Synthesis of Composite Fine Particles in the Gas Phase

Shigehisa ENDOH,† Kazuhisa OKUDA,†† Jiro KOGA,††
Shiro MATSUMOTO†† and Kazuo TAKEUCHI†

The objecting was to synthesize fine particles composed with ultra-fine particles by coagulation in the gas phase. The ultra-fine particles of TiO_2 were genarated by the thermal decomposition of titanium tetraisopropoxide vapor. At the temperature of decomposition above 600℃, the TiO_2 particles were anatase, and the size of those were less than 100nm. The ultra-fine particles were mixed and composed of Polystyrene latex particles having a diameter of 1000nm dried after atomization. The polystyrene latex particles were coated by the aggregate of ultra-fine particles. The process of the composition was discussed by using an electrostatic coagulation model.

Key Words : Composite Particles, Ultra-fine Particles, TiO_2, Alkoxide

Journal of the Crystallographic Society of Japan
Vol. 31, No. 8, (1989)
pp. 15

Yoshio MATSUI: High Resolution Transmission Electron Microscope Study of Modulated Structures in Bismuth-Based Superconducting Oxides.

Modulated structures in the new high-T_C superconducting oxides found in a Bi-Sr-Ca-Cu-O system are examined by high resolution transmission electron microscopy. Strong lattice distortions are induced in the $[Bi_2O_2]$ layers to form "Bi-concentrated" and "Bi-deficient" bands in both 80K phase $Bi_2Sr_2CaCu_2O_y$ and 110K one $Bi_2Sr_2Ca_2Cu_3O_y$. These distortion bands are arranged to form body-centered orthorhombic lattices with $b_S = 2.6$nm which is about 4.8 times of the b parameter of the tetragonal sub-structure. *Twinning with twin boundary* at the center of Bi_2O_2 layer is also observed in the 80K phase. The modulated structure in the 20K phase $Bi_2Sr_2CuO_y$ is, on the other hand, described by the monoclinic structure. Structural relations of various modulated structures are discussed.

Journal of the Physical Society of Japan
Vol. 58, No. 3, March, 1989
pp. 779 - 782

^{139}La NQR Study of Electronic States in Metallic Compounds $(La_{1-x}Sr_x)_2CuO_4$

Tatsuo KOBAYASHI, Shinji WADA, Yoshio KITAOKA,†
Kunisuke ASAYAMA† and Kiichi AMAYA†

College of Liberal Arts, Kobe University, Nada, Kobe 657
†Department of Material Physics, Faculty of Engineering Science, Osaka University, Toyonaka, Osaka 560

We measured the temperature dependence of the nuclear spin-lattice relaxation time T_1 of ^{139}La in metallic compounds $(La_{1-x}Sr_x)_2CuO_4$ with $x=0.045$, 0.075, 0.10 (high-T_C superconductors) and $x=0.15$ (nonsuperconductor) by NQR experimentation. T_1 for $x=0.15$ was found to conform to the Korringa relation (T_1T=const.) sufficiently, while the T_1 for $x=0.075$ and 0.10 in the normal state showed slightly stronger temperature dependence and were shorter than that for $x=0.15$, in spite of the increase of hole concentration with increasing x. Fluctuations of Cu d-spins are considered to play an important role for T_1 in superconducting compounds. The relaxation behavior in the compound with $x=0.045$ is also discussed.

Journal of the Physical Society of Japan
Vol. 58, No. 3, March, 1989
pp. 805 - 808

Observation of Secondary Magnetic Transition in Tetragonal $YBa_2Cu_3O_x$ $(6.1 \leq x \leq 6.4)$

Masahiro MATSUMURA, Hideki YAMAGATA, Yoshihiro YAMADA,†
Kenji ISHIDA,†† Yoshio KITAOKA,†† Kunisuke ASAYAMA,††
Hidenori TAKAGI,††† Hiroyuki IWABUCHI††† and Shin-ichi UCHIDA†††

Department of Physics, Faculty of Science, Kochi University, Kochi 780
†Department of Electrical Engineering,
Himeji Institute of Technology, Shosha, Himeji 671-22
††Department of Material Physics,
Faculty of Engineering Science Osaka University, Toyonaka, Osaka 560
†††Engineering Research Institute, Faculty of Engineering,
University of Tokyo, Bunkyo-ku, Tokyo 113

Temperature dependence of nuclear resonance spectra for the chain Cu(1) and the plane Cu(2) sites was investigated in the oxygen-deficient tetragonal $YBa_2Cu_3O_x$ ($6.1 \leq x \leq 6.4$). The divergence of the spin-echo decay rate for the NQR at the Cu(1) site was observed at about 20 K, irrespective of the oxygen concentration, x, in $x \geq 6.2$. Below this critical temperature, only the NQR line broadening becomes significant without any resonance shifts. The spin-echo decay rate for the NMR at the Cu(2) site in the sample with $x=6.2$ also increases divergently when the temperature is raised to the critical temperature. These facts directly indicate the *secondary transition* associated with the moments on the Cu(2) sites at about 20 K, which is well below the Néel temperature. Some discussions are included for the magnetic structure below the transition temperature.

[Cu-NMR, Cu-NQR, $YBa_2Cu_3O_x$, oxygen content, high T_c superconductor]

Journal of the Physical Society of Japan
Vol. 58, No. 3, March, 1989
pp. 813 - 816

Theory of X-Ray Emission in High-T_c Superconductors

Satoshi TANAKA, Kozo OKADA and Akio KOTANI

Department of Physics, Faculty of Science, Tohoku University, Sendai 980

We theoretically study X-ray emission spectra (XES) corresponding to the Cu $3d \rightarrow 2p$ electronic transition in high T_c-superconductors by using the impurity Anderson model with five filled valence bands, and by applying a formula of a coherent second-order optical process. It is shown that XES can be explained consistently with $2p$-XPS and $2p$-XAS by the same model, and that the many-body effect due to d-d Coulomb interaction plays an important role in these compounds.

Journal of the Physical Society of Japan
Vol. 58, No. 3, March, 1989
pp. 1048 - 1053

Anomalous Behavior of ^{1}H Spin-Lattice Relaxation Time in β-(BEDT-TTF)$_2$I$_3$—Possibility of Superconducting Glass

Yutaka MANIWA,* Toshihiro TAKAHASHI, Masashi TAKIGAWA,†,**
Hiroshi YASUOKA,† Gunzi SAITO,† Keizo MURATA,††
Madoka TOKUMOTO†† and Hiroyuki ANZAI††

Department of Physics, Gakushuin University, Mejiro 1-5-1,
Toshima-ku, Tokyo 171
†Institute for Solid State Physics, The University of Tokyo,
Roppongi 7-22-1, Minato-ku, Tokyo 106
††Electrotechnical Laboratory, Tsukuba, Ibaraki 305

Anomalous behavior of ^{1}H spin-lattice relaxation time T_1 in the superconducting state of β-(BEDT-TTF)$_2$I$_3$ is reported. A large enhancement of T_1^{-1} was observed in the high-T_c state under pressure. The enhancement starts to appear around the transition temperature, T_c, and forms a peak well below T_c. The possibility of superconducting glass, which is expected in granular superconductors, is suggested. Partial disorders in the orientations of ethylene groups may be responsible for the glassy behavior.

* Present address: Department of Physics, Tokyo Metropolitan University, Fukazawa 2-1-1, Setagaya-ku, Tokyo 158.
** Present address: Los Alamos National Laboratory, Los Alamos, New Mexico 87545, U.S.A.

Journal of the Physical Society of Japan
Vol. 58, No. 3, March, 1989
pp. 1095 - 1103

High-Energy Spectroscopy in Oxide Superconductors

Kozo OKADA and Akio KOTANI

Department of Physics, Faculty of Science, Tohoku University, Sendai 980

We consistently analyze the Cu $2p$-XPS, L_3-XAS, $3d$-XPS and resonant XPS in high-T_c superconducting materials, such as $(La_{1-x}Sr_x)_2CuO_4$ and $YBa_2Cu_3O_{7-\delta}$, on the basis of the impurity Anderson model. We introduce five valence bands into the model to take account of the anisotropic nature of the Cu $3d$ orbitals and the different $2p$ energy levels for nonequivalent O sites. The key parameter values which characterize these Cu $3d$ and O $2p$ states are estimated from the analysis, and their trends are discussed. We study the effect of hole doping on the $2p$-XPS and L_3-XAS, especially on the polarization dependence of L_3-XAS. For reference, we also analyze the spectra of CuO.

Japanese Journal of Applied Physics
Vol. 28, No. 2, February, 1989
pp. 167 - 173

Highly Efficient, Large-Area Polycrystalline Silicon Solar Cells Fabricated Using Hydrogen Passivation Technology

Kunihiro MATSUKUMA, Sigeru KOKUNAI, Yasuaki UCHIDA, Satoru SUZUKI, Yukoh SAEGUSA, Hideyuki YAGI, Tadashi SAITOH†, Kazuo NISHINOIRI, Ryuichi SHIMOKAWA†† and Keiichi MORITA†††

Hitachi Works, Hitachi, Ltd., Hitachi, Ibaraki 317
†Central Research Laboratory, Hitachi, Ltd., Kokubunji, Tokyo 185
††Electrotechnical Laboratory, Tsukuba, Ibaraki 305
†††Kumamoto Institute of Technology, Ikeda, Kumamoto 860

Highly efficient, large area polycrystalline silicon solar cells have been fabricated using ion implantation as a hydrogen passivation technique. A new high-current ion implanter with a bucket-type ion source has been developed to hydrogenate crystal defects in cast polycrystalline cells. Effective hydrogen passivation of the defects has been realized by implanting hydrogen ions into cast cells from the back surfaces and increasing the hydrogen ion energy and dose. A scanning light beam-induced current image of the polycrystalline cells shows that lowering of the induced current distribution at linear grain boundaries is almost completely eliminated, but not at irregular grain boundaries. The resultant polycrystalline cells exhibit a high conversion efficiency of 15.2% for a large area of 100 cm^2.

KEYWORDS: polycrystalline silicon solar cells, crystal defects in silicon, hydrogen passivation, hydrogen ion implantation, light beam-induced current

Japanese Journal of Applied Physics
Vol. 28, No. 2, February, 1989
pp. 187 - 188

Studies on Photo-Effects in Semiconductor Surfaces

S. S. DE, A. K. GHOSH, T. K. PATTANAYAK, P. K. PAL, J. C. HALDER, A. CHATTERJI and A. LAHIRI

Centre of Advanced Study in Radio Physics and Electronics, University of Calcutta, 1, Girish Vidyaratna Lane, Calcutta-700 009, India

Photo-voltage at the semiconductor surface has been investigated by using a new solution of Poisson-Boltzmann equation. Brattain and Bardeen modex for surface traps has been taken in the formulation. Dependence of normalised surface photo-voltage on surface potential under different carrier densities has been estimated and the results are presented graphically.

KEYWORDS: photo voltage, surface potential

Japanese Journal of Applied Physics
Vol. 28, No. 2, February, 1989
pp. 189 - 194

Optical Properties near the Fundamental Edge of an $AgGaS_2$ Single Crystal

Satoshi KOBAYASHI, Toshiaki OHNO, Nozomu TSUBOI†, Futao KANEKO and Takeo MARUYAMA

Department of Electronic Engineering, Faculty of Engineering, Niigata University, Ikarashi 2-no-cho, Niigata 950-21
†Graduate School of Science Technology, Niigata University, Ikarashi 2-no-cho, Niigata 950-21

The exciton energies of the *A* and *BC* excitons, which correspond, respectively, to the transitions from the uppermost valence band and the lower valence bands to the conduction band, in an $AgGaS_2$ single crystal have been evaluated by analyzing polarized reflectivity spectra in the temperature range 77-294 K. The *A* exciton energy is estimated to be 2.701 eV, in agreement with the findings of other researchers, at 77 K. The energy difference between the *A* and *BC* excitons is 270 meV and almost independent of temperature. Cathodoluminescence spectra have two peaks over the measured temperature range. The one at the higher photon energy is interpreted as the decay of the *A* exciton in consideration of the electron-beam voltage dependence on the peak position.

KEYWORDS: $AgGaS_2$, exciton energy, Lorentzian oscillator, reflectivity spectrum, transmission spectrum, cathodoluminescence

Japanese Journal of Applied Physics
Vol. 28, No. 2, February, 1989
pp. 195 - 199

Formation of Quasicrystalline Aluminium-Vanadium and Aluminium-Chromium Fine Particles by Gas-Evaporation Technique

Tsugio OKAZAKI, Takasi MAKI†, Yahachi SAITO† and Kazuhiro MIHAMA†

Department of Physics, Meijo University, Nagoya 468
†Department of Applied Physics, Nagoya University, Nagoya 464

Fine particles in icosahedral phase have been prepared by the gasevaporation method, and studied by electron microscopy. The particles are spherical ranging from 20 to 300 nm in diameter and show a characteristic contrast with an irregular striation. Edge lengths of the fundamental hexahedron in the Penrose tiling are 0.474 ± 0.002 nm in the Al-V system and 0.473 ± 0.003 nm in the Al-Cr system. Though most of the quasicrystalline particles are in a single phase,

composite particles of the icosahedral phase and the crystalline phase(β-Al_4V) are also observed in the Al-V system. From the orientation relationship between the two phases, atomic sites of vanadium in the icosahedral phase are discussed.

KEYWORDS: quasicrystal, aluminium-vanadium, aluminium-chromium, electron microscope, fine particle, gasevaporation method, Penrose tiling

Japanese Journal of Applied Physics
Vol. 28, No. 2, February, 1989
pp. 200 - 209

Growth Mechanism of GaAs during Migration-Enhanced Epitaxy at Low Growth Temperatures

Yoshiji HORIKOSHI and Minoru KAWASHIMA

NTT Electrical Communications Laboratories, Musashino-shi, Tokyo 180

The growth process of GaAs during migration-enhanced epitaxy at low temperatures is investigated using reflection high-energy electron diffraction. Observation of specular beam intensity during growth reveals that a flat growing surface is maintained at 300°C even when the number of Ga atoms deposited per cycle is not equal to the surface site number. The composition at the growing surface can deviate considerably from stoichiometry at low temperatures because of excess As adsorpt ion. This problem is avoided by optimizing the number of As_4 molecules deposited per cycle. The optimum number of As_4 molecules was discussed with respect to the number of Ga atoms on the growing surface.

KEYWORDS: molecular beam epitaxy, beam modulation, migration enhancement, stoichiometrie growth, RHEED specular beam

Japanese Journal of Applied Physics
Vol. 28, No. 2, February, 1989
pp. 219 - 222

Properties of Aluminum-Doped ZnO Thin Films Grown by Electron Beam Evaporation

Akio KUROYANAGI

Department of Electronic Engineering, Institute of Vocational and Technical Education, 1960 Aihara, Sagamihara, Kanagawa 229

Highly conductive thin films of ZnO have been prepared by conventional electron beam evaporation on glass substrates. The Al_2O_3 content of 0-5 wt% was added as dopant into ZnO to decrease resistivity of ZnO films. An Al-doped ZnO film with a resistivity of 1.0×10^{-3} Ωcm is obtained at a substrate temperature of 300°C with 1.0 wt% Al_2O_3 content; transmittance of this film is above 90% in the visible range with 100 nm thickness. The ZnO source material doped with Al_2O_3 is evaporated efficiently by a lower electron beam power compared to the case of nondoped ZnO. The *c*-axis orientation of ZnO films is facilitated by the addition of Al_2O_3 and the *c*-axis of Al-doped ZnO films is oriented perpendicular to glass substrates in the substrate temperature range of 60°C-350°C.

KEYWORDS: Al-doped ZnO, electron beam evaporation, conductive, transparent, oxide thin films, experimental study

Japanese Journal of Applied Physics
Vol. 28, No. 2, February, 1989
pp. 299 - 300

An Improved Optical Lever Technique for Measuring Film Stress

Takeshi AOKI, Yasuo NISHIKAWA and Seiichi KATO

Department of Electronic Engineering, Tokyo Institute of Polytechnics, Atsugi 243-02

This letter describes a simple and accurate method of measuring film stress. This method differs principally from the conventional optical lever method in utilizing two parallel beams instead of translating a sample. The apparatus assembled experimentally demonstrates a detectable deflection of the sample on the order of 1 μm.

KEYWORDS: optical lever, film stress, substrate curvature

Japanese Journal of Applied Physics
Vol. 28, No. 2, February, 1989
pp. L176 - L178

Critical Current Density and Coupling Nature of Grains in Textured Bi(Pb)-Sr-Ca-Cu-O Superconductors

Hiroaki KUMAKURA, Kazumasa TOGANO, Hiroshi MAEDA, Eiji YANAGISAWA† and Takeshi MORIMOTO†

National Research Institute for Metals, Tsukuba Laboratories, 1-2-1, Sengen, Tsukuba-City, Ibaraki 305
†Asahi Glass Research Center, Asahi Glass Co. Ltd., 1150, Hazawa-cho, Kanagawa-ku, Yokohama, Kanagawa 221

The $J_c - H$ property of Bi-Sr-Ca-Cu-O tape was improved by a combination of the doctor blade and cold working preparation processes. A.C. complex susceptibility measurement indicates that this improved property is attributable to the improvement in the intergrain coupling along the current direction due to the grain orientation alignment in the tape.

KEYWORDS: oxide superconductor, Bi-Pb-Sr-Ca-Cu-O, doctor blade process, cold working, texturing, critical current density, complex susceptibility, weak coupling

Japanese Journal of Applied Physics
Vol. 28, No. 2, February, 1989
pp. L179 - L182

Electron Tunneling Measurements of High-T_c Superconductor Bi-Sr-Ca-Cu-O by STM

Tetsuya HASEGAWA, Hideyuki SUZUKI, Seiji YAEGASHI†, Hidenori TAKAGI††, Kohji KISHIO, Shin-ichi UCHIDA††, Koichi KITAZAWA and Kazuo FUEKI†††

Department of Industrial Chemistry, University of Tokyo, Hongo, Bunkyo-ku, Tokyo 113
†Central Research Laboratories, Nippon Mining Co. Ltd., Niizo-Minami, Todashi 335
††Engineering Research Institute, University of Tokyo, Hongo, Bunkyo-ku, Tokyo 113
†††Department of Industrial Chemistry, Science University of Tokyo, Yamazaki, Nodashi 278

The tunneling spectra of $T_c = 80$ K single crystal and 110 K polycrystalline specimens have been measured at 4 K using a scanning tunneling microscope with a tungsten counter electrode. For the 80 K phase, we estimated the energy gaps $2\Delta/k_BT_c$ to be 4.9–5.3 and 4.2–5.0 in the directions perpendicular and parallel to the *a-b* plane, respectively, while $2\Delta/k_BT_c$ for the 110 K phase was in the range of 3.4–4.2. The energy gap data obtained in the present study will be discussed in terms of the anisotropy and coupling strength of the superconductivity.

KEYWORDS: scanning tunneling microscope, low temperature, Bi-Sr-Ca-Cu-O, conductance-voltage characteristics, superconducting gap, gap anisotropy, coupling strength

Japanese Journal of Applied Physics
Vol. 28, No. 2, February, 1989
pp. L187 - L189

Hole Donors in the High-T_c Phase of a Bi-Pb-Sr-Ca-Cu Oxide Superconductor

Hitoshi NOBUMASA, Takahisa ARIMA, Kazuharu SHIMIZU, Yuji OTSUKA†, Yukio MURATA† and Tomoji KAWAI††

Composite Material Lab., Toray Ind. Inc., 2-1, Sonoyama 3-chome, Otsu, Shiga 520
†Toray Research Center Inc. 1-1, Sonoyama 1-chome, Otsu, Shiga 520
††The Institute of Scientific and Industrial Research, Osaka University, Ibaraki, Osaka 567

The locations of Sr atoms in a crystal of the Bi-Pb-Sr-Ca-Cu oxide superconductor consisting of the high-T_c phase were studied by high-resolution analytical electron microscopy (HRAEM) with a spatial resolution of 17 Å using a probe 5 to 10 Å in diameter. The HRAEM showed that not only Pb atoms, but also Sr atoms were located in the Bi-O layers, indicating that these atoms might be hole donors in the Bi-Pb-Sr-Ca-Cu-O superconductor.

KEYWORDS: Bi-Pb-Sr-Ca-Cu oxide superconductor, high-T_c phase, high-resolution analytical electron microscopy (HRAEM), hole donor

Japanese Journal of Applied Physics
Vol. 28, No. 2, February, 1989
pp. L190 - L192

Composition Dependence on the Superconducting Properties of Bi-Pb-Sr-Ca-Cu-O

Utako ENDO, Satoshi KOYAMA and Tomoji KAWAI†

Research and Development Department, Chemical Division, Daikin Industries, Ltd., Nishi-hitotsuya, Settsu-shi, Osaka 566
†The Institute of Scientific and Industrial Research, Osaka University, Mihogaoka, Ibaraki, Osaka 567

Superconductors with a nominal composition close to the ideal high-T_c phase, $(Bi, Pb)_2Sr_2Ca_2Cu_3O_y$, were prepared to study the effect of composition variation on the superconducting properties. It was found that the deviation from the ideal composition delicately affects the $T_c(0)$, and that even a small surplus of Ca and Cu is enough to make it lower to around 95 K. In order to obtain a pure 110 K phase which allows a large current flow to yield a $T_c(0)$ above 100 K, the composition must be strictly controlled around Sr:Ca:Cu = 2:2:3 with the smallest excess of Ca and Cu. Lead was revealed to occupy Bi sites supplying positive holes to the system along with Sr defects.

KEYWORDS: Bi-Pb-Sr-Ca-Cu-O superconductor, high-T_c phase, composition dependence, hole donor

Japanese Journal of Applied Physics
Vol. 28, No. 2, February, 1989
pp. L193 - L196

Superconductivity in the $Bi_2Sr_{3-x}Ln_xCu_2O_y$ System and the Excess of Hole Concentration in $Bi_2Sr_2Ca_nCu_{1+n}O_y$ ($n = 0$ and 1)

Tohru DEN† and Jun AKIMITSU

Department of Physics, Aoyama-Gakuin University, Chitosedai, Setagaya, Tokyo 157
†Canon Research Center, Morinosato-Wakamiya, Atsugi-shi, Kanagawa 243-01

A new family of high-T_c superconductors of $Bi_2Sr_{3-x}Ln_xCu_2O_y$ (Ln = Pr, Nd, Sm, Eu, Gd, Tb, Dy, Ho, Er, Tm and Y) has been found by means of resistivity and magnetization measurements. The highest superconducting transition temperature was obtained when the substitution concentration x was about 0.3. The X-ray powder diffraction measurement showed that $Bi_2Sr_{2-x}Ln_xCuO_y$ (221 phase) is stable for $x < 0.3$ and $Bi_2Sr_{3-x}Ln_xCu_2O_y$ (232 phase) becomes major when x exceeds 0.3. The 232 phase has the same structure as $Bi_2Sr_2CaCu_2O_y$. It is also demonstrated that the hole number p of $[Cu\text{-}O]^{+p}$ in $Bi_2Sr_2CuO_y$ and $Bi_2Sr_2CaCu_2O_y$ is excessive compared with the proper value giving the highest T_c.

KEYWORDS: oxide superconductor, Bi-Sr-Ln-Cu-O system

Japanese Journal of Applied Physics
Vol. 28, No. 2, February, 1989
pp. L197 - L199

Superconducting Transition Temperature of the Quenched $Bi_{0.96}Pb_{0.24}SrCaCu_{1.6}O_x$: 110 K Phase

Takekazu ISHIDA

Department of Physics, Faculty of Science, Ibaraki University, Mito 310

The superconducting transition of a 110 K Bi compound has been examined as a function of quenching temperature T_q. We found that T_c is insensitive to T_q below 650°C. This is in marked contrast with the drastic T_c variation of low-T_c phase reported previously. But the influence of quenching on normal-state conduction resembles that in the case of the low-T_c phase. This situation is difficult to fathom. We propose the possibility that T_c is governed by a central layer of three CuO_2 stackings.

KEYWORDS: Bi-based oxide, high-T_c phase, quenching, transition temperature

Japanese Journal of Applied Physics
Vol. 28, No. 2, February, 1989
pp. L200 - L202

Superconductivity of New Compounds in the Systems Tl-Ln-Sr-Cu-O (Ln=Pr and Nd) and Tl-Pb-Ln-Sr-Cu-O (Ln=Pr, Nd and Sm)

Takao ITOH and Hiroshi UCHIKAWA

Ceramics Research Laboratory, Onoda Cement Co., Ltd., 1-1-7 Toyosu, Koto-ku, Tokyo 135

Superconductivity of new compounds with the T_c at about 40 K in the Tl-Ln-Sr-Cu-O (Ln=Pr and Nd) and the Tl-Pb-Ln-Sr-Cu-O (Ln=Pr, Nd and Sm) systems has been revealed through the temperature dependence of the resistivity and ac susceptibility. Introduction of PbO into the Tl-Ln-Sr-Cu-O system is found to stabilize the superconducting phase. The structure of the material in the Tl-Pb-Ln-Sr-Cu-O system can be regarded as tetragonal, and the composition may be described as (Tl, Pb)(Ln, $Sr)_2CuO_x$ with the Ln/Sr molar ratio of 0.5.

KEYWORDS: high-T_c superconductor, Tl-Ln-Sr-Cu-O, Tl-Pb-Ln-Sr-Cu-O, resistivity, synthetic method, composition

Japanese Journal of Applied Physics
Vol. 28, No. 2, February, 1989
pp. L203 - L206

EXAFS Study on Fe-Doped $YBa_2Cu_3O_y$

Akihisa KOIZUMI, Hironobu MAEDA†, Naruhiko BAMBA, Hiroshi MARUYAMA, Eiji TAKAYAMA-MUROMACHI††, Jun SHI, Kazuaki SHIMIZU, Michinobu MINO and Hitoshi YAMAZAKI

Department of Physics, Faculty of Science, Okayama University, Tsushima, Okayama 700
†Department of Chemistry, Faculty of Science, Okayama University, Tsushima, Okayama 700
††National Institute for Research in Inorganic Materials, 1-1 Namiki, Tsukuba 305

An extended X-ray absorption fine structure (EXAFS) method was applied to $YBa_2Cu_{3-x}Fe_xO_y$ with x=0.05, 0.1, 0.2, 0.3, 0.4 and 0.5. Fe atoms are surrounded by six oxygen atoms with a distance of about 1.85 Å, and they mainly substitute for the Cu(1) site over the whole concentration range. The local structures around Cu atoms and Y atoms are also reported.

KEYWORDS: oxide superconductor, Y-Ba-Cu-O, Fe substitution, EXAFS, local structure

Japanese Journal of Applied Physics
Vol. 28, No. 2, February, 1989
pp. L207 - L208

New Oxide Superconductor: $CaSr_2(Cu_{0.83}Bi_{0.17})_3O_Z$

E. L. BELOKONEVA, L. I. LEONYUK, N. I. LEONYUK, V. V. MOSHCHALKOV†, A. A. GIPPIUS† and Ho Hyu NYAN†

Department of Geology, Laboratory of High Tc Superconductivity, Moscow State University, Moscow 117234, USSR
†Department of Physics, Moscow State University, Moscow 117234, USSR

The new high T_c oxide superconductor $CaSr_2(Cu_{0.83}Bi_{0.17})_3O_Z$ has been found with T_c=75 K in as-grown single crystals and lattice parameters a=3.802 Å, b=12.901Å, c=3.296 Å and γ=107.14°.

KEYWORDS: high T_c superconductivity, single crystal, crystal structure

Japanese Journal of Applied Physics
Vol. 28, No. 2, February, 1989
pp. L209 - L212

Synthesis of Bi-Sr-Ca-Cu-O Ceramics with Large Intergrowth Defects

Seiji ADACHI, Hirohumi HIRANO, Yukihiro TAKAHASHI, Osamu INOUE and Syunichiro KAWASHIMA

Central Research Laboratory, Matsushita Electric Industrial Co., Ltd., 3-15 Yagumo-Nakamachi, Moriguchi, Osaka 570

Superconducting Bi-Sr-Ca-Cu-O ceramics with intergrowth defects larger than 1.8 nm in half of the c-axis length were synthesized at a nominal composition of $Bi_2Sr_2Ca_4Cu_{6.3}O_y$. Electrical resistance and a.c. susceptibility for the

ceramics were measured. No indication of a T_c higher than 110 K was obtained.

KEYWORDS: high-T_c superconductor, oxide superconductor, Bi-Sr-Ca-Cu-O, intergrowth defect

Japanese Journal of Applied Physics
Vol. 28, No. 2, February, 1989
pp. L213 - L216

Crystallization Behavior and Partially Melted States in Bi-Sr-Ca-Cu-O

Yoshio OKA, Naoichi YAMAMOTO, Hitoshi KITAGUCHI†, Kiichi ODA† and Jun TAKADA†

Department of Chemistry, College of Liberal Arts and Sciences, Kyoto University, Kyoto 606
†Department of Applied Chemistry, Okayama University, Okayama 700

High-temperature X-ray measurements were carried out on Bi-Sr-Ca-Cu-O. It was found that the 30 Å phase showed incongruent melting forming new crystalline phases which differed depending on the compositions. Crystallization from the melt by cooling first produced the 30 Å phase on solidification and then the 24 Å phase crystallized around 730°C. Crystallization from the glassy phase by heating started at 430°C and led to the 24 Å phase, which changed to the 30 Å phase above 800°C. As a rule, low-temperature crystallization from the amorphous phase takes place below 730°C to form the 24 Å phase in Bi-Sr-Ca-Cu-O.

KEYWORDS: Bi-Sr-Ca-Cu-O system, high-temperature X-ray measurement, incongruent melting, partial melt, crystallization

Japanese Journal of Applied Physics
Vol. 28, No. 2, February, 1989
pp. L217 - L218

A New Method for Improving the Superconducting Transition Temperature of Platy $ErBa_2Cu_3O_{7-\delta}$ Single Crystals

Shigeyuki HAYASHI, Takashi OHNO, Tetsuo INOUE and Hiroshi KOMATSU

Institute for Materials Research, Tohoku University, Sendai 980

Platy $ErBa_2Cu_3O_{7-\delta}$ single crystals grown from a high-temperature solution were improved to high-quality superconducting crystals of T_c (mid point) ~ 90 K by annealing with CrO_3 as an oxidizing agent.

KEYWORDS: new method, high-T_c superconductors, $ErBa_2Cu_3O_{7-\delta}$, single crystals

Japanese Journal of Applied Physics
Vol. 28, No. 2, February, 1989
pp. L219 - L221

Phase Diagram and Crystal Growth of $NdBa_2Cu_3O_{7-y}$

Kunihiko OKA, Masatoshi SAITO*, Masahiro ITO*, Kenji NAKANE**, Keizo MURATA, Yoshikazu NISHIHARA and Hiromi UNOKI

Electrotechnical Laboratory, Umezono 1-1-4, Tsukuba, Ibaraki 305

The phase diagram of a binary system between $NdBa_2Cu_3O_7$ and $3BaCuO_2 \cdot 2CuO$ has been studied. A liquidus line which is favourable for obtaining $NdBa_2Cu_3O_7$ single crystals from solution is found to exist in a rather wide range compared with that of $YBa_2Cu_3O_7$. Single crystals of $NdBa_2Cu_3O_{7-y}$ have been grown by both the slow-cooling method and the top-seeded solution growth (TSSG) method, in accordance with the obtained phase diagrams of the $NdBa_2Cu_3O_7$-$3BaCuO_2 \cdot 2CuO$ system and our earlier Y_2O_3-CuO-BaO system.

KEYWORDS: superconductivity, phase-diagram, crystal growth, $NdBa_2Cu_3O_{7-y}$, magnetization, electric conductivity

Japanese Journal of Applied Physics
Vol. 28, No. 2, February, 1989
pp. L222 - L225

Surface Analysis of $YBa_2Cu_3O_x$ and Bi-Sr-Ca-Cu-O Superconductors by Auger Electron Spectroscopy

Heizo TOKUTAKA, Satoru KISHIDA, Katsumi NISHIMORI, Naganori ISHIHARA, Yoshihide WATANABE, Yoshio NOISHIKI and Tomoji KAWAI†

Department of Electronics, Faculty of Engineering, Tottori University, Koyama, Tottori 680
†The Institute of Scientific and Industrial Research, Osaka University, Mihogaoka, Ibaraki, Osaka 567

The $YBa_2Cu_3O_x$ superconductors show critical temperatures at around 90 K. Although they are prepared from the different starting materials, they however exhibit similar intensities of AES spectra. For the superconductors of Bi-Sr-Ca-Cu-O and (Bi, Pb)-Sr-Ca-Cu-O, the AES intensity ratios of Ca/Sr increase when their critical temperatures increase. When the AES intensity ratios are transformed into the composition ratios using the sensitivity factor, the volume fractions of the phases of the critical temperatures (7 K, 80 K and 110 K) can be estimated from these ratios and the ideal composition ratio of each phase.

KEYWORDS: superconductor, Auger electron spectroscopy, X-ray diffraction, resistance-temperature characteristics, films, ceramics, Y-Ba-Cu-O, Bi-Sr-Ca-Cu-O, (Bi, Pb)-Sr-Ca-Cu-O

Japanese Journal of Applied Physics
Vol. 28, No. 2, February, 1989
pp. L226 - L228

Preparation of the High-T_c Superconductive Bi-Pb-Sr-Ca-Cu-O Film by Pyrolysis of Organic Acid Salts

Hiromasa SHIMOJIMA, Keizou TSUKAMOTO and Chitake YAMAGISHI

Central Research Laboratory, Nihon Cement Co., Ltd., 1-2-23, Kiyosumi, Koutouku, Tokyo 135

The high-T_c superconductive Bi-Pb-Sr-Ca-Cu-O film on Ag substrate was prepared by the pyrolysis of organic acid salts. The temperature for the high-T_c phase formation was 830-835°C in air. The film heated at 832°C contained a large amount of the high-T_c phase (2223 phase).

KEYWORDS: high-T_c superconducting film, Bi-Pb-Sr-Ca-Cu-O system, pyrolysis of organic acid salts

Japanese Journal of Applied Physics
Vol. 28, No. 2, February, 1989
pp. L229 - L232

Preparation of High-T_c Bi-Sr-Ca-Cu-O Films on MgO Substrates by the Liquid Phase Epitaxial (LPE) Method

Hiroyuki TAKEYA and Humihiko TAKEI

Institute for Solid State Physics, University of Tokyo, 7-22-1 Roppongi, Minato-ku, Tokyo 106

Thin films of high-T_c superconductor $Bi_2Sr_2CaCu_2O_x$ were prepared on MgO(100) substrates by a liquid phase epitaxial method. Several kinds of fluxes were applied for preparation of $Bi_2Sr_2CaCu_2O_x$ thin films, and KCl was found to be the best among them. The film consisted of two phases, $Bi_2Sr_2CaCu_2O_x$ and $Bi_2Sr_2CuO_x$. The onset T_c in the superconducting transition was at 95 K in an as-grown state, but zero resistivity was not observed over 50 K.

KEYWORDS: Bi-Sr-Ca-Cu-O superconductor, liquid phase epitaxy, superconducting film, KCl flux, misfit parameter

Japanese Journal of Applied Physics
Vol. 28, No. 2, February, 1989
pp. L233 - L235

XPS Study of Bi-Sr-Ca-Cu-O Superconducting Thin Films Prepared by the rf-Sputtering Method

Atsuo FUKUI, Hiroyuki ENOMOTO, Hidetaka NATSUME, Yoshiki TAKANO†, Natsuki MORI†† and Hajime OZAKI

Department of Electrical Engineering, Waseda University, Ohkubo 3-4-1, Shinjuku-ku, Tokyo 169
†Department of Physics, Nihon University, Kanda-Surugadai 1-8, Chiyoda-ku, Tokyo 101
††Department of Electrical Engineering, Oyama National College of Technology, Ohaza-Nakakuki 771, Oyama 323

The charge fluctuation of Cu ions in the superconducting Bi-Sr-Ca-Cu-O system was investigated using X-ray photoemission spectroscopy in thin films prepared by the rf-sputtering method. It was confirmed that long-time annealing was essential to form the high-T_c phase in thin films of this Bi-Sr-Ca-Cu-O system. From the peak decompositions of the Cu $2p_{3/2}$ core-level spectra obtained after Ar ion etching, the content ratio of the Cu^{2+} state to the Cu^{+} state was found to increase with an increase of the high-T_c phase content in the films.

KEYWORDS: high-T_c superconductor, Bi-Sr-Ca-Cu-O system, thin film, rf-magnetron sputtering, XPS, Cu $2p_{3/2}$ core-level spectra

Japanese Journal of Applied Physics
Vol. 28, No. 2, February, 1989
pp. L236 - L238

Effect of Indium-Tin Oxide Buffer Layers on Superconducting Y-Ba-Cu-O Thin Films with Glass Substrates

KOZO FUJINO

Central Research Laboratory, Nippon Sheet Glass Co., Ltd., 1, Kaidoshita, Konoike, Itami, Hyogo 664

Indium-tin oxide (ITO) thin films were examined as a buffer layer between high-T_c superconducting Y-Ba-Cu-O thin films and glass substrates. It was found that ITO film can become a diffusion barrier between the superconducting film and glass substrate, and that it does not cause any cracks in Y-Ba-Cu-O film if an appropriate silicate glass substrate is chosen. The superconducting film deposited on ITO/Glass below 700°C has shown onset transition temperatures up to 91 K and zero resistivity temperatures at 50 K.

KEYWORDS: indium-tin oxide,transparent conductive film, buffer layer, superconducting film, Y-Ba-Cu-O, glass substrate

Japanese Journal of Applied Physics
Vol. 28, No. 2, February, 1989
pp. L239 - L240

Superconducting Y-Ba-Cu-O Thick Films on Silicon and Alumina Substrates Prepared by the Plasma Spraying Method

Natsuki MORI, Yasuhiko ITOI† and Masaru OKUYAMA†

Department of Electrical Engineering, Oyama National College of Technology, Nakakuki, Oyama 323

†*Department of Industrial Chemistry, Oyama National College of Technology, Nakakuki, Oyama 323*

Thick films of Y-Ba-Cu oxides were prepared on silicon and alumina substrates by the plasma spraying method. As-sprayed films were semiinsulating, and postoxidation was necessary to obtain superconducting films. It was found that the content of copper in the starting material powder is important in producing good-quality samples with onset T_c's around 90 K.

KEYWORDS: superconducting thick films, Y-Ba-Cu oxide, plasma spraying method

Japanese Journal of Applied Physics
Vol. 28, No. 2, February, 1989
pp. L241 - L243

A New Fabrication Process for High-T_c Superconducting Oxide Ceramic Fibers

Hajime KONISHI, Takumi TAKAMURA, Hisashi KAGA and Keiichi KATSUSE

Hokkaido Industrial Technology Center, Hakodate 041

A new fabrication process for superconducting oxide ceramic fibers, the alginate method, is proposed. This process is based on a gelation of a sodium alginate aqueous solution by sodium ion exchange with protons or multivalent metal ions. Dense Y-Ba-Cu-O superconducting fibers have been successfully fabricated by firing Y-Ba-Cu-alginate fibers at temperatures above 900°C. The fibers have shown a tensile strength of 192 MPa and an end-point critical temperature of 85 K.

KEYWORDS: superconductor, oxide ceramics, Y-Ba-Cu-O, fibers, precursor, alginate, gelation, ion exchange

Japanese Journal of Applied Physics
Vol. 28, No. 3, March, 1989
pp. 324 - 329

Role of Rare Earth Ions (Gd, Dy, Ho and Er) in Phase Formation and Superconducting Properties of $Ba_{1-x}Ln_xCuO_{3-y}$ Compounds

Shigetoshi OHSHIMA*, Hiroyuki ISHIDA** and Tokuo WAKIYAMA

Department of Electronic Engineering, Faculty of Engineering, Tohoku University, Sendai 980

Ba-Ln-Cu-O compounds (Ln=Gd, Dy, Ho and Er) were prepared by a solid-state reaction. The optimum sintering temperature for obtaining a single phase of $Ba_2LnCu_3O_{7-\delta}$ was different for each Ln element, and this temperature decreased with increasing atomic number of Ln. A single phase with the perovskite structure was obtained only around the $Ba_2LnCu_3O_{7-\delta}$ composition. T_c's of these compounds prepared by a solid-state reaction in air increased with increasing atomic number of Ln. T_c's of samples prepared in oxygen atmosphere were almost the same. The magnetic moment of $Ba_{1-x}Ln_xCuO_{3-y}$ compounds is associated with each Ln, and its value is in good agreement with the Ln^{3+} Hund rules free ion values.

KEYWORDS: oxide superconductor, rare earth ions, $Ba_{1-x}Ln_xCuO_{3-y}$, X-ray analysis, magnetic properties

*Present address: Department of Electronic Engineering, Faculty of Engineering, Yamagata University, Yonezawa 992.
**Present address: Mitsubishi Heavy Industries, LTD., Kamakura 248.

Japanese Journal of Applied Physics
Vol. 28, No. 3, March, 1989
pp. 330 - 333

The ac Magnetic Response of Superconducting $YBa_2Cu_3O_{7-x}$

Masaki SATO, Takashi KAMIMURA and Takao IWATA

College of General Education, Tohoku University, Sendai 980

The nonlinear magnetic response of a high-T_c superconductor $YBa_2Cu_3O_{7-x}$ has been investigated by the ac induction method. At temperatures below 80 K, the fundamental and the third-higher harmonic susceptibility components of both the pellet and coarse powder samples strongly depends on the field amplitude. Also, *M-H* curves exhibit a hysteresis which bears a similarity to that of hysteretic superconductors. These characteristics are absent in well-isolated particles. Around the transition temperature, susceptibility components have a behavior distinct from that at low temperature and the magnetic response is nearly reversible. The observed magnetic behavior is interpreted as a superposition of the bulk property and the effect of weak linkage of superconducting particles.

KEYWORDS: high-T_c superconductor, $YBa_2Cu_3O_{7-x}$, nonlinear susceptibility, magnetic hysteresis, weak linkage

DAILY RECORD

* Nihon Donaldson has developed a small classifier for research and development of high value-added powders of fine ceramics. It classifies particles in a cyclone by the difference between centrifugal force and fluid resistance and can classify sizes of 0.5 to 5μm.

* Professor Jun Akimitsu of the Physics Department, the Faculty of Science and Engineering, Aoyama Gakuin University, has developed a high temperature superconductive material of a new type of oxide system consisting of Ln(Nd, Sm, Eu), Ce, Ba and Cu, which has a tetrahedral and octahedral structure and Tc=43K.

* Toa Nenryo Kogyo K.K., jointly with Noritake Co., has developed a compound material of long-fiber reinforced ceramics which has excellent heat-resistance and mechanical characteristics. The compound material uses a mixture of polysiloxane with either SiN or mullite, with carbon fibers of the pitch system added as reinforcing fiber. Its bending strength is 850 to 980MPa.

* The National Institute for Research in Inorganic Materials has developed an inexpensive output stabilizing apparatus for manufacturing equipment of single crystals by the FZ method. The apparatus uses a personal computer and two digital voltmeters to suppress fluctuation in heating output.

* The National Institute for Research in Inorganic Materials has succeeded in synthesizing ball-shaped fine particles of diamond by the micro-wave plasma chemical vapor deposition method.

* Matsushita Seiko Co., Ltd., in cooperation with Matsushita Research Institute Tokyo, Inc. and Nippon Ceramic Co., Ltd., has developed a carbon dioxide sensor of solid state electrolyte type which can detect carbon dioxide in the air. The sensor consists of a plate-shaped sodium-ion conductive ceramic sandwiched between two gold electrodes to form an electric cell. Because it does not have an optical system in the sensor, the size has been successfully reduced.

* Saito Mokuzai-ten has developed and started marketing fire-resistant and fireproof houses, by using inflammable composite wood panels coated with liquid ceramics.

* Sikoku Chemicals Corp. has developed high-performance $AlBO_2$ whisker which costs about one tenth of SiC whisker, for FRP and FRM.

* Nichiha has developed a non-asbestos roofing material with a refractory outer material whose surface is coated with special paints.

* Professor Hiroaki Kanda of the Research Center for Advanced Science & Technology, jointly with Nippon Carbon and Sogo Keibi Hosho, have developed a new type of high sensitivity infra-red ray sensor which uses SiC fiber for sensory elements. SiC fiber has been widely used for structural material, but this is the first time that it has been used as an electrically functional material. The response time has been improved four fold compared with previously available ones.

* Isuzu Motors Ltd. has successfully developed heat-insulated turbo-compound engines and decided to commercialize them. The engines come in either gasoline or diesel type and are capable of a speed of 150km/h at 7000 to 8000 revolutions with combustion efficiency of approximately 50%.

* Sigmax Ltd. has developed and commercialized a bar-code label with extremely high anti-hydrofluoric acid characteristics which consists of a ceramics substrate sealed with about 1mm thick fluoride resin.

* Nagoya Municipal Industrial Research Institute has determined the composition ratio of optimal PLZT for use in actuators. The ratio for a high voltage transition sensitivity is 9/70/30 and that of smallest hysteresis is 15/45/55.

* Hokkaido University, Muroran Institute of Technology and Showa Shell Sekiyu Kyodo have developed an efficient production method of fine orbicular ceramics using the in-fluid ball production method. The method can produce ball-making sintering substances for spherical particles of average diameter from 180 to 480μm and with 1.05 to 1.02 sphericity.

* The superconductivity research group of the University of Osaka has discovered metal additives which greatly improve superconductive characteristics of superconductive oxide. In the Y system, addition of 3% Ag will improve Jc=375A/cm^2, Tc=85K in a magnetic field of 6700G, while in the Bi system, Jc is increased to about 30-fold with the addition of 20% Cu.

* Mino Yogyo has completed and started marketing a gas-burning shuttle furnace for fine ceramics. Its whole sintering process ranges from 60° to 1,800°C with atmosphere control selectable by a single action. The furnace can be operated unattended from ignition to extraction.

* Nakanihon Rokogyo has succeeded in Ti_3N_4 single-layer coating. The processing temperature is between 680° and 800°C and its margin of error including changes in mother material is less than 10μm.

* Taisei Corp. in cooperation with Dainippon Ink & Chemicals, Inc. has developed a high-ratio strength inorganic material HMC. HMC is a mixture of a compound of cement, silica and special additives added with heat-hardening melamine resin, which when heated gets hardened from the state of high viscosity fluid to a strength from three to four fold that of concrete.

* Nihon Chemical Kensetsu has developed ceramics pavement material allows rain water to permeate into the soil. The material consists of spherical ceramics hardened by epoxy resin.

* Dipsol, jointly with Assistant Prof. Watanabe of the Faculty of Engineering, the University of Chiba, have developed a new technique to form a metal ceramic film by exposing silicic acid water solution to laser radiation. Using an NdYAG laser and silicon acid water solution, the method can form a high-density, thick SiN ceramic film without using an electric field.

* Osaka Gas Co., has developed an artificial charcoal of ceramic which has the characteristics and shape of natural charcoal. With Al_2O_3 and SiO_2 as its base material and special metal oxides as additives, it emits far infrared rays while

being highly heat-resistant and resistant to rapid heating and cooling.

* The Metal Technical Research Laboratory has developed a rolling press technique to highly refine powders used for oxide superconductive cable material which rolls powders not only by conventional rolling but also by high-speed repetitive motion of the lower-stage rollers.

* Associate Professor Okabe of the Faculty of Engineering of the University of Tokyo, jointly with Associate Professor Nakayama of the Faculty of Engineering, the University of Kanagawa, has succeeded in the formation of a tunnel coupling of high temperature superconductors of the Bi system. Using oxide superconductor of the Bi system as the lower electrode, 7nm of Au, 10nm of insulating MgO and 200nm of Nb as the upper electrode are vapor-deposited by the electron beam vapor deposition method.

* Professor Naoe of the Faculty of Engineering, the Tokyo Institute of Technology, jointly with Associate Professor Hoshi of the Faculty of Engineering, the Tokyo Institute of Polytechnics, has succeeded in forming non-crystalline ITO thin film of good quality at a low 80° substrate temperature, using the faced target sputtering method.

* Hitachi Zosen Sangyo has commercialized water permeable ceramic pavement board in a technical tie-up with Crayburne Ceramics. The board has a dual layer structure with a porous upper part and dense lower part.

* The Government Industrial Research Institute, Kyushu, of the Agency of Industrial Science and Technology has developed a theory to predict aperture ratio and the number of contact points between particles from sphericity dispersion coefficients of powder-state particles, using a filling model of the powder body.

* Mitsubishi Electric Corporation has developed a ion-beam vapor deposition system that can form films using up to four different materials simultaneously or alternately in a hyper-vacuum tank of 10^{-10} Torr class.

* Osaka Cement Co., Ltd. has developed and commercialized fine ceramics powder which emits far infra-red radiation, and kills odor and germs.

* Toshiba Tungaloy Co., Ltd., in cooperation with the Government Industrial Research Institute, Nagoya, of the Agency of Industrial Science and Technology and Daimei Kagaku Kogyo, has established a production method for high-strength, transparent Al_2O_3 ceramics. The ceramic has an average bending strength of 110kg/mm, surface roughness of 0.03μm, and permits the reading characters of through 1mm thickness.

* Osaka Diamond Kogyo has discovered that high-brilliance blue light emission can be obtained by adding artificial flaws to diamond crystal.

* Nara Kikai Seishakusho, jointly with the National Research Institute for Metals of the Science and Technology Agency, has developed solvent ejection powders that firmly connect metal with ceramics. The powders were obtained by attaching Y powders electrostatically to Al powders and fixing the Y powders inside Al powders by impaction. The connectivity of the metal and ceramics has been increased to seven fold of the previously used process.

* Hitachi Ltd., jointly with Northwestern University in the United States, has developed an electronic microscope that has 10^{-10} Torr hyper-vacuum sample chamber and resolution of 0.2nm.

* The Electrotechnical Laboratory has developed a technique to increase Jc by 10 to 20 times by irradiating superconductors of the Y system with a carbon dioxide laser beam. A small portion of Sr is added to the superconductor of the Y system to increase the strength of marginal faces, and the laser beam is irradiated on the mixed sintered body to recrystallize it, so that c axis orientation can be improved.

* At the International Superconductivity Conference under the auspices of IBM Japan, Inc., a proposition was made about the possibility of a third particle which is not either a Fermi particle nor Bose particle in an AVB state, and is not found in the natural world.

* The British Architecture Research Institute has developed a new quick-hardening cement which is composed of crushed particles of blast furnace slugs mixed with HAC, to prevent variation in strength due to chemical transformation.

* The National Research Institute for Metals, in cooperation with Asahi Glass Co., Ltd., has produced a superconductive tape of the Bi system which has Jc= 2000A/cm^2 performance at 77K, using a technique of combining the DB method and rolling.

* Simon has developed and started marketing long-life, high-efficiency ozone generators using semiconductor ceramics for electrical discharge.

Statistics

Imports (From May 1 to 31, 1989)

Source: The Ministry of Finance
For the three highest-ranking countries
(UNIT 1000 yen)

Commodity & country	Current Month Unit	Quantity	Value	Cumulative Year To Date Quantity	Value
Natural graphite, in powder or in flakes, of a kind of which 75% or more by weight can pass through the sieve with an aperture of 105 microns					
CHINA	MT	497	31739	1862	101727
SRILANK	MT	-	-	-	-
USA	MT	14	4705	57	18312
TOTAL	MT	743	48809	2639	171338
Natural graphite, crystalline, in powder or in flakes, other than of a kind of which 75% or more by which can pass through the sieve with an aperture of 105 microns					
CHINA	MT	3090	382444	15535	1709531
SRILANK	MT	176	13207	716	45655
MADAGAS	MT	-	-	128	17119
TOTAL	MT	3623	442713	18726	2001706
Natural graphite, amorphous, in powder or in flakes, other than of a kind of which 75% or more by weight can pass through the sieve with an aperture of 105 microns					
R KOREA	MT	2600	47959	5057	95193
CHINA	MT	-	-	679	14329
N KOREA	MT	-	-	2978	39478
TOTAL	MT	2600	47959	8743	149364
Silica sands and quartz sands					
MALAYSIA	MT	37580	123321	128558	409206
INDNSIA	MT	-	-	-	-
AUSTRAL	MT	99938	379744	498399	1884058
TOTAL	MT	137863	523925	642828	2439127
Natural sands, other than silica sands and quartz sands					
TAIWAN	MT	29250	51690	219962	364875
SNGAPOR	MT	-	-	12360	44337
PHILPIN	MT	32	544	187	2215
TOTAL	MT	36703	79841	265088	486080
Quartz other than natural sands					
CHINA	MT	360	3509	2870	24864
INDIA	MT	1394	16325	9824	106937
THAILND	MT	-	-	-	-
TOTAL	MT	3322	90586	20636	379543
Kaolin					
R KOREA	MT	4584	48992	20703	199186
USA	MT	75154	2292407	284859	8515083
BRAZIL	MT	-	-	44072	1068851
TOTAL	MT	101271	2787708	427960	11427867
Aluminous shale					
CHINA	MT	1500	15921	40018	380148
TOTAL	MT	1599	20151	40166	386181
Other clays, other than bentonite, decolourising earths, fuller's earth, fire-clay and aluminous shale					
R KOREA	MT	1429	9054	5979	25617
CHINA	MT	844	8079	18402	174599
USA	MT	591	27162	2604	110522
TOTAL	MT	3282	62336	28616	376905
Andalusite, kyanite and sillimanite					
USA	MT	298	11764	1304	45256
CHINA	MT	-	-	-	-
S AFRCA	MT	3007	78636	14928	362237
TOTAL	MT	3305	90400	17432	433188
Chamotte or dinas earths					
R KOREA	MT	1000	14500	6430	91163
CHINA	MT	2500	23848	9494	87530
TOTAL	MT	3500	38348	17016	196291
Natural calcium phosphates, natural aluminium calcium phosphates and phosphatic chalk, ground					
JORDAN	MT	16500	153171	93000	814839
USA	MT	17062	172427	225659	2111397
MOROCCO	MT	41930	388531	125528	1162325
TOTAL	MT	121541	1269151	581271	5603389

Commodity & country	Current Month Unit	Quantity	Value	Cumulative Year To Date Quantity	Value
Natural barium sulphate (barytes)					
CHINA	MT	19734	187845	51042	466893
TOTAL	MT	19756	189405	56551	522068
Siliceous fossil meals (for example, kieselguhr, tripolite and diatomite)and similar siliceous earths, whether or not calcined, of an apparent specific gravity of 1 or less					
FR GERM	MT	0	905	0	3095
USA	MT	495	30211	2589	155782
MEXICO	MT	-	-	-	-
TOTAL	MT	495	31116	2620	159417
Flint					
CHINA	MT	1	1350	1050	23618
FRANCE	MT	1119	22682	4365	89563
USA	MT	-	-	2	217
TOTAL	MT	1210	26517	5723	120765
Dolomite not calcined					
R KOREA	MT	27154	88220	124469	384322
TAIWAN	MT	15552	45910	85711	234644
PHILPIN	MT	38334	103642	115444	320172
TOTAL	MT	110648	326569	497325	1404371
Natural magnesium carbonate (magnesite)					
CHINA	MT	-	-	599	4745
USA	MT	-	-	-	-
TOTAL	MT	-	-	599	5021
Magnesium oxide other than calcined natural magnesium carbonate					
CHINA	KG	-	-	6268039	309866
U KING	KG	-	-	41007	10742
FR GERM	KG	-	-	-	-
TOTAL	KG	423050	30693	9333126	508798
Magnesia clinker					
N KOREA	MT	-	-	5495	68879
CHINA	MT	22127	423600	139167	2477265
TOTAL	MT	25423	545533	149813	2750647
Fused magnesia, dead-burned (sintered) magnesia; calcined natural magnesium carbonate, other than magnesia clinker					
CHINA	MT	4058	59379	17568	259009
INDIA	MT	100	3314	100	3314
TOTAL	MT	4194	65021	17832	273214
Gypsum; anhydrite					
THAILND	MT	251934	787657	932288	2845042
TOTAL	MT	287290	890690	1082562	3361001
Plasters, calcined gypsum					
THAILAND	MT	342	6668	1530	28966
FR GERM	MT	40	1261	100	3105
TOTAL	MT	458	10089	1875	38901
Plasters, consisting of calcium sulphate					
USA	MT	44	4797	215	21873
ITALY	MT	-	-	-	-
AUSTRIA	MT	-	-	-	-
TOTAL	MT	44	4797	221	23134
Limestone flux; limestone and other calcareous stone, of a kind used for the manufacture of lime or cement					
FRANCE	MT	80	2250	357	9880
TOTAL	MT	80	2250	367	11412
Portland cement, white cement, other than cement clinkers					
TAIWAN	MT	-	-	-	-
TOTAL	MT	-	-	-	-
Portland cement, other than white cement and cement clinkers					
R KOREA	MT	176781	1165099	817310	5220655
TOTAL	MT	336140	2163422	1560597	9755276

Commodity & country	Current Month Unit	Quantity	Value	Cumulative Year To Date Quantity	Value
Hydraulic cements, other than portland cement, aluminous cement and cement clinkers					
R KOREA	MT	-	-	1200	7842
TOTAL	MT	8	884	1848	13344
Asbestos, not more than 33 yen/kg in value for customs duty					
ITALY	MT	126	3306	842	21474
CANADA	MT	244	6382	3471	99652
S AFRCA	MT	342	10957	1368	39167
TOTAL	MT	1897	57641	16443	499939
Asbestos, more than 33yen/kg in value for customs duty					
USSR	MT	4940	183062	16400	612562
CANADA	MT	6935	411815	33299	1953834
S AFRCA	MT	7426	395093	34890	1631542
TOTAL	MT	23913	1218274	106067	5220507
Mica rifted into sheets or splittings					
CHINA	MT	-	-	-	-
INDIA	MT	243	14455	1221	68385
USA	MT	1	2413	1	7746
TOTAL	MT	503	26940	2503	177329
Mica powder					
INDIA	MT	69	3203	219	10148
TOTAL	MT	1587	68925	5972	244695
Mica waste					
INDIA	MT	410	25311	1010	55432
SRILANK	MT	170	6704	590	22284
TOTAL	MT	580	32015	1798	100838
Talc, not crushed, not powdered					
CHINA	MT	24893	243527	159118	1711692
TOTAL	MT	29106	295558	190347	2060537
Fluorspar, containing by weight more than 97% of calcium fluoride					
CHINA	MT	23718	365705	104887	1447460
TOTAL	MT	34223	606826	123392	1823798
Leucite; nepheline and nepheline syenite					
CANADA	MT	24	1605	501	21458
TOTAL	MT	24	1605	4355	167526
Chromium ores and concentrates					
S AFRCA	MT	89311	901318	296314	2947414
TOTAL	MT	142842	2259891	541227	7475458
Titanium ores and concentrates, not roasted					
MALAYSIA	MT	13580	194750	85600	995646
AUSTRAL	MT	38365	1285042	78882	2905292
TOTAL	MT	74657	1739876	294855	5510029
Zirconium ores and concentrates					
MALAYSIA	MT	309	36229	2684	278336
S AFRCA	MT	3566	285810	10923	843533
AUSTRAL	MT	3510	276260	50963	3389468
TOTAL	MT	8385	673109	68120	4819260
Artificial corundum, sized grains					
CHINA	KG	3214900	206925	14254995	843335
AUSTRIA	KG	94000	17165	543250	85121
BRAZIL	KG	40000	4326	2663300	237877
TOTAL	KG	4539460	334474	21317655	1514431
Artificial corundum, other than sized grains					
CHINA	KG	2518050	132384	14168888	671610
HUNGARY	KG	315180	36395	2782680	306057
BRAZIL	KG	-	-	345000	31853
TOTAL	KG	3106137	195776	18047600	1088237

Commodity & country		Current Month		Cumulative Year To Date	
	Unit	Quantity	Value	Quantity	Value
Aluminium oxide other than artificial corundum, not including those intended for use in manufacturing aluminium					
FRANCE	KG	360055	43329	1088534	161039
FR GERM	KG	123270	41264	560276	172718
USA	KG	153037	91479	6018412	563560
TOTAL	KG	636362	176072	11177614	1061862
Cerium oxide					
FRANCE	KG	17640	18116	58600	80988
USA	KG	28806	18285	161341	153114
TOTAL	KG	67281	51177	309210	300208
Crude rare earth metal chlorides, of a kind used as a basis for the manufacture of chemical compounds of rare earth metals; lanthanum nitrate					
CHINA	KG	103000	25699	171000	36804
INDIA	KG	-	-	250000	40144
USA	KG	50555	54696	241190	248813
TOTAL	KG	279540	101926	1207081	415606
Yttrium oxide					
CHINA	KG	70650	207879	319390	906140
NORWAY	KG	-	-	326	3960
FRANCE	KG	1500	15399	26800	261335
TOTAL	KG	75150	249159	349556	1198281
Lanthanum oxide					
FRANCE	KG	17200	41709	84450	205662
TOTAL	KG	18722	43918	92972	221657
Silicon carbides, sized grains					
CHINA	KG	635400	69988	4973841	433831
NORWAY	KG	231120	42879	1323720	229735
USSR	KG	122500	9600	267040	18977
TOTAL	KG	1707905	223911	10170365	1163084
Silicon carbides, other than sized grains					
CHINA	KG	2650850	175301	8708885	561220
NORWAY	KG	41000	5094	185960	27160
TOTAL	KG	3695752	280578	11846576	874500
Manufactured by the vitrified method or the resinoid method excluding those with axles, of agglomerated artificial abrasives					
R KOREA	KG	-	-	6955	2287
ITALY	KG	26864	9569	71760	45483
AUSTRIA	KG	17303	15493	77911	70121
TOTAL	KG	61195	39817	268264	188127
Other millstones, grindstones, grinding wheels and the like, of agglomerated artificial abrasives (except diamond), n.e.s.					
TAIWAN	KG	12209	10075	44422	31420
ITALY	KG	16126	7831	24889	23226
AUSTRIA	KG	2039	2599	14406	17728
TOTAL	KG	37139	82416	132701	297605
Other millstones, grindstones, grinding wheels and the like, of agglomerated natural abrasives (except diamond), or of ceramics					
R KOREA	KG	15460	5461	15555	7479
ITALY	KG	1960	1168	1962	1443
USA	KG	3630	919	21618	5714
TOTAL	KG	21050	7548	62204	25700
Other millstones, grindstones, grinding wheels and the like, of natural stone					
FR GERM	KG	-	-	35	5925
TOTAL	KG	17845	4996	53062	21728
Hand sharpening or polishing stones					
FR GERM	KG	43	958	87	4274
USA	KG	2185	8112	6216	28979
TOTAL	KG	7728	9884	15872	36322
Natural or artificial abrasive powder or grain, on a base of woven textile fabric only					
R KOREA	KG	3270	1688	20725	13569
FR GERM	KG	47	1102	1327	4168
USA	KG	2387	4994	10637	36414
TOTAL	KG	5973	9449	35221	62790
Slag wool, rock wool and similar mineral wools (including intermixtures thereof), in bulk, sheets or rolls					
DENMARK	KG	7540	2697	24675	6279
TOTAL	KG	17116	10066	100514	50533
Mixture and articles of heat-insulating, sound-insulating or sound-absorbing mineral materials					
AUSTRIA	KG	-	-	-	-
USA	KG	35432	36597	182923	143236
TOTAL	KG	47509	80209	340153	284034

Commodity & country		Current Month		Cumulative Year To Date	
	Unit	Quantity	Value	Quantity	Value
Other articles of plaster or of compositions based on plaster					
TAIWAN	KG	8193	3330	29255	12399
ITALY	KG	7721	1489	42861	5435
USA	KG	13115	64415	24940	152505
TOTAL	KG	33370	75521	122454	219194
Other articles of cement, of concrete or of artificial stone					
TAIWAN	KG	1922	2091	2956	3386
ITALY	KG	169279	141214	490277	309682
TOTAL	KG	482676	229254	3277334	559169
Other articles of asbestos-cement, of cellulose fibre-cement or the like					
U KING	MT	19	1768	114	11001
TOTAL	MT	19	3199	114	12432
Cords and string, of asbestos, or of mixtures with a basis of asbestos or with a basis of asbestos and magnesium carbonate					
USA	KG	40	580	100	1355
TOTAL	KG	40	580	3435	3346
Brake lining and pads, with a basis of asbestos, of other mineral substances, or of cellulose, (parts of motor vehicles)					
FR GERM	KG	3089	7166	14950	37457
USA	KG	1404	1207	3930	13845
TOTAL	KG	29161	28954	173744	157899
Worked mica and other articles of mica					
INDIA	KG	23278	18772	114989	61785
TOTAL	KG	23278	18772	115502	63063
Non-electrical articles of graphite or other carbon					
U KING	KG	18159	103141	80397	491817
FR GERM	KG	17364	53577	38422	120900
USA	KG	66105	132709	138153	511381
TOTAL	KG	114679	356916	367145	1548127
Bricks, blocks, tiles and other ceramic goods of siliceous fossil meals (for example, kieselguhr, tripolite or diatomite) or of similar siliceous earths					
U KING	MT	-	-	19	13030
TOTAL	MT	16	1021	76	28347
Refractory bricks, blocks, tiles and similar refractory ceramic constructional goods, containing by weight, singly or together, more than 50% of the elements Mg, Ca or Cr, expressed as MgO, CaO or Cr_2O_3					
USA	MT	32	4468	141	45361
TOTAL	MT	159	62228	982	183322
Refractory bricks, blocks, tiles and similar refractory ceramic constructional goods, containing by weight more than 50% of alumina (Al_2O_3), of silica (SiO_2) or of a mixture or compound of these products					
CHINA	MT	299	7039	3101	82437
FRANCE	MT	-	-	-	-
TOTAL	MT	320	19132	3827	146377
Other refractory ceramic goods, containing by weight more than 50% of graphite or other forms of carbon or of a mixture of these products					
U KING	KG	16575	12853	41334	30357
USA	KG	13868	15759	28121	52083
TOTAL	KG	32973	33458	96536	113009
Other refractory ceramic goods, containing by weight more than 50% of alumina (Al_2O_3) or of a mixture or compound of alumina and of silica (SiO_2)					
FR GERM	KG	3660	9199	20699	50504
USA	KG	1603	4815	3530	18517
TOTAL	KG	14128	22204	98785	116023
Other refractory ceramic goods, n.e.s.					
U KING	KG	12801	9184	84173	64478
USA	KG	13818	19246	35885	63222
TOTAL	KG	55375	48679	263307	230349
Ceramic building bricks					
R KOREA	MT	161	4575	740	21991
AUSTRAL	MT	1897	43040	10235	246327
TOTAL	MT	2203	58107	11634	300980
Ceramic roofing tiles					
CHINA	MT	215	32571	434	61432
SPAIN	MT	-	-	17	846
TOTAL	MT	219	32811	481	63898

Commodity & country		Current Month		Cumulative Year To Date	
	Unit	Quantity	Value	Quantity	Value
Unglazed ceramic flags, paving, hearth or wall tiles, mosaic cubes and the like, n.e.s.					
R KOREA	MT	-	-	390	29152
FR GERM	MT	91	10502	515	57151
TOTAL	MT	759	75459	3591	384259
Glazed ceramic flags, paving, hearth or wall tiles, mosaic cubes and the like, n.e.s.					
FR GERM	MT	376	69791	1089	207157
SPAIN	MT	52	9920	364	44609
ITALY	MT	784	144403	4008	616553
TOTAL	MT	1791	299716	8224	1189974
Ceramic wares for laboratory, chemical or other technical uses, of porcelain or china, other than catalyst carriers intended for use in manufacturing catalyst					
FRANCE	KG	-	-	16	1391
FR GERM	KG	90	510	1852	9375
USA	KG	2615	51566	13056	251384
TOTAL	KG	2761	53491	15201	275554
Catalyst carriers, intended for use in manufacturing catalyst, other than those of porcelain or china					
FR GERM	KG	34200	23792	102600	70563
USA	KG	-	-	78999	68326
TOTAL	KG	44200	33539	201599	158120
Ceramic troughs, tubs and similar receptacles of a kind used in agriculture; ceramic pot, jars and similar articles of a kind used for the conveyance or packing of goods					
U KING	KG	135	1286	813	1922
TOTAL	KG	2248	4436	91059	24857
Tableware and kitchenware, of porcelain or china					
CHINA	KG	25618	13821	247570	79958
U KING	KG	124441	508922	444578	1852935
FR GERM	KG	8384	47997	73191	298310
TOTAL	KG	261082	861453	1180173	3615901
Ceramic tableware, kitchenware, other household articles and toilet articles, other than of porcelain or china					
R KOREA	KG	5620	8662	93674	43041
U KING	KG	28439	65911	148828	389556
ITALY	KG	35180	33855	104750	166671
TOTAL	KG	169846	218766	727423	1012858
Cullet and other waste and scrap of glass; glass in the mass					
TAIWAN	KG	498400	29748	1966883	115857
SNGAPOR	KG	91842	3854	518664	18845
FR GERM	KG	625	9036	2316	31475
USA	KG	21555	73863	67448	165963
TOTAL	KG	887004	143700	4004643	445753
Glass in balls unworked					
CHINA	KG	-	-	5000	370
TOTAL	KG	-	-	9945	2603
Rods of fused quartz or other fused silica					
U KING	KG	1375	17065	6490	81506
FR GERM	KG	567	8321	6674	82270
USA	KG	2061	22183	4734	42914
TOTAL	KG	4003	47569	17898	206690
Tubes of fused quartz or other fused silica					
U KING	KG	10643	30141	34032	88061
FR GERM	KG	19861	110613	83494	430334
USA	KG	106580	346032	401091	1316586
TOTAL	KG	139827	495748	527416	1873191
Glass in tubes, n.e.s.					
R KOREA	KG	87922	77711	598146	384248
USA	KG	27138	78389	288593	404014
TOTAL	KG	181554	170542	1239657	856091
Cast glass and rolled glass, in non-wired sheets, coloured throughout the mass (body tinted), opacified, flashed or having an absorbent or reflecting layer					
TAIWAN	SM	15192	9519	216461	134003
FR GERM	SM	59	3686	9865	22515
TOTAL	SM	47628	159466	381351	530866

Commodity & country	Current Month Unit	Quantity	Value	Cumulative Year To Date Quantity	Value
Cast glass and rolled glass, in non-wired sheets, but not coloured throughout the mass, opacified, flashed or having an absorbent or reflecting layer, more than 2.5mm in thickness					
TAIWAN	SM	3270	4480	15209	13426
U KING	SM	3612	73407	5147	188458
FR GERM	SM	50	4259	1953	20329
USA	SM	418	7620	8386	38310
TOTAL	SM	10843	92098	271004	426937
Drawn glass and blown glass, coloured throughout the mass (body tinted), opacified, flashed or having an absorbent or reflecting layer					
TAIWAN	SM	187	241	3666	3061
FRANCE	SM	1410	9435	7998	18937
FR GERM	SM	2018	7981	9645	32550
TOTAL	SM	6264	21014	68763	78746
Cast glass and blown glass, not more than 2.5mm in thickness, other than those of coloured throughout the mass, opacified, flashed or having an absorbent or reflecting layer					
CHINA	SM	36156	8985	94453	25279
USSR	SM	13680	3404	100620	25040
TURKEY	SM	8464	2558	45161	13465
USA	SM	47366	202987	130577	491154
TOTAL	SM				
Cast glass and blown glass, more than 2.5mm and not more than 4mm in thickness, other than those of coloured throughout the mass, opacified, flashed or having an absorbent or reflecting layer					
NEWZELD	SM	34570	15958	99018	44545
TOTAL	SM	36262	33200	110380	82798
Cast glass and blown glass, more than 4mm and not more than 6mm in thickness, other than those of having an absorbent or reflecting layer					
FR GERM	SM	1098	6302	2033	17343
TOTAL	SM	1584	6639	3515	22062
Float glass and surface ground or polished glass, in sheets, not more than 4mm in thickness, coloured throughout the mass, opacified, flashed or merely surface ground, non-wired, not having an absorbent or reflecting layer					
MALAYSIA	SM	18478	13366	41640	31790
BELGIUM	SM	29282	35872	144127	171639
ITALY	SM	-	-	-	-
TOTAL	SM	91648	106194	710555	658138
Float glass and surface ground or polished glass, in sheets, more than 4mm and not more than 6mm in thickness, coloured throughout the mass, opacified, flashed or merely surface ground, non-wired, not having an absorbent or reflecting layer					
TAIWAN	SM	3365	3999	5233	6901
MALAYSIA	SM	-	-	6555	7197
TOTAL	SM	14979	23399	137535	276221
Float glass and surface ground or polished glass, in sheets, more than 6mm in thickness, coloured throughout the mass, opacified, flashed or merely surface ground or having an absorbent or reflecting layer					
R KOREA	SM	-	-	-	-
THAILND	SM	-	-	177538	63357
NETHLNDS	SM	-	-	-	-
TOTAL	SM	1500252	764664	5824245	2811447
Float glass and surface ground or polished glass, in sheets, more than 4mm and not more than 6mm in thickness, non-wired, but not coloured throughout the mass, opacified, flashed, merely surface ground or having an absorbent or reflecting layer					
TAIWAN	SM	45256	46140	470022	474154
MALYSIA	SM	160366	146726	318896	291771
TOTAL	SM	288971	273003	1393075	1257671
Float glass and surface ground or polished glass, in sheets, more than 6mm in thickness, non-wired, but not coloured throughout the mass, opacified, flashed, merely surface ground or having an absorbent or reflecting layer					
TAIWAN	SM	2004	4704	3239	9021
TOTAL	SM	58386	79918	116675	193750
Glass of heading No.70.03, 70.04 or 70.05, bent, edge-worked, engraved, drilled, enamelled or otherwise worked, but not framed or fitted with other materials					
FR GERM	KG	107	335	34263	21516
USA	KG	29171	81242	83642	240639
TOTAL	KG	120903	106387	379159	343932
Toughened (tempered) safety glass, of size and shape suitable for incorporation in vehicles, aircraft, spacecraft or vessels					
U KING	KG	474	854	1366	2625
FR GERM	KG	1734	1643	7105	7268
TOTAL	KG	138706	53193	776730	284777
Toughened (tempered) safety glass, other than those of size and shape suitable for incorporation in vehicles, aircraft, spacecraft or vessels					
TAIWAN	KG	51848	3953	192988	23666
TOTAL	KG	99012	11331	524370	82047
Laminated safety glass, of motor vehicles					
CANADA	KG	112223	50946	231424	122426
USA	KG	936744	446800	4308873	2055066
AUSTRAL	KG	104210	49347	524240	245907
TOTAL	KG	1334629	666571	6120040	3080608
Ampoules of glass, of a kind used for conveyance or packing of goods					
USA	KG	-	-	62	597
TOTAL	KG	130	600	192	1197
Carboys, bottles, flasks, jars, pots, phials, and other containers, of glass, of a kind used for conveyance or packing of goods; preserving jars of glass; stoppers lids and other closures, of glass					
R KOREA	KG	646583	53381	3466392	287733
TAIWAN	KG	204361	23942	740889	72261
FRANCE	KG	95785	30782	241476	83126
TOTAL	KG	962466	119300	4581083	509776
Glass envelopes (including bulbs and tubes), open, and glass parts thereof, for electric lighting					
FR GERM	KG	-	-	1857	5082
TOTAL	KG	16973	15064	74859	81374
Glassware of a kind used for table for table, kitchen, toilet, office, indoor decoration or similar purposes, of glass-ceramics					
U KING	KG	-	-	56275	24701
FRANCE	KG	258928	143143	1398831	753317
USA	KG	89647	30585	3380841	116524
TOTAL	KG	270849	459905	1081296	1577433
Drinking glasses of lead crystal					
FRANCE	KG	176129	227617	542048	744110
FR GERM	KG	5365	20875	37727	121867
TOTAL	KG	270849	459905	1081296	1577433
Drinking glasses other than those of glass-ceramics or of lead crystal					
TAIWAN	KG	88239	20283	182392	46084
FRANCE	KG	367529	119247	1175327	470945
USA	KG	42935	22966	127027	64179
TOTAL	KG	1355045	492540	4556393	1777550
Glassware of a kind used for toilet, office, indoor decoration or similar purposes, of lead crystal					
ITALY	KG	-	-	9706	18046
TOTAL	KG	102055	217535	431995	997510
Glassware of a kind used for toilet, office, indoor decoration or similar purposes, other than those of glass-ceramics or of lead crystal					
FRANCE	KG	22509	61083	73370	152936
FR GERM	KG	3043	10164	24152	50783
USA	KG	13222	26276	32484	94025
TOTAL	KG	531182	458517	1852626	1648252
Signalling glassware and optical elements of glass (other than those of heading No.70.15), not optically worked					
FRANCE	KG	33846	11667	278450	99706
FR GERM	KG	12134	27304	70747	183697
AUSTRIA	KG	-	-	1564	11806
TOTAL	KG	59729	77474	452638	445475
Glasses for corrective spectacles					
USA	KG	1590	6183	26509	54850
TOTAL	KG	46493	78501	228475	379632
Clock or watch glasses and similar glasses, glasses for non-corrective spectacles; hollow glass spheres and their segments, for the manufacture of such glasses					
SWITZLD	KG	0	387	0	629
TOTAL	KG	12186	20085	77356	115314
Leaded lights and the like					
FRANCE	KG	-	-	1795	8254
USA	KG	283	822	1568	7154
TOTAL	KG	9179	14487	37209	92762
Laboratory, hygienic or pharmaceutical glassware, of fused quartz or other fused silica					
U KING	KG	550	7975	1642	25831
FR GERM	KG	19	2272	81	9081
USA	KG	1410	13000	4035	45391
TOTAL	KG	1991	25747	10674	106910
Laboratory, hygienic or pharmaceutical glassware, of the glass having a linear coefficient of expansion not exceeding $5x10^{-6}$ per Kelvin within a temperature range of 0°C to 300°C					
TAIWAN	KG	3845	18541	17686	78251
TOTAL	KG	22960	33578	123268	183759
Laboratory, hygienic or pharmaceutical glassware, n.e.s.					
U KING	KG	455	3111	5489	18432
FR GERM	KG	3711	9146	14238	41851
USA	KG	43442	68328	153552	302296
TOTAL	KG	67746	100820	237514	458102
Woven fabrics, including narrow fabrics, of glass fibres					
R KOREA	KG	45255		103580	
SWEDEN	KG	4514		9548	
USA	KG	33549		210356	
TOTAL	KG	115002		448897	
Parts of diodes, transistors and similar semiconductor devices, of photosensitive semiconductor devices, devices, of photosensitive semiconductor devices, including photovoltaic cells whether or not assembled in modules or made up into panels, of light emitting diodes or of mounted piezo-electric crystals					
TAIWAN	KG	6868	12887	13483	30505
TOTAL	KG	11944	40175	39295	177136
Electrical insulators of glass					
FR GERM	KG	-	-	-	-
USA	KG	934	704	4624	2891
TOTAL	KG	1054	989	4744	3176
Electrical insulators of ceramics					
SWEDEN	KG	537	1417	3311	11616
U KING	KG	376	1470	6408	25606
USA	KG	344	2638	2797	9799
TOTAL	KG	1612	6425	17322	70685
Electrical insulators, other those of glass or ceramics					
U KING	KG	-	-	859	2943
SWITZLD	KG	-	-	148	5376
USA	KG	19	6923	101	13885
TOTAL	KG	191	8505	1741	30043
Insulating fittings of ceramics					
U KING	KG	-	-	32	4748
USA	KG	81	7800	3989	84344
TOTAL	KG	776	11552	10623	104785
Insulating fittings of plastics					
R KOREA	KG	1670	2042	9772	9862
USA	KG	1324	17750	5595	113367
TOTAL	KG	5752	45826	34272	212666

Exports (From May 1 to 31, 1989) Source: The Ministry of Finance

Source: The Ministry of Finance

UNIT 1000 yen

Natural graphite	85 t	49461
Natural sands of all kinds	290 t	21842
Quartz (other than natural sands; quartzite)	3091 t	14895
Kaolin	803 t	37201
Bentonite	189 t	16370
Refractory clay	350 t	14382
Other clay	3495 t	115312
Andalusite, kyanite, sillimanite	25 t	5542
Mullite	917 t	51260
Chamotte, dinas earth	22 t	1294
Natural calcium phosphate	-	-
Natural barytes, barium carbonate	-	-
Siliceous fossil meals and similar siliceous earths	195 t	14067
Corundum, natural garnet and other natural abrasives	1222278 kg	62154
Flint	-	-
Dolomite, agglomerated dolomite	160 t	4155
Magnesia clinker	8803220 kg	451559
Gypsum and anhydrite; calcined gypsum and plasters	500 t	38668
Limestone flux and calcareous stone	91613 t	100157
Portland cement, other hydraulic cements	592234 t	2128963
Asbestos	6 t	1553
Mica, including splittings; mica waste	46 t	32196
Natural steatite; talc	88 t	9152
Crude natural borates and concentrates	120 t	9439
Feldspar	2833 t	31755
Fluorite	-	-
Leucite	-	-
Aluminum ore	-	-
Chrome ore	54 t	1848
Titanium ore	-	-
Zirconium ore	65 t	9334
Artificial corundum	2531755 kg	376292
Aluminum oxide	19784415 kg	972771
Beryllium oxide	-	-
Cerium compounds	80999 kg	71684
Rare-earth chlorides	-	-
Yttrium oxide	-	-
Lanthanum oxide	-	-
Silirundum	527853 kg	125988
Diamond grindstones (artificial, natural)	80758 kg	688858
Artificial abrasive materials	484428 kg	655208
Abrasive cloth, abrasive paper	380622 kg	590620
Slagwool, rockwool, oxidised wool and vermiculite	3288467 kg	555889
Plastering materials	238406 kg	20516
Cement, concrete artificial stone products	691429 kg	65580
Artificial asbestos and products	288112 kg	245692
Brake linings of asbestos for motor vehicles	508952 kg	521080
Worked mica and mica articles	113558 kg	159967
Carbon or graphite products	352400 kg	1750948
Heating-insulating bricks, blocks and titles	35 t	4601
Porcelain or refractory products for construction	4850 t	954139
Other porcelain or refractory goods	1603210 kg	1080257
Porcelain or refractory bricks for construction, bricks for floor	6 t	7365
Roofing tiles, chimney-pots and other construction materials	1444 t	60278
Piping conduits and guttering	-	219
Unglazed setts, flags and paving, hearth and wall tiles	-	1283037
Laboratory, chemical or industrial ware	403560 kg	2343731
Bathrooms, tableware and other articles used for domestic or toilet purposes, of porcelain or china	95608 kg	66783
Porcelain (tableware, bathroom ware)	2838738 kg	2254546
Pottery (tableware, bathroom ware)	4929298 kg	2009751
Glass in balls, rods and tubes, unworked	956123 kg	382741
Unworked cast or rolled glass	17626 m^2	14862
Unworked drawn or blown glass	22827 m^2	47638
Glass, surface ground or polished	364464 m^2	336159
Cast, rolled, drawn or blown glass	1264775 kg	985252
Toughened glass; laminated glass		
Carboys, bottles, jars, flasks, and similar containers of glass	337950 kg	102730
Glass envelopes (including bulbs and tubes)	17960796 kg	5578993
Glass inners for vacuum flasks or for other vacuum vessels	45603 kg	23050
Tableware or kitchenware of glass; glassware for toilet or office purposes	1299824 kg	700871
Illuminating glassware, signalling glassware	298850 kg	457012
Clock and watch glasses; glass spheres	20051 kg	203611
Bricks, tiles, slabs, paving blocks and other articles of glass	152952 kg	53632
Laboratory, hygienic and pharmaceutical glassware	19429 kg	107918
Glass fiber and articles made from glass fiber, yarns or fabrics	4994412 kg	2035006
Ceramic condensers	1478403 pc.	3503068
Mounted piezo-electric crystals	178270908 pc.	4606660
Optical fiber cable (of glass)	185609 kg	455392
Artificial graphite electrodes	7027999 kg	1983010
Carbon articles for electrical purposes	190404 kg	382680
Insulators	2265982 kg	1169723
Insulating fittings for electrical machines	231977 kg	554128

Production, Shipment and Inventory (From May 1 to 31, 1989)

Source: The Ministry of International Trade and Industry

Unit: Cement (1000t). Flat glass (intern of 1000 boxes). Toughened glass (1000m^2). Gypsum board (1000m^2). Asbestos slates (thousand pieces). Autoclaved concrete pipe(m^2). Other products(t).

	Production			Shipment			Inventory		
Items	May	Change over previous month(%)	Change over the same month of previous year(%)	May	Change over previous month(%)	Change over the same month of previous year(%)	May	Change over previous month(%)	Change over the same month of previous year(%)
Glass products									
Fundamenta	68092	99	115	60912	99	107	85313	108	115
Containers	203819	98	102	217496	97	102	236721	94	91
Tableware	13011	88	94	13600	89	89	34823	98	109
Ceramics									
Tiles	103656	94	109	112188	89	108	214743	102	106
Sanitary ware	14290	90	97	13026	84	105	22935	102	96
Electrical appliances	7564	83	95	7950	97	97	14689	98	80
Tableware	34234	99	99	34381	97	100	35223	98	93
Flat glass	3014	102	104	3165	96	108	6444	102	88
Toughened glass	4436	101	109	4462	93	109	3379	110	112
Glass fiber	16584	101	101	15437	105	105	14370	108	107
Glass filament	32928	110	115	26079	101	113	38980	105	115
Cement	5945	97	103	5867	97	104	3210	104	97
Centrifugal reinforced concrete pipe	199398	94	96	138719	82	94	924729	108	111
Prestressed concrete pile	602739	97	105	609058	97	111	1136007	100	102
Concrete blocks for revetment	477303	83	100	376238	74	107	1170172	111	98
Concrete products for pipe	668988	94	107	517248	74	102	1874446	112	110
Autoclaved light weight concrete	318808	104	111	301192	100	110	228756	108	111
Asbestos slates	7042	97	103	6805	92	97	13535	104	120
Refractory bricks	78850	97	100	76755	96	92	118996	103	96
Castable refractory products	67713	94	103	70587	93	103	27690	100	89
Solid electrode	14738	87	100	13396	87	78	19178	107	97
Grinding stone	5651	96	108	5528	91	104	4942	107	92
Gypsum board	39432	88	102	41053	102	108	17303	91	92

Journal of Robotics and Mechatronics

Vol.1 No.1 June 1989

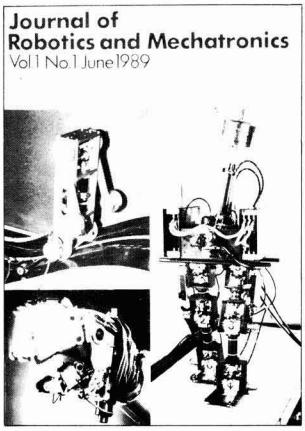

Otto Schott Research Award

1991

In 1991 the Ernst Abbe Fund will be presenting the Otto Schott Research Award for the first time. It will be awarded for outstanding achievements in basic research and application within the field of glass and glass ceramics. The sum of

DM 50.000,--

has been allocated to the award.

Qualified, preferably young scientists are eligible for this award; achievements of individuals and small groups can be considered. Direct applications will also be accepted from the candidates themselves.

Recommendations and personal applications should be sent before

31th January, 1990,

enclosing a review of the scientific work on which the application is based, a curriculum vitae and a brief outline of the candidate's scientific career, to the following address:

Ernst-Abbe-Fonds
c/o Stifterverband für die
Deutsche Wissenschaft
Brucker Holt 56–60
Postfach 23 03 60

D-4300 Essen 1
West Germany

ERNST-ABBE-FONDS

Member of the Donors' Association for the Promotion of Science and Humanities in Germany